Phase and polarization changes of pulsed Gaussian beams during focusing and propagation

PhD thesis

By

Balázs Major

Supervisor

Zoltán Horváth

associate professor

Department of Optics and Quantum Electronics, University of Szeged

Advisor

Miguel A. Porras

associate professor

Departamento de Energía y Combustibles, Universidad Politécnica de Madrid

Doctoral School of Physics

Department of Optics and Quantum Electronics

Faculty of Science and Informatics

University of Szeged

Szeged

2016

Contents

Chapter

One

Introduction

Light is an essential element for life, and not just by reason of being the primary energy source of Earth's flora, and through plants and unicellular organisms of its whole fauna, but also by serving as the most important intermediary agent between our planet's residents and their habitat. By asking the simple question which always served as the main driving force for science, "why?", one can simply arrive to the answer which also enlightens the rationale behind the usual experience that light is an indispensable tool for research in all scientific disciplines. This answer is the fact that almost all phenomena we can observe in our universe arise from the interaction of two physical entities: electromagnetic radiation and matter. Visible light is, of course, just a small segment of the broad set of electromagnetic waves, and the other slices of the spectrum are at least as important as the optical regime, but light[I] plays a fundamental role, as seeing is our dominant method for observation, not only by accident. Instead, it is evident, as the physical, chemical and biological mechanisms, which we encounter in our everyday life, are accompanied by the emission or absorption of light. As such, observing the interaction of light and matter gives us an evident way to study nature and its processes scientifically.

Necessarily, to carry out these investigations effectively, we have to know the participants of this interplay well enough. In the history of science, the study of light and matter dates back to ancient Greece, which is probably safe to say also when dealing with any of the different topics concerning the history of science. However, if we set aside from

[I] The term "light" in physics is ambiguous as sometimes it refers to any kind of electromagnetic radiation, and other times it only means the radiation from the wavelength regime that is visible to human eye. Although considerations presented in this work are primarily related to the visible range, this uncertainty of meaning is not resolved here since — by the similar nature of the different electromagnetic radiations — most of these findings can be applied to electromagnetic waves of other wavelengths.

the philosophical considerations of this ancient epoch, and jump to the early modernity of the 17th century, we already arrive to an era where in the mind of some scientist, like René Descartes, light and matter share very similar properties. Even though having this modern idea already, several of their thoughts of light, for example, turned out not to be long-standing. On the other hand, as an example of their incontrovertible merits, they (as well as other similarly influential predecessors and contemporaries not mentioned here) initiated the way of thinking that later, in the next three centuries, led Christiaan Huygens and Augustin-Jean Fresnel on their way laying down the foundations of the wave theory of light, or helped Ernest Rutherford and Niels Bohr to shape their model of the atom. Innumerable colleagues and companions of Albert Einstein and Werner Heisenberg contributed to the physics of light and matter as we know it nowadays, and which incorporates the similarity in behavior of these two entities, the seed of which appeared centuries earlier in the discussions of Isaac Newton.

In 1960, just a few decades after the birth of quantum theory and a whole new bunch of questions, a new experimental device, the *laser* was created. This new appliance, that was reported to be "a solution looking for a problem" after its invention[II], became one of the most important tools to further broaden our knowledge of light and matter, or the field ultimately connecting them, quantum science.

The laser, the apparatus which emits light with extraordinary properties, has since been further developed to meet the demands of curious scientists. And not just the needs of those researchers whose interest is "limited" to the complicated quantum physics, but also for the ones who aim to gain knowledge of subjects that are more tangible than quantum mechanical wave-packets, like biological samples, chemical compounds or nanometer-size artificial material structures.

One of the exceptional features of lasers, that scientists frequently utilize, is the ability to produce packets of light with extremely short duration. The importance of this capability lies in the fact that it opened the gate to electric field strengths and time scales which were unavailable before the laser came on scene. For this reason a few diagrams almost always appear in lectures dealing with the advancements of laser technology which illustrate how the peak intensity (temporal duration) of the generated laser pulses increased (decreased) in the last 50 years[III]. A feature that can be deduced from the two charts mentioned is that while the pulse duration in the optical regime is approaching its physical limits nowadays, the strength of the obtainable electric field is still increasing

[II] For a short sketch about the circumstances of the birth of the laser, see: Charles H. Townes, "The first laser," in *A Century of Nature: Twenty-One Discoveries that Changed Science and the World*, University of Chicago Press. pp. 107–112 (2003).

[III] For such diagrams see, for example, Figures 6 and 8 in: T. Brabec and F. Krausz, "Intense few-cycle laser fields: Frontiers of nonlinear optics," *Reviews of Modern Physics* **72**, 545–591 (2000).

and is predicted to be considerably increased in the near future.

Even with the more and more sophisticated technology and the increasingly amplified optical pulses one thing is inevitable to carry out the experiments performed with lasers in our days: *focusing* of the laser beam. Now going back to the thought that emerged earlier, that is, to use light as a tool for our investigations we have to know its properties well enough for the purpose, a question of great importance arises here: how much do we know about the "tool" we use? Even setting aside questions about the laser system itself and the optical setup between the light source and the focusing element, both of which are usually considered to be to a great extent under control, we still have one step short of ability to actually use it in an efficient manner. And here we arrive to the question that this dissertation, at least in some points, sets out to answer: "how does focusing affect pulsed beams?".

As a settling to this philosophical introduction and as an outline of the present work, the contents of this thesis can be summarized in the following main points. After a short introduction to the history and development of pulsed laser systems, a review of various recent applications of few-cycle optical wave packets is presented, all of them being closely related to the findings in this work. After that, a quick overview is given on the characteristics of pulsed waves that are further investigated in the following pages. The chapter dealing with the scientific background of this topic ends with the description of methods used for modeling or measuring specific features of pulsed beams during propagation or focusing. Finally, the motivational aspects and the scientific background are followed by the scientific achievements to which the author has contributed.

Chapter
Two

Scientific background

While lasers are relatively new inventions of humanity, the properties and descriptions of phenomena related to light have been the subject of scientific studies for centuries. Even so, as a beginning, the present chapter deals with the device that was first built by Theodore Maiman. More profoundly, the first sections discuss what this technology has become since then, and how the duration of the laser pulses became shorter and shorter during the decades. Then it is put into the bigger picture, into the discussion of the theories dealing with light, especially its diffraction, propagation and focusing, the effects laser itself is based on. At first sight, it could be argued that this is like starting *in medias res*, as light produced by lasers is just a special example among optical phenomena. However, this ordering serves an analysis better for which laser is mainly a motivation, and the findings presented later are based on the description of electromagnetic waves. After this latter, following the introduction to the theory on pulsed beams, some experimental methods are gathered which are used to study the discussed theoretical findings.

2.1 Few-cycle pulses and their applications

The subject of this thesis is ultrashort[I], few- and sub-cycle electromagnetic wave forms. These scientific tools have been serving humanity for only a few decades. Before carrying

[I] The term "ultrashort" is again ambiguous. It can be easily explained by the fact that as laser pulses got shorter and shorter, ultra got newer and newer interpretations when followed by the word short. Still, ultrashort is most widely used for pulses with less then a picosecond duration, in some cases even also for several picosecond-long wave packets (the expression begin to spread during the appearance of picosecond techniques). In this work it is as a synonym for femtosecond optical pulses, mostly referring to the sub-100-femtosecond regime.

out a more specific analysis on their characteristics, it is important to summarize the path that led to their realization. In the following, a short sketch is presented on the history and applications of lasers and technologies based on (or related to) them, with the aim to sum up the scientific topics related to the findings presented in this work.

2.1.1 The route to phase-stable, few-cycle optical sources

The first working laser was built in 1960 by Theodore Maiman [1], based on the proposal of the inventors of the maser [2, 3][II]. This first realization, the ruby laser, was only capable of pulsed operation. Ironically, this led to the fact that a high priority problem to solve was to make a continuously operational laser (the well-known helium-neon gas laser [4]), before the advantages of a pulsed application were envisioned.

The first step towards the controlled pulsed output of the ruby laser came just two years after the experimental demonstration of the laser principle, and this step was the attainment of Q-switching [5]. However, by temporally separating the pumping and the lasing process in an oscillator only the nanosecond (10^{-9} s) pulse duration and a few hundreds of kW peak power were achievable at that time [6]. As varying the quality factor of a resonator means a non-steady state condition of the laser, the pulse duration in this case is limited by dynamical factors, for example by the cavity decay time [7]. Even with this restriction, the picosecond (10^{-12} s) regime was accessible at the end of the 1980s using dye lasers, smart ideas and the development results of decades [8–10]. Still, the limitation mentioned before did not give an opportunity to significantly further shorten the laser pulses obtained by Q-switching.

Luckily, another technique was introduced almost concurrently with Q-switching. The idea of mode-locking, that is exploiting the broad bandwidth of the gain medium and the multi-mode operation of the laser oscillator, came up in 1964 [11]. Continuous advancements in laser technology and the discovery of new laser materials led mode-locked lasers to reach the few tens of femtoseconds (10^{-15} s) duration in the last decade of the 20th century [12, 13]. Soon, commercial solid-state lasers producing sub-100 fs pulses became available [14, 15]. By the invention of chirped mirrors in 1994 [16], sub-6 fs pulses were obtained directly from a titanium-sapphire laser oscillator [17]. This means only two cycles of the carrier wave, approaching a boundary set by the bandwidth of the laser medium through the Fourier theorem [18].

[II] An often forgotten contributor to the creation of laser, who gave this name to the device itself, is Gordon Gould. Even if the source of the idea for the laser can be questioned, it is indisputable that Theodore Maiman was the first to build a working laser and publish this result (first turned down by Physical Review then appearing in Nature). However, for the inquisitive, the decades-long trial of Gould trying to obtain legal justification of his leading role in the invention of laser is summarized in detail in: Nick Taylor, "Laser: The Inventor, the Nobel Laureate, and the Thirty-Year Patent War," Simon & Schuster Adult Publishing Group, 2000.

To overcome the restriction imposed by the gain material used, that is to obtain a broader spectrum, several ideas were introduced. One of these solutions is to utilize the non-linear response of a material, made available by the high intensities of the laser beams thanks to the different amplification schemes developed meanwhile [19–21]. To gain spectral broadening by self-phase modulation [18, 22, 23], for example, the core of a single mode fiber [24], or a noble gas filled into a hollow-core fiber [25], can be used. Harnessing the ever increasing pulse energies, it was shown later that this type of pulse shortening is possible — even with self-compression of the produced wave packet — without the always laborious task of coupling into a fiber [26, 27], thanks to the filamentation of the beam [18, 22, 28]. Another option often applied is to use optical parametric amplifiers [18, 22, 29], which even gives the possibility of wavelength tuning [30]. These methods, which are well optimized and are reaching a mature age nowadays, are still not the state-of-the-art in short optical waveform generation, as they remain restricted by the Fourier theorem, but this time not due to the amplification bandwidth of the material, but through the limited effective bandwidth of the nonlinear response of the material.

A recent solution to get around this limit is to coherently combine the output of several sources operating in different wavelength regimes. For an arbitrary waveform generation [31], that is, to produce controlled wave packets of light, the latest realizations are the so-called "optical waveform synthesizers" [32]. This type of apparatus has been carried out, for example, by the split manipulation and coherent addition of supercontinuum sources [33], discrete harmonics [34], independent mode-locked lasers [35], fiber lasers [36], or optical parametric systems [37]. All these solutions provide the possibility to produce sub-cycle wave forms [32], that is, to obtain wave packets that are so short in duration, that even a single oscillation of the carrier wave can not fully take place during this time.

The optical sub-cycle sources mentioned above are the current state-of-the-art in respect of the number of cycles of the carrier wave under the envelope (see Figure 2.1 for the explanation of the terms "carrier" and "envelope"). Certainly, there are other wavelength regimes where single-cycle pulses became available in the last decade, for example using terahertz [38] or attosecond (10^{-18} s) [39] pulse generation, but they are less wide-spread and their applications are not as diversified as those of pulsed lasers. As most of the phenomena discussed in this thesis mainly affect such sub-, single- and few-cycle electromagnetic wave forms, the optical regime is what currently mostly related to the results presented.

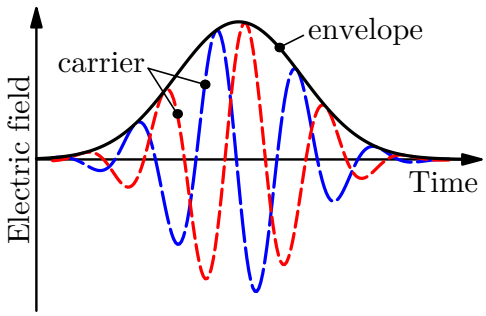

Figure 2.1. A few-cycle pulse with its envelope and two possible variations of the carrier wave.

It is unavoidable to mention that, of course, if someone regards shortness as the absolute duration of an electromagnetic wave packet, there are other type of solutions that surpass the femtosecond-long pulses of lasers. By setting up broadband electromagnetic sources which produce radiation with higher frequencies than in the visible domain and its direct neighborhood, duration much less than a femtosecond is available. The first experimental demonstration of sub-femtosecond optical wave form was published more than decade ago [40], and several methods of high-harmonic generation yielded isolated, attosecond-long pulses of ultraviolet radiation since then [41]. Even the zeptosecond domain may become achievable in the near future [42]. However, as these pulses are mainly generated with the help of lasers, they are a topic of a later section in this work.

Naturally, there are other ways of producing pulsed light than the lasers discussed in detail. The free-electron lasers serve as an important cousin of conventional lasers, with almost the same age, and which tools — true to their name — use free electrons instead of bound ones for light amplification. They provide high energy short pulses with a single amplification step, but they are far from table-top systems and their pulses are far from few-cycle, yet. However, X-ray free-electron lasers may provide few-cycle pulses in the X-ray regime in the future [43], even with stable phase [44].

The expression mentioned at the end of the previous sentence, the term “stable phase”, is an important feature, as the phase of optical pulses is a main topic of this thesis. By phase stability of laser oscillators it is usually meant that the so-called carrier-envelope phase (CEP) of the pulses leaving the laser source change by a known, fixed value from one pulse to another [45]. This aspect became important at the turn of the millennium, when few-cycle pulses became more widespread and it was realized that the physical phenomena studied with these wave packets depend on the exact temporal variation of the electric field [17]. As such, it heavily relies on the phase stable production of the optical wave packets whether an experiment is reproducible. What is exactly meant by CEP, however, is ambiguous, primarily when studies related to pulse trains and single pulses are compared to each other. When a single pulse is considered, CEP means a relative phase of the carrier wave with respect to the envelope, on the contrary to its already mentioned meaning for pulse trains regarding their phases relative to each other. For a more visual representation, two pulses that have the same envelope but different phase properties related to CEP can be seen in Figure 2.1. A more detailed discussion on the definitions and experimental determinations of CEP is presented in later sections. The important feature here is that the pulses originating from the laser system can be almost exactly the same at the electric field level, thanks to the different active and passive phase-stabilization schemes of the laser oscillators and amplifiers developed in the last two decades [31, 45, 46].

2.1.2 Applications of ultrashort and few-cycle wave forms

Applications of ultrashort laser pulses are numberless. For this reason, mentioning all the various utilizations is almost impossible. Apart from their evident usage in physics, for example in the hot topic of attophysics [47], they are important tools in other fields of natural sciences. For instance, if the considerations are restricted to basic research, ultrafast laser technology is what made the birth of the Nobel-prize winning topic of femtochemistry possible [48]. Also, femtosecond lasers allow biologist to study the dynamics of the most important light-induced biological processes in nature, like photosynthesis [49]. In areas that are closer to everyday life or direct applications, femtosecond lasers have shown their beneficial properties in material processing [50]. In addition, medical utilization is manifold as well, people just have to think about the therapeutic [51], surgical [52] or imaging methods they are used for [53].

As mentioned earlier, few-cycle pulses are quite new results of laser technology, but it has been shown already what advantages they have in the areas mentioned in the paragraph before. The benefit is not just the most obvious higher temporal resolution in the studies of femtochemistry and femtobiology. They also provide a better quality of the generated patterns in material science [50], or higher resolution in related optical imaging techniques, for example in optical coherence tomography [54].

A highlight of the important contributions of few-cycle pulses to research and applications is that they paved the way for a new scientific field, attosecond physics and -metrology [47, 55]. The origin of the name is simple: the short duration of the few- and sub-cycle optical wave forms and the attosecond pulses produced using them make it possible to directly study physical phenomena happening on the time-scale of electron motion, which is the order of a few (tens of) attoseconds. This is also the area where the importance of the exact temporal variation of the electric field in the electromagnetic pulses showed up. The influencing effect of the phase (or the CEP — this is how often it is referred to) has already showed up in high-harmonic generation [56–58], in the phase-sensitive nature of photoemission [59–61], in surface-plasmon electron acceleration [62], or during the generation of photocurrents [63].

It must not be forgotten — when the properties of the electromagnetic field is considered — that both the electric and magnetic fields are vector fields, so these physical quantities do not possess only amplitudes, but they have directions as well. As a result, these waves are characterized also by their polarization. Of course, the control given by this additional degree of freedom is exploited not just to provide three-dimensional experience during watching films in movie theaters, but also in the different areas of femtosecond sciences. Using pulses with more complex polarization states than linear can yield polarization-formed terahertz fields [64], or can help to reach optimal control on the

irradiated molecules or other materials, which is often mentioned as a way of coherent control [65–69]. On a similar basis, polarization control showed to be advantageous in pump-probe measurements of two-dimensional spectroscopy techniques [70, 71]. A femtosecond pulse with a given time-dependent polarization state is also a widely used tool for isolated attosecond pulse generation [41], and a polarization-shaped pulse has been proposed as a tool for CEP determination [72].

There is a common point in all the applications listed in the previous few paragraphs: the pulses are always focused. This is necessary because the intensities that are needed to observe the desired phenomena can only be achieved by focusing [47]. The effect of focusing on laser pulses, that is, how the carefully shaped wave packets change while they propagate from the focusing element to the focal point has been examined for decades, and the focusing attosecond pulses has also been the subject of studies recently [73, 74]. The material of the lens [75], the aberrations of the focusing systems [76], or the Gouy phase shift [77] — this latter being a general property of beams — can affect the spatio-temporal evolution of the electric field in the focal region [78]. The result of these changes — primarily affecting the phase properties — has been directly shown, for example, in attosecond pulse production [79], or in optical coherence tomography [80].

Taking into account the polarization of the wave, it has been known for a long time how the rotational symmetry of the intensity distribution in the focal region may disappear during tight focusing, due to the vector nature of the field [81]. The change in the polarization state and the appearance of a longitudinal components in case of non-paraxial waves is also well-known [82]. With the appearance of polarization-shaped ultrashort pulses [41, 67, 68], that is, with the usage of pulses with more complex or even time-dependent polarization states, how the field vector changes or how it can be controlled during focusing has become an important question too [83].

In the applications of ultrashort optical pulses the interaction of light and matter often happens in a larger volume, not just in a point in space or at a thin surface. In this case one has to take into account how the short wave packet propagates, changes its properties during its travel through the volume, and how this affects the phenomena in question. A general propagation issue of nonlinear optics — again a broad field enabled by ultrashort lasers — is phase matching [22], which is decisive in effective frequency mixing [22], or in efficient generation of high-order harmonics [84, 85]. As an other example, propagation dynamics also play crucial role in laser wake-field acceleration [86]. If one considers the CEP-characteristics of the few-cycle focused field, the variation of the CEP while the pulsed light travels in space is an important concern in terahertz emission from air plasma [87]. The changes of the electromagnetic field in these examples are, of course, not solely determined by how the focused electromagnetic field would vary in time and space, as the

interacting nonlinear material also influences the field as it behaves as a dipole source. Yet, the phase changes during free-space propagation of focused beams always appear as a separate term in the simplified equations of phase matching [84, 85]. As an implication, it is an important question how ultrashort, few- or sub-cycle electromagnetic pulses change their properties while they travel from the focusing element to the interaction point, or while they propagate in the focal region.

2.2 Description of ultrashort pulse properties

A very important step when describing and explaining a physical phenomenon is to choose the proper method to do it. Finding the right approach usually means finding the appropriate approximation. It is easy to understand, since most problems would be so complex without these simplifications, that they could not be solved (in an acceptable amount of time), or the tool used could not be called physical "model" anymore, as it would be something as complicated as the studied system itself. A common argument for simplifications is that the phenomenon is analyzed from only a point of view. This marked feature that is involved in this thesis is the wave nature of light. This means that in this section models are considered where quantum physics does not play a role. This is of course the case — in the questions studied in this work — as far as there is no interaction between the electromagnetic field and matter, and as the number of photons is so vast, that the quantum effects wash out. On the other hand, this gives some generality to the models presented in this section, as any analogous phenomena that possesses wave attributes can be described similarly. As specifically *pulsed* waves are the subjects of this study, it is an important first step to describe what they are. So, to start with, the most relevant general features of the temporally short wave packets are discussed.

2.2.1 Ultrashort wave packets

It was referred earlier that the propagation, interference and diffraction of light has been extensively studied a way before the appearance of lasers. To study these effects in the case of the ultrashort pulses emitted by lasers, it would be a nonsense to ignore the already available knowledge. However, one should be careful, as those studies usually only considered (quasi-)monochromatic light. The question is then how to apply the methods developed for monochromatic (infinitely long pulses of) light to the short wave packets. The answer is found in a mathematical transformation named after the French mathematician Jean-Baptiste Joseph Fourier. He was looking for a solution of the heat equation when he recognized that some functions can be written as a series of trigonometric functions [88] (not surprisingly the idea can be found in works of ancient Greek astronomers

as well [89]). This theory has since been developed into Fourier analysis, an important tool for mathematics, physics or engineering, and a link between electromagnetic pulses and harmonic waves.

While the Fourier theory is well-known and straightforward, there are some considerations and conventions in the treatise of few-cycle pulses which need clarification. A first important point is that, although the electric field depends both on spatial coordinates and time, for this step the spatial dependence is omitted, as it is not relevant in this case. For the sake of simplicity, the Fourier transform is applied on scalar functions here, but it can be easily generalized to vector quantities. The magnetic part of the electromagnetic field is not considered either (throughout this work), as it would be relevant only in relativistic interactions of light and matter.

While the electric field is a real quantity mathematically, it is convenient to use a complex representation instead [18, 90]. By applying the Fourier transform on the complex[III], time-dependent electric field $\tilde{E}(t)$, one can get the complex spectrum of the field by

$$\tilde{U}(\omega) = \mathscr{F}\left\{\tilde{E}(t)\right\} = \int_{-\infty}^{\infty} \tilde{E}(t)\exp[\iota\omega t]\ \mathrm{d}t\,. \tag{2.1}$$

The magnitude $|\tilde{U}(\omega)|$ of the complex spectrum tells what is the amplitude of the harmonic component with angular frequency[IV] ω, and its argument $\arg\left[\tilde{U}(\omega)\right]$ defines the (relative) phase of the monochromatic wave. From the spectrum $\tilde{U}(\omega)$, the time-dependent electric field can be readily obtained by inverse Fourier transform[V] according to

$$\tilde{E}(t) = \mathscr{F}^{-1}\left\{\tilde{U}(\omega)\right\} = \frac{1}{2\pi}\int_{-\infty}^{\infty} \tilde{U}(\omega)\exp[-\iota\omega t]\ \mathrm{d}\omega\,. \tag{2.2}$$

Using the complex, analytical representation instead of the real field $E(t) = \mathrm{Re}\left[\tilde{E}(t)\right]$ has several advantages. First of all, it allows one to use the original mathematical definitions (2.1) and (2.2) of the transformations regarding the integration limits [91]. As a more physical argument, by applying the Fourier transform on the analytical signal

[III] The complex representation is used in this work during the mathematical treatment of electromagnetic fields. To distinguish complex variables from real ones, a tilde represents complex numbers throughout these pages. The imaginary unit is symbolized by ι.

[IV] Even though "frequency" and "angular frequency" are not synonyms in physics, angular frequency ω is often referred only by the word frequency as the physical quantity $\nu = \omega/2\pi$ is only used a few times in this work, and in those cases it is directly stated, for example by using the Greek letter ν instead of ω.

[V] There are deviations in the exact definitions of Fourier and its inverse transformation in the literature. Sometimes the $1/2\pi$ factor is applied in the direct transformation instead of the inverse, or symmetrically a $1/\sqrt{2\pi}$ factor is applied both directions. The sign in the exponent can also be interchanged. These mathematical differences, however, do not introduce any changes in the physics behind. The only thing needs attention to get physically accurate results is if someone expresses the temporal evolution of the monochromatic electric field with a given sign convention, the same sign should be used in the exponent of the transform giving the field in time (inverse Fourier transform in this work).

instead of the real one, the resulting does not contain nonzero values at negative frequencies, which are physically not meaningful in this case [18]. It is also better in a practical sense, which originates from the fact that until the single-cycle regime is not approached, the spectrum of the pulse contains relevant components only in a tight frequency range. This means that to obtain a consistent result during the numerical evaluation of (2.2) the integration range is halved compared to the real case.

This mathematical theory named after Fourier gives a general way to decompose pulsed waves into the superposition of harmonic ones [92], and this gives a simple and frequently used method to solve problems of propagation and diffraction of wave packets. First, one has to assume an initial spatial and temporal distribution of the field at a plane or surface (or to be precise, spatio-temporal distribution, if spatio-temporal couplings are present [93]). After transforming the problem to frequency representation, the field in the region of interest can be calculated with laws for harmonic waves. Finally, the temporal evolution at any point can be obtained by inverse Fourier transformation. This approach is used, for example, in nonlinear pulse propagation models [94], or during solving diffraction phenomena of wave packets [93], which latter is a main subject of this thesis. While the physical consistency of such initial-value problems can be questioned in nonlinear propagation schemes due to backward propagating waves [94], such inaccuracies are easier to avoid when dealing with diffraction in free space.

Turning back to ultrashort pulses, there are some additional points needed to be mentioned. A well-established representation of pulsed wave forms is to separate them into an envelope and a carrier function (as depicted already in Figure 2.1). When considering the complex electric field this means a decomposition that can be written as

$$\tilde{E}(t) = \tilde{\mathcal{E}}(t)\exp[-\iota\omega_0 t] = A(t)\exp[\iota\hat{\varphi}(t) - \iota\omega_0 t] \ , \tag{2.3}$$

where $\tilde{\mathcal{E}}(t)$ is the so-called complex temporal envelope, ω_0 is the angular frequency of the harmonic carrier wave (central frequency or carrier frequency). The second step in (2.3) is just a separation of the complex envelope $\tilde{\mathcal{E}}(t)$ to a real envelope $A(t)$ (modulus) and a real temporal phase $\hat{\varphi}(t)$ (argument) according to Euler's law [91]. This decomposition is straightforward for optical pulses that are several hundreds or tens of femtoseconds long, because the bandwidth of the radiation is small compared to its center frequency, and ω_0 is well-defined (see Figure 2.2(a)). However, when the few-cycle regime is approached, the selection of the value of ω_0 may seem artificial (see experimental spectrum in Figure 2.2(a)). Fortunately, the exact choice for ω_0 is arbitrary and it does not influence the real envelope in the expression of (2.3), as it only means a linear term in the temporal phase [90]. It has also been show that this decomposition into envelope and carrier is unambiguous and self-consistent down to the single-cycle regime [95]. Of course, there

are better choices for ω_0 than others, it is advisable to choose ω_0 as the intensity weighted mean frequency of the spectrum, calculated as

$$\langle\omega\rangle = \frac{\int_{-\infty}^{\infty} \omega \left|\tilde{U}(\omega)\right|^2 \mathrm{d}\omega}{\int_{-\infty}^{\infty} \left|\tilde{U}(\omega)\right|^2 \mathrm{d}\omega}, \tag{2.4}$$

which minimizes the temporal phase variation of the complex envelope $\tilde{\mathcal{E}}(t)$ [18]. The carrier-envelope description has a practical advantage as well, because applying integration with substitution would result in transformation integrals (2.1) and (2.2) where the integrand varies more slowly according to the new integration variable [90]. This simplifies the numerical evaluation and enhances its precision. However, as noted already, the exact selection of ω_0 is arbitrary, and any choice close to the weighted average $\langle\omega\rangle$ would keep the practical benefits.

The decomposition of the complex spectrum is also a frequent approach, which already appeared during the era of picosecond optical pulses in the early 1980s [96], and it is still used for current laser technologies [18]. In this case the complex-valued function $\tilde{U}(\omega)$ is simply rewritten according to Euler's formula, similarly to the right-hand side of (2.3). This way one has a real valued amplitude spectrum $p(\omega)$ and a real valued spectral phase $\varphi(\omega)$, related to the complex spectrum by

$$\tilde{U}(\omega) = p(\omega)\exp[\imath\varphi(\omega)] \ . \tag{2.5}$$

Introducing real valued mathematical function again has practical benefits, as these are the measurable physical quantities. The square of the real spectral amplitude $[p(\omega)]^2 = \left|\tilde{U}(\omega)\right|^2$, the spectral density, is that appears as the output of a spectrometer, as with time-integrating detectors the light intensity can me measured [90]. The phase properties $\varphi(\omega)$ can be experimentally determined too, but this is detailed in later parts of the thesis. It is to be noted here as well, but it is reasoned afterwards, that to access the temporal variation of the electric field in a pulse, the most common way is the spectral approach, that is to obtain $\tilde{U}(\omega)$ and to apply an inverse Fourier transform to the data. Direct, temporal measurements are either much harder to perform, or even impossible yet for optical frequencies.

As for temporal information, usually spectral measurements are performed, a short summary on how spectral properties reflect the temporal shape of waves is necessary. Firstly, the amplitude spectrum $p(\omega)$ puts a primary restriction on the pulse duration, analogously to the famous inequality of Heisenberg in quantum mechanics [97]. Due to a purely mathematical inequality theorem, the multiplication of the width of two functions forming a Fourier transform pair can not take a value smaller then a certain number

[98]. This means that the shape and width of the spectrum gives a minimal duration for the pulse studied. The obscurity in the previous sentences about the exact value of this specific minimum originates in its dependence on the form of the function. As an example, if the width are defined as second-order moments, the number given by the mathematical theorem for this lower limit of duration–bandwidth product can only be reached for a pulse with Gaussian shape. For this reason, Gaussian wave packets have the smallest uncertainty in physics. There are other width definitions as well, which have proven to be more practical from the experimental point of view. One of these is the "intensity full width at half maximum" (abbreviated as FWHM in this work). In the case of the spectral profile the FWHM is the width in frequency where the function $\left|\tilde{U}(\omega)\right|^2$ reaches the half of the highest value on either side of the maximum point (see Figure 2.2(a)). This is a good and practical definition for well-behaving functions (as it can be seen in the Gaussian spectra of Figure 2.2(a)), but may become unreasonable for more complex ones [18] (see the experimental spectrum in Figure 2.2(a)). Although the width based on second-order moment is more general, FWHM is used in this work due to its wide-spread usage among experimentalists (also for the temporal duration).

The spectral amplitude, however, is not solely determining the pulse duration. The pulse is as short as the minimum given by the duration–bandwidth product — often called Fourier limit — only if the spectral phase $\varphi(\omega)$ has some favorable characteristics. In this case the wave packet is referred to as Fourier limited or transform limited. For further considerations on $\varphi(\omega)$ it is advantageous to expand this function as a Taylor series [7]. Expanding $\varphi(\omega)$ around the central frequency ω_0 yields

$$\begin{aligned} &\varphi(\omega) = \varphi_0 + \frac{\varphi_0'}{1!}(\omega-\omega_0) + \frac{\varphi_0''}{2!}(\omega-\omega_0)^2 + \frac{\varphi_0'''}{3!}(\omega-\omega_0)^3 + \dots, \\ &\text{where} \quad \varphi_0 = \varphi(\omega_0)\,, \quad \varphi_0' = \left.\frac{\mathrm{d}\varphi(\omega)}{\mathrm{d}\omega}\right|_{\omega=\omega_0}, \quad \varphi_0'' = \left.\frac{\mathrm{d}^2\varphi(\omega)}{\mathrm{d}\omega^2}\right|_{\omega=\omega_0}, \quad \dots \quad . \end{aligned} \tag{2.6}$$

This expansion is common since the appearance of optical communication with short pulses [96]. This is primarily due to the well-known typical pulse shape distortions that can be attributed to each term in the series [99] (see Figure 2.2(b)-(e)), and also because only the first few terms are relevant in most cases, even for broadband pulses [18].

To have a transform limited pulse, for example, only the first two terms φ_0 and φ_0' can have a nonzero value (see the formulas in Appendix A.1). Often this property is attributed only to the constant factor, forgetting that the linear term in the spectral phase only means a shift in the temporal picture (compare pulse shapes Figure 2.2(b) and (c)). This is the reason why φ_0' is called group delay (GD). If φ_0'' has a value different from zero, it emerges as a symmetrical broadening of the pulse in time for the given spectrum. This second-order factor is usually called group delay dispersion (GDD). It

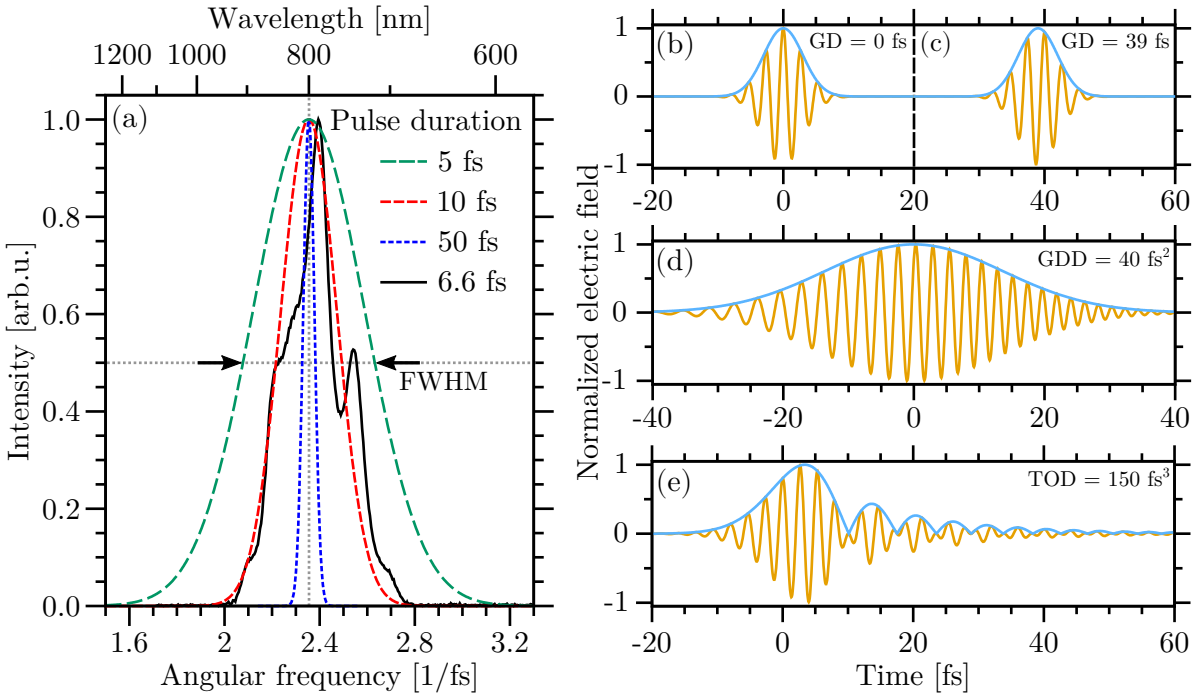

Figure 2.2. (a) Three Gaussian spectra centered at $\omega_0 = 2.355\,1/\text{fs}$ (corresponding to $\lambda_0 = 800\,\text{nm}$ central wavelength) and an experimental spectrum making possible a transform-limited pulses with duration T_{FWHM} (measured as FWHM) given in the figure legend. The facing arrows show a graphical definition of FWHM for the case of the 5 fs-duration supporting spectrum. (b)-(e) Normalized pulse shapes calculated using different spectral phases and the amplitude spectrum for the $T_{\text{FWHM}} = 5\,\text{fs}$ Fourier-limited pulse duration presented in (a). The spectral phases are expressed in the form presented in (2.6), with only one nonzero phase derivative in each case of the subfigures. The relevant phase term is highlighted in the upper right corner at each pulse shape.

gives a contribution also to the temporal phase $\hat{\varphi}(t)$. Due to the presence of GDD, a quadratic term in $\hat{\varphi}(t)$ appears for Gaussian pulses. This second order term in time is often called "chirp". In a general context chirp is a modulation of frequency, because it shows up as a frequency change of the carrier wave in time (see Figure 2.2(d)). The chirp caused by the factor φ_0'' is just a linear chirp, but in the topics of ultrashort pulses usually this is called chirp [18]. For Gaussian spectra, the relationship between the GDD and the factor of the quadratic term in $\hat{\varphi}(t)$ can be derived analytically (see Appendix A.1), just like the pulse shape when φ_0'' is the highest term in the spectral phase [18].

The higher order terms are simply named after their order, for example φ_0''' is called third order dispersion (TOD). The TOD is often neglected in some simple propagation problems of narrow bandwidth pulses [18]. Again, for Gaussian-shaped spectra the pulse shape can be given analytically in the presence of TOD, leading to an asymmetric pulse in time described by the Airy function [100–102] (see Figure 2.2(e) or the detailed calculations in Appendix A.1). The even and odd phase derivatives typically cause symmetric

and asymmetric pulse distortions, respectively [99].

While describing the spectral phase with the coefficients of a polynomial-like approximation of the Taylor series is widely spread and seems practical [103, 104], it also has its drawbacks and limits, especially when high-order terms are necessary. Due to numerical inaccuracies during polynomial fits caused by the fact that Taylor series is not an orthogonal set of basis [105], or because of material properties [106], the approximations with polynomial coefficients is questionable, and the direct use of the spectral phase function might be desirable [107].

2.2.2 The carrier-envelope phase

The phrase in the title of this subsection, the CEP, is something that was born with the introduction of the carrier-envelope decomposition. On the contrary to the fact that its importance has been recognized for two decades now [108], and that the survey to find its effects on different phenomena is heavily researched [56–63], it varies from study to study what is exactly understood as the expression "carrier-envelope phase". This ambiguity originates from terminology that spread in topics of laser oscillators and pulse trains, facing with the nomenclature of studies dealing with single short pulses. So it is an important and necessary step to gather these different "meanings" of CEP, and to clarify which one is used in this work.

As mode-locked lasers made few-cycle optical pulses available, it is worth starting with the CEP interpretation that is most common in the topic of laser oscillators and in the studies dealing with the series of short pulses generated by them. In the cavity of lasers several longitudinal modes co-exist. The locking of them means that their phases are fixed to each other, and as a result a short pulse is formed [18, 45]. From this point, that is from the initialization of mode-locked operation of a laser, it is advantageous to continue the treatise in temporal instead of the frequency picture, where the longitudinal modes of the cavity directly manifested. The pulse formed inside the oscillator travels back and forth, and it is outcoupled every time it reaches the semi-transparent mirror at one end. In the ideal case (some kind of steady-state operation) this means that a series of identical short pulses leave the laser (see Figure 2.3(a)). The pulses are repeated after each round trip inside the cavity, so they are spaced equally in the time domain by T_{rep}. Due to the dispersion inside the oscillator (caused by the laser material and other elements), the phase velocity of the carrier and the group velocity of the pulse (terms that are discussed in detail later) differ from each other. This means that the wave packets in the series are not identical on the electric-field level, because there is a slippage in phase between the carrier and the envelope. If the oscillator is stable, this is the same φ_{CEO} phase shift after each shot (see Figure 2.3(a)).

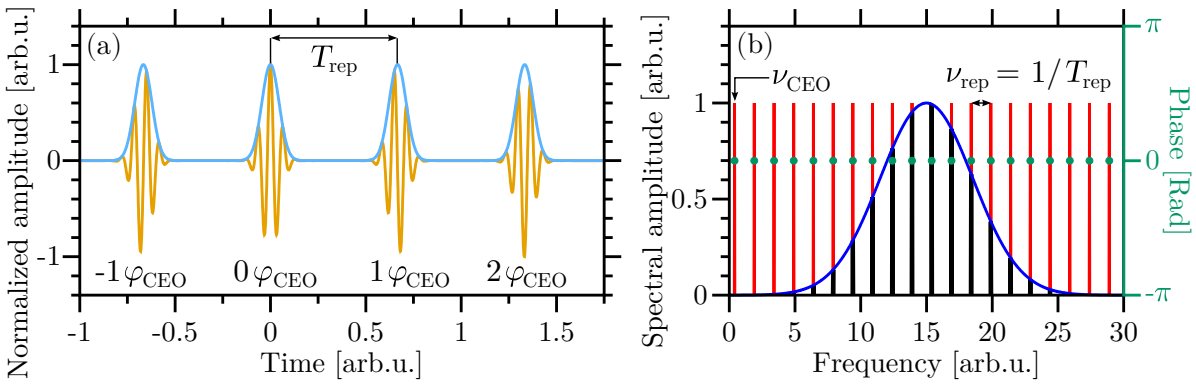

Figure 2.3. (a) A pulse train leaving an ideal mode-locked laser oscillator. The pulses are repeated after every T_{rep} time. There is a phase slippage between the carrier and the envelope from pulse to pulse due to the phase- and group velocity differences inside the cavity, which has a constant φ_{CEO} value. (b) The Fourier transform of the pulse train in (a). The spectrum consists of uniformly spaced Dirac delta functions (red lines) multiplied by and envelope function (blue curve), resulting in the comb structure depicted using the black lines. The lines in the comb are repeated at every integer multiple of $\nu_{\mathrm{rep}} = 1/T_{\mathrm{rep}}$, and the whole comb is offset from zero frequency by $\nu_{\mathrm{CEO}} = \varphi_{\mathrm{CEO}}\nu_{\mathrm{rep}}/2\pi$. The phases of the spectral lines are equal (green dots).

As a small detour, it is worth to consider what this means in the frequency domain. By Fourier transforming the pulse train of Figure 2.3(a) one can get an frequency comb [109], as depicted using black, thick lines in Figure 2.3(b). This consists of equally spaced lines (red lines in in Figure 2.3(b)), that are enveloped by a function that is the Fourier transform of a single pulse in the train (blue curve in Figure 2.3(a)). It can be shown analytically that this is true for an ideal pulse series of any kind of pulse shape [110]. The theory also shows that the Dirac delta functions of the comb are spaced at $\nu_n = n\nu_{\mathrm{rep}} + \nu_{\mathrm{CEO}}$, where $\nu_{\mathrm{rep}} = 1/T_{\mathrm{rep}}$ is the repetition frequency and $\nu_{\mathrm{CEO}} = \varphi_{\mathrm{CEO}}\nu_{\mathrm{rep}}/2\pi$ is the carrier-envelope offset frequency. The phase of the comb lines are constant (see the green dots in Figure 2.3(b)), which coincide with what is expected from mode-locking.

These combs are widely used for precise spectroscopic measurements, as mode-locked lasers with phase stabilization provide very stable frequency standards, surpassing any other such tool [109]. It is important to notice that the comb of mode-locked lasers is not the longitudinal modes made available by the cavity, as those would not be equally spaced do to the dispersion inside the oscillator [18, 111]. The phase stabilization of a laser oscillator means the stabilization of the ν_{CEO} frequency, and in the time domain it appears as a known pulse-to-pulse phase change of the carrier with respect to the envelope. Still, how the phase of the carrier is related to that of the envelope in a single pulse is unknown. Measuring ν_{CEO} serves as a method to get information on the φ_{CEO} phase [112].

The reason why this short note on laser oscillators had to be included here is the φ_{CEO} slippage in the carrier with respect to the envelope after each shot. This phase difference

from pulse to pulse is often understood as CEP, but most often called as carrier-envelope offset phase (CEO phase) for clarity [112]. If the oscillator length varies, then the path traveled is modified, and the phase difference changes. This in the spectral picture appears as a modification of the longitudinal modes, so the variation of ν_{CEO} and ν_{rep} (usually this latter can not even be defined, as the lines are not uniformly spaced any more). The instabilities of the cavity appear as an output of non-identical pulses unequally spaced in time. If someone measures ν_{CEO}, so φ_{CEO}, it does not give any information on how the envelope and the carrier is related to each other in a single pulse, just how the phase changes after each shot [45, 112]. In this work the propagation of single pulses is considered, so the CEO phase is not significant.

The CEP that is relevant in this work is the one that is also named as "absolute phase" [17]. The absolute phase, that is the CEP of a single pulse is the phase difference between the carrier and the envelope. Measuring this property of an optical wave packet is a very laborious task, and considerations on its determination are given later.

Even if the distinction between CEO phase and CEP is made, the exact (mathematical) framing of CEP is needed. It is formulated several different ways, usually leading to the same phase values, but some discrepancies can be found between the different interpretations. Sometimes it is said that the CEP is not else but the constant phase term that is decomposed from the complex electric field $\tilde{E}(t)$ — like the linear one in (2.3) —, so that the imaginary part of the complex temporal envelope $\tilde{\mathcal{E}}(t)$ is zero at $t = 0$ [17, 95]. In other cases it is simply considered as the time delay between the envelope peak and the closest maximum of the carrier converted to a phase value [45, 112].

If someone wants to be punctilious, these definitions could be picked at, especially taking into account that CEP is usually determined with spectral measurements. For example, when the interpretation with the temporal phase value at time zero is thought of, care should be taken if the pulse shape of Figure 2.2(e) is considered, when the pulse is distorted by TOD. Mostly, the spectral data is evaluated using Fourier transform, and as a result the temporal window is centered at the value of GD, which not necessarily coincides with the maximum of the envelope (see Figure 2.2(e)). So the phase at $t = 0$ has no direct information on the phase at the envelope peak, taking into account that the envelope can be "distorted" (like in Figure 2.2(e)).

For the second definition with carrier- and envelope peaks, the analogy with the properties of the damped oscillator can be referred. As is known, the maximums of the underdamped oscillations appear earlier then expected from the periodicity of the undamped oscillation [113]. This means that the distance between the maximums of the carrier and envelope can lead to a CEP value that is different from the previous definition or from what logically expected (see Figure 2.4). It is also visible, that the deviations are minimal

(in the order of 100 mrad in the examples of Figure 2.4), they are similar in magnitude to the CEP stability of laser amplifiers [114]. Also, the second definition usually serves only as graphical interpretation of the meaning of CEP, so it is generally not so relevant.

Still, a consistent CEP definition is needed for the present work. A logical demand from the formulation is that the zero value of CEP means that at the envelope maximum the electric field also peaks. To fulfill this, the following definition is used: *The CEP of a single pulse is the phase of the wave packet at the instant of time when the envelope reaches its maximum.* This also gives a numerical method to evaluate the CEP of any pulse shape.

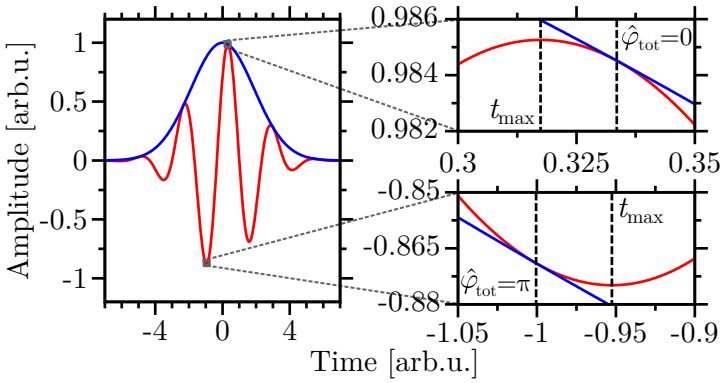

Figure 2.4. The difference between the CEP-definition variants. The left subfigure depicts a short pulse given by the function $\tilde{E}(t) = \exp[-t^2/2.67^2]\exp[\imath\hat{\varphi}_{\mathrm{tot}}(t)]$, where $\hat{\varphi}_{\mathrm{tot}}(t) = -2.355t + \pi/4$. It can be seen in the zooms of the right subfigures that the temporal distance t_{max} between the envelope peak ($t = 0$) and the closest maximums of the field do not coincide with the times when the harmonic carrier wave reaches its extrema, that is the times when $\hat{\varphi}_{\mathrm{tot}}(t) = 0$ or π ($\pm 2m\pi, m \in \mathbb{Z}$).

The above definition has several advantages over the previously mentioned ones. It can be used to properly describe the phase relation of the carrier and envelope even for complex pulse shapes (like the TOD-distorted pulse of Figure 2.2(e)). Such a CEP also possesses a practical property that its zero means the strongest electric field with the given envelope, which is often important in light-matter interactions [17]. Additionally, this approach gives the possibility to generalize the CEP in a physically meaningful way even for pulses with arbitrary polarization state [115], that again can be advantageous in nonlinear optical phenomena [116], and which leads up to the next topic of this theoretical overview.

2.2.3 Polarization

Polarization is an important property of vector waves. While in the majority of laser applications the polarization state is not considered — because the generated pulsed light is usually linearly polarized and can be treated theoretically as a scalar —, more and more studies are published where pulsed waves with complex polarization states are used [41, 64–72].

Polarization-shaped short pulses are primarily produced in the visible domain, where most of the methods are based on light manipulation by liquid crystals (spatial light modulators) [65–68]. This technique is under continuous development to yield simpler

setups [117–119], and has been applied to tailor the polarization state of pulses originating from different types of sources [120]. Other solutions, such as acousto-optical pulse shapers or plasmonic-crystal structures, have been proposed as well for polarization-state control [121, 122]. Polarization shaping in other wavelength regimes is also possible, for example, for pulses generated in the mid-infrared [70], terahertz [64, 123] or ultraviolet [124]. So, it is an important issue to discuss how the polarization state of short pulses can be described, and how they might change during the propagation or focusing of the pulsed beam.

As the polarization-shaped pulse-generation methods themselves are usually based on spectral control of the polarization ellipse (see Figure 2.5), it may seem logical to consider the characterization also in spectral picture. However, it is more important how the polarization changes in time — considering the applications —, as the additional control — which is their advantage — is achieved by properly manipulating the temporal variation of the electric field vector. The polarization-state description of monochromatic waves is a textbook topic. However, there are different ways to represent it. In the following, those ones are gathered, which are important for the discussion later, and it is shown how these representations can be generalized to short pulses having temporally varying polarization state.

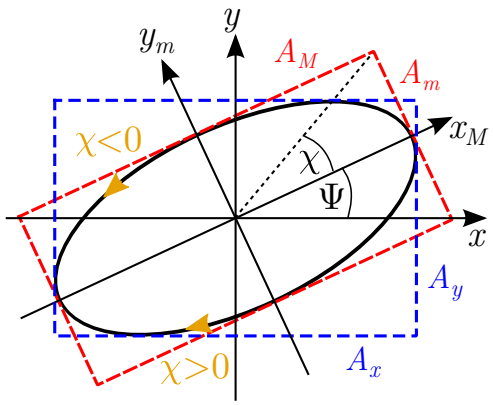

Figure 2.5. The polarization ellipse that is used to characterize the polarization state of transverse vector waves. The ellipse is defined by its angle Ψ with the reference axis x, by its ellipticity χ and by its semi-major axis A_M (or semi-minor axis A_m). The sign of ellipticity χ determines the round-trip direction of the harmonic-wave vector, or in other words it gives the helicity.

In the usual discussion of the polarization of monochromatic plane waves propagating in the z direction of the Cartesian coordinate system, two harmonic oscillations are considered along the x and y axis, as plane electromagnetic waves are transverse waves [90]. Assuming harmonic waves of the form $E_x(t) = A_x \cos[\hat{\varphi}_x - \omega_0 t]$ and $E_y(t) = A_y \cos[\hat{\varphi}_y - \omega_0 t]$, it can be easily shown that the resulting oscillations happen along an ellipse. This is why elliptical polarization is the most general type of polarization, and why the polarization state of monochromatic waves is usually described by the properties of this ellipse. The ellipse is unambiguously defined by two characteristic angles and a length: the orientation Ψ, the ellipticity[VI] χ and the size of the major (or minor) semi axis A_M (or A_m) (see Figure 2.5). The sign of the ellipticity gives the left- and right

[VI] There is another terminology to characterize the same property of an ellipse, that is, how much it is like a circle or a line, which are the two extremes of its shape. For example in astronomy or mathematics, the *eccentricity* is used instead of *ellipticity*, given by a slightly different definition. Using ellipticity instead of eccentricity has advantages in these topics, which appears later in the discussion.

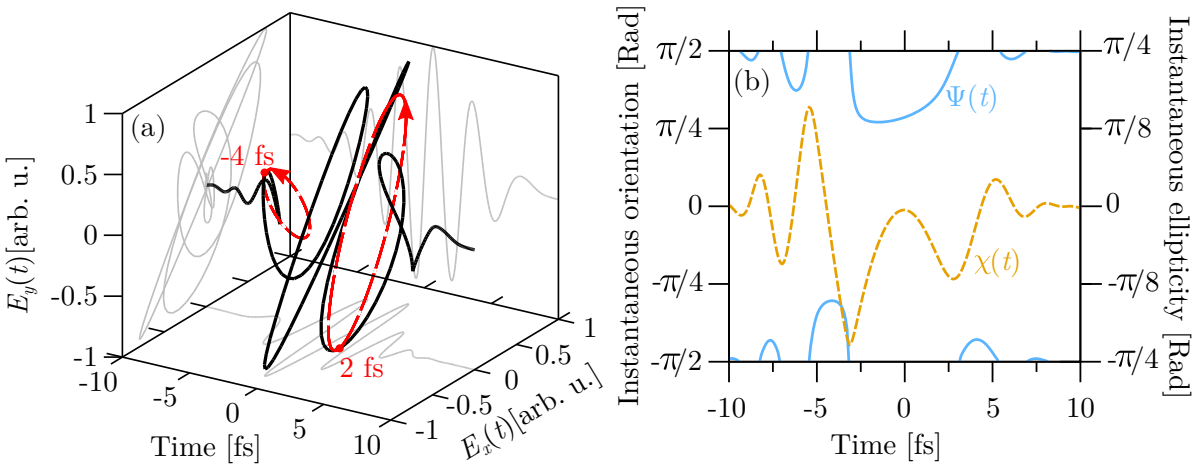

Figure 2.6. (a) Temporal evolution of the two-dimensional electric field vector in a polarization-shaped ultrashort pulse. The red dashed ellipses depict the instantaneous polarization state (ellipse) in two separate moments (−4 fs and 2 fs). (b) The temporal evolution of the orientation $\Psi(t)$ (blue continuous curve) and ellipticity $\chi(t)$ (yellow dashed curve) of the instantaneous polarization ellipse for the pulse depicted in (a).

handedness of the polarization. If χ is a positive (negative) angle then the polarization is right (left) handed, meaning that if someone faces against the direction of propagation, then the vector field rotates clockwise (counterclockwise) as time passes (see Figure 2.5). It can be shown that these ellipse characteristics can be generalized to instantaneous properties, and an instantaneous polarization ellipse can be defined characterizing the polarization of the radiation in a single moment in time (see the two red dashed ellipses of the polarization-shaped pulse in Figure 2.6(a)). This approach is unavoidable for short pulses where the amplitudes $A_{x,y} \geq 0$ and phases $\hat{\varphi}_{x,y}$ change in time, like the temporal shape of (2.3). This means that two pulses of the form

$$E_{x,y}(t) = A_{x,y}(t) \cos\left[\hat{\varphi}_{x,y}(t) - \omega_0 t\right] \tag{2.7}$$

are considered, which are linearly polarized along the two Cartesian axis x and y. In the following, the ellipse properties are considered as time-dependent quantities (see Figure 2.6(b)), describing the instantaneous polarization state and ellipse. In the next few lines only the expressions giving the ellipse parameters are listed. The details of the derivation of these instantaneous properties described by the x and y linear states can be found in Appendix A.2.1, based on [90, 115, 125, 126].

The instantaneous ellipticity of the ellipse can be calculated as

$$\chi(t) = \frac{1}{2}\text{asin}[\sin[2\alpha(t)]\sin[\Delta\hat{\varphi}(t)]] \quad \in [-\pi/4, \pi/4]\,, \tag{2.8}$$

where the

$$\alpha(t) = \operatorname{atan}\left[\frac{A_y(t)}{A_x(t)}\right] \quad \in [0, \pi/2] \tag{2.9}$$

auxiliary angle and the

$$\Delta\hat{\varphi}(t) = \hat{\varphi}_x(t) - \hat{\varphi}_y(t) \tag{2.10}$$

phase difference were introduced. The orientation is given by

$$\Psi(t) = \begin{cases} \hat{\Psi}(t) \in [-\pi/4, \pi/4] & \text{if } \alpha(t) \leq \pi/4 \\ \hat{\Psi}(t) + \pi/2 \in (\pi/4, \pi/2) & \text{if } \alpha(t) > \pi/4 \text{ and } \hat{\Psi}(t) < 0 \\ \hat{\Psi}(t) - \pi/2 \in [-\pi/2, -\pi/4) & \text{if } \alpha(t) > \pi/4 \text{ and } \hat{\Psi}(t) \geq 0 \end{cases}, \tag{2.11}$$

with

$$\hat{\Psi}(t) = \frac{1}{2}\operatorname{atan}[\tan[2\alpha(t)]\cos[\Delta\hat{\varphi}(t)]] \ . \tag{2.12}$$

The semi-major and semi-minor axes can be expressed as

$$A_M(t) = A_x(t)\sqrt{\frac{1+\tan^2[\alpha(t)]}{1+\tan^2[\chi(t)]}} \tag{2.13}$$

and

$$A_m(t) = A_M(t)\,|\tan[\chi(t)]| \ . \tag{2.14}$$

With the ellipse, the vector wave can be decomposed to two scalar waves oscillating along the axes of the ellipse x_M and y_m (see Figure 2.5), leading to the expressions

$$E_M(t) = A_M(t)\cos\left[\hat{\varphi}_M(t) - \omega_0 t\right] \ , \tag{2.15}$$

$$E_m(t) = \operatorname{sgn}[\chi(t)]\, A_m(t)\sin\left[\hat{\varphi}_M(t) - \omega_0 t\right] \ . \tag{2.16}$$

In the two previous formulas the quantity

$$\hat{\varphi}_M(t) = \hat{\varphi}_x(t) - \operatorname{sgn}[\Psi(t)\chi(t)]\operatorname{acos}\left[\frac{\cos[\chi(t)]\cos[\Psi(t)]}{\cos[\alpha(t)]}\right] \tag{2.17}$$

is the phase associated with the semi-major axis, and $\operatorname{sgn}(x) = \{1 \text{ if } x > 0, -1 \text{ if } x < 0, \text{ and } 0 \text{ if } x = 0\}$ is the signum function. Expressing the electric field along the rotated axes gives the possibility to generalize the meaning of CEP to pulses with arbitrary polarization state [115].

In some cases it is advantageous to switch to another orthogonal basis and leave the one based on the x and y linear polarization. It is less common, but at least as well-known approach to use the left- and right circularly polarized vectors as an expansion basis for

the polarization state [127]. As each circular polarization state means two perpendicular, linearly polarized waves with given shifted phases with respect to each other ($\pi/2$ and $-\pi/2$, respectively), in complex formalism they can be written as

$$\tilde{\mathbf{E}}_l(t) = \frac{A_l(t)}{\sqrt{2}} \exp[\iota\hat{\varphi}_l(t)] \left(\mathbf{u}_x + \iota\mathbf{u}_y\right) , \tag{2.18}$$

$$\tilde{\mathbf{E}}_r(t) = \frac{A_r(t)}{\sqrt{2}} \exp[\iota\hat{\varphi}_r(t)] \left(\mathbf{u}_x - \iota\mathbf{u}_y\right) . \tag{2.19}$$

In the previous expression the Cartesian unit vectors $\mathbf{u}_x$, $\mathbf{u}_y$ (and $\mathbf{u}_z$) have been introduced, and the electric field is now treated as a vector quantity (written in bold). There are several approaches to determine the properties of the polarization ellipse using the attributes of the circular basis vectors (2.18) and (2.19). For example, introducing phasors can yield the relationships in question [127], or Clifford (geometric) algebra can be used to find them [128]. Of course, simple algebraic manipulations can also lead to the expressions giving the properties of the polarization ellipse (see them in Appendix A.2.2). A reason behind using the circular basis instead of the linear one is that it results in simpler expressions (compare the ellipse parameters in Appendices A.2.1 and A.2.2), and as a consequences, in more expressive formulas later.

There is another representation of the polarization of light that is more often used in experiments than the ellipse parameters. The Stokes parameters can be more convenient in practical situations, as they can be directly measured [90], and a nice graphical representation is available for them, the Poincaré sphere (or plane) [90, 129]. The number of Stokes parameters is four (S_0, S_1, S_2 and S_3), which means one additional compared to the three necessary parameters of the ellipse. This is because with the ellipse only fully polarized radiation can be treated, while light can be partially polarized or fully unpolarized [90, 130]. For this reason a distinction must be made based on how the Stokes parameters are used to describe the polarization state of pulsed light.

One approach is to define instantaneous Stokes parameters, just like the instantaneous properties of the ellipse (see Figure 2.7). In this case, the Stokes parameters can be calculated just like for infinite harmonic waves [90], but every parameter depends on time, that is,

$$S_1(t) = S_0(t) \cos\left[2\chi(t)\right] \cos\left[2\Psi(t)\right] , \tag{2.20}$$

$$S_2(t) = S_0(t) \cos\left[2\chi(t)\right] \sin\left[2\Psi(t)\right] , \tag{2.21}$$

$$S_3(t) = S_0(t) \sin\left[2\chi(t)\right] . \tag{2.22}$$

The zeroth parameter is the total instantaneous intensity of the field, similarly to the case

of monochromatic waves, meaning the following equality is valid:

$$S_0(t) = \sqrt{[S_1(t)]^2 + [S_2(t)]^2 + [S_3(t)]^2}\,. \tag{2.23}$$

The instantaneous intensity can also be expressed using the ellipse parameters [115], with the formula

$$S_0(t) \sim \frac{[A_M(t)]^2 + [A_m(t)]^2}{2} + \frac{[A_M(t)]^2 - [A_m(t)]^2}{2} \cos\left[2\left(\hat{\varphi}_M(t) - \omega_0 t\right)\right]\,. \tag{2.24}$$

Using the instantaneous Stokes parameters and plotting them on the Poincaré sphere is a picturesque method to follow the variations of the instantaneous polarization state with time (compare Figures 2.7 and 2.6(b) depicting the same properties). It has to be noted that the instantaneous polarization state and Stokes parameters are only directly accessible theoretically. There are different methods to reveal the time-dependent polarization state, like electro-optical sampling for terahertz radiation [131], or based on a similar idea attosecond streaking can help to get polarization properties of femtosecond pulses [132]. However, in several cases these measurements are achieved in a pump-probe arrangement, so several subsequent pulses are sampled and a good reproducibility of studied pulse is assumed. A less direct, but possibly single shot solution is the tomographic retrieval of the two-dimensional vector field by an interferometric technique [133], but it means a relative measurement of the phases.

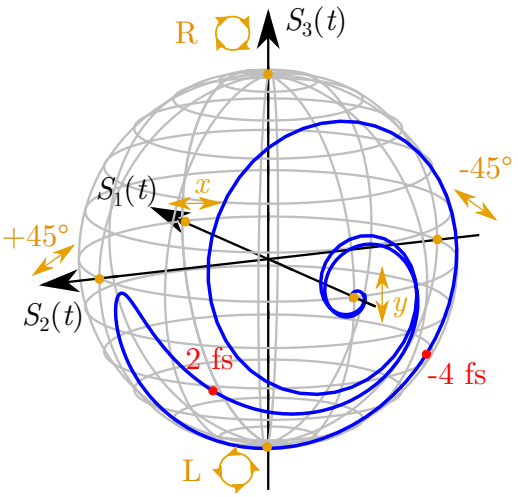

Figure 2.7. The instantaneous polarization state of the pulse plotted in Figure 2.6(a) represented on the Poincaré sphere (blue curve). The two red dots show the moment of time where the instantaneous ellipses are draw in Figure 2.6(a). The yellow dots show the six representative polarization states on the sphere which also appear in the measurement of the Stokes parameters. The $S_0(t)$ parameter is normalized to 1 for every moment.

As almost all light detectors are time integrating, it is necessary to consider the traditional Stokes parameters as well. The indisputable benefit of them is that they can be measured with very simple optical tools compared to the complex setups needed to obtain information on their time-dependent versions [131–133]. This can be seen from their definition [90], directly giving the method to experimentally obtain them,

$$S_0 = I_{\mathrm{m}}(0°, 0) + I_{\mathrm{m}}(90°, 0)\,, \tag{2.25}$$

$$S_1 = I_{\mathrm{m}}(0°, 0) - I_{\mathrm{m}}(90°, 0)\,, \tag{2.26}$$

$$S_2 = I_{\mathrm{m}}(45°, 0) - I_{\mathrm{m}}(135°, 0)\,, \tag{2.27}$$

$$S_3 = I_{\mathrm{m}}(45°, \pi/2) - I_{\mathrm{m}}(135°, \pi/2)\,, \tag{2.28}$$

where

$$I_{\mathrm{m}}(\theta, \epsilon) = \lim_{T\to\infty} \frac{1}{T} \int_{-T/2}^{T/2} \left[\mathrm{Re}\left\{\tilde{E}_x(t)\cos(\theta) + \tilde{E}_y(t)\exp[\iota\epsilon]\sin(\theta)\right\}\right]^2 \mathrm{d}t \tag{2.29}$$

is proportional to the measured, time-integrated intensity (fluence) of the light after passing through a polarizer with azimuth angle θ and a retarder causing ϵ phase shift between the y and x components. While they, of course, carry less information than time-dependent measurements, they can provide important information even in this case. The number of the parameters with them becomes meaningful, as mentioned earlier, because for time-integrated Stokes parameters

$$S_0 \geq \sqrt{S_1^2 + S_2^2 + S_3^2}\,, \tag{2.30}$$

the S_1, S_2 and S_3 parameters only describing the polarized part of the detected radiation. In these classical measurements the quasi-monochromatic light, or similarly the polarization-shaped short pulses, may appear as not totally polarized [130]. The ellipticity or the orientation of the polarization ellipse may also be calculated from the time-integrated Stokes parameters. As instantaneous Stokes parameters are defined based on the traditional Stokes parameters, by regrouping (2.22) it is easy to see that a time-integrated ellipticity can be obtained by [90]

$$\sin[2\chi] = \frac{S_3}{\sqrt{S_1^2 + S_2^2 + S_3^2}}\,, \tag{2.31}$$

while from (2.20) and (2.21) the time-integrated orientation is

$$\tan[2\psi] = \frac{S_2}{S_1}\,. \tag{2.32}$$

The time-integrated ellipse properties are generally only equivalent to instantaneous values for monochromatic waves.

2.3 Theoretical treatment and properties of propagating or focused pulsed beams

Up to this point the spatial properties of waves have been omitted. This intrinsically means that these electromagnetic oscillations were considered in a fixed point in space, or thought of as plane waves, which latter gives, for example, the strictly transverse nature of electric field vector in the previous section. Plane waves are pure theoretical idealizations, as these infinite waves would mean physical entities with unbounded spatial extensions, and as a result, measureless energies. In reality there are no waves which spread never ending in space, instead light exists in the form of beams. Beams are waves with a bounded spatial distributions of different shape. Fortunately, although plane waves are not physical reality, they serve as a good starting point or model for the more "complex" beams. This is simply because plane waves serve as an expansion basis for waves with any spatial distribution. Analogously to the temporal picture, where any wave form in the temporal picture can be expressed as an infinite sum of harmonic waves using Fourier transform, the spatially limited wave form is expandable to a unlimited number of plane waves propagating in different directions (having wave vectors $\mathbf{k}$ of various orientations). Of course, other expansion bases can be found (for example spherical waves), which may result in simpler solutions in some cases due to the symmetry of the problem, but they can be expressed in the fundamental basis of plane waves as well.

Plane waves are also trivial solutions of the wave equation. So, the behavior of light beams, that is, how they change during time and in space (often simply referred to as propagation), is also controlled by the wave equation, which is directly obtainable from the equations of Maxwell in the case of electromagnetic radiation. In the following, a specific type of beam, some physical properties related to the spatial dependence of waves, and some less- and more complex wave propagation and diffraction models are described, with paying special attention to the limits of methods presented.

2.3.1 Ray tracing

An extensively used method in optics to model the propagation properties of light is ray tracing [90]. However, when using ray tracing, the wave nature of light is partly lost. This is because geometrical optics is based on neglecting the wavelength ($\lambda \to 0$ limit), in which case the equations of Maxwell simplify to the eikonal equation, which treats light as pencils of rays [90]. These rays propagate along straight lines until they reach a region in space where the refractive index is different, and there they change their direction according to the geometrical laws of refraction or reflection (see Figure 2.8).

Ray tracing can be thought as applying the expansion of different waves into the sum of plane waves, mentioned in the introductory part of this section, as rays represent the wave vectors $\mathbf{k}$ of plane waves, being perpendicular to the wave fronts[VII] and traveling along the path given by the laws of geometrical optics. The optical path $\mathcal{S}(\mathbf{r})$ (physical distance multiplied by the index of refraction) along a ray from an origin to a point given by $\mathbf{r}$ is called eikonal. The basic equation of geometrical optics — the eikonal equation — describes the behavior of the function $\mathcal{S}(\mathbf{r})$. One advantage of using this fundamental geometrical optics quantity is that the wave nature of light is not totally hidden, since spatial points defined by the $\mathcal{S}(\mathbf{r}) = const$ equation can be thought as "geometrical wave fronts" [90]. Assuming an initial wave front (like the one defined by the eikonal $\mathcal{S}(\mathbf{r}) = \mathcal{S}_1$ in Figure 2.8), ray tracing can be used to track the the changes of the wave front while the wave travels through an optical system (for example a lens in Figure 2.8), and the wave front can be given at any position (like the wave front just behind the lens given by $\mathcal{S}(\mathbf{r}) = \mathcal{S}_2$ in Figure 2.8).

Ray tracing is a very robust numerical tool for calculating light propagation. In its most simple form it only requires the following main steps: 1, an initial wave front and a bunch of rays have to be defined, these rays being perpendicular to the wave front in every point in space; 2, the rays have to be propagated along straight lines until they hit a surface separating volumes with different refractive indices; 3, the new directions of the rays at the surface have to be calculated using the laws of refraction and reflection [90, 134]. The last two steps have to be repeated as long as there are new boundary surfaces (see Figure 2.8). Ray tracing, of course, has its limitations as well. Modeling the intensity distribution of beams with rays is not trivial, for example. Also, geometrical optics can not deal with such fundamental aspects of waves like interference or diffraction. These effects usually take place when light meets obstacles that are comparable in size to its wavelength, or where many light rays meet, like in the surrounding of the focal point [90, 135]. To properly treat the case of focusing — the main topic of this work — other models have to be used, which take into account the wave nature of light more profoundly.

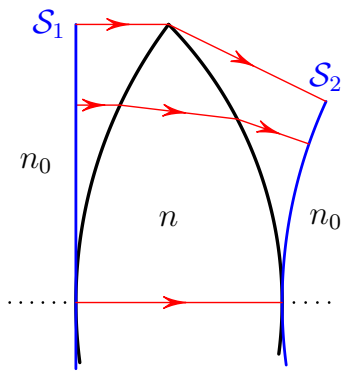

Figure 2.8. An example of ray propagation through a lens with $n > n_0$ index of refraction, n_0 being the refractive index of the environment. A task of ray tracing is to determine the optical path (eikonal) of rays from surface defined by the constant eikonal $\mathcal{S}_1$ and to give the geometrical wave surface given by constant eikonal $\mathcal{S}_2$.

[VII] While the meaning of "wave front" is clear here when monochromatic waves are discussed, there are ambiguities when pulsed beams are considered. In this work "wave front" is used as the synonym of "phase front", which gives a surface in space along which the phase of the wave is constant. The surface which gives the position of the pulse maximum is referred as "pulse front".

2.3.2 Gaussian beams in ABCD formalism

One property of lasers is that they can produce light beams with uniquely small divergence. It is not surprising, as only those photons can travel back and forth between the mirrors of the oscillator, which do not get too far from the optical axis during traveling the distance between the two reflecting elements. The domain of optics, which describes the propagation of such low-divergence waves, is called paraxial optics. In the paraxial approximation the solution of the scalar wave equation

$$\nabla^2 \tilde{E}(\mathbf{r},t) - \frac{1}{c^2}\frac{\partial^2 \tilde{E}(\mathbf{r},t)}{\partial t^2} = 0\,, \tag{2.33}$$

is pursued in a special form. Note that the above equation is only valid in a space which is homogeneous, isotropic, and where no charges or currents are present. The Laplace operator in (2.33) reads as $\nabla^2 = \partial^2/\partial x^2 + \partial^2/\partial y^2 + \partial^2/\partial z^2$, c is the speed of light and $\mathbf{r} = (x,y,z)$ is the position vector. First of all, only monochromatic waves have to be considered, because everything else can be built from them using Fourier transform, as pointed out in Section 2.2.1, so the wave can be expressed as $\tilde{E}(\mathbf{r},t) = \tilde{G}(\mathbf{r})\exp[-\iota\omega t]$. This simplification leads to the well-known Helmholtz equation for the function $\tilde{G}(\mathbf{r})$ [90]. The second assumption is that the solution can be written in the form $\tilde{G}(\mathbf{r}) = \tilde{\Gamma}(x,y,z)\exp[\iota kz]$, with the wave number $k = \omega/c$, and $\tilde{\Gamma}(x,y,z)$ is assumed to be a slowly varying function of z, coinciding with the presumption of a low-divergence beam. This gives the equation

$$\nabla_\perp^2 \tilde{\Gamma}(x,y,z) + \iota 2k\frac{\partial \tilde{\Gamma}(x,y,z)}{\partial z} = 0\,, \tag{2.34}$$

known as paraxial Helmholtz equation [136], $\nabla_\perp^2 = \partial^2/\partial x^2 + \partial^2/\partial y^2$ only containing derivatives perpendicular to the axis z. It can be shown that a paraxial beam solution of this equation is the Gaussian beam given by [137]

$$\tilde{G}(\mathbf{r}) = \frac{s}{w(z)}\exp\left[-\frac{x^2+y^2}{w(z)^2}\right]\exp\left[\iota\left(kz + k\frac{x^2+y^2}{2R(z)} - \operatorname{atan}\left[\frac{z}{L}\right]\right)\right]\,. \tag{2.35}$$

Of course, (2.35) multiplied with a constant amplitude is still a solution, and for a full spatio-temporal description the $\exp[-\iota\omega t]$ term is necessary. In (2.35) s is the radius of the beam waist (the plane where the beam has the smallest transverse extension),

$$w(z) = s\sqrt{1+\left(\frac{z}{L}\right)^2} \tag{2.36}$$

is the radius of the beam at distance z from the plane of the beam waist,

$$R(z) = z + \frac{L^2}{z} \tag{2.37}$$

is the radius of the spherical wave front at z, and

$$L = \frac{\omega s^2}{2c} \tag{2.38}$$

is the Rayleigh range (or Rayleigh length). The last term in the phase of (2.35), the one written as $-\mathrm{atan}[z/L]$, is the so-called Gouy phase shift. While it has been first observed with light waves [77], it has been revealed since then that it is a general property of beams of any physical entity [138].

Gaussian beam is of particular interest in laser physics as it is the fundamental mode present in a laser oscillator [107]. Providing again an analog with the temporal domain, Gaussian beam is the the spatial distribution providing the smallest beam-parameter product [107] — a parameter giving the product of the angular spread and smallest beam size — similarly to the bandwidth-duration product of pulses. This can be considered as a lucky situation, since this means that lasers usually provide a beam that can be focused to the smallest physically possible spot, important for high-intensity physics [19]. A theoretical advantage — apart from the one that using Gaussian function can lead to analytical solutions of several problems — is that in the paraxial approximation, Gaussian beams remain Gaussian after passing through optical elements (this is a physical reason behind the experience that the stable modes of oscillators are Gaussian) [137]. This fact is utilized by the introduction of the complex beam parameter $\tilde{q}(z)$, which is given by

$$\tilde{q}(z) = z + \tilde{q}(0) = z - \iota L\,, \tag{2.39}$$

that is, $\tilde{q}(0) = -\iota L$, or expressed as

$$\frac{1}{\tilde{q}(z)} = \frac{1}{R(z)} + \iota \frac{2}{kw(z)^2}\,. \tag{2.40}$$

Using the complex beam parameter $\tilde{q}(z)$ to describe the Gaussian beam is practical because it fully contains the propagation law of the beam in free space. This can bee seen from the equivalence of (2.35) and the expression

$$\tilde{G}(\mathbf{r}) = \frac{\tilde{q}(0)}{\tilde{q}(z)} \exp\left[\iota\left(kz + k\frac{x^2+y^2}{2\tilde{q}(z)}\right)\right]\,, \tag{2.41}$$

obtainable using several different approaches [7].

To simply depict how the monochromatic Gaussian beam evolves when it passes through or reflects from optical elements, one more property of the wave described by (2.35) is exploited: its cylindrical symmetry. Due to this simplification, the ABCD formalism of geometrical optics can be used to study propagation properties of Gaussian beams [7, 137]. In this method, the optical system through which the light passes is described by a 2×2 matrix, the four letters referring to the for elements of it. The formalism gives the complex beam parameter transforms as

$$\tilde{q}_2 = \frac{A\tilde{q}_1 + B}{C\tilde{q}_1 + D}\,, \tag{2.42}$$

when the beam passes through a system given by the elements A, B, C and D of the matrix. If a Gaussian beam of the form (2.41) is taken with $z = 0$, that is,

$$\tilde{\Gamma}_1(x, y, 0) = \exp\left[\iota k \frac{x^2 + y^2}{2\tilde{q}_1(0)}\right]\,, \tag{2.43}$$

and it is assumed that its further propagation is described by an ABCD matrix, then the function $\tilde{\Gamma}_2(\mathbf{r})$ behind the ABCD system is given by [7]

$$\tilde{\Gamma}_2(\mathbf{r}) = \frac{1}{A + B/\tilde{q}_1}\exp\left[\iota k \frac{x^2 + y^2}{2\tilde{q}_2}\right]\,, \tag{2.44}$$

where A and B are the elements of the first row in the matrix describing the system, $\tilde{q}_2$ is given by (2.42), and the same refractive indices are assumed before and behind the optics. Using (2.44) with the matrix of free-space propagation ($A = 1, B = z, C = 0, D = 1$), (2.41) can be regained. Similarly, assuming a focal element with focal length f and free-space propagation of distance z after it, the focused Gaussian beam is found to be [139]

$$\tilde{G}_f(\mathbf{r}) = \frac{\tilde{q}_f(-f)}{\tilde{q}_f(Z)}\exp\left[\iota k \frac{x^2 + y^2}{2\tilde{q}_f(Z)}\right]\exp[\iota k(Z + f)]\,, \tag{2.45}$$

where $\tilde{q}_f(Z)$ is the complex beam parameter of the focused beam (for explicit expressions in different approximations see Appendix B.1) and $Z = z - f$ is the distance measured from the geometrical focal point. Equation (2.45) being formally the same as (2.41) coincides with the mentioned fact that Gaussian beams remain Gaussian after propagating in the ideal paraxial system. For more details on (2.45) and its derivation see Appendix B.1.

2.3.3 Focusing using scalar diffraction theory

While using the ABCD formalism is practical, and the results obtained using it are general — as the effects found are present even in the most idealistic cases — there are several

limitations of this method. When the case gets farther from ideal, the results from ABCD matrix analysis become less comparable to the real experimental situation.

Although ABCD matrices may not fulfill the requirements in some cases, there is no need for brute force solution of the Maxwell equations to find the properties of electromagnetic waves in the focal region (for example by finite difference [140] or finite element methods [141], discrete dipole approximation [142], ... etc., collectively often referred to as Maxwell- or electromagnetic field solvers). From the point that the wave has traversed the material of the lens or has been reflected from the mirror, focusing can be treated as free-space propagation. An "intermediate" solution, which is more detailed than the ABCD matrix analysis but less time consuming than Maxwell solvers, is given by the scalar diffraction theory of waves (or light) [90].

Diffraction theory of focusing is based on the Huygens–Fresnel principle. This law states that every point of a wave front can be considered as a secondary source of elementary spherical waves, and the disturbance in any later moment can be given as the interference of waves originating from these secondary sources. Focusing can be treated with this theory, because it can be considered as the diffraction of a wave front from a circular aperture (of course only if the focusing optics used is circularly symmetric). Mathematically, the Huygens–Fresnel principle can be expressed using the Huygens–Fresnel integral. According to this integral, in the case of an ideal spherical, monochromatic, converging wave the field in point P close to the focus is given by (omitting again $\exp[-\iota\omega t]$)

$$\tilde{G}(P) = -\frac{\iota}{\lambda}\frac{\exp[-\iota kR]}{R}\iint_H \frac{\mathcal{A}(Q)\exp[\iota kh]}{h}\,\mathrm{d}H\,, \tag{2.46}$$

where it has been assumed that the angles that characterize the problem are small[VIII](the paraxial approximation is used), so the so-called inclination factor can be taken constant [90], giving the $-\iota/\lambda$ factor. In (2.46) the amplitude $\mathcal{A}$ is interpreted along the surface H, $k = 2\pi/\lambda$ is the wave number, R is defined as the radius of the converging spherical wave front, and h is the distance of an arbitrary point Q of the surface H and point P (see Figure 2.9). The $\exp[-\iota kR]/R$ factor is only introduced for convenience (the amplitude and phase can be set arbitrarily along the surface H), to have a zero geometrical phase and a "comfortable" value for the amplitude in the focus.

Of course it can be questioned straight away how well this phenomenological principle can describe the physics which is governed by the more fundamental laws of Maxwell. The answer is the integral theorem of Kirchhoff, which gives the pathway from Maxwell's

[VIII] It is always a question what can be considered "small" in such statements. Here, for the diffraction of a converging spherical wave on a circular aperture it means that the point of interest is close to the center of the spherical wave front. Referring to Figure 2.9, it mathematically means that the cosine of the angle between the $\overline{QO}$ and $\overline{QP}$ lines is negligible when compared to 1, which is true when $a^2/R^2 \ll 1$ and $|\overline{OP}|/R \ll 1$ [143].

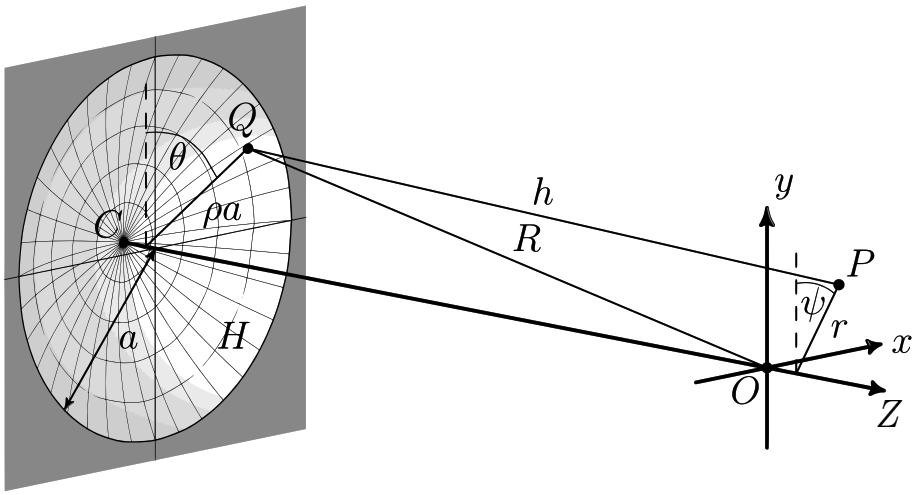

Figure 2.9. The usual coordinate system to evaluate the Huygens–Fresnel integral for the diffraction of a monochromatic, converging spherical wave on a circular aperture. This problem is equivalent to the focusing of waves with ideal spherical wave fronts. The integration is carried out along the points Q of the spherical surface H with radius of curvature R, diffracted on a circular aperture with radius a. The point Q can be uniquely referred on the surface H by coordinates ρa and θ. The origin O of the coordinate system is placed in the center of the spherical surface, and the point of interest in space is nominated as P (coordinates (x, y, Z) in Cartesian and (r, ψ, Z) in cylindrical coordinate systems[IX]). The distance between Q and P is named h. The distance of O and every $Q \in H$ (including C) is R.

equations to an expression equivalent to (2.46); simply through the equation of Helmholtz, by applying Green's theorem and the assumption of the spherical wave "basis" [90]. The Kirchhoff diffraction theory has been shown to be mathematically inconsistent [144], still, the results obtain with it agree very well with experimentally obtained data. Later, mathematically correct formulations, based on similar assumptions, have also been given, called Rayleigh–Sommerfeld diffraction theory. It has been shown that if the aperture is much larger then the wavelength ($a \gg \lambda$), then the two diffraction theories give essentially the same result in the far field (meaning the vicinity of the focus if focusing is considered) [145]. Also, in the general case of a plane or spherical waves, the difference between the two theories is only a boundary wave originating from the edge of the aperture [145], which is not relevant if Gaussian beams are studied which have almost zero intensity at the aperture edge.

An important, here utilized addition of diffraction theory compared to the ABCD formalism — apart from the other trivial benefits rising from using waves instead of rays — is that the aberrations of the wave front can be taken into account. A well-

[IX] Note here that the the azimuth angle ψ is measured from the y axis in contrary to the usual definition of the cylindrical coordinate system, where the azimuth angle is what the position vector makes with the x axis. The difference caused by this is given later. The reason for that is the traditions of this topic, most probably originating from the symmetries of the treated physical problems [90].

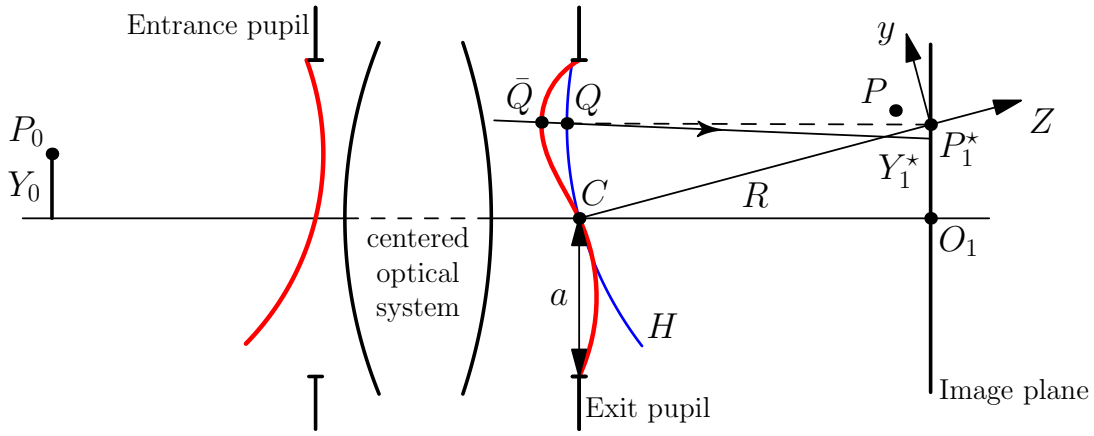

Figure 2.10. The definition of the aberration function for the general case of imaging an object point P_0 which is Y_0 distance from the optical axis. The Gaussian (paraxial) image point of the object is $P_1^\star$ being $Y_1^\star$ distance away from the axis of symmetry. The real wave front deviates from the ideal one H (Gaussian reference sphere). The aberration function Φ gives the distance between the arbitrary point $\bar{Q}$ of the wave front and Q of the reference sphere along the ray which traverses through $\bar{Q}$ (the line with arrow in the middle). Φ is positive if the direction of $\overline{\bar{Q}Q}$ coincides with the direction of the ray. In the case of focusing a spherical wave with the source being on the optical axis, the assumption of $Y_1^\star = 0$ can be used, meaning that $P_1^\star = O_1 = O$, so the origin of the coordinate system is the geometrical focal point, and the case coincides with that of Figure 2.9. In focusing the image plane is the focal plane, and the exit pupil is the edge of the aperture of the lens/mirror.

established approach is to introduce the aberration function $\Phi(\rho, \theta)$ [90]. The aberration function gives the spatial distance of the ideal wave front (which is spherical and called as Gaussian reference sphere) and the distorted one (see in more detail in Figure 2.10 and its caption). There are only two arguments of this spatially-dependent function, because it is interpreted along the points Q of surface H given by the Gaussian reference sphere. In general, Φ also depends on the image point $P_1^\star$ chosen, but it is fixed in all studied cases in this work, as focusing of spherical or plane waves is discussed originating from a source on the optical axis. For this reason the explicit dependence of Φ on $Y_1^\star$ is omitted.

The aberration function $\Phi(\rho, \theta)$ can have a very complex shape and is often expanded in the orthogonal set of Zernike polynomials [90]. However, frequently only some simple distortions of imaging are present in the focusing known also from textbooks on optics [127, 130]. These are called primary (or Seidel) aberrations, and they are the well-known primary spherical aberration, coma, astigmatism, curvature of field and distortion. For primary aberrations, using the polynomials of Zernike is not necessary, an equivalent representation, known also from geometrical optics, can be used [90]. In this work, the aberration function of a single aberration is written in the form

$$\Phi_{lnm}(\rho, \theta) = A_{lnm}\rho^n \cos^m(\theta) = \mu_{lnm}\lambda\rho^n \cos^m(\theta)\,, \tag{2.47}$$

Primary (Seidel) aberration	l	n	m	Aberration function
Spherical aberration	0	4	0	$A_{040}\rho^4$
Coma	0	3	1	$A_{031}\rho^3\cos(\theta)$
Astigmatism	0	2	2	$A_{022}\rho^2\cos^2(\theta)$
Curvature of field	1	2	0	$A_{120}\rho^2$
Distortion	1	1	1	$A_{111}\rho\cos(\theta)$

Table 2.1. The indexes and explicit forms of the aberration functions of primary (Seidel) aberrations [90].

where the indexes l, n and m are the unique indexes of the corresponding aberrations, l being contained implicitly in the coefficient A_{lnm} (l is related to the omitted $Y_1^\star$ dependence of Φ). The dimensionless μ_{lnm} factor has only been introduced in (2.47) because it is often more graphical to express the amount of aberration with its ratio to the wavelength of the radiation. The form of the aberration functions for the above mentioned five primary aberrations can be found in Table 2.1.

With the introduced aberration function, the Huygens–Fresnel integral (2.46) can be extended for the treatment of non-ideal focusing. In the presence of distortions it reads as [90]

$$\tilde{G}(P) = -\frac{\iota}{\lambda}\frac{\exp[-\iota kR]}{R}\iint_H \frac{\mathcal{A}(Q\in H)\exp[\iota k(h+\Phi)]}{h}\,\mathrm{d}H\,. \tag{2.48}$$

The only difference between (2.46) and (2.48) is that the phase modification on the Gaussian reference sphere, due to the distortions, is taken into account by Φ. It is to be noted here that there is a slight discrepancy between how Φ has been introduced and how it is used in (2.48). The way of use in (2.48) assumes that Φ gives the distance between the wave front and the reference sphere along the dashed line in Figure 2.10, while by definition, Φ gives the distance along the ray of Figure 2.10. However, with the already mentioned assumptions in the text or footnotes ($a^2 \ll R^2$, $\lambda \ll a$), and presuming an experimentally reasonable amount of aberration, the difference is negligible.

For later convenience, from this point, the arbitrary amplitude distribution $\mathcal{A}(Q\in H)$ is written as

$$\mathcal{A}(\rho) = \exp\Big[-(\rho a)^2/w^2\Big] = \exp\Big[-\kappa\rho^2\Big]\,, \tag{2.49}$$

that is, a wave with Gaussian amplitude distribution along the reference wave front is assumed to be focused. As wave fronts of Gaussian beams are spherical, and they have transverse amplitude distribution given by functions like (2.49) (see Section 2.3.2), this is a proper treatment of focusing Gaussian beams. It is also supported by the fact that evaluating (2.48) with (2.49), taking $\Phi\equiv 0$, and assuming that the aperture does not cut from the beam ($\kappa \gg 1$), the resulting electric field distribution corresponds to a Gaussian beam [135, 143], as expected [137]. In (2.49) a new parameter is introduced for brevity,

called truncation coefficient [143, 146], given by

$$\kappa = \frac{a^2}{w^2}\,. \tag{2.50}$$

True to its name, it describes how much the aperture clips from the Gaussian beam. The two limits, $\kappa \to 0$ and $\kappa \to \infty$, give the case of homogeneous illumination and an untruncated Gaussian beam, respectively.

An other notation introduced here is advantageous in the treatise of focusing of pulsed beams, which is discussed in a later section. Consider a beam consisting of several monochromatic components and that we are interested in the effect of their superposition in the vicinity of focus. Due to the chromatic aberration of the focusing element [75, 76, 130, 147–149], or because the different radii of the wave fronts, the focusing of each harmonic wave would be treated in a different coordinate system with different positions of the origin O. This is due to the wavelength dependence of the wave front radius $R = R(\omega)$, which is measured from plane of the exit pupil, which has a fixed place. Fortunately, in the treated cases, the position of the origin varies with wavelength only along the optical axis, depending on where the center of the Gaussian reference sphere is, so $Z = Z(\omega)$ depends on frequency [147]. For a treatment with one frame of reference, the origin corresponding to the case of a given angular frequency ω_0 is chosen (it is the carrier wave here, but could be any other), and the electric field in a point P is given in that corresponding coordinate system, with the axial coordinate $Z_0 = Z(\omega_0)$.

With the assumptions and notations detailed in the previous paragraphs, and utilizing the cylindrical symmetry of the problem, the physical law named after Christiaan Huygens and Augustin-Jean Fresnel can be written in a more explicit form than (2.48). Following the steps detailed in textbooks or journal articles [90, 143, 146, 147], it can be shown that the field distribution in point P close to the focus can be evaluated from (2.48), assuming the Gaussian amplitude form (2.49), giving

$$\tilde{G}(P) = -\frac{\iota\omega}{2c}\frac{a^2}{(Z_0+R_0)R}\exp[\iota k(Z_0+R_0-R)]\exp\left[\iota k\frac{r^2}{2(Z_0+R_0)}\right]\frac{1}{\pi}\tilde{\mathcal{I}}(u,v,\psi)\,, \tag{2.51}$$

where

$$\tilde{\mathcal{I}}(u,v,\psi) = \int_0^1\int_0^{2\pi}\exp\left[-\kappa\rho^2\right]\exp\left[\iota\left(k\Phi - v\rho\cos(\theta-\psi) - \frac{u}{2}\rho^2\right)\right]\rho\,\mathrm{d}\theta\,\mathrm{d}\rho\,, \tag{2.52}$$

and

$$u = \frac{\omega}{c}\frac{a^2}{R}\frac{Z_0+R_0-R}{Z_0+R_0}\,, \tag{2.53}$$

$$v = \frac{\omega}{c}\frac{a}{Z_0 + R_0} r \,. \tag{2.54}$$

In the previous expressions subscript 0 (zero) means evaluation of the given angular frequency-dependent quantity at ω_0, and $r = \sqrt{x^2 + y^2}$ is the transverse coordinate.

Expression (2.51) can be further simplified. Namely, the focused field evaluated using (2.51) contains a focal shift [146, 150], meaning that the position of highest intensity does not coincide with the geometrical focus (the diffraction focus differs from the geometrical optics focus). This does not appear in most experimental situations, as this is only present if very loose focusing is applied. Similarly to the treatment with ABCD formalism, an additional approximation can be used, which bears the name of Peter Debye[X] (detailed also in Appendix B.1 for the ABCD matrix analysis of Gaussian beams). If the Fresnel number[XI] of the Guassian beam defined by $N_w = w^2/(\lambda R)$ (or $N_a = a^2/(\lambda R)$ if homogeneous illumination is considered) is large enough ($N_w, N_a \gg 1$, meaning that the focusing is not extremely loose), the focal shift disappears and the Debye approximation can be used [143, 151]. In this case the field in the vicinity of focus is given by

$$\tilde{G}_D(P) = -\frac{\iota\omega}{2c}\frac{a^2}{R^2}\exp[\iota k(Z_0 + R_0 - R)]\,\frac{1}{\pi}\tilde{\mathcal{I}}(u_D, v_D, \psi)\,, \tag{2.55}$$

where the integral $\tilde{\mathcal{I}}$ is the same as before (see (2.52)), but taken with different arguments expressed by

$$u_D = \frac{\omega}{c}\frac{a^2}{R^2}(Z_0 + R_0 - R)\,, \tag{2.56}$$

$$v_D = \frac{\omega}{c}\frac{a}{R} r \,. \tag{2.57}$$

It is easy to see that the simplification in the ABCD formalism, also termed Debye approximation (see Appendix B.1), really means the same approximation for (untruncated) Gaussian beams as in diffraction theory. It has to be expressed differently with mathematical formulas, due to the differences of the two treatments, but in both cases it means that the focusing is not highly loose.

While generally the Debye integral for focusing is satisfactorily precise, special care has to be taken when aberrations are present. In that case one has to be aware of the fact that there are more strict requirements for the Debye approximation to be valid, which might become important when the high intensity spatial regions are shifted compared

[X] In diffraction theory Debye representation means that the waves of the secondary sources of the Huygens–Fresnel principle are approximated by plane waves.

[XI] The Fresnel number is the number of the Fresnel zones that are filling the center part of the aperture covered by the incoming beam spot (for Gaussian beam) or the whole aperture (for homogeneous illumination) and that are constructed from the focal point [90].

to the undistorted case [152, 153]. At the same time, the Debye approximation can be extended to high numerical apertures, that is, it can provide results not treatable in the paraxial approximation [154]. The primary difference is that the vectorial nature of the electromagnetic waves can no longer be neglected, vector field quantities have to be used, mentioned also in the introduction referring to [81, 82] (see Section 2.1.2). Aberration-distorted focusing can also be properly treated using vector diffraction theory [155, 156], but this is not a topic of this work. The only relevant idea regarding the vector nature of light that the longitudinal components of the field can be neglected in the paraxial approximation, so the the propagation of the two transverse components (the x- and y-linear or left- and right-circular constituents) can be treated independently [157, 158].

2.3.4 Pulsed beam propagation

In the previous sections propagation properties of monochromatic beams were discussed. However, this work deals with the focusing and free-space propagation of pulsed Gaussian beams. As discussed earlier, this can be achieved by using Fourier transform to convert findings applied in the case of monochromatic waves to the treatment of pulsed beam propagation. Like for wave equations (or any differential equations), the first step is to define "initial" (or "boundary") conditions [94]. For pulsed beam propagation this usually means that in an initial plane the electric field in the spectral domain is known and is given by

$$\tilde{\mathcal{P}}(\mathbf{r},\omega) = \tilde{U}(\omega)\tilde{G}(\mathbf{r},\omega)\,, \tag{2.58}$$

where $\tilde{G}(r,\omega)$ describes the spatial distribution in a plane (for example Gaussian, like (2.41) for $z=0$) and $\tilde{U}(\omega)$ is given by (2.5), that is, determined by the temporal shape of the pulse through the inverse Fourier transform (see (2.2)). The (2.58) type of decomposition of the field $\tilde{\mathcal{P}}(r,\omega)$ in the spectral domain means no restriction or loss of generality, applied usually for pulsed beam diffraction or focusing. If one wants to obtain the temporal variation of the electric field in an other point in space, the $\tilde{G}(\mathbf{r},\omega)$ has to be evaluated in that point for every ω, and the focused or propagated field can be calculated as

$$\tilde{E}^{(p)}(\mathbf{r},t) = \mathscr{F}^{-1}\left\{\tilde{\mathcal{P}}(\mathbf{r},\omega)\right\}\,. \tag{2.59}$$

The above approach is the most general way, it can be applied irrespective of the exact method used to obtain the factor $\tilde{G}(\mathbf{r},\omega)$, containing the propagation. For ultrashort pulse focusing, it has been utilized both for precise numerical calculations and approximate solutions performed to obtain information on the pulse properties in the focal region [76, 135, 139, 147, 149, 159–161]. Such results have even been compared with experimental data providing very nice agreements [162, 163].

While numerical simulations can give results that make direct comparison with measured data possible, it is often hard to extract the exact physical origin of a given effect from it. When the aim is not a case study, or to check if the given model reproduces some experimental observations, but to know how exactly or for what reason the given phenomenon occurs, analytical formulas are more appropriate tools. Of course, analytical approaches need simplifications, and can not treat as complex cases as numerical ones, but they directly show the physical relationships.

For pulsed beams, an analytical theory was developed, which can provide such straightforward information on the diffraction of these spatially confined wave packets [164]. To use this theory, the propagation factor $\tilde{G}(\mathbf{r},\omega)$ in (2.58) is rewritten using Euler's formula as

$$\tilde{G}(\mathbf{r},\omega) = \mathcal{G}(\mathbf{r},\omega)\exp[\iota\varphi_G(\mathbf{r},\omega)] \ . \tag{2.60}$$

The approximation here is that both the modulus $\mathcal{G}(\mathbf{r},\omega)$ and the complex phase $\varphi_G(\mathbf{r},\omega)$ of $\tilde{G}(\mathbf{r},\omega)$ can be expanded into Taylor series in frequency around ω_0, and can be terminated after the first few orders. So

$$\mathcal{G}(\mathbf{r},\omega) = \mathcal{G}_0(\mathbf{r}) + \frac{\mathcal{G}_0'(\mathbf{r})}{1!}(\omega-\omega_0) + \dots \ , \tag{2.61}$$

$$\varphi_G(\mathbf{r},\omega) = \varphi_{G,0}(\mathbf{r}) + \frac{\varphi_{G,0}'(\mathbf{r})}{1!}(\omega-\omega_0) + \dots \ , \tag{2.62}$$

with prime sign denoting differentiation with respect to ω, and subscript zero evaluation at the central frequency ω_0 (that is, $\mathcal{G}_0(\mathbf{r}) = \mathcal{G}(\mathbf{r},\omega_0)$, $\mathcal{G}_0'(\mathbf{r}) = (\mathrm{d}\mathcal{G}(\mathbf{r},\omega)/\mathrm{d}\omega)|_{\omega=\omega_0}$, $\dots$). It can be shown that with the above assumption of terminating the series at first order, the temporal variation of the propagated electric field in point P (pointed by $\mathbf{r}$) at local time

$$\tau = t - \varphi_{G,0}'(\mathbf{r}) \tag{2.63}$$

can be written as

$$\tilde{E}^{(p)}(\mathbf{r},\tau) = \tilde{\mathcal{E}}^{(p)}(\mathbf{r},\tau)\exp[-\iota\omega_0\tau] \ , \tag{2.64}$$

with the complex envelope approximated by

$$\tilde{\mathcal{E}}^{(p)}(\mathbf{r},\tau) \simeq \mathcal{G}_0(\mathbf{r})\tilde{\mathcal{E}}^{(i)}(\tau)\left[1+\iota\frac{\mathcal{G}_0'(\mathbf{r})}{\mathcal{G}_0(\mathbf{r})}\frac{\mathrm{d}\tilde{\mathcal{E}}^{(i)}(\tau)/\mathrm{d}\tau}{\tilde{\mathcal{E}}^{(i)}(\tau)}\right]\exp\Big[\iota\left(\varphi_{G,0}(\mathbf{r})-\omega_0\varphi_{G,0}'(\mathbf{r})\right)\Big] \ . \tag{2.65}$$

In the expression above

$$\tilde{\mathcal{E}}^{(i)}(\tau) = \frac{1}{2\pi}\int_{-\infty}^{\infty}\tilde{U}(\omega)\exp[-\iota\,(\omega-\omega_0)\,\tau]\ \mathrm{d}\omega \tag{2.66}$$

is the complex temporal envelope of the input pulse (given by the initial conditions), with

carrier frequency ω_0, determined by the complex spectrum $\tilde{U}(\omega)$. Using the local time τ instead of t means only a temporal shift, and using it is practical, because this way the relevant part of the pulse is around $\tau = 0$ (see considerations on the phase derivatives in Section 2.2.1). With a further assumption (see in Appendix B.2), the relation of the real envelope $A^{(p)}(\mathbf{r},\tau) = \left|\tilde{\mathcal{E}}^{(p)}(\mathbf{r},\tau)\right|$ and phase $\hat{\varphi}^{(p)}(\mathbf{r},\tau) = \arg\left[\tilde{\mathcal{E}}^{(p)}(\mathbf{r},\tau)\right]$ of the propagated field to that of the input pulse can be expressed [115]. It can be shown that, in this approximation, the relationships are

$$A^{(p)}(\mathbf{r},\tau) \simeq \mathcal{G}_0(\mathbf{r})\exp\left[-\frac{\mathcal{G}_0'(\mathbf{r})}{\mathcal{G}_0(\mathbf{r})}\frac{\mathrm{d}\hat{\varphi}^{(i)}(\tau)}{\mathrm{d}\tau}\right]A^{(i)}(\tau)\,, \tag{2.67}$$

$$\hat{\varphi}^{(p)}(\mathbf{r},\tau) \simeq \hat{\varphi}^{(i)}(\tau) + \varphi_{G,0}(\mathbf{r}) - \omega_0\varphi_{G,0}'(\mathbf{r}) + \frac{\mathcal{G}_0'(\mathbf{r})}{\mathcal{G}_0(\mathbf{r})}\frac{\mathrm{d}\ln\left(A^{(i)}(\tau)\right)}{\mathrm{d}\tau}\,, \tag{2.68}$$

with $A^{(i)}(\tau) = |\tilde{\mathcal{E}}^{(i)}(\tau)|$ and $\hat{\varphi}^{(i)}(\tau) = \arg\left[\tilde{\mathcal{E}}^{(i)}(\tau)\right]$. The above first-order expressions can be used to obtain analytical formulas on the carrier frequency, the envelope form, the CEP or the polarization state changes of pulsed beams occurring during the propagation or focusing, happening due to diffraction [115, 139, 164]. For the exact presumptions used in this theory, see the detailed derivations in Appendix B.2.

2.3.5 Phase and group velocity

The phase and group velocity has already been mentioned, related to laser oscillators, where the difference between them caused the CEP slippage of mode-locked lasers shot to shot. As several nonlinear optical phenomena depend on the CEP [17, 56–63], it is important to know its changes during the focusing of the pulse. While in the laser oscillator the difference between these two velocities is caused by the dispersion of the materials inside, in the free space it is a result of the wavelength dependence of diffraction, acting as a kind of dispersion [164].

The quantity called "phase velocity" (v_p) is used to describe how fast the cophasal surfaces of a monochromatic wave are propagating in space [90]. For plane waves, it is easy to give this velocity in vacuum, it equals to the physical constant c, the speed of light, and its direction is in the wave vector $\mathbf{k}$. If the propagation happens in a material, it is only modified by the refractive index n of the given material, giving $v_p = c/n = k/\omega$ [18, 90]. However, when a wave having a phase with spatial dependence is considered — like a (Gaussian) beam —, its cophasal surfaces are not planes, and the case is different. The general definition of phase velocity, which can be spatially varying, is [90]

$$v_p(\mathbf{r},\omega) = \frac{\omega}{|\nabla\varphi_G(\mathbf{r},\omega)|}\,, \tag{2.69}$$

where $\nabla = \mathbf{u}_x \partial/\partial x + \mathbf{u}_y \partial/\partial y + \mathbf{u}_z \partial/\partial z$ is the gradient operator. Phase velocity is a very important property in nonlinear optics [22], where the difference between the propagation speeds of the fundamental laser light and the generated "secondary" radiation in the material determines the efficiency of the process. This aspect, the "phase matching", is very important in high harmonic generation [84, 85], for example, but the changes of the phase velocity has been shown to be important in the more practical problem of high precision distance measurement as well [165]. The phase velocity can be greater than c, which happens for beams due to Gouy phase shift [77], but it does not contradict causality of the theory of relativity [166], as phase velocity has no direct physical significance since it cannot carry information [90].

The "group velocity" (v_g) describes the propagation speed of a wave packet as a whole. While the expression is again simple for plane waves ($v_g = \mathrm{d}\omega/\mathrm{d}k$), the general formula is more complex. The group velocity of the wave packet with carrier frequency ω_0 (can be calculated at any other frequency, but in this work it is always interpreted at ω_0) is given by

$$v_g(\mathbf{r}) = \frac{1}{|\nabla \left(\partial \varphi_G(\mathbf{r}, \omega)/\partial \omega|_{\omega=\omega_0}\right)|} \,. \tag{2.70}$$

It is to be noted that (2.70) is strictly valid only for narrow bandwidth beams, when the ratio of the pulse's bandwidth $\Delta\omega$ and central frequency ω_0 are sufficiently small ($\Delta\omega/\omega \ll 1$) [90]. The group velocity of short pulses got considerable attention when it was shown that a superluminal value of the group velocity ($v_g > c$) is possible in amplifying media [167]. Later it was shown that the wave packet can travel with a group velocity faster than the speed of light even in vacuum [168, 169]. This, however, does not contradict special relativity either, as in the presence of dispersion — even if it is caused by diffraction — the group velocity is not necessarily equal to the speed of energy propagation, so it does not give how fast the information travels (which never travels faster than c) [170, 171]. It has been also confirmed by mathematical means that the superluminal group velocity of focused, pulsed beams does not violate causality [78]. Still, the group velocity is relevant, because, together with phase velocity, it determines the CEP, as discussed in the beginning of this section.

2.4 Measuring the changes of the carrier-envelope phase

The control and measurement of CEP is a very important task for highly nonlinear optical sciences, for the sake of reproducible experiments [47]. In the case of mode-locked laser oscillators, the control is achieved by phase-stabilization [45], which makes it possible to

obtain (almost) identical pulses at the electric field level at every nth shot (n is determined by the CEO phase set, see Section 2.2.2). When optical parametric amplifiers are used as sources, the control is even better, the pulses are alike in every single shot [172].

Of course, for appropriate control, the measurement of the phase is inevitable. When the measurement is considered, a distinction has to be stressed again between the CEO phase of a pulse train and the CEP of a single pulse. While for the measurement of the CEO phase the quite standard procedure of f-to-2f interferometry exists [112], finding an easily and widely applicable method for determining the CEP of single pulses is still under research. Only the pulse-to-pulse change (or drift) of the CEP can be determined with methods measuring the CEO phase, and the "absolute" value of the CEP remains undetermined. In the following, the most common experimental methods are gathered which aim to give the amount of change of the CEP (or its absolute value).

2.4.1 Methods utilizing nonlinear optics or light-matter interaction

As highlighted in the title of the present section, the most common methods are based on either nonlinear optical processes, or rely on data provided by light-matter interaction related phenomena. While the most widely used and accepted solutions for CEO-phase detection depend on theoretical assumptions in the frequency domain (think of the frequency combs of mode-locked laser oscillators discussed in Section 2.2.2), there are several new ideas that break up with this approach.

The first attempt to measure the CEP changes (or CEO phase in other words) of a mode-locked oscillator arose when the laser technology was reaching the sub-10-fs regime [108]. The idea was to measure the temporal cross-correlation of subsequent pulses coming from the laser oscillator (see Figure 2.11(a)). This was achieved by sending the laser beam into a Michelson interferometer, in which one arm (long arm) was much longer than the other (short arm), to make a pulse coming from the short arm overlap temporally with a previous pulse coming from the long arm. By focusing the combined beams into a nonlinear crystal, and detecting the signal behind it, the temporal cross-correlation function between subsequent pulses could measured by varying the time delay Δt (for example, by varying the length of the short arm, see Figure 2.11(a)). The CEP can be obtained from the position of the function peak with respect to delay zero (see red dot in the plot of Figure 2.11(a)) [108]. While this solution is not practical due to slow data acquisition, it was used in the first precise frequency measurements with lasers [173].

Another solution, which became quite a standard for CEO-phase measurements, is f-to-2f interferometry [112] (see Figure 2.11(b)). The basic idea of f-to-2f interferometry is that, through the nonlinear process of frequency doubling, the low frequency part of

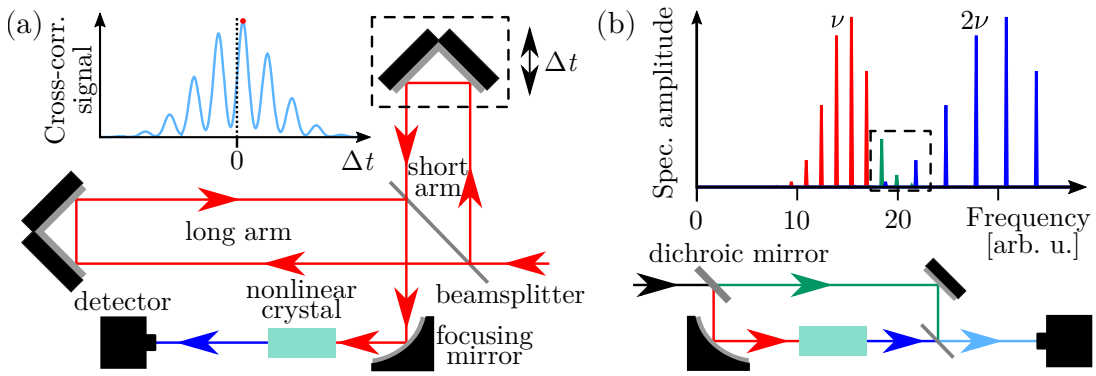

Figure 2.11. The most important aspects of two prominent methods for CEP change detection of laser oscillators. (a) The cross-correlation technique, which is based on the measurement of the temporal cross-correlation function of two subsequent pulses in the pulse train (plot in the upper left corner). The figure also depicts a basic sketch of the experimental setup for the measurement. (b) The f-to-2f interferometry which relies on the measurement of the beat note between the frequency comb and its up-converted replica. The higlighted region in the spectrum is where this beating can be measured. The components of the experimental setup that are depicted with the same graphic as in (a) have the same role as in (a).

the comb structure is upconverted two higher frequencies (see blue spectrum in Figure 2.11(b)). It is then combined with high frequency part of the original spectrum (green combs in the spectrum of Figure 2.11(b)). It can be shown that in the limited detection range (dashed region in spectrum of Figure 2.11(b)) a beat note comes off, which is the ν_{CEO} frequency, and as a such "low" frequency, it can be detected by a fast photodiode. From this, the CEO phase can be determined using the considerations detailed in Section 2.2.2 [112]. A simple outline of the experimental realization of this measurement can also be seen in 2.11(b). A big drawback of this approach is that, to have an overlapping spectral region between the fundamental and the second harmonic, a spectrum covering at least an octave is needed. Similar methods, based on frequency conversion and beat note detection, have been developed [174], some of them eliminating the need of the broad bandwidth [112], although through other sacrifices (the need of even higher intensity for the more highly nonlinear phenomena exploited).

Another limitation of the procedures above — apart from the necessity of high intensities because of nonlinear processes and the limitation to at least an octave bandwidth in some cases — is the constraint to multiple shot usage. Both the ones measuring in the frequency domain, and the correlation signal acquisition, need the detection of several pulses, otherwise they do not work. So some phase stability of the oscillator is preliminary assumed (or provided). A very successful solution for precise, single-shot CEP detection was the idea of measuring the electron spectra ionized by the laser field in a special way [175]. This certain method is often called stereo-ATI, because the electrons ionized by

the process of above threshold ionization (ATI) are detected in the two directions being parallel to laser polarization. Since its first demonstration, it has been developed to a very reliable single-shot CEP measurement method [176]. It can even can provide information on the "absolute" phase [177, 178]. Detecting photoelectrons for phase measurement was applied before the appearance of the current stereo-ATI setup [179, 180], and the idea has been studied widely theoretically as well [181], which gives a stable background to this solution. This detection method, however, needs a complicated and expensive setup [176]. Of course, any other phenomenon that depends on CEP could be used to give such a measurement method. A promising tool has been recently demonstrated, for example, in which the photocurrents induced by the focused laser pulse are detected [182].

2.4.2 CEP-change measurements with spectral interferometry

Spectral interferometry and its analogs are important and widely used pulse characterization methods of ultrafast optical sciences [104]. It is not surprising that, only a few years after the appearance of few-cycle optical pulses, a CEP-change measurement method based on spectral interferometry (SI) was proposed [183]. However, this first method still used nonlinear optics. Since then, it has been proven that SI with its several branches can provide a simple, linear optical method for CEP-drift measurements [184, 185]. Using a linear method for the detection of pulse-to-pulse CEP changes is beneficial, because it needs neither high intensities (low-energy pulses can be measured and no focusing is needed) [186], nor the broad bandwidth is necessary (applicable for multi-cycle pulses) [187]. The setups can be extremely simple, at least compared to detection techniques presented in the previous section. Of course, being a relative measurement method, SI alone can not provide information on the "absolute" phase, that is, on the value of the CEP of a single pulse in the train. Still, the simple method of SI can be used to verify the usability of new CEP-shifting equipment [188], or to study the spatial distribution of the CEP in a pulsed beam [189].

Being an easily applicable method to measure the spatial variations of the phase of pulsed beams, SI serves as an important tool for experimental investigation of the properties studied in this work. For this reason, a short description on the principles of SI is given in the following. As its name suggests, SI is based on resolving the interference of two temporal signals with a spectrometer (see an example signal in Figure 2.12(a)). In the most simple cases this is achieved by using a Mach–Zehnder type interferometer (see Figure 2.12(b)). The sample, the dispersion properties of which is to be determined, is placed in one arm of the interferometer (sample arm), and the other arm is empty (reference arm). The beam passing through this latter serves as a reference for the measurement. The combined signal from the two arms is then resolved by a spectrometer.

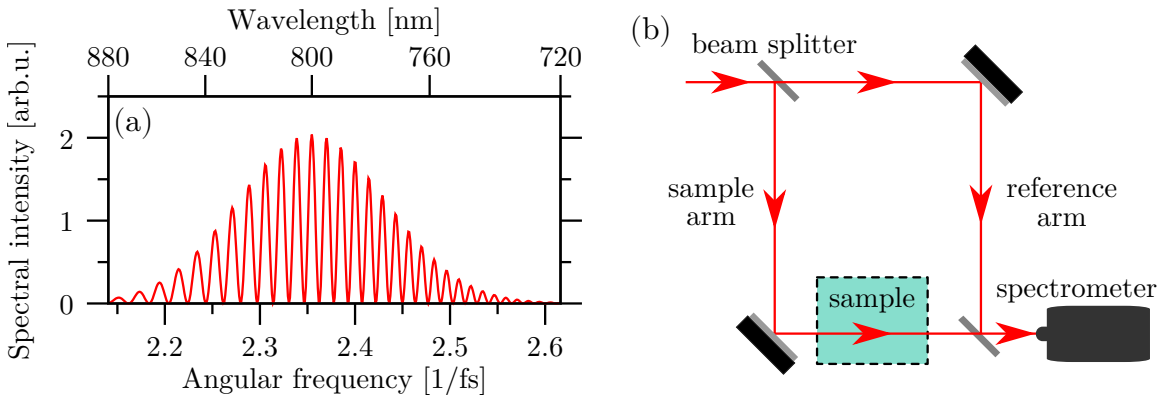

Figure 2.12. (a) The simulated, spectrally resolved interference signal $I_{\mathrm{ifg}}(\omega)$ of a transform-limited pulse of $T_{\mathrm{FWHM}} = 15\,\mathrm{fs}$ duration and one with the same bandwidth but having GDD $= 600\,\mathrm{fs}^2$ second order phase derivative and delayed by GD $= 400\,\mathrm{fs}$ with respect to the transform-limited one. (b) The sketch of a basic experimental setup for SI based on a Mach–Zehnder type interferometer used to determine the spectral phase shift of a sample.

The signal detected by the spectrometer (called interferogram) is given by the fundamental equation of interference [130], and can be written in the form

$$I_{\mathrm{ifg}}(\omega) = I_{\mathrm{sam}}(\omega) + I_{\mathrm{ref}}(\omega) + 2\sqrt{I_{\mathrm{sam}}(\omega) I_{\mathrm{ref}}(\omega)}\cos\left[\Delta\varphi(\omega)\right] . \tag{2.71}$$

In the previous expression, $I_{\mathrm{sam}}(\omega)$ and $I_{\mathrm{ref}}(\omega)$ are the intensity spectra of the beams from the sample and reference arms, respectively, and $\Delta\varphi(\omega) = \varphi_{\mathrm{sam}}(\omega) - \varphi_{\mathrm{ref}}(\omega)$ is the spectral phase difference of the light coming from each arm of the interferometer (see the decomposition (2.5) in a previous section). If the experimental setup is like in Figure 2.12(b), then $\Delta\varphi(\omega)$ purely gives the spectral phase modification caused by the sample. For the CEP-drift measurement [186, 187], for example, the Mach–Zehnder interferometer is built in asymmetric form (like it was done with the Michelson interferometer for the cross-correlation measurement in Figure 2.11(a)), so every pulse in the pulse train interferes with the consecutive ones (the closest being the most important). This way the phase difference corresponds to the phase difference between the subsequent pulses (determined by the CEP difference and the delay between them, this latter adjustable by making the length of one arm variable).

If the reference pulse is transform limited, or its spectral phase is known $\varphi_{\mathrm{ref}}(\omega)$, then $\varphi_{\mathrm{sam}}(\omega)$ can be calculated from $\Delta\varphi(\omega)$. Together with $I_{\mathrm{sam}}(\omega)$ they fully describe the pulse of the sample arm by (2.5). The temporal pulse shape can be given by simply using inverse Fourier transform. So, to have an experimental method to measure the phase or shape of a pulse, the only step remaining is to get the phase difference $\Delta\varphi(\omega)$ from the measured interferogram $I_{\mathrm{ifg}}(\omega)$. Several methods exists for this [190], one of the

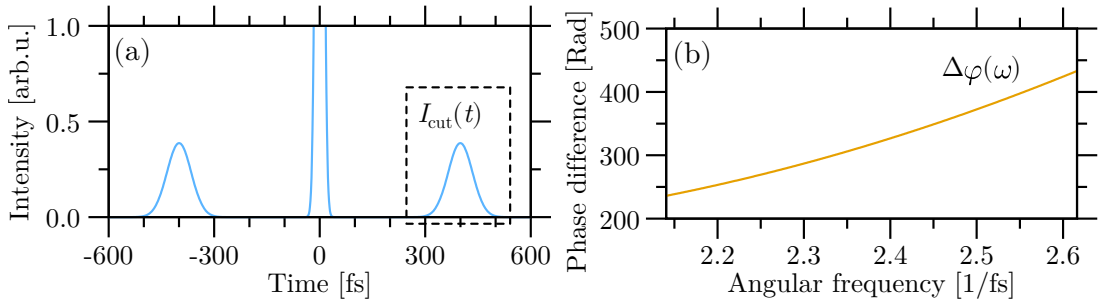

Figure 2.13. (a) The inverse Fourier transform of the interferogram of Figure 2.12(a), the first step of FTSI. The next step is to filter the relevant part of the temporal data (the $I_{\mathrm{cut}}(t)$ in the dashed rectangle), which in the simplest case means replacing everything with zero in the data series except the part in the dashed rectangle if fast-Fourier transform is used. (b) The spectral phase difference $\Delta\varphi(\omega)$ retrieved as the complex argument of the $I_{\mathrm{cut}}(t)$ limited signal's Fourier transform: $\Delta\varphi(\omega) = \arg[\mathscr{F}\{I_{\mathrm{cut}}(t)\}]$.

most widely used ones is Fourier-transform spectral interferometry (FTSI) [191], which was shown to be the most reliable one from the several others, in specific applications [190]. Apart from its general usage for ultrafast measurements [104], this is the evaluation method in all previous examples of CEP-change measurement with SI [186–189]. The most important steps of FTSI, and the spectral phase difference $\Delta\varphi(\omega)$ obtained with it from the interferogram of Figure 2.12(a), can be seen in Figure 2.13(a)-(b).

Using FTSI to evaluate an interferogram is technically very simple [104, 190, 191]. The first step is to apply an inverse Fourier transform[XII] on the interferogram, which yields a temporal signal (like the one in 2.13(a), obtained by transforming the interferogram of 2.12(a)). This temporal signal contains three peaks (if the interferogram is the result of only two pulses' interference), one at zero delay, and two symmetrically on the two sides of zero delay, these last two corresponding to the interference of the two pulses. The next step is to filter this temporal data, and restrict it to one of the interference peaks (only the part in dashed rectangle is not replaced by zero in 2.13(a), named $I_{\mathrm{cut}}(t)$[XIII]). As a last step, this filtered temporal signal $I_{\mathrm{cut}}(t)$ has to be Fourier transformed. The spectral phase difference $\Delta\varphi(\omega)$ is the complex argument of the Fourier transformed filtered signal (see 2.13(b)). Although not highlighted explicitly in Figure 2.13(b), the resulted $\Delta\varphi(\omega)$ curve can be perfectly fit by a second-order polynomial (up to numerical precision), reproducing the coefficients written in the caption of Figure 2.12.

[XII] Of course, the normal Fourier transform could also be used. In that case in a later step its inverse should be applied. The only reason here for using the inverse transformation for this step is that this way it is consistent with the previous discussion (inverse Fourier transform yields the temporal signal).
[XIII] The pulse at negative delay could also be used.

Chapter

Three

Results

The purpose of the preceding parts of this work is to give an overview on the scientific areas serving as motivation, to gather theoretical and experimental background that was necessary for achieving the results presented in the following sections, and to summarize the prior or recent accomplishments in these topics. This chapter is dedicated to review my contributions to findings on the phase and polarization property changes of pulsed (Gaussian) beams happening during focusing (or during propagation in free space).

This chapter first discusses our study on the phase velocity and group velocity variations of focused, pulsed Gaussian beams. The analysis covers not just cases when focusing is undistorted, but also situations when the diffraction of the broadband beam is modified by primary aberrations [T1].

The next topic covers a theoretical discussion on a strongly related property: the CEP. In our associated publications, we studied the possibility of undistorted focusing of transform-limited or chirped few-cycle pulses with lenses or more complex optical systems, even allowing some control over the CEP [T2–T4].

An important result was the experimental verification of the CEP-affecting features highlighted in our theoretical works. The experiments were performed using spectral interferometry, and included also a detailed investigation on the wavelength dependence of beam properties [T5].

Finally, the last section of this chapter deals with the polarization state of polarization-shaped ultrashort pulses. Our findings on the polarization-state changes, occurring during focusing or free-space propagation, highlight new effects of diffraction on pulsed beam propagation that may influence current or future experiments carried out using pulses with temporally varying polarization states [T6, T7].

3.1 On-axis phase velocity and group velocity variations of focused, pulsed Gaussian beams

As it was discussed previously, the phase velocity is a very important property of propagating electromagnetic waves in nonlinear optical sciences [22], as it determines the efficiency of phase matching [22, 84, 85]. During the experiments studying these nonlinear optical phenomena, the focusing of the laser pulse is necessary [47]. So the question is, that was raised already: how focusing influences phase velocity? Of course, as the change of phase velocity on axis is a consequence of the Gouy phase shift of beams, the answer affects linear optical studies as well [165, 192, 193] (and references therein).

A question of similar importance is the variation of the group velocity, which was shown to behave superluminally in the focus in some cases (see Section 2.3.5). However, not all light-diffraction properties were taken into account in previous studies analyzing phase- and group-velocity changes. Also, while the intensity distribution in the aberration-distorted focusing of monochromatic or pulsed beams has been widely investigated [75, 76, 147–149, 159–162, O5], the phase properties were examined directly only in a few cases [194, 195]. As an attempt to fill in this gap, some theoretical considerations on the phase and the group velocity are discussed in the following, which can arise during aberration-free and aberration-distorted focusing of Gaussian beams. To fulfill this, those recipes are used, which were given in Section 2.3.5 for the calculation of the phase velocity v_p and the group velocity v_g. According to (2.69) and (2.70), the necessary quantity, to calculate the velocities in question, is the spatially dependent phase. For a focused Gaussian beam, the expression (2.51) (along with (2.52)) can be used, the phase of which is

$$\varphi_G(r, Z_0, \psi, \omega) = -\frac{\pi}{2} + \frac{\omega}{c}(Z_0 + R_0 - R) + \frac{\omega}{c}\frac{r^2}{2(Z_0 + R_0)} + \arg\left[\tilde{\mathcal{I}}(u, v, \psi)\right] . \tag{3.1}$$

For the sake of simplicity, only on-axis points are considered in the following, that is when $r = 0$, and as a consequence $v = 0$ (see definition (2.54) of v).

3.1.1 On-axis phase and group velocity in aberration-free focusing

In most experimental cases, the aperture of the optics used is chosen so large that it does no cut from the beam. Also, the aberrations of the beam is usually avoided. So the untruncated-beam limit ($\kappa \to \infty$, or less strictly $\kappa \gg 1$ [78]) with zero aberration is the most important to consider, and for which analytical expressions can be obtained. In the case of an undistroted, untruncated Gaussian beam the on-axis phase (3.1) can be written

in the simpler, more explicit form of [78]

$$\varphi_G(r=0,Z_0,\omega) = -\frac{\pi}{2} + \frac{\omega}{c}(Z_0 + R_0 - R) - \operatorname{atan}[\omega\mathcal{T}(Z_0,\omega)] \ . \tag{3.2}$$

The ψ dependence of φ_G has been omitted in the previous expression, because the considered situation has cylindrical symmetry without aberrations. The newly introduced variable is

$$\mathcal{T}(Z_0,\omega) = \frac{w^2}{2cR}\frac{Z_0 + R_0 - R}{Z_0 + R_0} \ . \tag{3.3}$$

As a reminder, $w = w(\omega)$ is the radius of the Gaussian beam in the exit pupil of the focusing element (see (2.49)). The radius of curvature $R = R(\omega)$ of the phase fronts can also be frequency dependent (not highlighted explicitly), for example, due to chromatic aberration. Subscript 0 means evaluation at ω_0. Using (2.69) on (3.2) (here equivalent with calculating the gradient of (3.1) on axis) yields the on-axis phase velocity (see details in Appendix C.1)

$$\frac{v_p(Z_0,\omega)}{c} = \frac{1+\omega^2\mathcal{T}^2}{1+\omega^2\mathcal{T}^2 - (\partial_z\mathcal{T})c} \ , \tag{3.4}$$

where $\partial_z\mathcal{T}$ is the short form for the partial derivative of $\mathcal{T}$ with respect to its spatial argument, or explicitly

$$\partial_z\mathcal{T} = \frac{\partial\mathcal{T}(Z_0,\omega)}{\partial Z_0} = \frac{w^2}{2c}\frac{1}{(Z_0+R_0)^2} \ . \tag{3.5}$$

Note here that dimensionless parameters could be introduced in (3.4), but the advantages of such step are lost due to the nonlinear relationship between $\mathcal{T}$ and Z_0 (see (3.3)). However, in the Debye approximation, where $\mathcal{T}$ is a linear function of Z_0, the expression of v_p can be given in a dimensionless form. The expression obtained this way can be applied to the particular situation by simple scaling (see Appendix C.1).

There are two important mathematical properties of the derivative $\partial_z\mathcal{T}$, easy to see from its form (3.5). First, $\partial_z\mathcal{T} \geq 0$ for $\forall Z_0 \in (-\infty;\infty)$, since every factor in (3.5) is positive. The other is that it tends to zero for the two "ends" of the Z_0 axis ($\lim_{Z_0\to\pm\infty}\partial_z\mathcal{T} = 0$). Looking at (3.4), it implies on the phase velocity that v_p is never less than the speed of light, so the phase velocity is always superluminal on axis, if an ideal Gaussian beams is focused. The second property gives that the phase velocity tends to c far from the focus. Both features can be seen in Figure 3.1(a)-(b). This is, of course, not surprising, as the phase velocity is determined by the Gouy phase term ($-\operatorname{atan}[\omega\mathcal{T}]$) in (3.2). It must not be forgotten that the diffraction integral gives realistic information only in the vicinity of the focus. This is why the mathematical problem that could arise from $\lim_{Z_0\to -R}\partial_z\mathcal{T} = \infty$ does not contradict the physics behind.

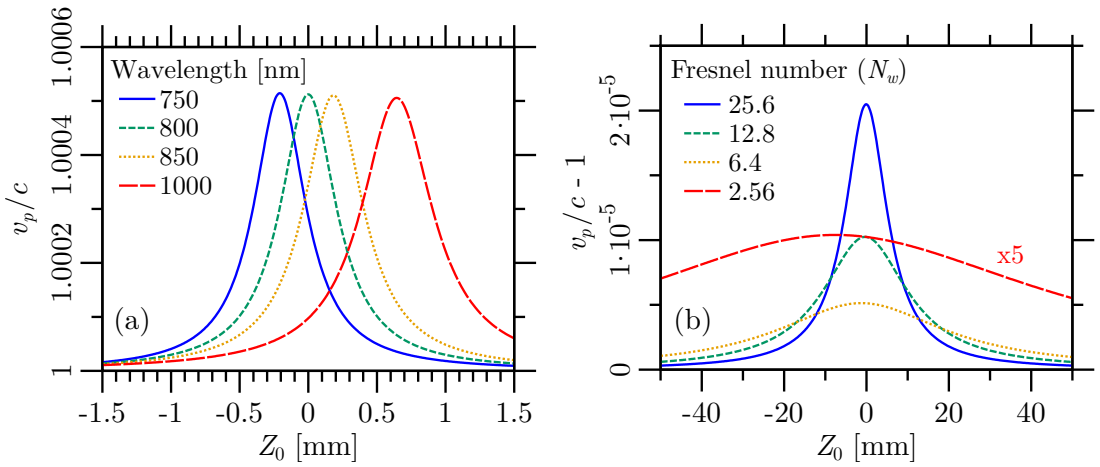

Figure 3.1. The changes of phase velocity v_p on axis. (a) On-axis v_p variations for different wavelengths. In the simulation the beam size w at the exit pupil was assumed to be wavelength independent. The wave front curvature R was changed for each wavelength according to the focal length variation of lens made of an N-BK7 (Schott) material ($R(\omega) = f(\omega) = (n_0 - 1)f_0/(n(\omega) - 1)$ [135], $f_0 = 100\,\text{mm}$, subscript zero again meaning values at central wavelength $\lambda_0 = 800\,\text{nm}$). Due to both the wavelength and the focal length variation, the plot of each wavelength corresponds to different Fresnel numbers. ($\lambda = 750, 800, 850$ and $1000\,\text{nm}$ correspond to $f = 99.79, 100, 100.17$ and $100.65\,\text{mm}$; so $N_w = 136.8, 128, 120.2$ and 101.7, respectively.) The Debye approximation is valid for all wavelengths in this situation. (b) The variation of on-axis v_p with Fresnel number N_w. The calculation is for $f_0 = 500\,\text{mm}$ focal length at $\lambda_0 = 800\,\text{nm}$. The Fresnel numbers $N_w = 25.6, 12.8, 6.4$ and 2.56 mean beam radii $w = 3.2, 2.26, 1.6$ and $1.01\,\text{mm}$, respectively. The curve for $N_w = 2.56$ has been scaled for better visibility.

Another feature expected from the shape of the Gouy phase shift is the single maximum of the phase velocity on axis. It can be simply shown that the function $v_p(Z_0, \omega)$ of (3.4) reaches its maximum in the point (see Appendix C.1 for details)

$$Z_{0,\max(v_p)} = R - R_0 - \frac{R}{1 + \pi^2 N_w^2}\,, \tag{3.6}$$

where $N_w = w^2/(\lambda R)$ is the Fresnel number of the Gaussian beam emerging from the exit pupil of the focusing element (see Section 2.3.3). This means that the phase velocity of a Gaussian beam, with a given wavelength, reaches its maximum in the diffraction focus. When $N_w \gg 1$, then $Z_{0,\max(v_p)} = R - R_0$, so the diffraction focus coincides with the geometrical focus [150] (see Figure 3.1(a)-(b)).

The curves of Figure 3.1(a) show the differences of on-axis phase velocity variations for different wavelengths. The situation depicted can be imagined as focusing a broadband Gaussian beam, which has a wavelength-independent beam size (it is shown later that this might not be the case in experimental situations), and the curvatures of wave fronts after the lens are purely defined by the lens used for focusing. This graph shows the conclusion

of (3.6), that the maximum of v_p is shifted to the corresponding focal point for each frequency. The $\lambda = 1000\,\mathrm{nm}$ case is depicted to better visualize that the Fresnel number N_w also varies by frequency (due to the dependence on both the wavelength and the focal length), which makes the variation curve different in shape as well, not just shifted (see the broadened and less high peak of $\lambda = 1000\,\mathrm{nm}$). In Figure 3.1(b), the effect of the diffraction-focus shift is plotted. It is visible that the focal shift has an appreciable effect only in very extreme cases (the numerical aperture in the last example of Figure 3.1(b) is $w/f \approx 1/500$).

As it has been mentioned several times, the phase velocity changes during propagation is interesting for nonlinear optical studies. For example, when radiation with shorter wavelength is generated using lasers, through nonlinear phenomena, it would be advantageous to slow down the phase of the fundamental field to match the phase velocity of the generated radiation (in the case of normal dispersion the index of refraction is higher for higher frequency, giving lower propagation speed). It is visible from the results above that on axis, where the intensity of the beam is highest, it is not possible. For slower light, one has to study the transverse variation of the Gouy phase [196], which has been shown to yield subluminal ($v_p < c$) light propagation off axis [168]. Spatial points not lying on the optical axis are not topic of this work, however, this question is considered later due to the special property of an optical aberration.

The phase velocity of different-wavelength components are also interesting, because they determine the velocity of the wave packet as a whole. The on-axis velocity of the wave packet, the group velocity, can also be obtained analytically for the undistorted, untruncated Gaussian beam. Applying definition (2.70) on (3.1) along the optical axis gives

$$\frac{v_g(Z_0)}{c} = \frac{(1+\omega_0^2\mathcal{T}_0^2)^2}{(1+\omega_0^2\mathcal{T}_0^2)^2 - g_v c(\partial_z\mathcal{T}_0)(1-\omega_0^2\mathcal{T}_0^2) + \gamma_v\omega_0^2\mathcal{T}_0(\partial_z\mathcal{T}_0)w_0^2/R_0}\,, \tag{3.7}$$

which is the expression for a wave packet having carrier frequency ω_0. The two new dimensionless variables are

$$g_v = 1 + 2\frac{w_0'}{w_0}\omega_0\,, \tag{3.8}$$

expressing the wavelength dependence of the beam size at the exit pupil, and

$$\gamma_v = -\frac{R_0'}{R_0}\omega_0\,, \tag{3.9}$$

quantifying the frequency dependence of the wave front curvature emerging from the aperture. Just like before, the prime sign denotes derivative with respect to angular frequency ($w_0' = \mathrm{d}w/\mathrm{d}\omega|_{\omega=\omega_0}$ and $R_0' = \mathrm{d}R/\mathrm{d}\omega|_{\omega=\omega_0}$). Details of the calculation can be found in Appendix C.2.

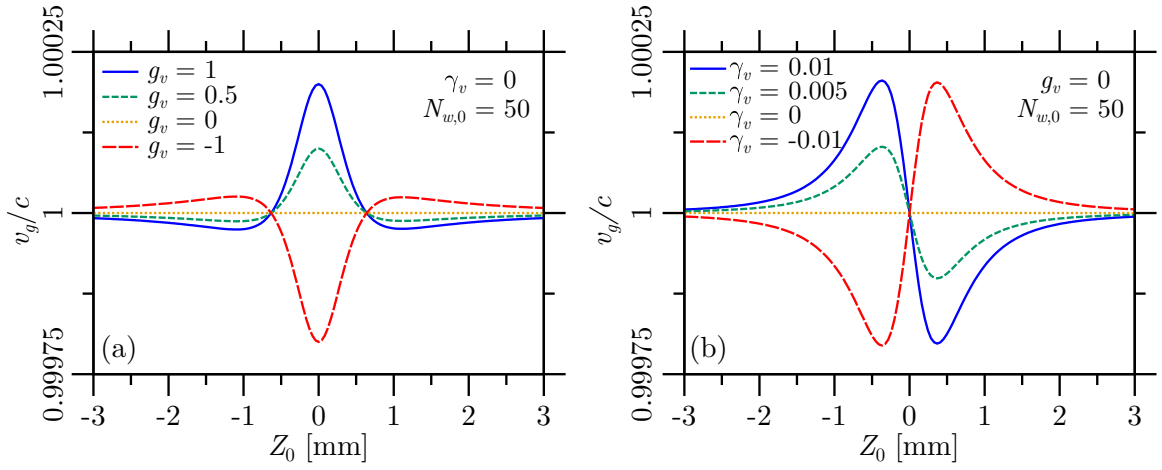

Figure 3.2. The on-axis group-velocity variation of a pulsed Gaussian beam with exit-pupil beam radius $w_0 = 2\,\text{mm}$ and wave-front curvature $R_0 = 100\,\text{mm}$ at central wavelength $\lambda_0 = 800\,\text{nm}$. (a) The dependence of v_g variation on the parameter g_v describing the wavelength dependence of the beam size. (b) The dependence of v_g variation on the parameter γ_v describing the wavelength dependence of wave-front curvature at the exit pupil.

Some special cases of (3.7) had been formulated before [78, 169]. While the notation is different in the works referred, it is easy to see that Equation (29) of [78] is the same as (3.7) with $g_v = 1$ and $\gamma_v = 0$. Equation (35) of [169] is more general than the previous one, and contains the possible variation of beams size with wavelength, but the wave-front is assumed to be frequency independent, so substituting $\gamma_v = 0$ into (3.7) gives the same result. The (3.7) formula of this work can be considered as a generalized expression of the cases published before.

It can be seen from (3.7), and in Figure 3.2(a)-(b), that the variation of the group velocity on axis is determined by the values of g_v and γ_v, so it is given by how the beam size and wave-front curvature of the wave changes with wavelength at the exit pupil of the focusing system. An important thing to note is that the group velocity is only constant in a specific condition ($g_v = 0$ and $\gamma_v = 0$). The conditions for this is given later.

For a simple explanation of the group-velocity variations in Figure 3.2, the diffraction properties of Gaussian beams have to be considered. If $g_v \neq 0$ (and $\gamma_v = 0$, see Figure 3.2(a)), it is true for beam size in the exit pupil that $w_0' \neq -w_0/(2\omega_0)$. It can be shown numerically that the condition $w_0' = -w_0/(2\omega_0)$ basically results in a focused Gaussian beam that has a wavelength independent Rayleigh length[I]. So when $g_v \neq 0$, the different Rayleigh lengths of the focused monochromatic components mean different amounts of phase shift in a given distance due to Gouy's phase. These phase shift differences induce

[I] It can also be shown analytically using the expressions in Appendix B.1 for the focused beam in Debye approximation, utilizing that the distance of the focused beam waist is the same for all frequencies ($Z = -R_0$ due to $\gamma_v = 0$) and that the focused Rayleigh length is less then the "focal length" ($L_D \ll R_0$).

a group velocity variation that is most pronounced in the vicinity of the focus, since Gouy phase shift has the largest changes there. As the variation of the phase velocities of components are changed in a symmetric fashion with respect to focus (see Figure 3.1(b) as a reference), the resulted v_g variation is also symmetric to the focal point. Of course some asymmetries would appear if very loose focusing is considered, and the diffraction focus is shifted.

When $\gamma_v \neq 0$ (and $g_v = 0$, see Figure 3.2(b)) the situation is different. The monochromatic components are focused at different points on axis (see Figure 3.1(a)), which gives phase changes that are not symmetric with respect to the distance from the focal point. So the group-velocity variation is and odd function of Z_0 in Figure 3.2(b). There are other influencing properties in this case as well, since, due to R, the Fresnel number N_w also varies with wavelength. This causes similar changes to the $g_v \neq 0$ case, but they are obscured by the much larger effect of $\gamma_v \neq 0$.

An important solution to find is the expressions of g_v and γ_v parameters, appearing in (3.7), for specific experimental situations. In the previous works referred, only cases were considered when the pulsed Gaussian beam was focused at its waist, and the plane of the waist was the same for all wavelengths [78, 169]. In this simple situation, g_v simply refers to the wavelength variation of source beam's waist size. Similarly, the value of γ_v is defined by the longitudinal chromatic aberration of the focusing element. However, in general, laser beams are not focused at their waist, and the exact position of the waist can differ for different frequencies. In the following, the formulas of g_v and γ_v are given, which are applicable in general situations.

Consider a Gaussian beam with beam waist radius $s = s(\omega)$ and Rayleigh length $L = L(\omega) = \omega s^2/(2c)$, following the nomenclature given in Section 2.3.2. Allow the possibility that the distance $d = d(\omega)$ between the beam waist and the focal element is also wavelength dependent (see Figure 3.3). With the assumption that the beam size is the same just before the focusing element and directly behind it[II], the simple formalism of Section 2.3.2 can be used to obtain an expression on g_v changes with input beam properties

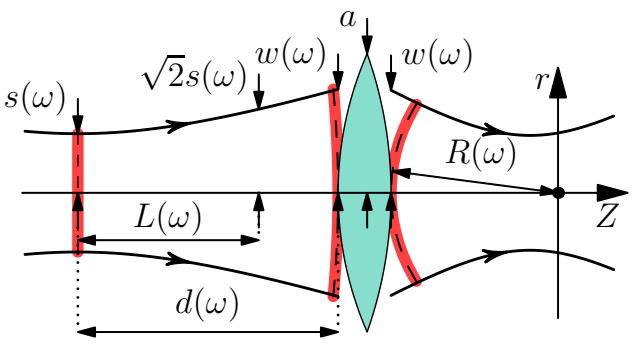

Figure 3.3. The description of Gaussian beam properties before and behind the focusing element. The focusing element is depicted as a lens, but can be a focusing optics of any kind in paraxial approximation.

[II] This presumption is general for thins lenses, and is naturally valid for focusing mirrors. Care must be taken when thick lenses are used for a very strong focusing situation.

(see details in Appendix C.3). The resulted formula is

$$g_v = g_s + (\varepsilon_s - g_s)\frac{2\xi_s^2}{1+\xi_s^2}\,, \tag{3.10}$$

where the newly introduced dimensionless parameters are

$$g_s = 1 + 2\frac{s_0'}{s_0}\omega_0 = \frac{L_0'}{L_0}\omega_0\,, \tag{3.11}$$

$$\varepsilon_s = \frac{d_0'}{d_0}\omega_0 \tag{3.12}$$

and

$$\xi_s = \frac{d_0}{L_0}\,. \tag{3.13}$$

The g_s parameter describes the wavelength dependence of the beam waist size for the source beam, or the same feature of the Rayleigh range, if expressed differently (see (3.11)). As an example, $g_s = +1, 0$ and -1 correspond to a Gaussian beam of frequency-independent waist size, Rayleigh range (isodiffracting beam) and divergence (isodiverging beam), respectively [139]. This is why such values of g_v are depicted in Figure 3.2(a). The isodiffracting beam, for example, is the stable mode of laser oscillators [197]. The ε_s parameter gives how the position of the beam waist changes with wavelength, while ξ_s is a dimensionless measure of the waist-lens distance.

The behavior of g_v, described by (3.10), can be seen in Figure 3.4(a). The most important is that if the focusing element is at the beam waist ($d_0 = 0$), then $g_v = g_s$, only the g_s parameter of the input beam is what matters. Using $\lim_{x\to\infty} x^2/(1+x^2) = 1$, it is visible that $\lim_{\xi_s\to\infty} g_v = 2\varepsilon_s - g_s$, so g_v has an asymptotic limit when the focal element is put far from the waist ($d_0 \gg L_0$). Practically, the region within a Rayleigh length is most important, because, in usual experimental setups, the focusing is performed in this range. As it can be seen in Figure 3.4(a), there is a strong dependence on the exact position of the lens in the vicinity of $\xi_s = 1$. The difference between the g_v parameters for a Gaussian beam focused at its waist and at one Rayleigh length ($\xi_s = 0$ and $\xi_s = 1$) is $g_v = g_s$ against $g_v = \varepsilon_s$. Only an isodiffracting, pulsed Gaussian beam ($g_s = 0$), that has the waists of all components at the same plane ($\varepsilon_s = 0$), has a g_v parameter that is independent of the distance between the focal element and beam waist. This is the case for an idealistic laser oscillator [197]. If $\varepsilon_s = 0$, all monochromatic components have the same beam size at the Rayleigh range ($g_v = 0$ at $\xi_s = 1$), irrespective of the value of g_s.

The γ_v parameter can also be expressed using source-beam properties and focal-element characteristics (see details in Appendix C.3). Again, using the expressions of Section 2.3.2 for Gaussian beams and the formulas of focusing/imaging in paraxial optics,

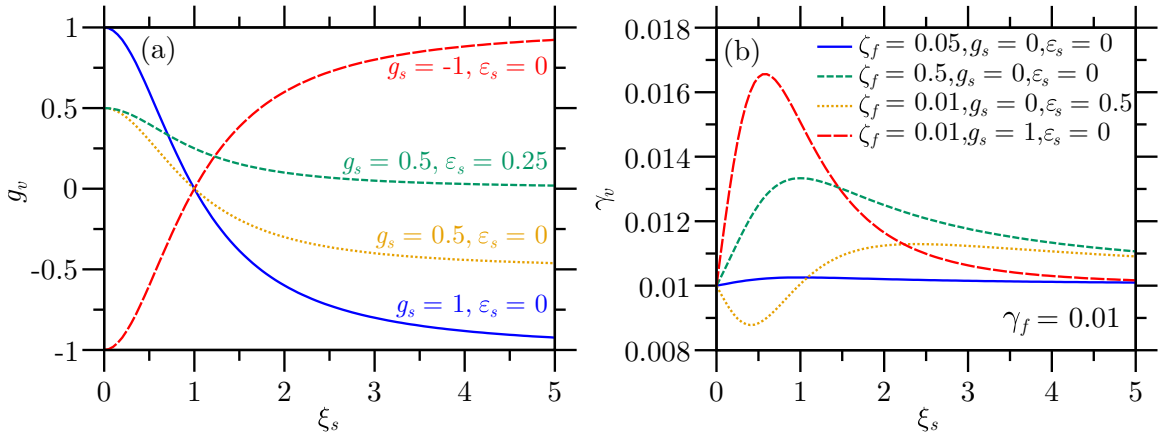

Figure 3.4. (a) A few examples of the variation of parameter g_v of the focused beam with properties g_s, ε_s and ξ_s of the input beam. (b) A few examples of the variation of parameter γ_v of the focused beam with properties g_s, ε_s and ξ_s of the input beam and characteristics γ_f and ζ_f of the focusing element.

one can get

$$\gamma_v = \gamma_f \frac{\xi_s + 1/\xi_s}{\xi_s + 1/\xi_s - \zeta_f} + \frac{\zeta_f}{1+\xi_s^2} \frac{(\xi_s^2 - 1)\varepsilon_s + 2g_s}{\xi_s + 1/\xi_s - \zeta_f} \,. \tag{3.14}$$

From the expression above, it is clearly visible that γ_v depends on other parameters in a more complex way than g_v, especially as additionally the focal element plays a role through

$$\gamma_f = -\frac{f_0'}{f_0}\omega_0 \tag{3.15}$$

and

$$\zeta_f = \frac{f_0}{L_0} \,. \tag{3.16}$$

Parameter γ_f quantitatively describes the chromatic aberration of the focusing element, while ζ_f is a dimensionless form for the focal length $f_0 = f(\omega_0)$ at the carrier frequency. A few examples for γ_v values can be seen in Figure 3.4(b).

When the focusing element is placed at the waist of the beam ($\xi_s = 0$), the wavefront curvature-change with wavelength is determined by the chromatic aberration of the focal element ($\gamma_v = \gamma_f$). This can be seen in Figure 3.4(b), where γ_f is set to 0.01 for all curves. The value was set so because this lies in the order of magnitude of γ_f values for standard bi-convex lenses. For the N-BK7 lens of Figure 3.1(a), for example, $\gamma_f = 0.031$. For achromatic lenses the value is an order of magnitude smaller. In general, all singlet and most achromatic lenses have $\gamma_f > 0$, since they focus blue components closer to the focal element, introducing a group velocity increase before the focus (see Figure 3.2(b)). These facts are the reason for the γ_v values of Figure 3.2(b). From Figure 3.4(b), it can be deduced that other parameters do not change usually the order

of magnitude of γ_v from the value of γ_g. This is because in the most common situations $f_0 \ll L_0$ ($\zeta_f \ll 1$), and also since the second term of (3.14) is usually less or comparable to the first term in magnitude. It also means that, if the focusing element has no chromatic aberration ($\gamma_f = 0$), the other effects described by the second term of (3.14) can still yield a similar effect to the chromatic aberration of a lens, analogous both in characteristics and amplitude. It is hard to deduce other direct implications from (3.14).

There are two important consequences of the findings in this section that should be highlighted. First, the on-axis group velocity of a pulsed Gaussian beam in the focus is only constant if an isodiffracting beam having wavelength-independent beam-waist position is focused with a focusing element that has no chromatic aberration. Second, a chromatic aberration-like effect can appear even in those cases when the focusing element has no chromatic aberration.

3.1.2 Phase and group velocity in aberration-distorted focusing

While the idealistic cases of the previous subsection are generally applicable, usually the situation is more complex, and the pulsed beam can not be considered as a pure Gaussian beam with spherical phase fronts. When the pulsed Gaussian beam is distorted by aberrations or truncation, analytic evaluation of the phase or the group velocity is not possible. There are a few cases when analytical expressions for the distorted field in the focus can be obtained. One example is the limit of very strong truncation of the beam ($\kappa \to 0$), but in this case the meaning of group velocity evaluated on axis with (2.70) is physically doubtful [78]. An other case is when the focusing suffers from spherical aberration, but due to the appearance of special functions in the expression of the focused field [T3, 195], the evaluation of phase and group velocity needs numerical means.

The necessity of numerical evaluation is raised by the last term $\arg\left[\tilde{\mathcal{I}}(u,v,\psi)\right]$ in (3.1). By taking a look at the formulas (2.69) and (2.70), giving the phase and group velocity, it is easy to see that, to get these physical quantities, the following steps are necessary. First, to obtain $\varphi_{\mathcal{I}}(u,v,\psi) = \arg\left[\tilde{\mathcal{I}}(u,v,\psi)\right]$, a complex integral of the form (2.52) has to be calculated. Then, it is required to evaluate the complex phase of these integrals. Finally, the derivative of this phase is needed with respect to three variables to calculate the gradient appearing in the formulas of v_p and v_g. In the case of the group velocity, an other derivative with respect to frequency is also present. This way of solving this problem is a direct source of numerical errors. Calculating the derivative of an integral is especially a procedure that needs special attention, with the additional intermediary step of evaluating a complex phase.

To avoid these numerical glitches, the following steps are taken. Firstly, it is assumed that the order of calculating the integral and taking the derivative can be interchanged.

This, of course, has specific mathematical conditions that are needed to be fulfilled, but they are not examined here. The functions appearing in this work are well-behaving expressions, and the applicability of this step was checked by numerical means for simple cases. This way the integrand can be differentiated analytically, so numerical calculation of the derivative can be fully avoided. A second simplification is the calculation of the phase and its derivatives using analytical expressions instead of the numerical atan2(z) function [91] (see Appendix D.1 for formulas). As a result, the evaluation of the phase and group velocity in distorted focusing can be simplified to calculating integrals and applying simple mathematical operations between them, without any additional steps which increase the chance of numerical errors. For explicit expression see Appendix D.2.

In the results presented, several simplifying physical conditions are assumed. First of all, only primary aberrations are considered, which have an aberration function of the form (see Section 2.3.3)

$$\Phi_{lnm}(\rho,\theta) = \mu_0\lambda_0\rho^n\cos^m(\theta)\,. \tag{3.17}$$

This here means that all presented plots of phase and group velocity refer to the case of central wavelength $\lambda_0 = 800\,\mathrm{nm}$. It is to be noted here again that the value of μ_0 generally depends on the object and image points (P_0 and P_1 of Figure 2.10, respectively). However, it can be omitted, since the object is fixed [90]. It is the shape of the wave front that is relevant in the wave optical description, which is given by the reference sphere and the aberration function Φ together. When someone changes the reference point in imaging applications (the origin, $Y_1^\star$, see Figure 2.10), the reference sphere and the aberration function have to be recalculated, for example, by ray tracing (see Section 2.3.1). Also, the amount of the aberration is wavelength dependent usually ($\mu = \mu(\lambda)$) [198–200]. This group-velocity changing property, however, is not taken into account in the examples presented, but the fully detailed calculation given in Appendix D.2.3 gives a way of treatment for this case as well. The wave-front distorting effect of beam truncation and primary aberrations are also examined separately, to see the effect of each feature independently.

For simpler graphical representation, and as for most applications this spatial region is the most important, results and expressions only for on-axis points are presented here. The on-axis phase velocity of the carrier wave in the presence of primary aberrations and beam truncation is given by

$$\frac{v_p(Z_0)}{c} = \left|\frac{c\nabla\varphi_G\big|_{\substack{r=0\\ \omega=\omega_0}}}{\omega_0}\right|^{-1},$$

$$\frac{c\nabla\varphi_G\big|_{\substack{r=0\\ \omega=\omega_0}}}{\omega_0} = \left[1+\left(\frac{a}{Z_0+R_0}\right)^2 \frac{\partial\varphi_{\mathcal{I}}}{\partial u}\bigg|_{\substack{v=0\\ \psi=0\\ \omega=\omega_0}}\right]\mathbf{u}_z + \left[\frac{a}{Z_0+R_0}\,\frac{\partial\varphi_{\mathcal{I}}}{\partial v}\bigg|_{\substack{v=0\\ \psi=0\\ \omega=\omega_0}}\right]\mathbf{u}_r\,, \tag{3.18}$$

while the on-axis group velocity can be obtained by

$$\frac{v_g(Z_0)}{c} = \left|c\nabla\left(\frac{\partial\varphi_G}{\partial\omega}\bigg|_{\substack{r=0\\ \omega=\omega_0}}\right)\right|^{-1},$$

$$c\nabla\left(\frac{\partial\varphi_G}{\partial\omega}\bigg|_{\substack{r=0\\ \omega=\omega_0}}\right) = \left[1+\omega_0\left(\frac{a}{Z_0+R_0}\right)^2 \frac{\partial^2\varphi_{\mathcal{I}}}{\partial u\partial\omega}\bigg|_{\substack{v=0\\ \psi=0\\ \omega=\omega_0}}\right]\mathbf{u}_z + \left[\omega_0\frac{a}{Z_0+R_0}\,\frac{\partial^2\varphi_{\mathcal{I}}}{\partial v\partial\omega}\bigg|_{\substack{v=0\\ \psi=0\\ \omega=\omega_0}}\right]\mathbf{u}_r\,, \tag{3.19}$$

where $\mathbf{u}_z, \mathbf{u}_r$ (and $\mathbf{u}_\psi$) are the cylindrical unit vectors. Thanks to the symmetry properties of primary aberrations (they only contain dependence on θ through $\cos(\theta)$), the $\mathbf{u}_\psi$ component needs no evaluation to obtain the gradient in the expressions of the on-axis phase and group velocity. This is because the optical axis is a line of singularity in the cylindrical coordinate system considering coordinate ψ. This means that if $r = 0$, then, for all ψ coordinates, the $\mathbf{u}_r$ and $\mathbf{u}_\psi$ components add up to the same vector, which is equivalent to the $\mathbf{u}_r$ component at $\psi = 0$ (see details in Appendix D.2). Additionally, if an aberration with even value of index m is considered, the component $\mathbf{u}_r$ is also zero, so only the component $\mathbf{u}_z$ (the one along Z_0) needs evaluation in (3.18) and (3.19).

As mentioned previously, to avoid numerical errors, the derivatives of the phase $\varphi_{\mathcal{I}} = \arg\left[\tilde{\mathcal{I}}(u,v,\psi)\right]$, in expressions (3.18) and (3.19), are evaluated without calculating the phase itself according to (see detailed derivation in Appendix D.1)

$$\frac{\partial\varphi_{\mathcal{I}}}{\partial x} = \frac{\mathrm{Re}\left[\iota\tilde{\mathcal{I}}(\partial_x\tilde{\mathcal{I}})^*\right]}{|\tilde{\mathcal{I}}|^2} \tag{3.20}$$

and

$$\frac{\partial^2\varphi_{\mathcal{I}}}{\partial x\partial y} = \frac{|\tilde{\mathcal{I}}|^2\mathrm{Re}\left[\iota\tilde{\mathcal{I}}(\partial^2_{xy}\tilde{\mathcal{I}})^* + \iota(\partial_x\tilde{\mathcal{I}})(\partial_y\tilde{\mathcal{I}})^*\right]}{|\tilde{\mathcal{I}}|^4} - \frac{2\mathrm{Re}\left[\iota\tilde{\mathcal{I}}(\partial_y\tilde{\mathcal{I}})^*\right]\mathrm{Im}\left[\iota\tilde{\mathcal{I}}(\partial_x\tilde{\mathcal{I}})^*\right]}{|\tilde{\mathcal{I}}|^4}\,, \tag{3.21}$$

where x and y should be replaced with the corresponding variable u, v or ω, and superscript $*$ means complex conjugation. The necessary derivatives of the integral $\tilde{\mathcal{I}}(u,v,\psi)$ for the on-axis expressions are as follows:

$$\frac{\partial\tilde{\mathcal{I}}}{\partial u}\bigg|_{\substack{v=0\\ \psi=0\\ \omega=\omega_0}} = -\frac{\iota}{2}\int_0^1\int_0^{2\pi}\tilde{\Upsilon}_{a,0}(\rho,\theta)\rho^3\,\mathrm{d}\theta\,\mathrm{d}\rho\,, \tag{3.22}$$

$$\left.\frac{\partial\tilde{\mathcal{I}}}{\partial v}\right|_{\substack{v=0\\ \psi=0\\ \omega=\omega_0}} = -\iota\int_0^1\int_0^{2\pi}\cos(\theta)\tilde{\Upsilon}_{a,0}(\rho,\theta)\rho^2\,\mathrm{d}\theta\,\mathrm{d}\rho\,, \tag{3.23}$$

$$\left.\frac{\partial\tilde{\mathcal{I}}}{\partial \omega}\right|_{\substack{v=0\\ \psi=0\\ \omega=\omega_0}} = \frac{1}{\omega_0}\int_0^1\int_0^{2\pi}\tilde{\Upsilon}_{a,0}(\rho,\theta)\tilde{\Lambda}_a(\rho,\theta)\rho\,\mathrm{d}\theta\,\mathrm{d}\rho\,, \tag{3.24}$$

$$\left.\frac{\partial^2\tilde{\mathcal{I}}}{\partial u\partial \omega}\right|_{\substack{v=0\\ \psi=0\\ \omega=\omega_0}} = -\frac{\iota}{2\omega_0}\int_0^1\int_0^{2\pi}\tilde{\Upsilon}_{a,0}(\rho,\theta)\left[1+\tilde{\Lambda}_{a,0}(\rho,\theta)\right]\rho^3\,\mathrm{d}\theta\,\mathrm{d}\rho\,, \tag{3.25}$$

and

$$\left.\frac{\partial^2\tilde{\mathcal{I}}}{\partial v\partial \omega}\right|_{\substack{v=0\\ \psi=0\\ \omega=\omega_0}} = -\frac{\iota}{\omega_0}\int_0^1\int_0^{2\pi}\cos(\theta)\tilde{\Upsilon}_{a,0}(\rho,\theta)\left[1+\tilde{\Lambda}_a(\rho,\theta)\right]\rho^2\,\mathrm{d}\theta\,\mathrm{d}\rho\,. \tag{3.26}$$

In the previous integrals the following functions were introduced for brevity:

$$\tilde{\Upsilon}_{a,0}(\rho,\theta) = \exp\left(-\kappa_0\rho^2+\iota k_0\Phi(\rho,\theta)-\iota\frac{u_0}{2}\rho^2\right)\,, \tag{3.27}$$

$$\tilde{\Lambda}_a(\rho,\theta) = -\rho^2(1-g_v)\kappa_0+\iota k_0\Phi(\rho,\theta)-\frac{\iota\rho^2}{2}\left(u_0+\gamma_v\frac{\omega_0 a^2}{cR_0}\right)\,, \tag{3.28}$$

where in the (3.28) form of $\tilde{\Lambda}_a(\rho,\theta)$ the possible wavelength dependence of the aberration is neglected. The subscript a of $\tilde{\Lambda}_a(\rho,\theta)$ and $\tilde{\Upsilon}_{a,0}(\rho,\theta)$ means that these function are only for on-axis evaluation, and like before, subscript 0 of every function (or variable) means its evaluation at carrier frequency ω_0. The formulas that are valid also in off-axis point of the neighborhood of focus are given in Appendix D. As a summary of the expressions above, after evaluating the integrals in (3.22), (3.23), (3.24), (3.25) and (3.26); they can be substituted into (3.20) and (3.21) to acquire on-axis phase and group velocities using (3.18) and (3.19). The phase and group velocity data presented in the plots of the following few paragraphs were generated using the steps given above.

A detailed derivation and description of formulas for the calculation of phase and group velocity of focused Gaussian beams in the presence of aberrations can be found in Appendix D.2. The expressions presented there can used to obtain the properties of v_p and v_g in any point in space near the focus. There is no restriction on the shape of the aberration function, and it can even be wavelength dependent.

If cases with large Fresnel numbers are considered, the Debye approximation might be used. In the case of phase velocity evaluation with (3.18), Debye approximation simply means the replacement of factor $a/(Z_0+R_0)$ with a/R_0. This can also be done for the group velocity in (3.19), if $\gamma_v = 0$. Care should be taken, however, since, in the presence of aberrations, some other conditions may become important for the validity of the Debye approximation, and they can give more constraints on when this simplification can be used, compared to the undistorted case [152, 153]. Some signatures of these

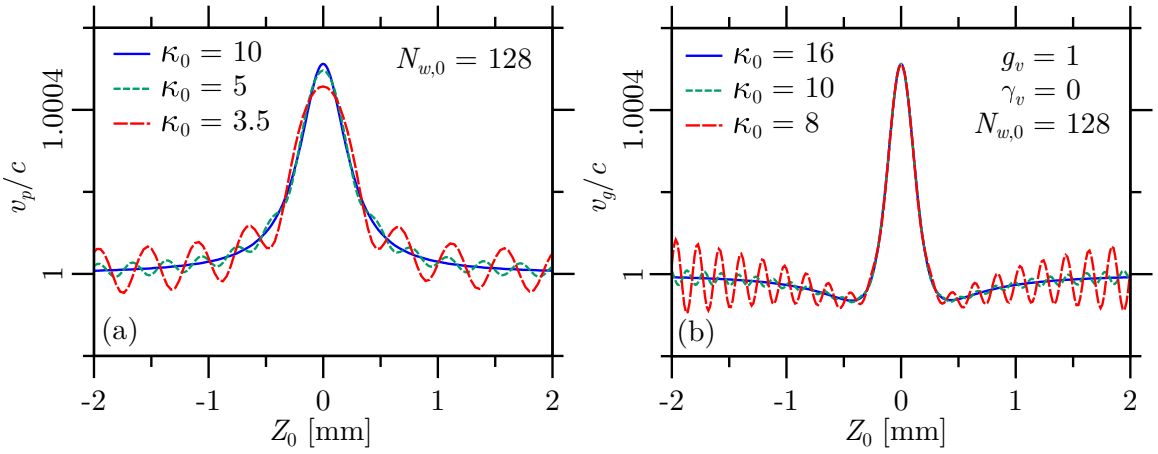

Figure 3.5. The on-axis change of phase and group velocity of a focused, truncated Gaussian beam. The central wavelength is $\lambda_0 = 800\,\text{nm}$, the Gaussian beam radius just before the exit pupil is $w = 3.2\,\text{mm}$ and the radius of curvature of the Gaussian reference sphere leaving the exit aperture is $R_0 = 100\,\text{mm}$. This would result in a Rayleigh length of approximately $250\,\mu\text{m}$ without truncation. (a) The effect of different amounts of truncation on the phase velocity. (a) The effect of different amounts of truncation on the group velocity.

more strict conditions are presented in later plots. Further considerations on using Debye approximation with the expressions presented can be found in Appendix D.3.

Beam truncation The effect of truncation has been investigated for several types of beams, but these studies were mainly concentrated on the focal shift [146, 201], the beam quality [202, 203] or the intensity distribution of truncated beams [143, 204]. The phase and group velocities, however, are also affected by the phase changes induced by the truncation of the pulsed Gaussian beam. Figure 3.5 shows the effect of truncation on the on-axis phase and group velocity for different amounts of truncation. It can be seen in both plots that the clipping of the beam primarily induces an oscillation of the velocities around the focal region. In Figure 3.5 the beam size is chosen to be large, so the focal shift due to the small Fresnel number is negligible. The variation of the beam spot size at the focusing element with wavelength is characterized by $g_v = 1$, to better visualize the extent of this effect compared to the group-velocity variation caused by diffraction.

An important property that can be seen in the curves of Figure 3.5 is the effect of truncation on phase velocity, which becomes comparable to the effect of beams size variation – with the chosen parameters – for as weak truncation as $\kappa \lesssim 10$. In the case of group velocity, these distortions already appear for $\kappa \lesssim 15$. For smaller values of g_v, the requirement for comparable effect with diffraction would even be more strict. This shows that while the intensity distribution was found to be negligibly affected by truncation for $\kappa \gtrsim 4$ [143], the underlying phase changes are much more pronounced. On

the other hand, it is noted that the focused Rayleigh range of the beam plotted in Figure 3.5 is approximately 250 µm, and in this region the group velocity is almost unchanged, even for strongly truncated beams (see Figure 3.5(b)). However, the phase velocity is more profoundly altered, even within the focal depth (see Figure 3.5(a)). In the next few paragraphs, which examine primary aberrations, the truncation of the beam is avoided, to study the effects of wave-front distortions alone.

Spherical aberration Primary spherical aberration is a very common form of aberration present in many cases, as often spherical lenses or spherical mirrors are used for focusing. This distortion of the wave front is intrinsic to the shape of the focusing element, so not related to a misalignment or error. The aberration function in this case is indexed by $l = 0$, $n = 4$ and $m = 0$ (see Section 2.3.3 or [90, O5]), which means that the aberration function of primary spherical aberration is

$$\Phi_{040}(\rho, \theta) = \mu_0 \lambda_0 \rho^4 \,. \tag{3.29}$$

As it is visible in Figures 3.6(a)-(d), primary spherical aberration has an effect on the phase properties primarily before the focus. This is, of course, only true when the coefficient of the aberration function is negative, which means that the rays that are farther from axis are focused to a focal point that is closer to the focal element. This is a well-known property of spherical aberration [90, 130], and this is why cases with negative aberration coefficient are plotted in Figures 3.6(a)-(d).

An other expected property is the effect of spherical aberration on highly non-paraxial rays, which appears in the (3.29) form of the aberration function by the fourth power dependence on the radial distance from axis. This also means that a higher amount of aberration is necessary for a visible effect on the velocity variations compared to other aberrations (cf. the magnitude of aberration coefficients μ_0 in Figure 3.6 for spherical aberration and Figures 3.7, 3.8, 3.9 and 3.10 for other primary aberrations). It is enough to plot cases with negative coefficients, because it has been shown previously that the field in the presence of primary spherical aberration in Debye approximation possesses a mirror symmetry in the dimensionless axial coordinate u_D, with the change of sign of the aberration coefficient μ_0 [195]. This means that, if the Debye approximation is valid, only the $u_D \leftrightarrow -u_D$ and $\gamma_v \leftrightarrow -\gamma_v$ exchanges are necessary if the interchange $\mu_0 \leftrightarrow -\mu_0$ is done. One has to be cautious, however, because, in general, there are more conditions to be fulfilled for the validity of Debye approximation than just the high value of the Fresnel number N_w [152, 153]. For example, one has to take into account the Z_0-dependent scaling in the expression of (3.18) and (3.19), which is a nice example of requirement $u_D \ll 2\pi N_w$ (so $Z_0 \ll f_0$) in this case [152]. So, this additional limit restricts distance of the spatial

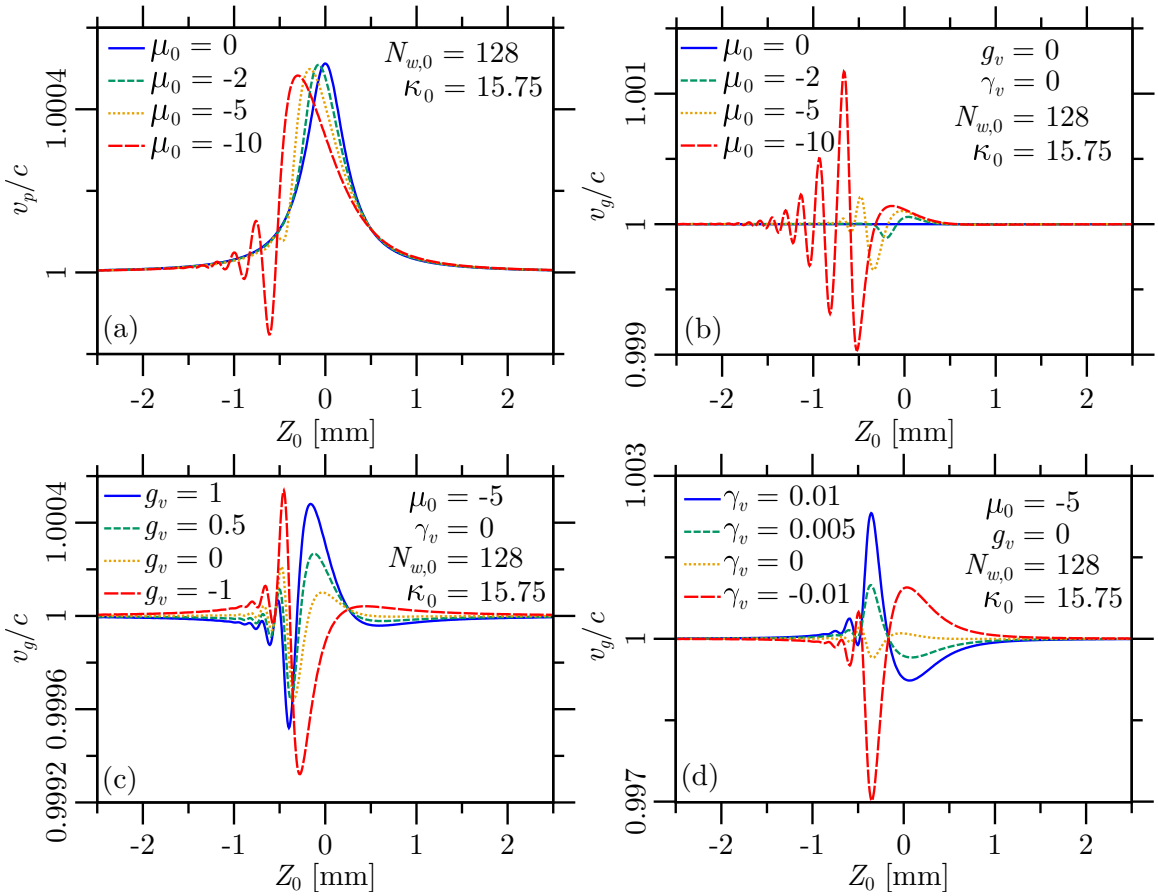

Figure 3.6. The on-axis change of phase and group velocity in the presence of primary spherical aberration. The central wavelength is $\lambda_0 = 800\,\text{nm}$, the Gaussian beam radius at the exit pupil is $w = 3.2\,\text{mm}$ and the radius of curvature of the Gaussian reference sphere leaving the exit aperture is $R_0 = 100\,\text{mm}$. This results in a Rayleigh length of approximately $250\,\mu\text{m}$. (a) The on-axis phase velocity for different amounts of primary spherical aberration. (b) The on-axis group velocity for different amounts of primary spherical aberration. (c) The on-axis group velocity variation with g_v. (d) The on-axis group velocity variation with γ_v.

coordinate from the focal point in Debye approximation, and can be relevant, since the interesting region (where the intensity is highest, or where the phase variations are most pronounced) can be shifted from the geometrical focus due to the presence of aberrations. More visible effects of the scaling with Z_0 is presented in the case of other aberrations.

Astigmatism Astigmatism is again a well-known aberration of laser beams, caused, for example, by off-axis reflection from cavity mirrors [18]. The aberration function of primary astigmatism is indexed by $l = 0$, $n = 2$ and $m = 2$, giving the form

$$\Phi_{022}(\rho, \theta) = \mu_0 \lambda_0 \rho^2 \cos^2(\theta)\,. \tag{3.30}$$

Two distinct focal lines appear in the presence of primary astigmatism. These are

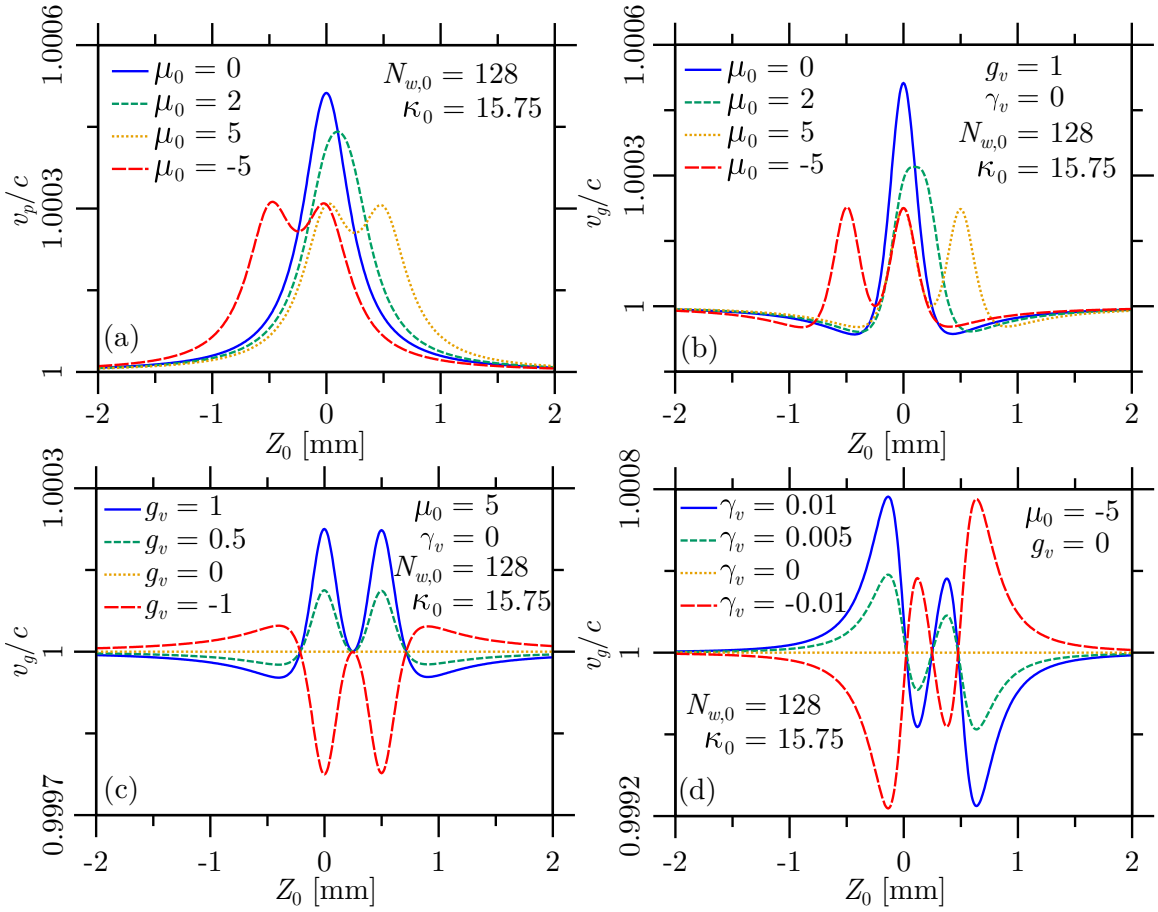

Figure 3.7. The on-axis change of phase and group velocity in the presence of primary astigmatism. The central wavelength is $\lambda_0 = 800\,\text{nm}$, the Gaussian beam radius at the exit pupil is $w = 3.2\,\text{mm}$ and the radius of curvature of the Gaussian reference sphere leaving the exit aperture is $R_0 = 100\,\text{mm}$. This results in a Rayleigh length of approximately $250\,\mu\text{m}$. (a) The on-axis phase velocity for different amounts of primary astigmatism. (b) The on-axis group velocity for different amounts of primary astigmatism. (c) The on-axis group velocity variation with g_v. (d) The on-axis group velocity variation with γ_v.

called meridional and sagittal focal spots, since the meridional rays (that traverse through the plane of symmetry, given by $\theta = 0$) and sagittal rays (traveling in the plane of $\theta = 90°$) are focused at each of them.

An interesting feature of astigmatism, which has been shown both theoretically and experimentally [194, 205], that the total π phase shift of Gouy happens in two steps of $\pi/2$. This appears as double peaks in the plots of phase and group velocity in an astigmatism-distorted situation (see Figure 3.7(a)-(b)). When a non-isodiffracting beam is considered, there can be a double decrease in group velocity (see Figure 3.7(c)), or a decrease and increase can follow each other in the two focal points (see Figure 3.7(d)). With a bigger amount of aberration, the focal points become more distinct and the magnitude of velocity change decreases (see Figure 3.7(a)-(b)).

Astigmatism is unique in the group of primary aberrations, because it is the only one with a nonzero, even value of index m. As a result, the group velocity is constant along axis if $g_v = 0$ and $\gamma_v = 0$, as it can be seen in Figure 3.7(b). Astigmatism has a similar symmetry to spherical aberration, that is, if the Debye approximation is valid in the studied region, $u_D \leftrightarrow -u_D$ and $\gamma_v \leftrightarrow -\gamma_v$ exchanges are enough to obtain the phase and group velocities on axis for the $\mu_0 \leftrightarrow -\mu_0$ replacement. This is related to the even value of index n.

Coma Coma is closely coupled to astigmatism. The main difference is that coma only appears for non-paraxial rays, while astigmatism is present also for paraxial rays. Both astigmatism and coma are related to the disappearance of cylindrical symmetry in imaging. The aberration function of primary coma is indexed by $l = 0$, $n = 3$ and $m = 1$, giving the form

$$\Phi_{031}(\rho, \theta) = \mu_0 \lambda_0 \rho^3 \cos(\theta)\,. \tag{3.31}$$

An important feature of primary coma is the increased distance along which a given amount of phase change occurs due to the Gouy phase shift. As the total amount of phase shift is restricted ($-\pi$[III] from $Z_0 = -\infty$ to $Z_0 = +\infty$), it means a depressed phase variation along the axis. This lengthening of the characteristic range of Gouy phase shift appears as a region where the phase changes almost linearly with distance. As a consequence, the spatial region where phase velocity has a constant $v_p > c$ value is increased (see Figure 3.8(a)).

Note that, in the $\gamma_v = 0$ case, the group velocity variation is symmetric with respect to $u_D = 0$ in the Debye approximation. This symmetry is only broken by the scaling with Z_0, visible in regions where the velocity is most decreased compared to c in Figures 3.8(b), (c) and (d). The variation of v_g is overall more complex than it is directly expected from the effect of coma on the phase velocity.

It is also important that both the phase velocity and the group velocity make an angle with the optical axis, since they have radial components. This stands for every primary aberration where m is odd. So coma is an aberration where the component $\mathbf{u}_r$ can not be neglected when (3.18) or (3.19) is evaluated. In the case of coma, in the Debye approximation, the on-axis variation of the amplitude of the phase and group velocities are identical when $|\mu_0|$ is the same.

Curvature of field Primary curvature of field is an aberration that is more often mentioned in the topics of photography, since this aberration causes an imaging error

[III] In the case of opposite sign convention, when the temporal phase changes are taken with $+\imath\omega t$ and the spatial with $-\imath kz$, complex conjugate forms appear, and the Gouy phase shift is $+\pi$ from $Z_0 = -\infty$ to $Z_0 = +\infty$. As described previously, this is just a sign convention having no physical consequences.

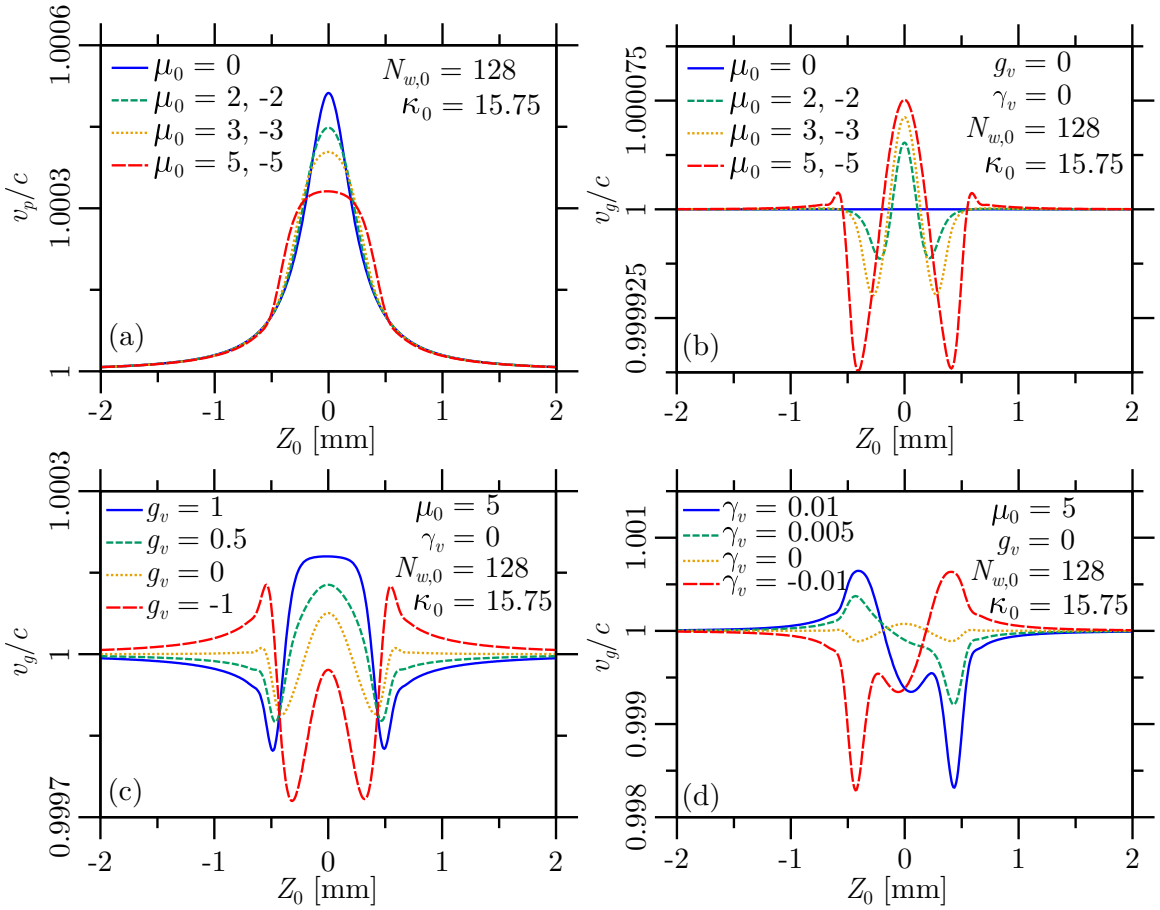

Figure 3.8. The on-axis change of phase and group velocity in the presence of primary coma. The central wavelength is $\lambda_0 = 800\,\text{nm}$, the Gaussian beam radius at the exit pupil is $w = 3.2\,\text{mm}$ and the radius of curvature of the Gaussian reference sphere leaving the exit aperture is $R_0 = 100\,\text{mm}$. This results in a Rayleigh length of approximately $250\,\mu\text{m}$. (a) The on-axis phase velocity for different amounts of primary coma. (b) The on-axis group velocity for different amounts of primary coma. (c) The on-axis group velocity variation with g_v. (d) The on-axis group velocity variation with γ_v.

that is not so fortunate, because the CCD chips or detectors are flat. Due to field of curvature, objects (for example a flat object with perpendicular plane to the optical axis) can not be imaged sharply in every point to a plane (image plane). The aberration function of primary curvature of field is indexed by $l = 1$, $n = 2$ and $m = 0$, so has the form

$$\Phi_{120}(\rho, \theta) = \mu_0 \lambda_0 \rho^2 \,. \tag{3.32}$$

It is a known fact that, in the Debye approximation, primary curvature of field means a spatial and temporal shift compared to the aberration-free case [O5]. This is easy to verify, since with the substitution of (3.32) into (2.52), the change is just a shift of variable u by $u_{\text{shift}} = \mu_0 4\pi$. As mentioned several times, the validity of the more strict requirements of

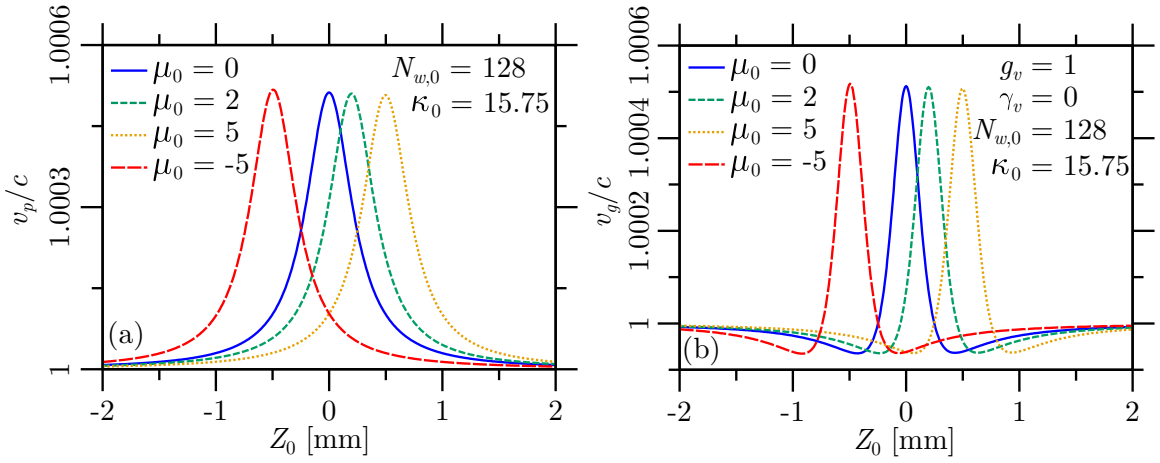

Figure 3.9. The on-axis change of phase and group velocity in the presence of primary curvature of field. The central wavelength is $\lambda_0 = 800\,\text{nm}$, the Gaussian beam radius at the exit pupil is $w = 3.2\,\text{mm}$ and the radius of curvature of the Gaussian reference sphere leaving the exit aperture is $R_0 = 100\,\text{mm}$. This results in a Rayleigh length of approximately $250\,\mu\text{m}$. (a) The on-axis phase velocity for different amounts of primary curvature of field. (b) The on-axis group velocity for different amounts of primary curvature of field. (c) The on-axis group velocity variation with g_v. (d) The on-axis group velocity variation with γ_v.

Debye approximation have to be taken into account in aberration-distorted focusing [152]. It is the easiest to see in Figures 3.9(a) and (b), among the presented plots , that the coordinate-dependent scaling appears, and breaks this nice property of simple shifting, valid only in Debye approximation. Here, the $u \ll 2\pi N_w$ restriction is very important to be considered, especially if the simplification — the shift by u_{shift} — is about to be used.

Distortion Distortion is again mostly known from imaging, and it means the change of magnification in different points of the image. Due to distortion, straight lines of the object are bended curves in the image, making a regular net look more like a barrel or pincushion (the names of the most well-known examples of distortion-type aberration). The aberration function of primary distortion is indexed by $l = 1$, $n = 1$ and $m = 1$, so has the form

$$\Phi_{111}(\rho, \theta) = \mu_0 \lambda_0 \rho \cos(\theta)\,. \tag{3.33}$$

An interesting property of primary distortion is visible in Figure 3.10(a). It induces a huge decrease in phase velocity. This decrease is symmetric with respect to the focal point, and overwhelms the changes $(v_p/c - 1)$ by an order of magnitude compared to other types of aberrations of the same amount (same value of μ_0, cf. Figures 3.6, 3.7, 3.8 and 3.9). This, however, is not an applicable method for phase-velocity reduction in the focus, as distortion means a spatial shift along axis y in Debye approximation (see Figure 2.9) [O5]. So the axis is not the region of highest intensity anymore. It is also

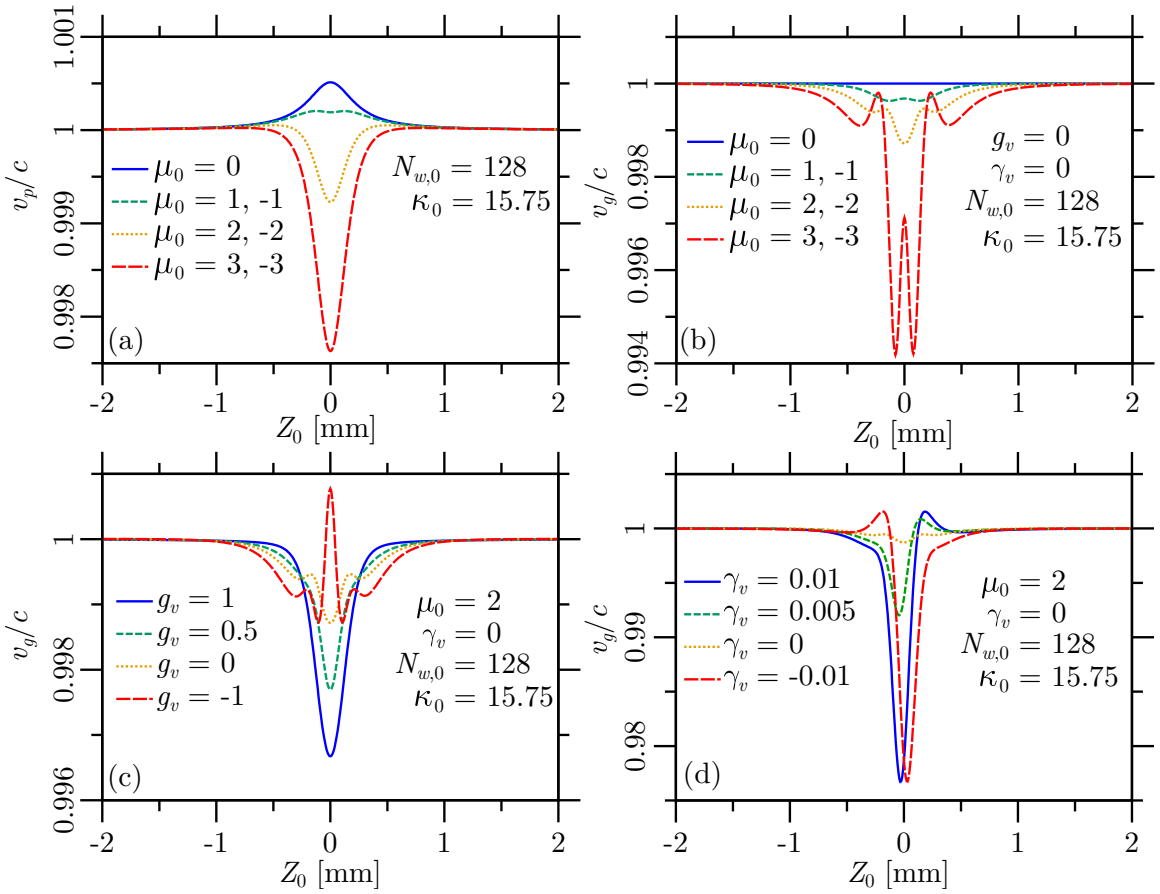

Figure 3.10. The on-axis change of phase and group velocity in the presence of primary distortion. The central wavelength is $\lambda_0 = 800\,\text{nm}$, the Gaussian beam radius at the exit pupil is $w = 3.2\,\text{mm}$ and the radius of curvature of the Gaussian reference sphere leaving the exit aperture is $R_0 = 100\,\text{mm}$. This results in a Rayleigh length of approximately $250\,\mu\text{m}$. (a) The on-axis phase velocity for different amounts of primary distortion. (b) The on-axis group velocity for different amounts of primary distortion. (c) The on-axis group velocity variation with g_v. (d) The on-axis group velocity variation with γ_v.

known that off-axis the phase shift is different, and instead of phase-velocity increase it causes a decrease [168, 196], which can be much bigger then the on-axis increment [168]. By adding primary distortion to (3.18) and (3.19), one can get phase variations along a line in plane $y - z$, which is parallel to the optical axis, and its distance increases from axis with increasing amount of primary distortion. So assuming the presence of primary distortion is equivalent to calculating off-axis properties in Debye approximation.

Like other primary aberrations with an aberration function having an odd value of index m, primary distortion gives the same result for velocity variations for aberration coefficients of the same amplitude but opposite sign in the Debye approximation. The phase and group velocity have radial components in this case, just like in the presence of coma.

Summary I. *I developed analytical formulas for the on-axis phase velocity and group velocity of focused Gaussian beams which take into account the wavelength-dependent properties of the focused beam. I specified the parameters which determine the changes of group velocity, and I established expressions for the calculation of these focused beam features using the characteristics of the source beam and the focusing system. Based on the previous attainments, I gave the specific conditions only under which the group velocity of a focused Gaussian beam is constant during propagation through the focal region. Using these results I highlighted that a chromatic aberration-like effect can occur not solely due to the focusing element, but also because of beam features.*
I presented formulas for the calculation of the phase velocity and the group velocity of focused Gaussian beams when focusing is affected by chromatic and primary monochromatic aberrations. Specific attention is paid to the analytical evaluation of expressions to increase the precision and to widen the applicability of the numerical simulations. I used these results to analyze the effect of beam truncation, monochromatic aberrations and chromatic aberration on the on-axis phase-velocity and group-velocity variations of pulsed Gaussian beams. I made a comparison between recent and previous results on primary aberrations and their affect on phase properties in the vicinity of focus [T1].

3.2 Focusing of few-cycle optical pulses with controlled electric field using lenses

Apart from the beneficial variation of the phase (and group) velocity during propagation through the focal region, an important requirement for nonlinear optical sciences is to maintain the shape and short duration of the laser pulses, even after focusing. To fulfill this condition, lenses are often avoided for focusing few-cycle pulses, because of their long-known distorting effects, especially the ones increasing pulse duration [75, 147]. The first issue with lenses is that — as being refractive optics — the light passes through their material, which — due to dispersion — increases their temporal duration (see Section 2.2.1). The other problem is that different parts of the beam traverse different extent in the material, as lenses have a spatially varying thickness. One effect of the different amounts of dispersive material is the propagation-time difference (PTD) of rays [75]. This causes pulse broadening, especially in the focal region [147]. The resulted inhomogeneous pulse broadening along the beam profile can not be compensated with standard pulse compression techniques [18]. The problem can not be addressed properly by up-to-date pulse-shaping techniques either [206, 207].

However, the effect of PTD — which is caused in fact by the chromatic aberration [147] — was examined originally with fully illuminated lenses and using ultraviolet wavelengths,

which enhance this unwanted phenomenon [75, 147]. Most femtosecond lasers operate in the infrared regime, not the whole cross-section of the lens is used, and the focusing is loose compared to that considered in the cited articles [75, 147]. Triggered by this, the aim of the next sections is to investigate the conditions under which the pulse-distorting effects of lenses can be avoided during focusing, and to examine the possible additional benefits of using lenses.

3.2.1 Accurate model of focusing few-cycle pulses with lens systems

To examine how a few-cycle pulse behaves in the focal region, an accurate model is necessary, which considers all the aspects that could have a relevant effect on the electric field in the focus. The model, which was developed, consists of two main steps, which are summarized by Figure 3.11. The first part is to choose the reference sphere and to determine the field on it using ray tracing. The second is to calculate the field in point P using scalar diffraction theory.

The ray tracing calculations — specifically developed by the author for these simulations — are carried out assuming cylindrical symmetry, and uses the presumption that the focusing system consists of optical elements with spherical surfaces. The former means that the rays passing through a plane perpendicular to the optical axis can be uniquely described by the radial coordinate of the point where they pass through and the angle they form in that point with the optical axis (like in the ABCD formalism). The first step is to determine the radius of curvature of the Gaussian reference sphere behind the focusing element, which is necessary for second part of the calculations based on diffraction theory. This is done by taking a paraxial ray in the entrance pupil (ray very close the the optical axis) and tracing its path while it traverses the optical system and after that it intersects the optical axis. Assuming a plane input wavefront, the radius of the Gaussian reference sphere for a singlet lens is equivalent to the back focal length of the lens. So the ray racing result equals the back focal length given by the analytical formula [208]

$$f_{\mathrm{back}}(\omega) = \left[(n(\omega)-1)\left(\frac{1}{R_1}-\frac{1}{R_2}\right)+\frac{(n(\omega)-1)^2}{n}\frac{D}{R_1R_2}\right]^{-1} + \frac{R_2 D}{n(\omega)(R_1-R_2)-(n(\omega)-1)D}\,. \tag{3.34}$$

In the previous expression, $n(\omega)$ is the relative refractive index of the lens material with respect to the surrounding material (vacuum in all the cases considered here), R_1 and R_2

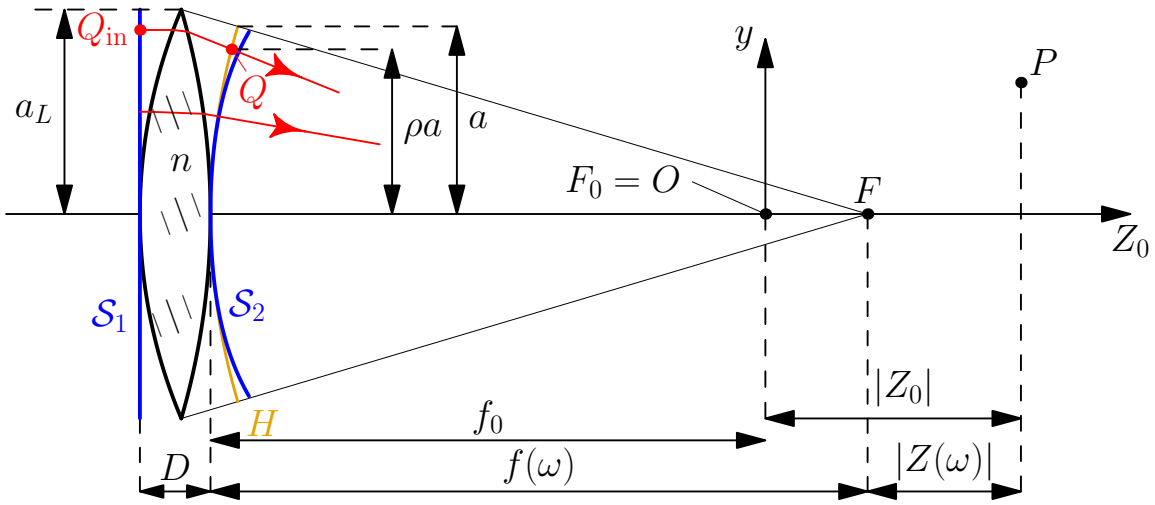

Figure 3.11. A summary figure with the example of a singlet lens on how the model of focusing short pulses with lenses and lens systems is built up. Cylindrical symmetry is assumed. The wave front in the exit pupil of the focusing system is calculated by tracing the path of the rays from the wave front $\mathcal{S}_1$ at the input pupil to the reference sphere H at the exit pupil for each wavelength (from point Q_{in} to point Q of the example ray depicted using a red line). The real geometrical wave front $\mathcal{S}_2$ differs from the ideal spherical one (reference sphere H), the real one given by the eikonal $\mathcal{S}(\mathbf{r}) = \mathcal{S}_2$ (distorted by spherical aberration in this figure). The position F of the geometrical focal point — and the radius of the Gaussian reference sphere $f(\omega)$ (a flat input wave front $\mathcal{S}_1$ is assumed) — is obtained from the ray-tracing result of a paraxial ray. With the known phase properties along the reference sphere the electric field is calculated in point P by diffraction theory (see Section 2.3.3). The distance a of the edge of the exit pupil and the optical axis is in general different from the aperture radius a_L of the lens with central thickness D and refractive index n.

are the radii of curvature of the two spherical surfaces of the lens[IV] and D is its central thickness (see this latter in Figure 3.11).

The second part of ray tracing deals with the calculation of the wave front distortion along the reference sphere and the aperture size in the exit pupil. To achieve this, rays are initiated from the input spherical wave front (plane wave front in this section, as depicted in Figure 3.11) at different radial distances from the optical axis, and the optical path they travel is simulated up to the point where they intersect the reference sphere. Subtracting the on-axis optical path from the optical paths at different ρa radial coordinates gives the aberration function $\Phi(\rho)$ (see Section 2.3.3). The refraction on spherical surfaces is calculated using Snell's law.

It is important to note that as broadband radiation is considered, this calculation has to be carried out for several wavelengths. The radius of the entrance pupil $a(\omega)$, the truncation coefficient $\kappa(\omega)$ if a Gaussian beam is considered, the radius of the Gaussian

[IV] The sign convention of the surfaces is that the radius of curvature is positive if the surface is convex when one looks in the direction of ray propagation, and negative if it is concave.

reference sphere $R(\omega)$ (or $f(\omega)$ with plane input wavefront) and the aberration function $\Phi(\rho,\omega)$ are all wavelength dependent. All these effects are taken into account using this method. As highlighted in Figure 3.11, in general, the radius a of the exit pupil is different from the radius of the lens aperture a_L ($a < a_L$). However, in most practical cases, they are approximately the same ($a_L \approx a$), and even if they are not not, then still κ is the same in the exit and entrance pupils [200]. In the simulations presented in this section, the aberration function $\Phi(\rho,\omega)$ was fitted with a function given by the expression $\mu\lambda\rho^4$, corresponding to primary spherical aberration, to obtain the wavelength-dependent aberration coefficient $\mu_{040}(\omega)$, meaning the dominant aberration in these cases.

With the wavelength-dependent reference-sphere data (radius of curvature, aperture size) and the aberration function, everything is available to calculate the focused field using diffraction theory. Following the considerations given for the ray tracing, the field of a monochromatic component on the surface of Gaussian reference sphere H is given by

$$\tilde{\mathcal{P}}_H(\omega) = \tilde{U}(\omega)\exp\left[-\left(\frac{\rho a}{w}\right)^2\right]\exp\left[\iota\frac{\omega}{c}\left(l_\mathrm{a}+\Phi(\rho,\omega)\right)\right]. \tag{3.35}$$

In the previous expression $\tilde{U}(\omega)$ contains the phase and spectral amplitude properties on the input wave front ($\mathcal{S}_1$ in Figure 3.11), similarly to (2.58). The exponential expression $\exp\left[-(\rho a/w)^2\right]$ assumes a Gaussian beam, while the phase factor $\exp[\iota k l_a]$ gives the phase along the reference sphere with respect to the input wave front, since the optical path between the input wave front and reference sphere is l_a for the on-axis ray. The ray tracing implementation contains the calculation of l_a. For the singlet lens of Figure 3.11, the optical path along the axis from the entrance pupil to the exit pupil is $l_a = n(\omega)D$. Following the Huygens-Fresnel principle, the focal field can be calculated by the surface integral

$$\tilde{\mathcal{P}}(P,\omega) = -\frac{\iota}{\lambda}\iint_H \tilde{\mathcal{P}}_H(\omega)\frac{\exp[\iota k h]}{h}\,\mathrm{d}H\,, \tag{3.36}$$

H being the surface of the reference sphere and h is the distance of point Q on H and the point of interest P, similarly to (2.46) in Section 2.3.3. It can be shown with reprouping that, in fact, the integral (2.48) previously calculated can be exactly formed from (3.36), and the results of Section 2.3.3 can be reused. So the complex spectrum in point P is given by

$$\tilde{\mathcal{P}}(P,\omega) = \tilde{U}(\omega)R\exp[\iota k(R+l_a)]\underbrace{-\frac{\iota}{\lambda}\frac{\exp[-\iota kR]}{R}\iint_H \exp\left[-\left(\frac{\rho a}{w}\right)^2\right]\frac{\exp[\iota k(h+\Phi)]}{h}\,\mathrm{d}H}_{\tilde{G}(\omega)\text{ of (2.51) or }\tilde{G}_D(\omega)\text{ of (2.55)}}\,, \tag{3.37}$$

forming it similarly to how it is done in [135].

In this section the considerations are limited to cases when only spherical aberration is present and the Debye approximation is applicable (so $\tilde{G}_D(\omega)$ of (2.55) is used in (3.37) from the highlighted two possibilities). Also, only on-axis points in the focal region are studied, but expressions valid for off-axis points in spherical-aberration distorted focusing can be found in Appendix E.1 (see expression (E.2)). For brevity, it is worth introducing the dimensionless aberration coefficient for spherical aberration

$$\alpha_S = kA_{040} = \frac{2\pi}{\lambda}\mu_{040}\lambda = 2\pi\mu_{040}\,, \tag{3.38}$$

and the complex dimensionless axial coordinate

$$\tilde{u}_D = u_D - \iota 2\kappa\,, \tag{3.39}$$

where u_D is given by (2.56), and truncation coefficient κ by (2.50). From (3.37), it can be shown that, in the case of $\alpha_S = 0$, the on-axis electric field of a monochromatic component can be written as [78, 135, 143, 200]

$$\tilde{\mathcal{P}}(Z_0,\omega) = -\frac{\iota\omega\tilde{U}(\omega)a^2}{2cR}\exp[\iota k(R+l_a)]\exp\left[\iota\left(\frac{R}{a}\right)^2 u_D\right]\frac{\exp[-\iota\tilde{u}_D/2]-1}{-\iota\tilde{u}_D/2}\,. \tag{3.40}$$

Note that both the complex ($\tilde{u}_D$) and the real (u_D) valued form of the longitudinal coordinate appears in the expression above. If $\alpha_S \neq 0$, then (see details in Appendix E.1 or the main steps in [200])

$$\begin{aligned}\tilde{\mathcal{P}}(Z_0,\omega) = &-\frac{\iota\omega\tilde{U}(\omega)a^2}{2cR}\exp[ik(R+l_a)]\exp\left[\iota\left(\frac{R}{a}\right)^2 u_D\right]\\ &\times\exp\left[-\iota\frac{\tilde{u}_D^2}{16\alpha_S}\right]\sqrt{\frac{\pi}{2|\alpha_S|}}\frac{1+\iota\mathrm{sgn}(\alpha_S)}{2}\\ &\times\left[\mathrm{erf}\left(\frac{1-\iota\mathrm{sgn}(\alpha_S)}{2}\sqrt{2|\alpha_S|}\left(1-\frac{\tilde{u}_D}{4\alpha_S}\right)\right)+\mathrm{erf}\left(\frac{1-\iota\mathrm{sgn}(\alpha_S)}{2}\sqrt{2|\alpha_S|}\frac{\tilde{u}_D}{4\alpha_S}\right)\right]\,.\end{aligned} \tag{3.41}$$

In the formula above

$$\begin{aligned}&\mathrm{erf}(z) = \frac{2}{\sqrt{\pi}}\int_0^z \exp\left[-t^2\right]\,\mathrm{d}t && \text{is the error function with complex argument [209],}\\ &\mathrm{sgn}(x) = \begin{cases}-1 & \text{if } x<0\\ 0 & \text{if } x=0\\ +1 & \text{if } x>0\end{cases} && \text{is the signum function.}\end{aligned} \tag{3.42}$$

Note again that $\tilde{u}_D$ and u_D are both present in (3.41), just like it is in (3.40).

A formula similar to (3.41) was formed also by Pang *et al.* [195] later, giving the same result. Both (3.41) and the expression of [195] suffer from the same problem: for low amount of aberration, or far from the geometrical focus, numerical issues arise, because a zero-times-infinity type of multiplication is present in both formulas. For the same reason, the $\alpha_S = 0$ case can not be evaluated directly, it is a limit of the function presented. So, for non-negligible amount of aberration and close to the focus, the use of (3.41) is preferable, because of faster evaluation. However, in general, to avoid numerical errors, direct evaluation of integral (E.2) is suggested. This latter solution is what is used mainly in this work.

As a summary of the main steps of the simulation, first, the ray tracing of the monochromatic components is carried out, assuming an initial spherical wave front for each wavelength. With the resulted radii for the Gaussian reference sphere, the exit aperture sizes, the truncation coefficients, the on-axis optical paths, the aberrations and with the initial spectral data $\tilde{U}(\omega)$, the diffraction integral is calculated for all wavelengths in the points of interest. Finally, at each spatial coordinate in the vicinity of focus, an inverse Fourier transform is performed to yield the temporal electric field $\tilde{E}(P,t) = \mathscr{F}^{-1}\left\{\tilde{\mathcal{P}}(P,\omega)\right\}$ (see Section 2.3.4).

3.2.2 Undistorted focusing of short pulses with lenses

As it was discussed in the introduction of this section, lenses are often avoided for focusing few-cycle pulses. Their material dispersion, which is not homogeneous along the beam cross section, and their chromatic aberration keep scientist, working with these laser pulses, from using them. However, it is shown in this section that, when certain conditions are met, these unwanted effects can be escaped in the experiments where few-cycle pulses are used. First, simplified formulas are discussed, which can be derived for the focused electric field when no aberrations are present. Then some guidelines are given, which can be used to estimate in which situations the effects of spherical and chromatic aberrations can be disregarded. These approximate rules are then justified by the model described in the previous section.

A possible basis for a condition, so to tell when the effect of spherical aberration can be neglected, is the tolerance condition theory developed decades ago [90]. According to this tolerance theory used in imaging, the intensity distribution of the focused field is not appreciably changed (peak intensity deviates from undistorted case in 20% maximum), if the condition $\mu_{040} < 0.94$ is met [90], that is, the aberration coefficient of spherical aberration is less then 94% of the wavelength. However, when broadband radiation, and especially short pulses are considered, a condition appropriate for imaging might not be

precise enough, as it was highlighted in Section 3.1.2 of the results. Until the specific conditions are not clarified, let us assume the absence of spherical aberration for the following few paragraphs.

When no spherical aberration is present, or its effect can be ignored, the on-axis field is given by (3.40), which can be written also as

$$\tilde{\mathcal{P}}(Z_0,\omega) = -\frac{\iota\omega\tilde{U}(\omega)a^2}{2cR}\exp[\iota k l_a]\exp[\iota k z]\,\frac{\exp[-\kappa-\iota u_D/2]-1}{-\kappa-\iota u_D/2}\,, \tag{3.43}$$

where the definitions of coordinate u_D (see (2.56)) and other parameters, like $z = R_0 + Z_0 = Z + R$ (distance from the back vertex of the lens), are given in Section 2.3.2. When the truncation is negligible ($a_L \gg w$, that is, $\kappa \to \infty$)

$$\frac{\exp[-\kappa-\iota u_D/2]-1}{-\kappa-\iota u_D/2} \approx \frac{1}{\kappa+\iota u_D/2}\,. \tag{3.44}$$

For further convenience, let us assume that the Gaussian beam is focused at its waist, and this position is the same irrespective of wavelength, so the input wave front is flat ($R = f_{\text{back}}$), and the beam size w is the waist radius s. With the previously mentioned assumption of $a_L \approx a$, one can arrive to the expression (see details in Appendix E.2)

$$\tilde{\mathcal{P}}(Z_0,\omega) = \tilde{U}(\omega)\exp[\iota k l_a]\exp[\iota k z]\,\frac{-f_{\text{back}}}{Z-\iota L_D}\,, \tag{3.45}$$

which is equivalent to expression (B.13) of Appendix B.1 obtained using ABCD formalism, if $f_{\text{back}} = f$ is assumed, which is natural for the ABCD matrices. In (3.45) (and similarly in the ABCD formalism), the axial coordinate is $Z = Z_0 + f_0 - f$, and according to (B.12) the focused Rayleigh range in the Debye approximation is $L_D = 2cf^2/(\omega s^2)$. The important conclusion of this result is that if the above conditions are met, then the focusing lens can be thought of as a combination of a dielectric slab of thickness l_a ($\exp[\iota k l_a]$ term of (3.45)) and an idealistic focusing element with focal length $f_{\text{back}} \approx f$ having zero thickness ($-f_{\text{back}}/(Z-\iota L_D)$ term of (3.45)). So practically, standard pulse shaping techniques can be used to compensate for the dispersion of the lens material, and otherwise it works as an ideal focal element with chromatic aberration.

Before turning to the above simplified formula and considerations on the CEP changes in the focal region, it is shown under what circumstances a few-cycle pulse is focused without appreciable distortion, and when (3.45) can be used. Figure 3.12 shows the case of focusing a Gaussian beam with $s = 5\,\text{mm}$ radius at its waist using a fused silica bi-convex lens. It was calculated using the model described in the previous section (see Section 3.2.1). See detailed lens and pulse beam parameters in the caption of Figure 3.12.

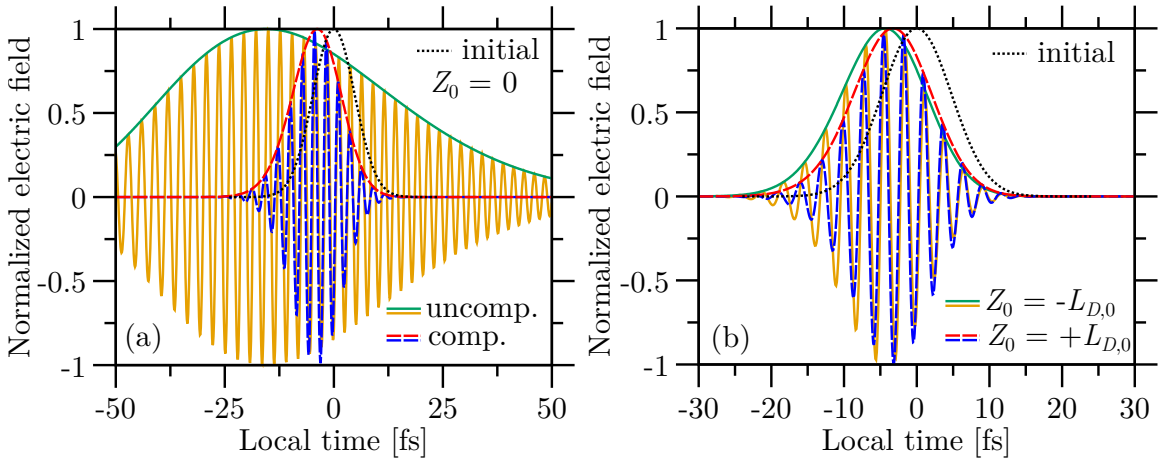

Figure 3.12. On-axis temporal shapes of a pulse in the focal region of a bi-convex fused silica lens. The transform-limited duration of the Gaussian-shaped pulse is $T_{\mathrm{FWHM}} = 8\,\mathrm{fs}$, and the Gaussian waist of the beam has $s = 5\,\mathrm{mm}$ radius. The lens was taken from a commercial catalog, and the radii of its two spherical surfaces are $R_1 = 91.08\,\mathrm{mm}$ and $R_2 = -91.08\,\mathrm{mm}$, the center thickness is $D = 3.78\,\mathrm{mm}$, the aperture radius is $a_L = 12.5$ and has a back focal length of $f_{\mathrm{back},0} = 99.8\,\mathrm{mm}$. For refractive index values the Sellmeier equation[V] is used. Local time means that on the horizontal axis zero corresponds to the group delay from the entrance pupil to the point of interest. (a) Pulse shape in the geometrical focus of the carrier wave ($\lambda_0 = 800\,\mathrm{nm}$) when the the dispersion of the lens material on-axis is not compensated (dashed curves) and when the dispersion is pre-compensated up to the third order phase derivative (continuous curves). (b) Pulse shape at one Rayleigh length ($L_{D,0} \approx 0.1\,\mathrm{mm}$) before and behind the focal point with pre-compensation of lens center material up to third order. The dotted curve represents the transform-limited pulse shape in the entrance pupil.

In Figure 3.12(a), the on-axis pulse shape is depicted in the geometrical focal point of the carrier frequency. The two pulse shapes correspond to the case when a transform-limited pulse reaches the lens (uncompensated case) and when the GDD and TOD terms of the material dispersion of a slab with equal thickness to the center thickness of the lens is assumed to be pre-compensated (compensated case). This pre-compensation appears as a second- and third-order term of the spectral phase in the expression of $\tilde{U}(\omega)$ in (E.1), describing the input spectral amplitude and phase properties, GDD and TOD coming from the application of (2.6) on $\varphi_{\mathrm{mat}}(\omega) = n(\omega)D$. So the explicit form of input complex spectrum is

$$\tilde{U}(\omega) = p(\omega)\exp\left[-\iota\frac{\mathrm{GDD}}{2}(\omega-\omega_0)^2 - \iota\frac{\mathrm{TOD}}{6}(\omega-\omega_0)^3\right]. \tag{3.46}$$

The $p(\omega)$ spectrum is a Gaussian, like (A.1). The transform-limited duration of the input pulse is also depicted with black dotted curve, for comparison. The local time means that

[V] The Sellmeier equation is an empirical formula for the refractive index of transparent, non-absorbing materials, an it is often used in the visible regime [130]. Specifically, the coefficients available on `http://refractiveindex.info/` are used for the materials in this work.

the horizontal axis is shifted by the time necessary for an undistorted pulse to travel to the point of interest (equal to the group delay, so $\tau = t - \mathrm{GD}(Z)$, which in this case is $\mathrm{GD}(Z) = \partial\left[k(Dn(\omega) + Z + f)\right]/\partial\omega$). Comparing the pre-compensated case with the uncompensated one shows that the pulse broadening due to passing through lens material can be decreased at a large degree by compensating for the dispersion of a slab, possible with pulse shaping techniques [206, 207]. However, the transform limited duration can not be fully retained like this in this specific example, and there is also a temporal shift of the pulse peak due to chromatic and spherical aberrations.

For a wider picture, the pulse shapes at the edges of the depth of focus is also shown in Figure 3.12(b). The two pulse shapes at $Z_0 = \pm L_{D,0}$ highlight the coordinate-dependent effect of the aberrations, and its is also visible that the pulse is a bit broadened in the whole focal region. Still, these plots show that, even with pre-compensating for a slab with properties defined by the lens center, the pulse broadening can be hugely decreased. A primary reason for this is that — as it was shown previously [75] — the ratio of the pulse lengthening-effect of chromatic aberration (that is PTD) and that of the material dispersion is proportional to the pulse duration and beam radius (the radius of the illuminated part of the lens). So, few-cycle pulsed beams are not necessarily stretched more by chromatic aberration than dispersion, and material dispersion can be the dominant effect that causes the increased duration.

While the pulse duration is not that much increased in the pre-compensated case, there are still visible effects of spherical and chromatic aberrations on the pulse shapes in Figure 3.12(b), namely the temporal shift. To avoid these issues, some rule-of-thumb expressions can be given [T2, T3]. Based on the previously mentioned rule known from imaging, the effect of spherical aberration on the pulse shape in the focus is negligible if

$$\mu_{040}\left(\frac{s}{a_L}\right)^4 < 0.94\,. \tag{3.47}$$

Note that in one sense the condition is less strict because not a uniform illumination is used, and at the same time a bit more strict because not monochromatic, but broadband radiation is considered, and for undistorted pulse shape the phase properties are also important (see Section 3.1 of results or [T1]). For the chromatic aberration, it is worth introducing the parameter $\gamma_p = f_0'\omega_0/L_{D,0}$ (note that this is different from the γ_v parameter defined in the previous section, see details later or in Appendix E.2). With γ_p a guideline can be given, according to which the chromatic aberration does not increase pulse duration relevantly if

$$|\gamma_p| \ll \frac{\omega_0 T_{\mathrm{FWHM}}}{4\ln(2)}\,. \tag{3.48}$$

This expression can be obtained using the demand that the focal-length change in the

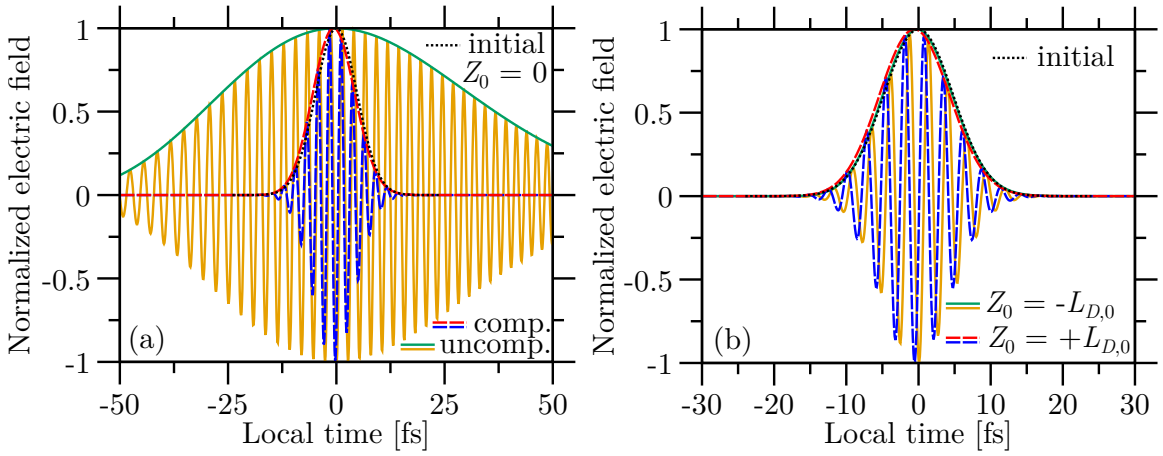

Figure 3.13. On-axis temporal shapes of a pulse in the focal region of a bi-convex fused silica lens. The lens and pulsed beam properties are the same as in Figure 3.12 except that the waist of the Gaussian beam has a radius of $s = 1\,\text{mm}$. (a) Pulse shape in the geometrical focus of the carrier wave ($\lambda_0 = 800\,\text{nm}$) when the the dispersion of the lens material on-axis is not compensated (dashed curves) and when the dispersion is pre-compensated up to the third order phase derivative (continuous curves). (b) Pulse shape at one Rayleigh length ($L_{D,0} \approx 2.5\,\text{mm}$) before and behind the focal point with pre-compensation of lens center material up to third order. The dotted curve represents the transform-limited pulse shape in the entrance pupil.

pulse spectrum is less then the focal depth ($2L_{D,0}$) [T3], and applying that the product of the transform-limited duration T_{FWHM} and the corresponding bandwidth for a Gaussian pulse equals 4ln(2) (see Appendix A.1).

It can be seen from (3.47) and (3.48) that, to fulfill both requirements for a given focusing lens, the decrease of the beam size is the solution. For spherical aberration, the benefit from smaller beam is directly visible from (3.47). In the case of chromatic aberration, the focal length variation with frequency and the central wavelength is determined by the focal element and the pulsed source, respectively, so the only option is to increase the focal depth $L_{D,0}$, so γ_p can be made smaller and condition (3.48) can be met. This is also achieved by beam-size decrease.

Figure 3.13 depicts a case when the above conditions, (3.47) and (3.48), are met for both the chromatic and spherical aberrations with the same lens as in Figure 3.12. In Figure 3.13(a) the on-axis pulse shapes in the focal point with the pre-compensated and the uncompensated slab dispersion are compared, obtained using the "accurate" focusing model. In this case it can be seen that the transform-limited duration can be fully retained simply by the pre-compensation of lens center material. Compared to the situation of the larger beam size (see Figure 3.12(a)), the temporal broadening is symmetrical, as neither chromatic nor spherical aberration play an important role, and the dominant dispersion term is GDD. There is only a slight temporal shift due to chromatic aberration, but a transform-limited shape (black dotted curve) is achieved in the focal point.

Figure 3.13(b) shows the on-axis pulse shapes at one Rayleigh length distance from the focal point, both behind and before the focus. With the calculations for all points in between $Z_0 = -L_{D,0}$ and $Z_0 = +L_{D,0}$ (not depicted here), this verifies that focusing to transform-limited pulses with lenses is indeed possible, and the envelope shape is preserved in the whole region of the optical axis, which is usually important in the experiments.

It is to be noted that the example presented here, in Figures 3.12 and 3.13, are chosen to be extreme, deliberately. The spherical aberration of the bi-convex lens with aperture size $a_L = 12.5\,\mathrm{mm}$ is very big, in the order of $\mu_{040} \approx 15$, which varies heavily with wavelength. Bi-convex lenses with equal radii of curvature for both surfaces are known to suffer from large spherical aberration, and, by choosing lens parameters appropriately, it can be decreased [90]. In the next section, another example is shown where the spherical aberration of the focusing element is much smaller and condition on the maximum beam size are considerably less strict.

The two examples of this section showed that focusing of few-cycle pulses is possible with lenses without (or with only small) distortion of the pulse shape, if the material dispersion of the central part of the lens (or lens system) is compensated up to third order dispersion. If the small increase in pulse duration is not an issue, not fully compensating the chirp of the material dispersion can be a tool for controlling the temporal variation of the electric field in the focal region, which is discussed in the next section.

3.2.3 Tailoring the propagation-induced CEP variation of focused, pulsed Gaussian beams

Since the CEP changes shot-to-shot in several laser systems, the primary issue of undistorted pulse generation is the shape of the envelope. This was discussed in the previous section, so a method was described to make the focused pulse retain its envelope-shape while it propagates through the focal region.

It was shown earlier that the temporal shape of the few-cycle pulse can be sustained upon focusing, even on the electric field level for some segments of the focal region simply by using dispersive material [210]. However, the solution provided there is only applicable in cases when the desired focal depth is in the order of micrometer. So for high-field sciences, where much bigger Rayleigh lengths are general, other approach is necessary to achieve a same result. Fortunately, the chromatic aberration of lenses results in the same effect as the one shown in [210]. If the requirements on the chromatic and other aberrations discussed in the previous section are fulfilled and the pre-compensation of the on-axis dispersion of the lens material is assumed (see main steps of the calculation developed by M. A. Porras in Appendix E.2), the CEP change on-axis can be derived based on the first-order propagation theory given in Section 2.3.4. According to these

results, the on-axis CEP change of a pulsed Gaussian beam with Gaussian temporal envelope during propagation through focus can be given by

$$\Delta\varphi_{\mathrm{CEP}}(Z_0) = -\mathrm{atan}\,(\xi) + g_C\frac{\xi}{1+\xi^2} + \gamma_C\frac{\xi^2}{1+\xi^2}\,. \tag{3.49}$$

The CEP of this expression is interpreted following the definition used in this work, given in Section 2.2.2 (on page 19). The change of the CEP in (3.49) should be understood as a relative change with respect to the CEP value in the geometrical focus of the carrier wave. As the "absolute" value of the phase may change shot-to-shot, it is logical to examine relative values. In the previous expression

$$\xi = \frac{Z_0}{L_{D,0}} \tag{3.50}$$

is the dimensionless axial coordinate measured from the geometrical focal point of the carrier frequency (normalized using the focused Rayleigh length $L_{D,0}$ in the Debye approximation, see (B.12)), and

$$g_C = g_p - \frac{2C}{T^2_{\mathrm{G,min}}}\gamma_p, \tag{3.51}$$

$$\gamma_C = \gamma_p + \frac{2C}{T^2_{\mathrm{G,min}}}g_p \tag{3.52}$$

are introduced for brevity. The relevant parameters are

$$g_p = -\frac{L'_{D,0}}{L_{D,0}}\omega_0 \tag{3.53}$$

describing the wavelength dependence of the focused Rayleigh length, and

$$\gamma_p = \frac{f'_0}{L_{D,0}}\omega_0 \tag{3.54}$$

typifying chromatic aberration (introduced also in previous section about undistorted focusing with lenses). The remaining, not explained quantities of (3.51) and (3.52) are the "spectral chirp" C[VI] and the minimal (transform-limited) Gaussian duration of the pulse $T_{\mathrm{G,min}}$ (related to the transform-limited FWHM duration by $T_{\mathrm{FWHM}} = T_{\mathrm{G,min}}\sqrt{2\ln(2)}$). The (3.49) form of CEP change is only valid for Gaussian pulses with linear chirp. This chirp comes from, for example, the not full compensation of the lens's dispersion, so the

[VI] The parameter C is a second-order phase derivative, so it is the same in dimensions as the GDD of Section 2.2.1. It is referred to as "spectral chirp", or shortly as chirp in the following, because it causes a linear chirp in time domain, as discussed earlier.

input complex spectrum in the numerical evaluation of the focused field by (E.1) is

$$\tilde{U}(\omega) = p(\omega)\exp\left[-\iota\frac{\mathrm{GDD}-C}{2}(\omega-\omega_0)^2 - -\iota\frac{\mathrm{TOD}}{6}(\omega-\omega_0)^3\right], \tag{3.55}$$

different from the spectrum (3.46) of the previous section.

If higher order phase derivatives are present than the second, analytical expression for the CEP is not possible to obtain. Even though the pulse shape can be evaluated analytically (see Appendix A.1), due to the appearance of complex special functions, the pulse peak can not be determined (see (A.24) and the derivation in Appendix E.2.2).

Formula (3.49) has the advantage that it gives a simple analytical expression to analyze the variation of the CEP on-axis. Furthermore, if the chirp of the pulse is taken to be zero ($C = 0\,\mathrm{fs}^2$), then the resulted expression is valid for every pulse shape and every beam profile as long as the on-axis spatial phase of the beam is determined by the Gouy phase shift and the pulse envelope is not changing during propagation (see details in Appendix E.2.1). The former, the generality of the Gouy anomaly for every beam, has been established by several means (as mentioned in the theoretical overview of this work) [138, 211, 212]. This gives a general applicability to the expression derived, irrespective of the shape of the pulse envelope and regardless of pulse duration as long as the pulse envelope does not change during propagation.

Note that similar quantities to that of g_p and γ_p ((3.53) and (3.54), respectively) have been introduced previously in Section 3.1.1, while discussing results on phase and group velocity changes (see g_v of (3.8) and γ_v of (3.9)). Two parameters of the present section, g_p and γ_p, can only be interpreted if an ideal Gaussian beam is focused and the Debye approximation is valid, so no monochromatic aberration or truncation of the beam is present. If these conditions are met and the pulsed beam is focused at its waist — as assumed in this section —, the correspondence between the dimensionless parameters of this and the previous section are

$$g_p = 2\gamma_v + g_v \approx g_v\,, \tag{3.56}$$

$$\gamma_p = -\gamma_v\frac{\omega_0 s^2}{2cf_0}\,. \tag{3.57}$$

In Figure 3.14 on-axis CEP variations of various pulsed beams are plotted focused by two different focusing system (in Figure 3.14(a) an idealistic focusing element and in Figure 3.14(b) a mirror-lens system).

Figure 3.14(a) depicts CEP variations of an unchirped pulse ($C = 0\,\mathrm{fs}^2$), and shows how the two parameters — g_p giving the beam size variation with wavelength and γ_v characterizing the chromatic aberration — modify the on-axis phase changes. According

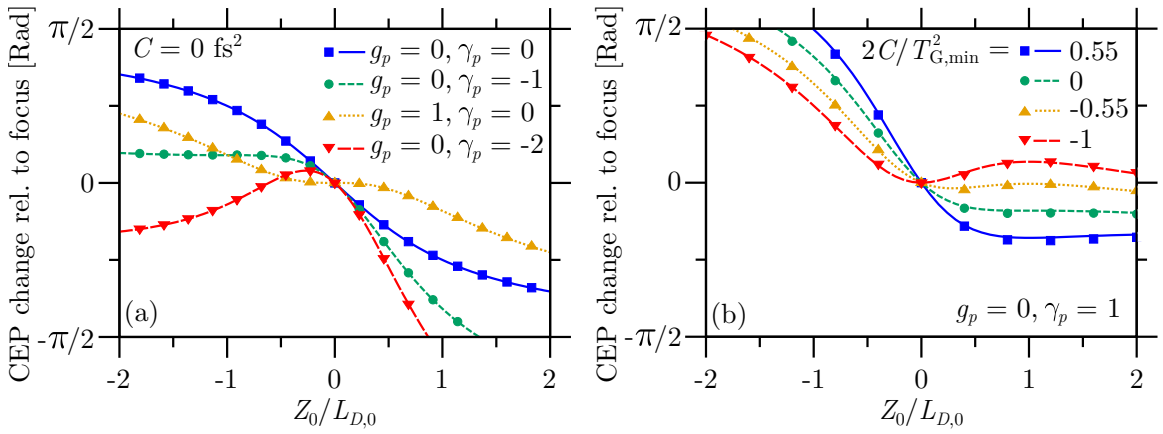

Figure 3.14. (a) On-axis CEP variation of a transform-limited pulse ($C = 0\,\mathrm{fs}^2$) propagating through focus. The curves correspond to different amount of chromatic aberration (γ_p) and different wavelength dependence of beam-waist size (g_p). The curves show the result of the analytical expression (3.49) and the points are the results obtained using the findings of Section 3.1 on the group delay. In the simulations a beam with $s_0 = 3.2\,\mathrm{mm}$ waist radius is assumed to be focused with a lens of $f_0 = 100\,\mathrm{mm}$ focal length and $a_L = 15\,\mathrm{mm}$ aperture radius. The resulted Rayleigh length of the focused beam is $L_{D,0} = 250\,\mu\mathrm{m}$. (b) On-axis CEP variation of a chirped Gaussian pulse focused by a mirror-lens system for different amounts of chirp C. The curves represent the results of (3.49) while the points show the result of the precise model described in a previous subsection (see Section 3.2.1). The input beam with $s = 10\,\mathrm{mm}$ waist radius is focused with the mirror-lens system having a total back focal length of $f_0 = 990\,\mathrm{mm}$, resulting in a focused Rayleigh length of $L_{D,0} = 2.5\,\mathrm{mm}$. The system is formed by an $f_M = 877\,\mathrm{mm}$ focal length mirror and a CaF_2 lens with $f_L = -7632\,\mathrm{mm}$ both with aperture radii $a_L = 40\,\mathrm{mm}$ [T4].

to (3.49), in the $g_p = 0, \gamma_p = 0$ case the CEP changes following the Gouy phase shift. This is easy understand from the results of Section 3.1.1, which highlighted that in this case the group velocity is constant on-axis, while the phase itself changes according to Gouy's phase, so the CEP has to follow the same course. Form the other curves a particularly interesting case is the one obtained using (3.49) with $g_p = 0$ and $\gamma_p = -1$, because it shows that the CEP has a constant value along a big part of the half focal depth before the focal point. This means that in this region the pulse retains its shape on the electric-field level during propagation with an unchanging pulse envelope. As the $g_p = 0$ value means an isodiffracting beam —being a natural mode of laser oscillators [197] —, this can be obtained by proper choose of the focusing element giving a small chromatic aberration yielding $\gamma_p = -1$.

The symbols of 3.14(a) are the results of CEP simulation using the results of Section 3.1, according to the followings. In agreement with the definition of CEP, its value can be given by calculating the phase of the carrier wave at the given spatial coordinate, then taking into account that the peak of the wave packet is possibly delayed with respect to the carrier. If the peak is only shifted due to group delay, so there is no reshaping of the

envelope, then

$$\begin{aligned}\varphi_{\mathrm{CEP}}(\mathbf{r}) &= \varphi_G(\mathbf{r},\omega_0) - \omega_0 \left.\frac{\partial\varphi_G(\mathbf{r},\omega)}{\partial\omega}\right|_{\omega=\omega_0} \\ &= -\frac{\pi}{2} - \gamma_v\omega_0\frac{f_0}{c} + \arg\left[\tilde{\mathcal{I}}(u,v,\psi)\right] - \omega_0 \left.\frac{\partial\varphi_{\mathcal{I}}}{\partial\omega}\right|_{\omega=\omega_0},\end{aligned} \tag{3.58}$$

where (D.14) and (D.30) have been used for the phase and its derivative, respectively, and it has been applied that $R = f$ and $w = s$. When no aberrations are present and only on-axis points are in question, (3.2) can be used for the phase and (C.15) for its derivative to give the analytical expression

$$\varphi_{\mathrm{CEP}}(Z_0) = -\frac{\pi}{2} - \gamma_v\omega_0\frac{f_0}{c} - \mathrm{atan}[\omega_0\mathcal{T}_0] + \omega_0\frac{\mathcal{T}_0 + \omega_0\mathcal{T}_0'}{1+\omega_0^2\mathcal{T}_0^2}, \tag{3.59}$$

where (3.3) and (C.17) are taken at ω_0 to yield $\mathcal{T}_0 = s_0^2 Z_0/\left[2cf_0(Z_0+f_0)\right]$ and $\mathcal{T}_0' = (g_v-1)\mathcal{T}_0/\omega_0 + \gamma_v s_0/(\omega_0 2cf_0)$, respectively. Note that the results of the CEP expressions (3.58) and (3.59) differ from the that of (3.49) by a constant, because they are relative phases with respect to an other reference point (this is the reason for the different notation, $\Delta\varphi_{\mathrm{CEP}}$ against φ_{CEP}). For the relative changes it is enough to evaluate the last two terms of (3.58) and (3.59), as the first two ones are only constants.

In Figure 3.14(b) the effect of pulse chirp can be seen for an isodiffracting beam focused by a mirror-lens system with a total chromatic aberration yielding $\gamma_p = 1$. This value of γ_p gives a constant CEP in the second half of the focus (see $C = 0$ case in Figure 3.14(b)). By assuming that the on-axis dispersion of the lens of the focusing system is not fully compensated, and there is a small residual chirp C, the CEP variation can be further tailored, and it can be reached that the region with constant CEP extends to the focal point. For this the $2C/T_{\mathrm{G,min}}^2 = 0.55$ condition is necessary, as it can be seen in the corresponding curve of Figure 3.14(b). The additional symbols of Figure 3.14(b) are simulation results of the accurate focusing model described in Section 3.2.1, and the CEP extracted following the definition of Section 2.2.2 (phase of the carrier at envelope peak). The numerical model was necessary because (3.58) and (3.59) can not predict properly the CEP change in this case. This is caused by the fact that the phase-, group velocity and group delay calculations of Section 3.1 are based purely on the wavelength-dependent phase of the pulsed beam. However, there is also a spectral amplitude reshaping during focusing [164, 213], which can modify the temporal envelope (this spectral reshaping is relevant also in the explanation of an other effect detailed in this work, see later Section 3.4). In the case of a Gaussian pulse with chirp, for example, the reshaping is a temporal shift of the peak (see Appendix E.2.2). This causes a change in the CEP. So the chirp of

the pulse gives an additional degree of freedom in the control of on-axis CEP changes.

Figure 3.15 depicts the pulse shapes in the focal region of the mirror-lens system described in the caption of Figure 3.14(b). The pulse shapes are a result of the numerical simulation described in Section 3.2.1. It can be seen that the small residual chirp resulting from the not full compensation of the lens-material GDD causes only a very small broadening of the pulse compared to the transform limit (see black dotted curve). This broadened duration subsists in the whole focal region. Together with the negligible change of the CEP in the second half of the focal region, this means identical temporal variation of the electric field on axis in every point from $Z_0 = 0$ to $Z_0 = L_{D,0}$. The two pulse shapes of Figure 3.15 verifies the possibility of undistorted focusing of pulses with controlled CEP variation during propagation through the focal region, which can even yield unchanged temporal shape at the electric field level.

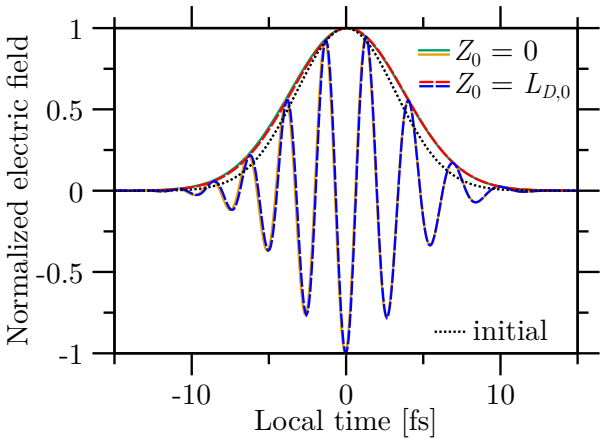

Figure 3.15. Pulse shapes in the focal point and one Rayleigh length behind the focal point for the focusing system described in Figure 3.14(b) for the $2C/T_{\mathrm{G,min}}^2 = 0.55$ case. The dotted black curve shows the transform-limited shape of the input pulse. The $Z_0 = L_{D,0}$ case has been shifted in time by -0.38 fs to better highlight the identity of the temporal variation of the electric field.

Summary II. *I developed an accurate model of focusing with lenses and lens systems based on ray tracing calculations and scalar diffraction theory. I used this model to verify numerically that it is possible to focus few-cycle pulses with refractive optics without relevant distortion of the pulse envelope by simply compensating for the material dispersion of a dielectric slab corresponding to the phase-modifying properties of the focusing system on axis. I also confirmed the validity of an analytical model describing the on-axis CEP variation of focused, pulsed Gaussian beams. Based on the above two findings, I showed that focused, few-cycle pulses can propagate in the focal region of lenses with unmodified temporal shape at the electric field level* [T2–T4].

3.3 Measuring the carrier-envelope phase variations of focused pulses

While the theoretical considerations of the previous section suggest a good possibility for using lenses (or lens systems) to focus few-cycle pulses, the experimental verification of the

simulation results is an important step in justifying its applicability. In the following, the outcome of an experimental campaign is summarized, which aimed to measure both the pulse shape and the CEP-changes of a focused pulses in the focal region of an achromatic lens using spectrally-resolved interferometry.

The key factor of both the undistorted pulse shape and the control of the CEP variation is the γ_p parameter. As it was shown previously (see (3.54)), its value is defined by the chromatic aberration of the lens and the Rayleigh length of the focused beam. Both are affected by the material and the geometrical parameters of the lens. So a predefined CEP-variation curve can be reached with a lens designed for a specific application [T3]. As the aim of this measurement series was to experimentally verify the theoretical findings, so there was no planned utilization of the measured setup, the chosen focusing element is a commercially available one. Using an achromatic lens was needed to have small chromatic aberration that does not lengthen the duration of the pulse.

In the following, firstly, the measurement of the CEP changes on axis is presented. The second part of this section deals with the simulation of the experimental case and the necessary auxiliary measurements of wavelength-dependent beam properties serving as an input for the calculations.

3.3.1 Carrier-envelope phase-shift measurement using spectral interferometry

The basic idea of the CEP-change measurement comes from the usage of spectral interferometry for CEP-drift determination [186, 187]. The CEP drift means here the shot-to-shot changes of the CEP in a series of pulses, and not called CEO phase because it might contain additional phase slippages not traditionally called CEO phase (for example originating from an amplifier [214]). In that case the Mach–Zehnder interferometer is built in a way that the pulse entering the setup interferes with the subsequent pulses from the pulse train, because the length of one arm introduces a delay that matches the delay between the pulses in the train. So the reference for the phase measurement is the preceding pulse, giving the relative, shot-to-shot phase changes.

As SI alone is only capable to measure “relative” phases. To obtain information on variations induced by a specific physical phenomena, a stable reference is needed. In order to measure the propagation-induced phase changes a wave is needed that serves as a spatially constant reference. This spatially-stable reference can be, for example, a collimated beam when the CEP changes of a focused beam is the question. The schematic drawing of experimental setup that was implemented for the CEP-variation measurement of focused pulses, and that uses a collimated beam as a reference can be seen in Figure 3.16.

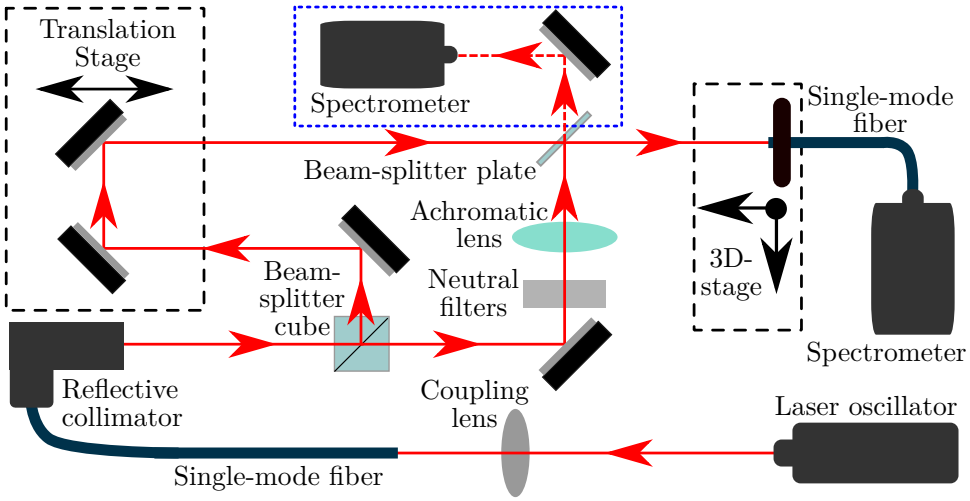

Figure 3.16. The experimental setup used for measuring the on-axis CEP-change in the the focal region of an achromatic doublet lens. The parts surrounded with black dashed rectangles are placed on translation stages (one- or three-dimensional). The additional spectrometer and other optical elements in the blue dotted rectangle were used only for preliminary measurements.

The laser light source providing the short pulses (or huge-bandwidth radiation) was a commercial femtosecond laser oscillator (Femtolasers Rainbow). The output of this laser was spatially filtered to provide a high-quality Gaussian beam. This filtering was carried out by a 5-meter long single-mode fiber (Thorlabs-Nufern 780-HP). An achromatic, 30-mm focal-length lens (Thorlabs AC254-030-B-ML) was used to couple the laser light into the single-mode fiber. The single-mode property of the fiber was necessary to have single pulses exiting it. The out-coupling was performed by a (reflective) mirror collimator (Thorlabs RC08). According to the data sheet of the collimator appliance, the resulted beam is a high quality Gaussian beam. This was confirmed by the simulations carried out and which are detailed in the next section. With this a broadband, collimated Gaussian beam was available as a source. To be able to make comparisons with the simulations this was a necessary step, as those are developed for Gaussian beams (see Section 3.2.1). Due to the dispersion of the fiber, the pulse was definitely not few-cycle any more, but this does not invalidate conclusions drawn, as explained later.

The interferometric setup was built as follows. The beam exiting from the reflective collimator was sent through a broadband beam splitting cube, guiding the two beams into the two arms of the interferometer. In the reference arm of the interferometer no manipulation of the beam happened, just like in the most cases when Mach–Zehnder-type interferometers are used. The only setting that could be changed was the length of this arm, implemented by mirrors placed on a one-dimensional translation stage, so the delay between the sample and reference pulses could be varied. The sample arm contained a neutral filter series and the achromatic lens, the focal volume of which was the region of

interest. The neutral filters were necessary because without them the focused beam of the sample arm would have had an intensity that is orders of magnitude larger then that of the collimated beam of the reference arm, and in that case the interference of the two beams would not have had enough visibility to make the evaluation possible. The two beams of the interferometer arms were combined with a broadband beam-splitter plate. The setup was built in a way that the focused beam was reflected from the beam-splitter plate and the reference beam passed through it, so distortions due to focusing through a dispersive material could be avoided. Finally, the interference of the beams was spectrally resolved by a spectrometer (Ocean Optics HR-4000) coupled with a single-mode fiber (same type as the one used for spatial filtering, but with 1-meter length). The small size of the fiber core (core radius of 2 µm) made a much higher spatial resolution available than the entrance slit of the spectrometer (10 µm × 200 µm slit size). The end of the fiber was placed on a three-dimensional delay stage making spatial scanning available. The photo of the interferometric setup (the spatial filtering and out-coupling from the fiber is not visible), can be seen in Figure 3.17.

A crucial property of interferometric setups is their stability. When the arm length is long, active stabilization is necessary (like for the CEP-drift measurement of [186, 187]). However, when the interferometric setup is compact, its stability could be good enough to provide reliable data within the error range of other effects. To test the stability of the interferometric setup an additional, fixed-position interferometer was placed at the other output of interferometer (see the spectrometer in blue dotted rectangle on Figures 3.16 and 3.17). This spectrometer was able to provide interferometric data, the recording of which was synchronized to the acquisition of the spectrometer combined with the fiber of movable end. So while the fiber end was moved and interferograms were recorded to provide data on how spatial phase changes, the fixed-position spectrometer could give information on possible phase changes caused by the temporal and mechanical instability of interferometer arms. The measurement software — implemented by the author in LabView — was able to give synchronized data (up to the precision of software and electronics, so in the order of milliseconds), giving

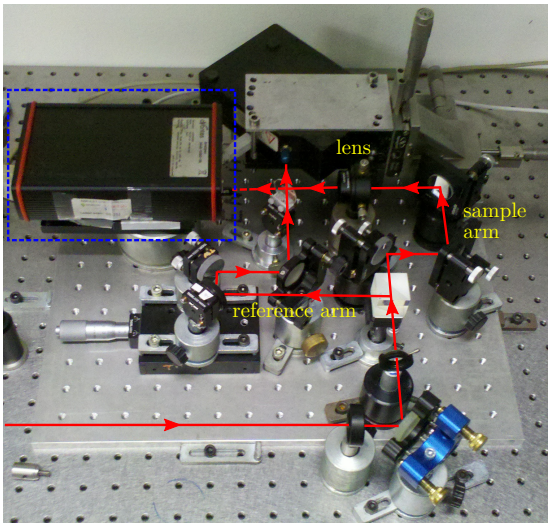

Figure 3.17. The photo of the interferometric setup when off-line with the direction of beam propagation highlighted. The spectrometer in the blue dotted rectangle was used only for preliminary measurements.

the possibility to make corrections to the measured data. However, all measurements carried out this way confirmed that the interferometer is stable enough in order to avoid the errors caused by the temporal variations, or at least they were not above the error range of the measurement given by other factors. So the synchronized measurement with the fixed spectrometer was abandoned later.

It must be highlighted also that the recording of the interferograms were carried out with an integration time that included several laser shots (between 100 and 300 ms integration time with the 75.14 MHz repetition rate of the laser oscillator). This does not cause a misinterpretation of the results either, as the spectral interference is a result of the phase difference between the two arms (this is also why it is not relevant that the pulse is broadened during the spatial filtering). If the arm lengths are temporally stable — which was confirmed by the fixed-position spectrometer — integration of multiple shots together does not alter measurement data. If there were some effects that blurred the phase stability from shot to shot, then it would have appeared as a decrease of fringe visibility in the interferogram as well (this idea, the change of interference visibility, was proposed as a method to measure CEP-drift earlier [185]).

An important thing needing clarification is the phase which is exactly measured in this case and the method to extract the CEP from the data by using FTSI (detailed in Section 2.4.2). The main steps of the CEP evaluation is summarized in the following, and depicted also in Figure 3.18. A question that can immediately rise, when one looks at the experimental setup of Figure 3.16, is the way FTSI can give information on few-cycle pulses if there are dispersive materials in the sample arm (the neutral filters and the lens) while the reference arm is empty. The solution of this is the assumption of dispersion pre-compensation, similarly to the theory in Section 3.2.2. For a more detailed study, let us summarize the phase modifications happening while the beams propagate from the beam splitter cube at the entrance of the interferometer to the point of measurement (see Figure 3.16). Let l_{ref} be the length of the reference arm, l_f distance of the plate combining the two beams at the output of the interferometer and the focal point, and Z_0 is the axial coordinate of the point of interest measured from the focal point (just like in the theoretical discussion). The phase change happening in the reference arm in this case is

$$\varphi_{\mathrm{ref}}(\omega, Z_0) = \frac{\omega}{c}\left[l_{\mathrm{ref}} + l_f + n_{\mathrm{BSP}}(\omega) l_{\mathrm{BSP}} + Z_0\right] , \tag{3.60}$$

with $n_{\mathrm{BSP}}(\omega)$ and l_{BSP} being the refractive index and thickness of the beam-splitting plate that combines the two beams, respectively. In the previous expression it has been assumed that the volume in which the measurement point lie can be described by a cylinder that has a much smaller radius and height than the beam radius and the Rayleigh length of the collimated beam, respectively. This way both the phase shift due to Gouy's phase

and the radial dependence of the phase of a Gaussian beam can be neglected, and the phase change can be described by the kz term of (2.35). Similarly, the phase delay of the sample arm is

$$\varphi_{\mathrm{sam}}(\omega, Z_0, r) = \frac{\omega}{c}\left[l_{\mathrm{free}} + n_{\mathrm{NF}}(\omega) l_{\mathrm{NF}} + n_{\mathrm{lct}}(\omega) l_{\mathrm{lct}}\right] + \varphi_{\mathrm{foc}}(\omega, Z_0, r)\,, \tag{3.61}$$

where l_{free} is all the propagation distance in free-space from the beam-splitter cube to the lens entrance pupil, $n_{\mathrm{NF}}(\omega) l_{\mathrm{NF}}$ is the optical path traveled in the neutral filters, $n_{\mathrm{lct}}(\omega) l_{\mathrm{lct}}$ is the same for the lens central material, and $\varphi_{\mathrm{foc}}(\omega, Z_0, r)$ is the phase change due to focusing (from the reference sphere in the exit pupil of the lens to the point of interest). It is assumed again that the collimated beam up to the lens suffers a phase shift that can be described with the plane-wave phase-term kz, since its Rayleigh length is much bigger than l_{free}[VII]. As it was described in Section 2.4.2, the measured phase is the phase difference of the above two, so one can obtain $\Delta\varphi(\omega, Z_0, r) = \varphi_{\mathrm{sam}}(\omega, Z_0, r) - \varphi_{\mathrm{ref}}(\omega, Z_0)$ using FTSI (see Figure 3.18(a) for an example interferogram and Figure 3.18(b) for a phase difference extracted from it). The question is: how the terms describing focusing-induced phase changes can be extracted from it?

In usual experiments the neutral filters or the beam-splitting plate would not be present. Fortunately, their phase delay $kn_{\mathrm{NF}}(\omega) l_{\mathrm{NF}}$ and $kn_{\mathrm{BSP}}(\omega) l_{\mathrm{BSP}}$ along with that of the lens's central material ($kn_{\mathrm{lct}}(\omega) l_{\mathrm{lct}}$) can be omitted. The reason for the possibility of suppressing these terms will be given later. So the relevant phase difference is

$$\Delta\varphi(\omega, Z_0, r) = \frac{\omega}{c}\left[l_{\mathrm{free}} - (l_{\mathrm{ref}} + l_f + Z_0)\right] + \varphi_{\mathrm{foc}}(\omega, Z_0, r)\,. \tag{3.62}$$

The first term in the previous expression can be made zero by setting properly l_{ref}, so by adjusting the length of the reference arm, and with this adjusting the delay between the sample- and reference pulses. In that case the phase difference is purely the phase difference caused by focusing. Of course, this can not be done experimentally, because the interference fringes would disappear, and the interferogram could not be evaluated. The reference-arm length are usually set in a way that the linear term of the phase difference in ω causes such a modulation of the spectrum that can make precise evaluation possible.

In order to eliminate the linear term (caused by the delay) along with the higher-order terms (introduced by the dispersive material) from $\Delta\varphi(\omega, Z_0, r)$ during evaluation, and get the information on the focusing-induced phase changes, the following was done. A reference measurement point was chosen (for example, the focal point), in which the

[VII] There is, of course, a change in phase with the radial coordinate. However, at given r coordinate the phase change along propagation direction is described by a plane-wave phase, since the Rayleigh length is large. How the radial dependence of phase contributes is only important from the point of focusing, and contained in the term $\varphi_{\mathrm{foc}}(\omega, Z_0, r)$.

$\Delta\varphi(\omega, 0, 0)$ function, obtained using FTSI, was fitted with a third-order polynomial, giving a reference phase $\Delta\varphi_{\mathrm{pol}}(\omega)$. This step is the reason while the effect of the neutral filter, the beam splitter and the lens central material could be omitted previously, as these are independent of Z_0, so subtracting the reference phase removes their impact on the measured phase. The usage of polynomial-phase instead of $\Delta\varphi(\omega, 0, 0)$ validated that the effect of the lens material could be experimentally compensated, and nearly transform-limited pulse shape can be retrieved. This subtraction is equivalent to the experimental case of applying the methods for phase manipulation given also in Section 3.2.2 to reach the shortest possible pulse duration [206, 207]. When the interferograms where measured in different points, all measured $\Delta\varphi(\omega, Z_0, r)$ phases where corrected with the same $\Delta\varphi_{\mathrm{pol}}(\omega)$, giving the corrected phase (see an example in Figure 3.18(c))

$$\Delta\varphi_{\mathrm{corr}}(\omega, Z_0, r) = \Delta\varphi(\omega, Z_0, r) - \Delta\varphi_{\mathrm{pol}}(\omega)\,. \tag{3.63}$$

By measuring the spectrum from the sample arm $I_{\mathrm{sam}}(\omega, Z_0, r)$ (by blocking the reference beam in the interferometer, see an example spectrum in Figure 3.18(d)), the amplitude spectrum is also available, and the pulse shape that would correspond to the theoretical consideration of the previous section is obtained by

$$\tilde{E}_{\mathrm{exp}}(t, Z_0, r) = \mathscr{F}^{-1}\left\{\sqrt{I_{\mathrm{sam}}(\omega, Z_0, r)}\exp[\imath\Delta\varphi_{\mathrm{corr}}(\omega, Z_0, r)]\right\}\,. \tag{3.64}$$

A pulse shape calculated as explained above can be seen in Figure 3.18(e). The CEP of the pulse in a given point is then simply acquired by looking for the moment of the maximum of $|\tilde{E}_{\mathrm{exp}}(t, Z_0, r)|$ and taking the phase $\arg\left[\tilde{E}_{\mathrm{exp}}(t, Z_0, r)\right]$ at that instant.

So during the measurements the interferograms were recorded along with the spectrums of the sample arm at different spatial coordinates in the vicinity of focus. These different spatial points mean measurement series along lines that are parallel to the optical axis, but that lie different distance from it. The CEP change is interpreted as relative change with respect to the measured value in the focal plane. So the resulted plots (see Figure 3.19(a)) are shifted to zero at $Z_0 = 0$, as the interferometric measurement does not provide absolute values, the acquisition was multiple shot and the laser was not CEP stabilized.

An important thing to note is that the spectrometer — used to measure both the sample-arm spectra and the interferograms — did not cover the whole spectral range (approximately 300 nm bandwidth) of the light source. This means that the pulse shape could not be fully retained. However, if the phase changes measured show that there is no relevant modification in the spectral phase that would significantly alter the temporal shape of the pulse, this does not contradict the conclusions. When the envelope is non-

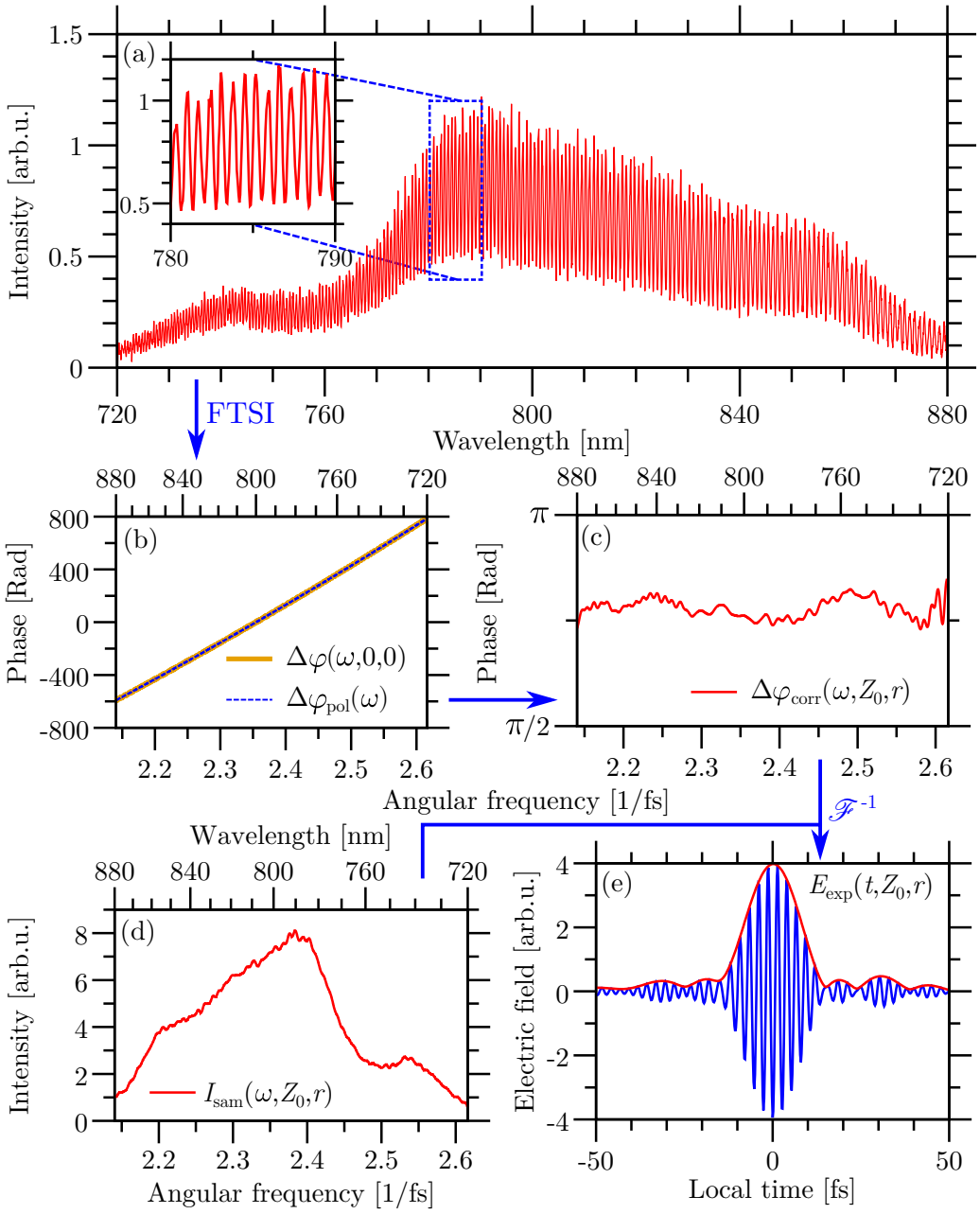

Figure 3.18. The main steps of the method used to obtain CEP from interferometric measurements using the setup of Figure 3.16. (a) A measured interferogram. (b) The phase difference $\Delta\varphi(\omega)$ extracted from the interferogram using Fourier-transform spectral interferometry (see Section 2.4.2) and the polynomial $\Delta\varphi_{\rm pol}(\omega)$ fitted to it. (c) The corrected phase obtained by (3.63) using the result of (b). (d) The measured spectrum of the sample arm. (e) The pulse shape calculated by (3.64) using the spectrum of (d) and the phase of (c).

reshaping in the focal region, the spectral phase fully contains the necessary information on the CEP (see the theoretical discussion of Appendix E.2.1). Also, the last step of the evaluation detailed above (and described also in Figure 3.18) can be skipped, and the CEP can be obtained from the measured phase difference. Just like in CEP-drift

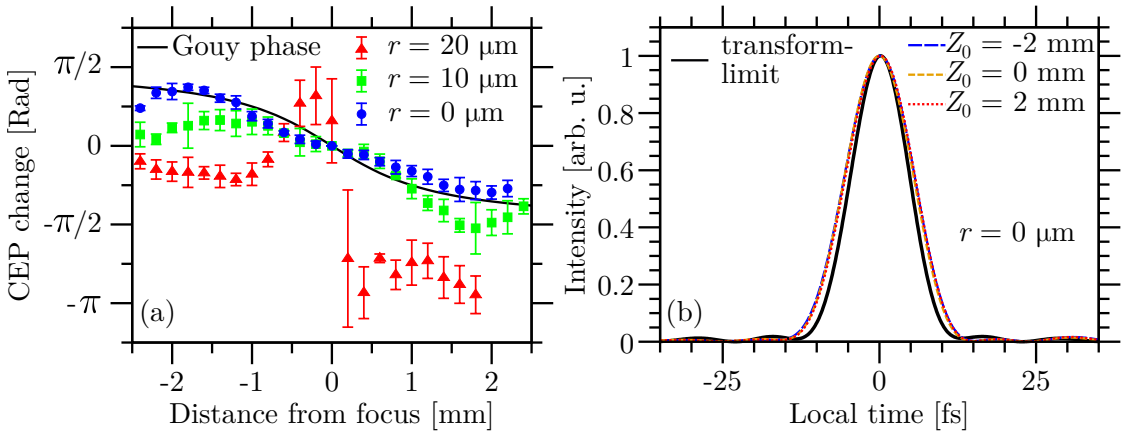

Figure 3.19. (a) CEP-variation measurement results in the vicinity of focus of an achromatic dublet lens (Thorlabs AC254-200-B-ML). The different symbols correspond to the measurement series carried out along lines that are parallel to the optical axis and lie at different distances from the axis. The black continuous curve is the Gouy phase shift for reference. The CEP change is interpreted as change with respect to its value in the focal plane. (b) Pulse shapes on-axis at different distances from the focal point. The shapes correspond to the CEP-results with blue circles in (a). The transform-limited shape corresponds to the inverse Fourier transform of the amplitude spectrum.

measurements [186, 187, 214], by fitting the measured $\Delta\varphi(\omega)$ with a polynomial, the CEP change can be obtained from the zeroth- (φ_0) and first-order (GD) coefficient as $\Delta\varphi_{\mathrm{CEP}} = \varphi_0 - \mathrm{GD}\omega_0$ (see the case with linear spectral phase in Appendix A.1). However, this only gives correct results if the higher order terms of the polynomial and the amplitude spectra are "identical" in every measurement point, so there are no pulse shape changes from one recording to another, just absolute-phase modifications and temporal shifts of the envelope. When there are known changes of the envelope, then the full evaluation method described above is necessary.

Figure 3.19(a) depicts measurement results carried out in the vicinity of focus of a commercial achromatic doublet lens. As mentioned in the introduction of this section, the achromatic property of the lens was necessary to avoid pulse broadening or distortion due to chromatic aberration. The evaluation method of Figure 3.18 confirmed that the pulse envelope in fact does not change relevantly in the focal region (see Figure 3.19(b)). Although it was not necessary, the full evaluation method of Figure 3.18 was used to obtain the data presented in 3.19(a). The simplified evaluation with the first two coefficients of the polynomial fit was also carried out and gave almost identical result to the ones presented. The small differences can originate from the very small envelope reshaping. The full evaluation is considered more precise, as it would given correct CEP values even with a reshaping envelope. The error bars[VIII] of Figure 3.19(a) originate from the repetition of measurement series on different days, and even with full resetting of the

[VIII] All error estimates in this work correspond to 90% confidence interval.

experimental setup. Several of the measurements were done by Dániel Nemes.

The envelope shapes of Figure 3.19(b) justify the applicability of the non-reshaping pulse approximation in real experimental situations (see in Section 3.2.3 and in Appendix E.2.1). The transform-limited pulse shape of Figure 3.19(b) is obtained by inverse Fourier transformation of the measured $I_{\mathrm{sam}}(\omega)$ spectrum using (3.64) with $\Delta\varphi_{\mathrm{corr}}(\omega) \equiv 0$. The broadening of the pulse is related to the non-constant phases measured, and those phases are used for pulse shape evaluation (see Figure 3.18(c)).

The above results show that the simple, linear optical method of SI can provide information on the spatial variation of the CEP in the focus. Similar measurement previously has only been carried out using nonlinear optical phenomena, and they did not make such high spatial resolution available [180, 215]. For this reason, they could not provide information on how the wavelength dependence of beam features could modify the variation of the CEP during the propagation of the pulse through focus, as they integrate the information from a bigger volume that could smear out the exact changes. They could not report on phase variations along the cross section of the beam. The measurement method presented here, however, can give this additional information.

3.3.2 Simulations of the experimentally studied carrier-envelope phase

An important question is the relation of these measured CEP variations to the ones predicted by simulations. Since, according to the theory, these phase changes are affected by the wavelength dependence of beam size and wave-front curvature, these are needed for the simulation, so they have to be measured. This can also lighten how much these aspects alter the phase in real situations, and it is relevant in verifying the theory of Section 3.2.3.

A frequency-resolved measurement of beam size and wave-front curvature can be carried out with different methods [216, 217], some even allowing single-shot characterization of all spatio-spectral (or spatio-temporal) properties [218]. The method used here is a very simple realization with a single spectrometer. The idea is to make wavelength-resolved measurements of beam cross-section at different points along the propagation direction. This is executed by recording spectra in points along lines perpendicular to the optical axis and plotting the radial dependence of intensity for all wavelengths (see example in Figure 3.20(a)). The resulted data points were fitted with Gaussian functions. Then the beam radius could be extracted from the fitting parameters. It can be seen in Figure 3.20(a) that the data measured as such can be fitted very well with Gaussian functions (symbols are the measured data series and the curves are the fitted functions). This verifies the statement of the the manufacturer of the reflective collimator that the appliance

provides a high-quality Gaussian beam.

The initial idea was to repeat these beam cross-section measurements at different distances from the reflective collimator, then — like in an M^2-measurement [107]— the properties of the Gaussian beam (Rayleigh length, beam-waist size and position) can be extracted by fitting the beam-size data as a function of distance from the collimator with a function similar to (2.36). However, it turned out that the beam is so well collimated that, even with meters-long propagation, the beam size does not increase enough that the results become reliable within the error range of the measurement. When the z-dependent beam sizes of different frequencies were fit with the beam-size expression (2.36) of Gaussian beams, and the fit-resulted wave-front curvatures and beam radii were introduced in the simulation of Section 3.2.1 as an input, the CEP-variations were basically different from the measurement results of Figure 3.19(a). So, to have the necessary beam-properties for the simulation (the beam radius and phase-front curvature at the entrance pupil of the lens, as from that point ray tracing and diffraction theory deals with the further propagation of light, see Section 3.2.1), an other approach was needed.

The solution that provided reliable data was more based on simulation. As there was no possibility to directly measure the wavelength-dependent wave fronts (see the complexity of approaches in [216–218]), calculations were carried out based on the beam size measurements. Like in the previous approach, the beam-sizes were determined in various distances from the collimator output. This time these data were compared with simulation results carried out with Zemax OpticsStudio Demo, a commercial beam propagation software. This software gave a simple tool for describing diffraction-based propagation of the beam, since the manufacturer of the collimator provides compatible files with this software for their products. The information from the software is available for both the beam size and the phase-front curvature.

To have proper data using this approach, the following had to be considered. The single-mode fiber used for spatial filtering of the beam, and the output of which is coupled to the reflective collimator, does not guide light with same mode radii for all wavelengths [107, 219]. The mode field radius (the radius of the Gaussian mode propagating in the fiber) can heavily depend on the wavelength. This had to be taken into account in the simulations. The following procedure was followed. The experimentally-deduced beam sizes at different positions were compared with beam radii obtained from beam-propagation software at the same distance from the collimator output, assuming different mode field radii for different wavelengths. This way the frequency dependence of the fiber mode sizes could be determined. The measurements were repeated at several distances from the collimator with two different spectrometers (Ocean Optics HR-4000 and Avantes Avaspec-3648).

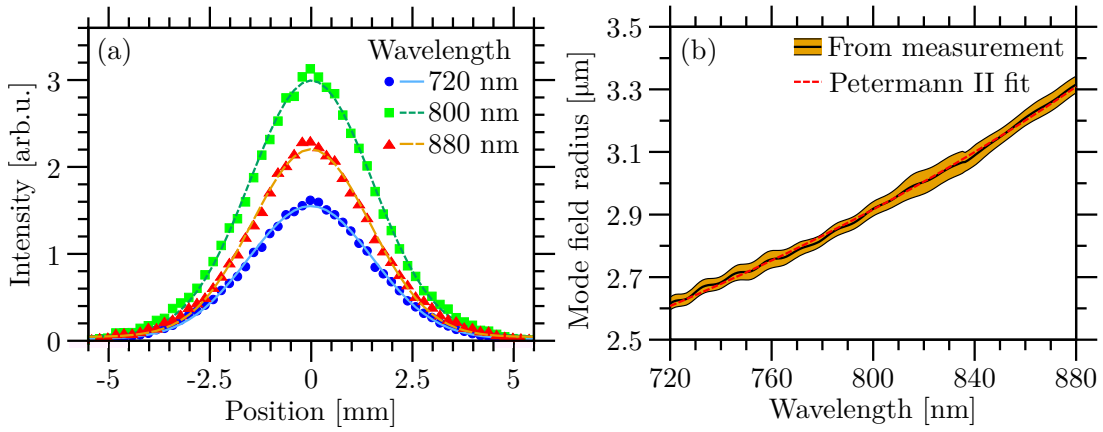

Figure 3.20. (a) Beam cross-section measurements for three different wavelength carried out with a spectrometer. The curves are the fitted Gaussian functions. The data has been vertically scaled for better visibility. The beam radius is obtained by finding the radial distance from center were intensity drops to its $1/e^2$ from its maximum. (b) The wavelength dependence of the mode field radius in the single-mode fiber used for spatial filtering of the beam. The black curve with yellow faded region is the result deduced from beam-size measurement, the faded part showing error estimate. The red dashed curve is obtained by fitting the Petermann II formula (3.65) to the data.

The resulted frequency dependence of the mode field radius in the single-mode fiber can be seen in Figure 3.20(b). The continuous, thick black curve is the result of the above defined method, while the yellow faded region shows the error range.

A question needing answer before stepping forward is whether these values for the size of the propagating modes in the fiber can be correct. There are several analytical formulas for the mode field radius of step-index fibers. One of the reliable ones is the so-called Petermann II formula [107]. According to this, the ratio of the mode field radius w_{MFR} and the radius of the core a_{core} of the step-index fiber can be approximated by

$$\frac{w_{\mathrm{MFR}}}{a_{\mathrm{core}}} \approx 0.634 + \frac{1.619}{V^{3/2}} + \frac{2.879}{V^6} - \frac{1.561}{V^7}\,, \tag{3.65}$$

where $V = (2\pi/\lambda)a_{\mathrm{core}}\mathrm{NA}$ is the V-number of the fiber for the given wavelength, $\mathrm{NA} = \sqrt{n_{\mathrm{core}}^2 - n_{\mathrm{cladding}}^2}$ being the numerical aperture of the fiber [107]. Using the core radius a_{core} and the numerical aperture NA as the fitting parameters, the obtained frequency variation of mode field radius can be perfectly fit with (3.65), as it can be seen in Figure 3.20(b). The result of the fit for the core radius and numerical aperture are $a_{\mathrm{core}} = 2.07\,\mu\mathrm{m}$ and $\mathrm{NA} = 0.11$, respectively, which are very close to the values of $2.2\,\mu\mathrm{m}$ and 0.13 given by the manufacturer. In the wavelength range used, the V-number is in the region where the Petermann II formula is accurate within 1% [107] (V-number is between 1.5 and 2.5, as it is 2.496 for 720 nm and 2.042 for 880 nm). So it can be concluded that the above

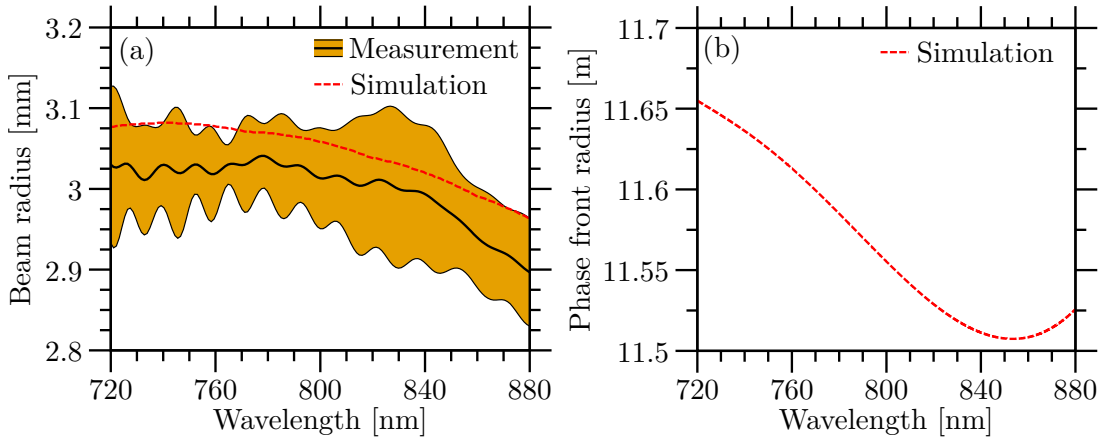

Figure 3.21. (a) The measurement results of wavelength dependence of the beam size at the position of the focusing lens being under study. The continuous black curve is the mean value of the measurements, while the yellow-faded region is the error range. The red dashed curve is the simulation result based on the mode-field radius data obtained previously. (b) The simulated phase-front radius attained on the same basis as the beam size of (a).

method serves as a reliable source for the mode size in the fiber, and the results obtained from the Zemax OpticsStudio Demo should provide information on the beam size and the wave front that correspond to the experimental situation.

Figure 3.21 depicts the wavelength dependence of beam size (Figure 3.21(a)) and wave-front radius (Figure 3.21(b)) retrieved from the Zemax simulation. The beam size was measured at the position of the lens (70 cm from the collimator) with the two spectrometers used also for the previous study. The resulted data can be seen in Figure 3.21(a), with the faded yellow region being the error estimation based on the several measurements carried out with the two spectrometers. The red dashed curve is the one from the Zemax simulation assuming the mode field radius of Figure 3.20(b). While the simulation result does not overlap with the mean values of the measurement, it lies within the error range of the measurement. For wave-front data only simulation data is available in Figure 3.21(b).

With the above data everything is available to use the theoretical considerations of Section 3.2.1 to simulate the CEP of the focused pulse. For the off-axis cases, expression (E.2) can be used instead of the on-axis (E.3). An important thing to consider in the simulations is that while the calculated values correspond to phase values obtainable in a single point in space, the measurement integrates a small surface together, specifically the cross section of the fiber used for probing. If the CEP varies fast spatially in the plane perpendicular to the optical axis, there is a bigger uncertainty in what is the measured value. The simulated CEP variation corresponding to the measurement of Section 3.3.1 can be seen in Figure 3.22. The faded regions around each curve shows the uncertainty originating from the above reason of recording data with the $\sim 4.4\,\mu$m-diameter single-

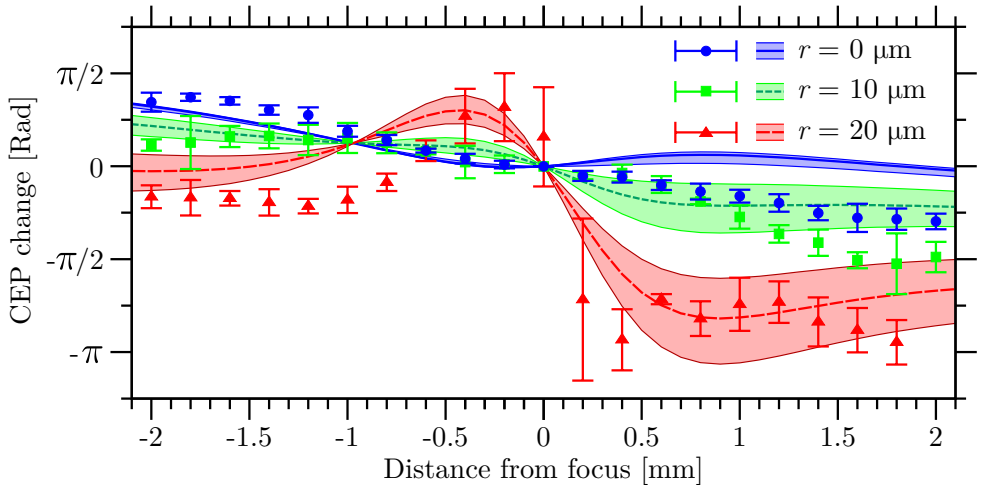

Figure 3.22. The simulation results of the CEP variation along lines parallel to the optical axis but lying at different distances from it. The faded regions show the uncertainty due to the finite size of the fiber. For comparison the measurement results of Figure 3.19(a) are also depicted. The waist radius and Rayleigh length of the beam were $\sim 1\,\text{mm}$ and $\sim 16\,\mu\text{m}$, respectively, based on both the measurement and simulations data of the focused pulsed beam.

mode fiber (as mentioned before in the description of the experimental setup, the same type of fiber was used with the spectrometer as for spatially filtering the beam). For a direct comparison, the measurement results are also highlighted with the same symbols as in Figure 3.19(a).

There are clear differences between the simulation and experimental results, even with the error and uncertainty estimates. The tendencies overall are, however, similar. This qualitative agreement supports that the wavelength-dependent beam properties (beam size and wave-front curvature) in fact have an effect on the phase variations in the focus.

To investigate what causes the difference between calculation and measurement, the following study was performed. One possibility could be that the method describe previously does not give the proper values for the wave fronts (and the beam sizes). To check this, the focusing simulation was modified to serve as a fitting algorithm. The fitting parameters were the wavelength dependence of the beam size and that of the wave-front curvature. The initial values were the ones obtained from Zemax simulation described previously. The algorithm developed tried to minimize the difference between the measured and simulated CEP variations in parallel for all three values of radial distance in Figure 3.22. This fitting simulation, however, could not provide better correspondence between the calculated and measured data then it can be seen in Figure 3.22.

The above suggests that it is not the inaccuracy of the beam-size and wave-front curvature data in which the deviation originates. The most probable possibility is that the simulation itself can not describe the case fully properly. The property known with least certainty in this beam description is the real shape of the phase fronts, as those are

not measured directly. The wave fronts are obtained indirectly from beam-size measurement combined with simulation, and it contains the highest possibility of errors. In the simulation, the wave fronts reaching the lens are assumed to be spherical. Even if the collimator provides a high quality beam, it is very probable that the wave fronts emerging from it are not perfectly spherical. Also, aberrations that are not cylindrically symmetric might be present in the beam due to the misalignment of the lens or other optics. With a method that can measure wave fronts in a frequency-resolved manner [216–218], and with a simulation that can provide focused field features even without the assumption of cylindrical symmetry, more cases could be described with better correspondence to experimental results. The first could help in the presented simulations results of this work as well to better match experimental data, which already supports the theory it is aimed to verify.

Summary III. *I designed and built an experimental setup which is capable of measuring the spatial phase changes of pulsed beams with high spatial resolution. This setup was used to deduce experimental information on the carrier-envelope phase variations of few-cycle pulses in the focal region of an achromatic lens. I carried out wavelength-resolved measurement of properties of the source beam that was focused, and the phase changes of which were examined. With the measured beam properties I performed numerical simulations on the focused phase variations that correspond to the analyzed experimental case. With the comparison of the simulation and experimental results, I verified the main aspect of the theory, that is, I showed the effect of the wavelength dependence of the focused beam on the carrier-envelope phase changes, and that it results in variations which are different from Gouy phase shift* [T5].

3.4 Modifications in the polarization state of few-cycle pulses during propagation or focusing

As it was detailed in the introduction, tailoring the temporal variation of the polarization state of few-cycle pulses has been introduced recently as a new way of coherent control [64–72]. In the experiments, these polarization-shaped pulses are also focused. However, it was shown that during free-space propagation of beams the instantaneous polarization state can change [115]. These variations are not a consequence of strong focusing [81], of the spatial inhomogeneity of the polarization state across the beam cross section [220], nor of partial coherence or partial polarization of the beam [221, 222]. The changes shown in [115], using the first-order theory of Section 2.3.4, are — as a consequence of the theory used — related to beam diffraction, being more fundamental than the previously listed

reasons for polarization-state modifications.

What is not clarified in [115] is, firstly, the exact physical origin of this effect, and, secondly, if there are some simple rules that can — at least approximately — describe these phenomena. The aim of this section is to answer these questions, give examples that are related to polarization-shaped pulses used in nowadays experiments, and to give simple methods that can bring experimental evidence to these effects.

3.4.1 Propagation of polarization-shaped pulses with particular examples

The polarization state of wave packets can be described by the instantaneous polarization ellipse introduced in Section 2.2.3. One has to be careful, however, as beams generally do not have purely transverse polarization (see introduction of Section 2.3). Still, as it was mentioned in Section 2.3.3 (or in [157, 158]), using paraxial approximation has the advantage that Gaussian beams can still be considered as transverse waves without causing flaws in the conclusions drawn. So, using the same theory as in Section 2.2.3, the vector electric field can be described by two components, either the linearly polarized scalar components x and y, or the left- and right circularly polarized ones. Using this latter two, it can be shown by applying the first-order propagation theory of Section 2.3.4 (see details of the calculation developed by M. A. Porras in Appendix F.1) that the instantaneous orientation of the propagated/focused field relate to that of the initial one in point P (with position vector $\mathbf{r}$) by

$$\Psi^{(p)}(\mathbf{r},\tau) \simeq \Psi^{(i)}(\tau) + \frac{\mathcal{G}_0'(\mathbf{r})}{\mathcal{G}_0(\mathbf{r})} \frac{1}{1-\tan^2[\chi^{(i)}(\tau)]} \frac{\mathrm{d}\tan\left[\chi^{(i)}(\tau)\right]}{\mathrm{d}\tau}\,. \tag{3.66}$$

At the same time, the instantaneous ellipticity can be expressed by

$$\tan\left[\chi^{(p)}(\mathbf{r},\tau)\right] \simeq \tan\left[\chi^{(i)}(\tau)\right] - \frac{\mathcal{G}_0'(\mathbf{r})}{\mathcal{G}_0(\mathbf{r})}\left(1-\tan^2\left[\chi^{(i)}(\tau)\right]\right)\frac{\mathrm{d}\Psi^{(i)}(\tau)}{\mathrm{d}\tau}\,, \tag{3.67}$$

where $\mathcal{G}(\mathbf{r})$ is again the term describing the beam propagation, like (2.41) or (2.45) in the case of Gaussian beams. The method to obtain the orientation $\Psi(\tau)$ and the ellipticity $\chi(\tau)$ from the pulse envelopes and phases for the source and propagated beams can be found in Section 2.2.3. Specifically, if the focal point or the far field[IX] on axis is considered,

[IX] Far field strictly means infinite propagation distance, but for Gaussian beams in practical cases it is enough to consider a propagation distance that is approximately five times the Rayleigh length. Fraunhofer diffraction is the theory dealing with the diffraction in the far field, also providing information of the field distribution in the focal plane [90]. Due to this, the focal plane and the far field can be treated the same way in several aspects.

it can be shown that the change of orientation and ellipticity modifies to [T6]

$$\Psi^{(p)}(\tau) - \Psi^{(i)}(\tau) \simeq \frac{1}{\omega_0} \frac{1}{1 - \tan^2[\chi^{(i)}(\tau)]} \frac{\mathrm{d} \tan\left[\chi^{(i)}(\tau)\right]}{\mathrm{d}\tau}, \tag{3.68}$$

and[X]

$$\tan\left[\chi^{(p)}(\tau)\right] - \tan\left[\chi^{(i)}(\tau)\right] \simeq -\frac{1}{\omega_0} \left(1 - \tan^2\left[\chi^{(i)}(\tau)\right]\right) \frac{\mathrm{d}\Psi^{(i)}(\tau)}{\mathrm{d}\tau}. \tag{3.69}$$

The above expressions are general for all waves, as the $\mathcal{G}_0'/\mathcal{G}_0|_{\text{far field}} = 1/\omega_0$ identity is a general consequence of the wave equation. This can be seen either by using Green functions to solve the focusing problem [223], or it can be obtained from the fact that in the (2.46) mathematical expression of the Huygens–Fresnel principle a $1/\lambda$ term [213] appears. Whatever approach is used, for a general spherical wave $\mathcal{G}(\omega) \sim \omega$, giving the above result. It is to be noted that unique beam properties can modify this behavior obtained for spherical waves, but it is always present. Considerations on this are given in the next few paragraphs.

An important conclusion that can be drawn from (3.66) and (3.67) that a time-varying ellipticity induces a change in the instantaneous orientation during propagation, and vice versa, a time-varying orientation causes a modification of the instantaneous ellipticity. Waves with time-independent polarization state, for example, monochromatic waves do not change their polarization state during propagation or focusing. The question is then, why is there a change in the polarization state of pulsed beams with time-varying polarization?

The answer lies in the effects that can modify the spectral amplitude upon propagation, for example the one shown already for the far field or focal plane. These different diffraction properties of the monochromatic components cause a frequency-dependent scaling of the amplitude spectrum, which causes the modification of the temporal variation of the polarization state (see an example later). This spectrum scaling can be a red shift of the Wolf effect caused by source correlation [224]. It can also be the previously mentioned amplitude scaling, which is simply due to the wave nature, and which causes a blue shift on axis and which turns into red shift far enough from axis. This can also be thought as a kind of Wolf effect [213].

If the pulsed beam have some special properties, it can modify the $\mathcal{G}(\mathbf{r}, \omega) \sim \omega$ correlation. For example, for Gaussian beams it can be shown both for propagation to the far field (see (2.35)) and for focusing into the focal plane (see (B.7)) that $\mathcal{G}_0'/\mathcal{G}_0|_{\text{far field/focal plane}} = g_s/\omega_0$. As (B.7) also corresponds to focusing at waist, g_s is given by (3.11) both for propagation and focusing. This means that in the case of an isodiffracting Gaussian beam

[X] Note that in [T6] and in [T7] the equivalent expressions to (3.69) have a wrong sign.

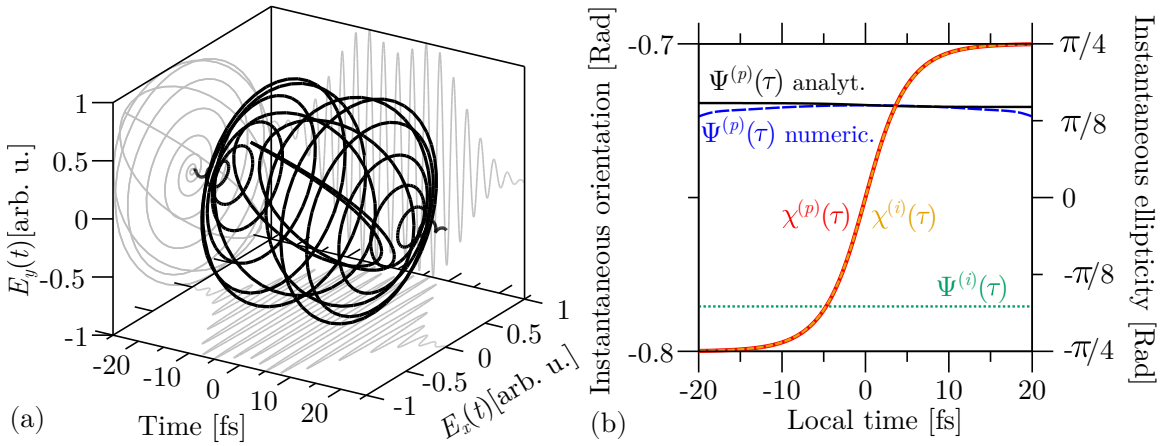

Figure 3.23. (a) The temporal variation of the electric field in an idealistic polarization gating pulse given by (3.70) and (3.71) with $\tilde{E}_{\text{pulse}}(t) = \exp\left[-t^2/T_{\text{G,min}}^2\right] \exp[-\imath\omega_0 t]$. The source pulse is four cycle ($T_{\text{G,min}} = 9.07\,\text{fs}$) and the delay is $\Delta t = 12.68\,\text{fs}$. (b) The time variation of the instantaneous ellipticity and orientation of the pulse in (a) (the properties with superscript (i)) and the same properties when the pulse has propagated to the far field on axis (the properties with superscript (p)).

($g_s = 0$) the effect of size variation cancels out the effect of the Green propagator, and as a results the polarization state is not modified while propagating to the far field or to the focal plane. The case of a Gaussian beam with constant waist size ($g_s = 1$) gives the same result obtained with the more general approaches of Green propagator or Huygens–Fresnel principle [213, 223], not surprisingly.

In the following, two examples are presented which nicely show the properties of the polarization-state variation rules given by (3.66) and (3.67), and also they can highlight the physical reason behind the effect. The first one is the so-called "polarization-gating" pulse used for isolated attosecond pulse generation [39, 41]. This pulse is a particularly good example, because this polarization-shaped pulse has a time-constant orientation and a time-varying ellipticity. If the time variation of the polarization is examined, it is initially circularly polarized, then it gradually turns into a linearly polarized in its middle, most intense part, and finally shifts to circularly polarized in the opposite direction than in the beginning (see Figure 3.23(a) and (b)).

It can be shown, based on a picturesque model of the experimental generation of polarization-gating pulses (sending a source pulse through two quarter-wave plates [39, 41]), that the x and y components of the electric field can be written as (see details in Appendix F.2)

$$\tilde{E}_x^{(i)}(t) = \frac{1}{2}\left[\tilde{E}_{\text{pulse}}\left(t + \frac{\Delta t}{2}\right) + \tilde{E}_{\text{pulse}}\left(t - \frac{\Delta t}{2}\right)\right], \tag{3.70}$$

$$\tilde{E}_y^{(i)}(t) = \frac{\iota}{2}\left[\tilde{E}_{\text{pulse}}\left(t+\frac{\Delta t}{2}\right) - \tilde{E}_{\text{pulse}}\left(t-\frac{\Delta t}{2}\right)\right], \tag{3.71}$$

where $\tilde{E}_{\text{pulse}}(t)$ is giving the pulse shape of the source (for example, in this case $\tilde{E}_{\text{pulse}}(t) = \exp\left[-t^2/T_{\text{G,min}}^2\right]\exp[-\iota\omega_0 t]$), and Δt is a time delay introduced by the wave plates used for generation. In the circular-components representation this is equivalent to two left- and right circularly polarized components of identical pulse shapes but delayed by Δt with respect to each other [T6]. The small pulse chirp and broadening caused by propagating through the birefringent material is neglected in this case. Using expressions (3.66) and (3.67) on the left- and right circularly polarized components, it can be shown that during propagation the instantaneous ellipticity of the polarization-gating Gaussian pulse does not change, while the orientation is subject to a shift that results in $\Psi^{(p)}(\tau) = \Psi^{(i)}(\tau) + (\mathcal{G}_0'/\mathcal{G}_0)(\Delta t/T_{\text{G,min}}^2)$ (see Appendix F.2). This shift is time independent, and in the far field it is equal to

$$\Delta\Psi = \Psi^{(p)} - \Psi^{(i)} = \frac{\Delta t}{\omega_0 T_{\text{G}}^2} \tag{3.72}$$

if a Gaussian pulsed beam with Gaussian temporal envelope and wavelength-independent waist size is assumed. The above means that the polarization-gating pulse with the above beam properties rotates as a whole while it propagates up to the far field or to the focal plane, the latter being the place where it usually interacts with the target.

To check the above predictions and to see the precision of the expressions based on the first-order theory of pulsed-beam propagation can give the propagated field, numerical simulation were also performed. The simulations took the Fourier transform of (3.70) and (3.71) as the spectrum of two independent source electric fields $\tilde{\mathcal{P}}_{x,y}^{(i)}(\omega) = \tilde{U}_{x,y}(\omega) = \mathscr{F}\left\{\tilde{E}_{x,y}^{(i)}(t)\right\}$, then the usual expression of $\tilde{\mathcal{P}}_{x,y}^{(p)}(\mathbf{r},\omega) = \tilde{G}(\mathbf{r},\omega)\tilde{U}_{x,y}(\omega)$ (see (2.58)) was applied to obtain the propagated spectra. Finally, the inverse Fourier transform $\tilde{E}_{x,y}^{(p)}(\mathbf{r},t) = \mathscr{F}^{-1}\left\{\tilde{\mathcal{P}}_{x,y}^{(p)}(\mathbf{r},\omega)\right\}$ (see (2.59)) gave the temporal variation of the electric field for each component. From complex electric fields $\tilde{E}_{x,y}^{(i,p)}(\mathbf{r},t)$ the properties of the instantaneous polarization ellipse was deduced using the expressions of Section 2.2.3. The propagation was calculated using $\tilde{G}(\mathbf{r},\omega)$ given by the ABCD formalism ((2.35) for propagation and (2.45) without Debye approximation for focusing). ABCD formalism was used because the aim was to show the generality of this effect, and not to study the additional polarization-state changes caused by aberrations or further distortions. For this purose, the diffraction theory of focusing can be used ((2.51) or (2.55)).

Figure 3.23(b) compares the on-axis temporal variation of the ellipse properties of the polarization-gating pulse at the source and in the far field. It can be seen that the temporal variation of the instantaneous ellipticity does not change during propagation to the far field, while the orientations is altered. This verifies the proposal of the first-order

theory that the time-variation of ellipticity induces the change of the orientation during propagation. The analytical theory suggests a time-independent shift for the orientation of the polarization-gating pulse (black continuous curve of $\Psi^{(p)}(\tau)$), while the numerical results shows that it is not totally true (blue dashed curve of $\Psi^{(p)}(\tau)$). The analytical orientation shift on axis for the initially transform-limited Gaussian pulse in the specific case of Figure 3.23 gives $\Delta\Psi \approx 0.065\,\mathrm{Rad} = 3.75°$ (see Appendix F.2 for the derivation of the expression). This value is in agreement with the numerical simulation (see Figure 3.23(b)).

An interesting question is the possible modification of the effect when more realistic pulses are considered. The more realistic means here that the pulse chirp is taken into account by assuming a simplified, initial chirped pulse shape given by

$$\tilde{E}_{\mathrm{pulse}}(t) = \exp\left[-\frac{t^2}{T_{\mathrm{G}}^2}\right] \exp\left[-\iota\left(\omega_0 t + \frac{\hat{C}_t}{T_{\mathrm{G}}^2} t^2\right)\right] \tag{3.73}$$

in (3.70) and (3.71). The $\hat{C}_t$ term is a dimensionless temporal chirp. It can bee seen easily that this temporal shape is equal to (A.14) with $\hat{C}_t = \mathrm{GDD}\sigma^2$ and $T_{\mathrm{G}}^2 = 2\Pi^2/\sigma^2$ if the amplitude and the constant phase terms (even the one caused by the GDD) are disregarded. The Gaussian pulse duration nomenclature (T_{G}) is the same as the one used in the analytical CEP-change calculations (see Appendix E.2.2).

Figure 3.24(a) shows the time evolution of the polarization state of the polarization-gating pulse on the Poincaré sphere when a transform-limited source pulse shape is considered and when the source pulse is chirped. The Stokes parameters were calculated using (2.20), (2.21) and (2.22) with $S_0(t) \equiv 1$. The delay Δt has been modified for the chirped pulse so the curves do not overlap on the surface of the sphere[XI]. The two curves for each case show changes in temporal variation of the polarization state when the polarization-gating pulse propagates from the near field to the far field. It can be seen that the temporal chirp causes a linear temporal variation of the orientation (see (F.21) in Appendix F.2). However, this variation is so small that it does not modify the ellipticity relevantly during propagation, which is suggested by the analytical theory. See that the curve of the propagated chirped pulse (black dashed) has the same shape as the initial one (green continuous). The analytical (and numerical) results show that the chirped pulse is subject to the same constant orientation shift as the transform-limited one (see (F.26) in Appendix F.2). In the example of 3.24(a) the amount of rotation is decreased compared to the transform-limited case (3.45° against 3.75°) because of its increased duration due to pulse chirp.

[XI] The modification of Δt is an orientation shift of the initial unchirped pulse as it can be given by $\Psi^{(i)} = \Delta t\omega_0/2$ (see (F.21) in Appendix F.2).

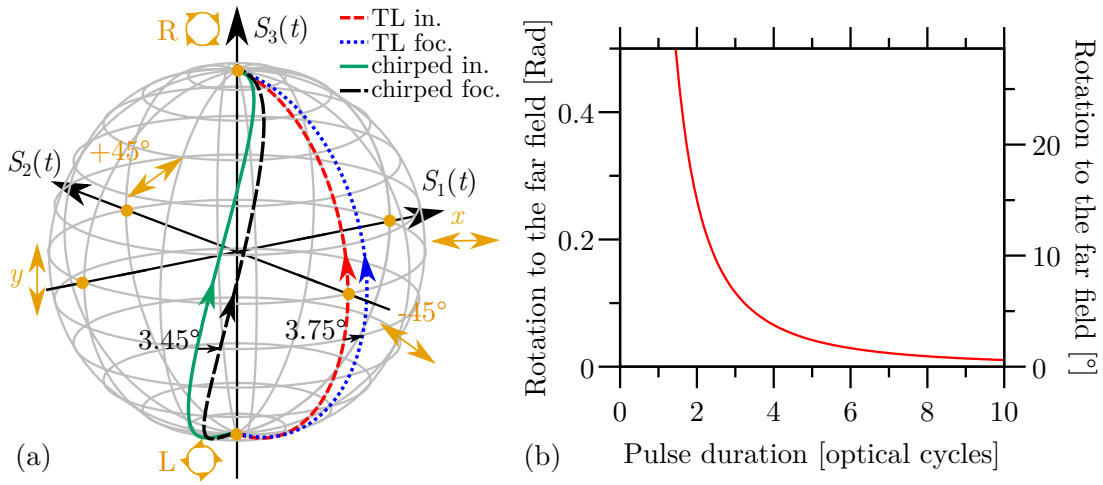

Figure 3.24. (a) The time variation of the instantaneous polarization ellipse of polarization-gating pulse that is generated using a transform-limited Gaussian pulse (TL) and a chirped Gaussian pulse (chirped) depicted on the Poincaré sphere. The two curves for each pulse show how the polarization changes while propagating from the source (in.) to the focal plane (foc.). The arrows on the curves show the direction of time evolution. The TL pulse is the same as in Figure 3.23, while in the chirped case GDD = 10 fs^2 chirp is assumed for the same amplitude spectrum as in the unchirped case (the resulting dimensionless temporal chirp is $C_t = 0.243$). (b) The dependence of the rotation of the polarization-gating pulse on the pulse duration. The time delay is kept constant, the carrier wavelength is $\lambda_0 = 800$ nm (optical cycle is $T_0 = 2.67$ fs) and the pulse duration should be understood as $T_{\mathrm{FWHM}} = T_{\mathrm{G}}\sqrt{2\ln(2)}$.

Figure 3.24(b) shows changes of the rotation of the orientation with pulse duration. While the plot is based on the analytical expression (3.72), the above results for the chirped pulse are the same. The plot of Figure 3.24(b) corresponds to a fixed central frequency and a given Δt delay. This corresponds to a case when the same source and the same experimental setup is used used. So the curve of Figure 3.24(b) can be obtained experimentally with a single source and a simple generation setup, because the pulse duration can be simply tuned by adding chirp to the pulse reaching the system producing the polarization-gating pulse. The chirp of the pulse should not alter the results. More on the possible experimental measurement of the orientation or quantities related to it is given in the next section.

As it is shown by the plot of Figure 3.24(b), or by expression (3.72), and as it was mentioned earlier, monochromatic beams do not change their polarization state (if fully coherent and fully polarized) on free-space propagation [221]. The question that has been raised and needs an answer is the reason behind the changes of the polarization state of a short pulse. To answer this, the spectral polarization state has to be studied. This can be done by Fourier transforming the temporal shapes (3.70) and (3.71), giving

$$\tilde{\mathcal{P}}^{(i)}_{x,y}(\omega) = \mathscr{F}\left\{\tilde{E}^{(i)}_{x,y}(t)\right\} = p_{x,y}(\omega)\exp[\imath\varphi_{x,y}(\omega)] \ . \tag{3.74}$$

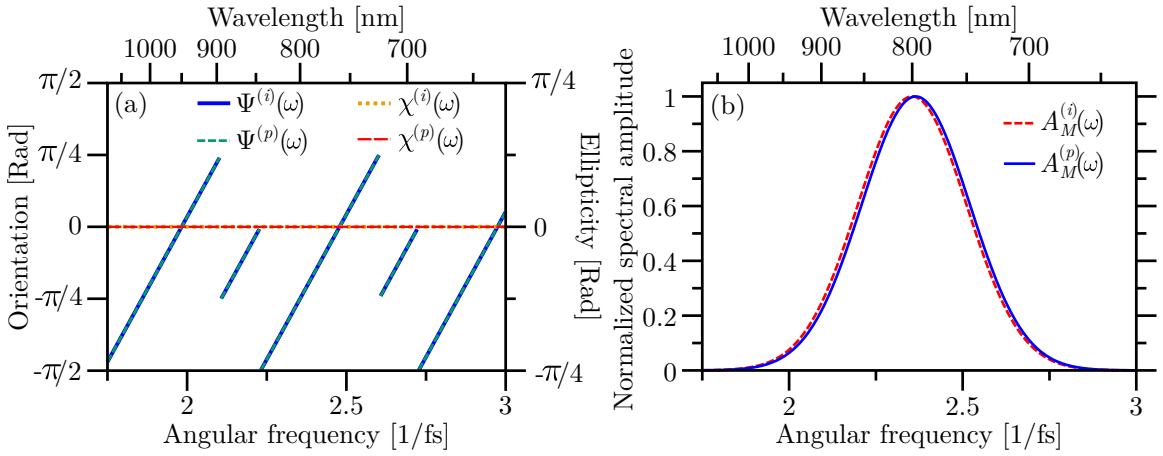

Figure 3.25. The (a) orientation, ellipticity and (b) semi-major axis of the monochromatic components of the polarization-gating pulse of Figure 3.23 in the initial plane and when the pulse is propagated to the far field on axis.

Then the expressions of Section 2.2.3 are to be used with the resulted spectral amplitudes $p_{x,y}(\omega)$ (in the propagated case $p_{x,y}(\omega)\mathcal{G}(\omega)$, see (2.58)) and spectral phases $\varphi_{x,y}(\omega)$ (in the propagated case $\varphi_{x,y}(\omega)+\varphi_{G,(x,y)}(\omega)$, see (2.58)) substituted into the formulas instead of temporal envelopes $A_{x,y}(t)$ and temporal phases $\hat{\varphi}_{x,y}(t)$, respectively. This way the polarization state of each monochromatic component in a polarization shaped pulse can be examined. The results of such a calculation can be seen in Figure 3.25(a) and (b), which correspond to the polarization-gating pulse of Figure 3.23.

It can be deduced from Figure 3.25(a) that, in fact, the polarization of the monochromatic components do not change upon propagation, as they can be represented with a polarization ellipse of the same shape and orientation. In the case of the polarization-gating pulse, the spectral components are linearly polarized with an orientation that depends on wavelength. The reason for the change of instantaneous polarization state is given in Figure 3.25(b), where it can be seen that the size of the semi-major axis bears a spectral modification. As the components are linearly polarized, this is simply the on-axis blue shift of the spectral amplitude. Since the beam-waist size is wavelength independent, the Rayleigh length of bluer components are bigger (see (2.38)), they are less diffracted, meaning that on axis their amplitude is less reduced than the amplitudes of redder components during propagation. This is something not relevant for monochromatic beams, as it is naturally expected that they change their amplitude upon propagation, so it is not considered as a polarization-state change [221]. However, when these infinite waves with modified semi-major axis sizes add up to a short wave packet in the far field, they result in a different time varying polarization state compared to the near-field.

Of course, strictly speaking, the above results are for a Gaussian beam with frequency-

independent waist size and for on-axis propagation. When off-axis points are considered, the spectral shift is different. The caustic defined by the equation $r(z) = w(z)/\sqrt{2}$ (the $w(z)$ beam radius given by (2.36)) are the spatial points where the spectrum is not subject to a shift caused by diffraction [164]. In all points closer to the axis are blue shifted, farther are red shifted [164]. So, experimentally the spectral shift may not be visible in several cases, either because the pulsed beam does not have a wavelength-independent beam size (for example, it is instead isodiffracting, in which case there is no frequency shift in any point), or because the measurement integrates results spatially containing blue- and red-shifted parts at the same time (this point is addressed later). The rotation of the polarization-gating pulse has been checked for other (experimental) pulse shapes, and the non-Gaussian shape of the envelope does not modify relevantly the result, according to simulation.

After the long discussion of the first example verifying (3.66) of the orientation change, a second is given to exemplify (3.67) defining the ellipticity change, separately. The polarization-gating pulse of the previous case was a good example, because, by having a time-independent orientation, it showed that the instantaneous ellipticity is not changed upon propagation. To have a pulse that has a constant ellipticity and a time-varying orientation, the following artificial example is taken. The rotating pulse (similar to that of [72] proposed for CEP measurement) consist of left- and right-circularly polarized components which have a slightly different amplitudes and carrier frequencies (see Appendix F.2), and its linearly polarized components can be written as

$$\tilde{E}_x(t) = \frac{\tilde{E}_{\text{pulse}}(t)}{\sqrt{2}} \left[a_l \text{exp}[-\iota\omega_d t] + a_r\right] , \tag{3.75}$$

$$\tilde{E}_y(t) = \frac{\iota\tilde{E}_{\text{pulse}}(t)}{\sqrt{2}} \left[a_l \text{exp}[-\iota\omega_d t] - a_r\right] . \tag{3.76}$$

In (3.75) and (3.76), $\tilde{E}_{\text{pulse}}(t) = \tilde{\mathcal{E}}(t)\text{exp}[-\iota\omega_0 t]$ is again an arbitrary pulse shape (like for the polarization-gating pulse), a_l and a_r are amplitudes, while $\omega_d \ll \omega_0$ is the slight angular frequency difference between the two circular components. It can be shown that the instantaneous ellipse of the above pulse has a linearly time-varying orientation defined by the frequency deviation according to $\Psi^{(i)}(t) = \omega_d t/2$, while the ellipticity is the $\tan(\chi^{(i)}) = (a_r - a_l)/(a_r + a_l)$ time-independent value (see details of calculation in Appendix F.2). The pulse shape and the temporal variation of the instantaneous ellipse properties can be seen in Figure 3.26(a) and (b).

While this rotating pulse of Figure 3.26(a) is hard to achieve experimentally (if even possible), it gives a perfect way, with its time-independent ellipticity, to check the validity of the first order theory and (3.67). Figure 3.26(b) shows the time variation of ellipticity

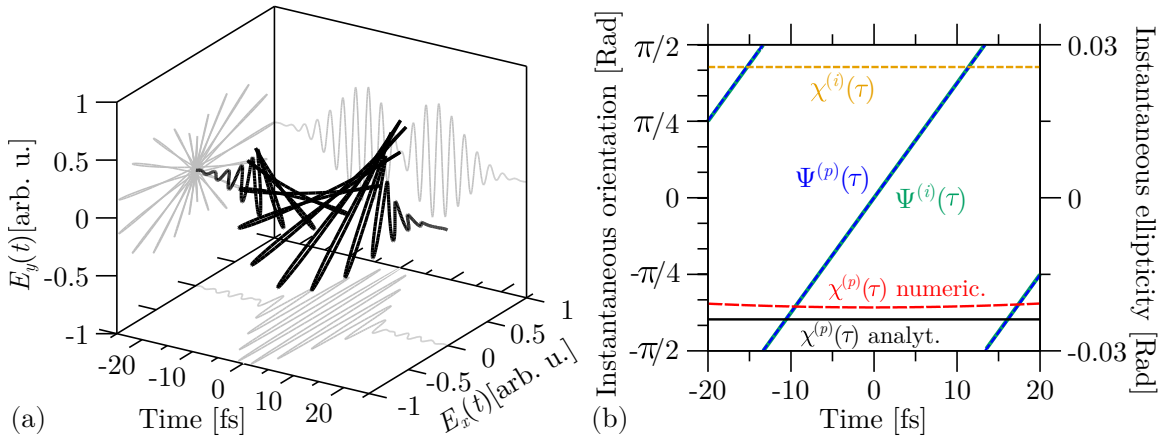

Figure 3.26. (a) The temporal variation of the electric field of a polarization-shaped pulse given by (3.75) and (3.76). The envelope is Gaussian ($A(t) = \exp[-t^2/T_G^2]$) with 5-cycle duration $T_{FWHM} = T_G\sqrt{2\ln(2)} = 13.34\,\text{fs}$. The carrier wavelength is $\lambda_0 = 800\,\text{nm}$. The amplitudes are $a_l = 0.95\,\text{arb.u.}$ and $a_r = 1.0\,\text{arb.u.}$, while the frequency difference is $\omega_d = 0.1\omega_0$. (b) The time variation of the instantaneous ellipticity and orientation of the pulse in (a) (the properties with superscript (i)) and the same properties when the pulse has propagated to the far field on axis (the properties with superscript (p)).

and orientation at the source and at the far field. It can be seen from the numerical results that the orientation does not change upon propagation on axis, as expected from (3.66), while the ellipticity changes due to the rotation of the polarization direction. It is also visible that both the analytical expression (3.67) and the numerical calculation suggests that the pulse changes its instantaneous helicity from right-handed to left-handed. However, the analytical theory can predict the amount of change less precisely than it can do it for the orientation change (see Figure 3.23(b)). This is a consequence of the higher number of approximations used to obtain (3.67) compared to the method used to achieve (3.66) (see Appendix F.1). The numerical results of Figure 3.26 were obtained the same way as for the polarization-gating pulse. In Figure 3.27 the polarization-state variation of this rotating pulse can be seen depicted on the Poincaré sphere.

The Poincaré representations of the polarization-gating and rotating pulses (Figures 3.24(a) and 3.27) show that they serve as two complementary examples to verify the prediction of the first theory given by (3.66) and (3.67). The time evolution of the polarization ellipse of the polarization-gating pulse goes along a line of longitude of the Poincaré sphere, while the same property of the rotating pulse is a line of latitude. The orientation of the polarization-gating pulse and the ellipticity of the rotating pulse determine which line of longitude and which line of latitude of the Poincaré sphere they can be represented by, respectively, and the positions of these grid lines on the surface are those properties, which are changed during propagation.

The numerical results presented in this section confirm the possible polarization-state

changes upon propagation or focusing predicted earlier [115]. Steered by the analytical theory, the simulations also show the pulsed-beam features which are responsible for these phenomena. The numerical simulations are capable of verifying the validity of the analytical expressions and, at the same time, picture the limitations of them [T6].

3.4.2 Measurement of the polarization-state changes by classical methods

The measurement of the instantaneous polarization state is a very laborious task in the optical regime [132, 133]. It would be much favorable if the reported polarization state changes would appear when classical, time-integrating methods for polarization measurements are carried out, for example those that has been discussed in the end of Section 2.2.3. In the case of the polarization-gating pulse the question is the time-integrated measurement method which can detect the orientation of the instantaneous polarization ellipse.

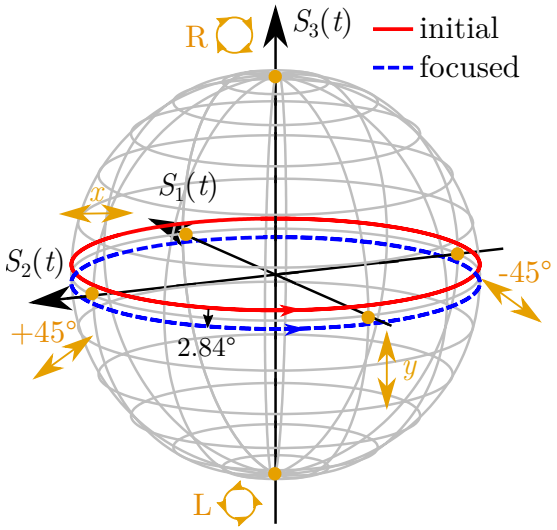

Figure 3.27. The time evolution of the instantaneous polarization state of the initial and propagated rotating pulse of Figure 3.26 represented on the Poincaré sphere.

To examine the orientation of polarization-gating pulse, the following simple experiment was simulated. The important quantity in these calculations is the angle of the polarizer — that the beam tarverses — at which the energy or fluence behind the polarizer is maximal. This angle for a linearly polarized beam is the angle of polarization, and the signal has very high contrast. This can be simulated by substituting the x and y electric-field components into the (2.29) expression of time-integrated intensity (fluence) measurement. By choosing $\epsilon = 0$ in (2.29) and evaluating it at different θ values the results is the same as the experiment with the polarizer explained above.

Figure 3.28(a) depicts the result of such a simulation carried out for the polarization-gating pulse at the source (initial, blue dashed curve) and infinitely far from the source (far field, red dotted curve), in both case on axis. The simulation corresponds to the same pulse as in Figure 3.23, so (3.70) and (3.71) fields were substituted into (2.29) with $\Delta t = 12.68\,\mathrm{fs}$ delay and a Gaussian pulse of $T_{\mathrm{G,min}} = 9.07\,\mathrm{fs}$ duration. By comparing the orientation angles in Figure 3.23 (or the transform-limited pulse of Figure 3.24(a)) with Figure 3.28(a), it can be seen that the direction of polarizer with maximal transmitted fluence coincides with the orientation of the polarization-gating pulse. This is also true

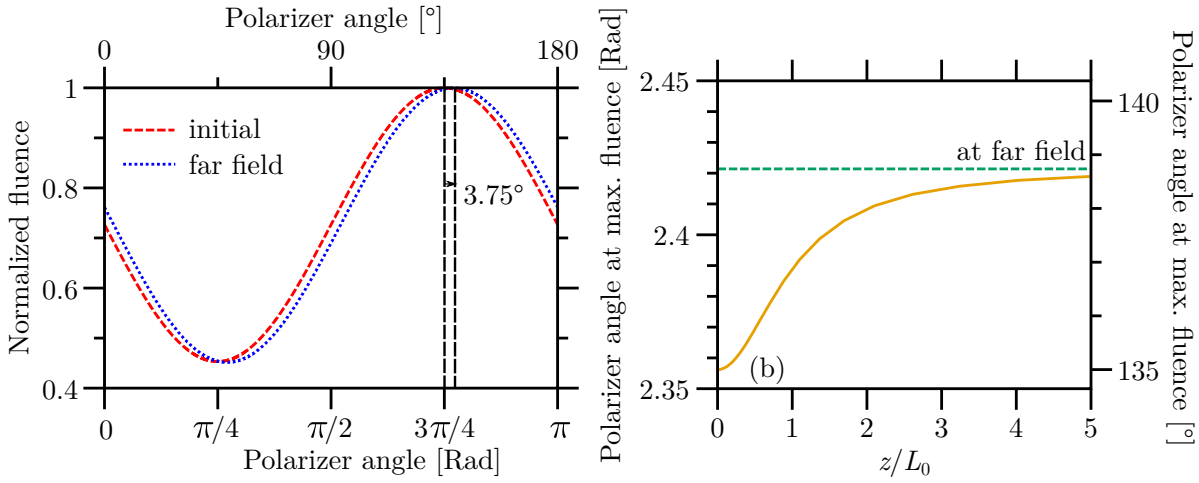

Figure 3.28. (a) Simulated fluence measurement of a polarization-gating pulse behind a polarizer in the near- and the far field on axis as a function of polarizer angle. Zero angle means a polarizer that is parallel to the x axis. The pulse is the same as in Figure 3.23. The vertical dashed lines show the angle of maximum fluence. (b) The polarizer angle that gives the maximum transmitted fluence on axis as a function of distance from the source. The distance is measured in the units of Rayleigh length $L_0 = 9.8\,\mathrm{m}$ (see (2.38)) of the pulsed beam with wavelength-independent beam waist radius $s = 5\,\mathrm{mm}$.

for the chirped polarization-gating pulse (see that case in Figure 3.29(a)).

So, with this fluence (or energy, see later) measurement behind a polarizer, the rotation of the polarization direction of the polarization-gating pulse during propagation can be detected. Figure 3.28(b) shows the polarizer angle which gives the maximum transmitted fluence as function of propagation distance on axis. The results show that, if the source Gaussian beam had a wavelength independent waist size ($g_s = 1$), the polarization-gating pulse generated from a $T_{\mathrm{G,min}} = 9.07\,\mathrm{fs}$ long pulse would rotate approximately 3.75° when propagating 5 Rayleigh length distance. If the pulse was shorter, the rotation would be much bigger (see Figure 3.24(b)).

The example of Figure 3.28 corresponds to a measurement in a single point on axis, which is, of course, practically not realizable. That case only shows that for the polarization-gating pulse the rotation of the instantaneous ellipse can be visualized without a temporally resolved measurement of the electric field or related quantities. This is related to the fact that the whole pulse rotates its orientation during propagation.

To investigate a more realistic case, simulations must take into account that fluence or energy detectors have a finite size, and they integrate data not just temporally, but also spatially. This is important because — as it was mentioned previously — diffraction properties change along the cross section of the beam, and the on-axis blue shift turns into a red shift when the studied point lies farther from axis than $w(z)/\sqrt{2}$. This turns into an orientation change of opposite direction, so spatial integration of detectors might blur

the studied phenomenon. So calculations were carried out where the spatial integration is included. Since the Gaussian beam has a cylindrical symmetry, this means the calculation of integral

$$\mathscr{E} = 2\pi \int_0^{r_{\mathrm{det}}} I_{\mathrm{m}}(r, \theta, \epsilon) r \, \mathrm{d}r \,, \tag{3.77}$$

where $I_{\mathrm{m}}(r, \theta, \epsilon)$ should be understood as in (2.29), but an additional parameter is added, since it depends on the radial coordinate r through the radial dependence of the electric field. Equation (3.77) gives the energy $\mathscr{E}$ measured by a circular detector that has an active surface with radius r_{det}. The input pulse was assumed to be chirped, and focusing is simulated instead of free space propagation. Both the chirp and the focusing is aimed to provide data that are closer to experimental feasibility, as free space propagation would need huge laboratory space, and pulses are usually not truly transform limited. The results of such simulations can be seen in Figure 3.29(a).

The curves of Figure 3.29(a) show that the spatial integration washes out the rotation of polarization direction of the polarization-gating pulse. In the simulation, the focused beam has a waist size of $s_{f,0} = 25\,\mu\mathrm{m}$ and a focused Rayleigh length of $L_{f,0} = 2.55\,\mathrm{mm}$. The source has a frequency-independent beam size ($g_s = 1$). The pulse features are the same as in Figure 3.24, except delay Δt, so it can be seen that a chirped polarization-gating pulse has the same initial and propagated orientation as the unchirped one, and the amount of rotation is determined purely by the pulse duration (compare Figure 3.29(a) with Figure 3.28(b)). It is visible that the relevant change in orientation happens in a two focal depth distance. If the probing of the field happens in a sufficiently small region, for example with a single-mode fiber in this case (like in the experiment of Section 3.3.1), so that the probing is much smaller then the focused spot size, then the effect can be resolved (see green dashed curve of Figure 3.29, which runs really close to the on-axis variation depicted with blue continuous curve). When the measurement happens with a detector that has the same radius as the focused beam, the visibility drops already to the half (yellow dotted curve of Figure 3.29(a)). Bigger surface of sampling results in the almost total disappearance of the signal of this effect (red dashed curve of Figure 3.29(a)). Such experiments are planned to be carried out with few-cycle terahertz pulses in cooperation with colleagues from the University of Pécs.

It is also worth to examine whether the ellipticity reversal of the rotating pulse can also be measured with time-integrating detectors. The simulation of a time-integrated measurement could be carried out following the same recipe as for the polarization-gating pulse, so the x and y components of the electric field of the rotating pulse is substituted into (2.29). The recipe for the polarizer angles θ and the phase shifts of the retarder ϵ are defined by (2.25), (2.26), (2.27) and (2.28), giving the time-integrated Stokes parameters. Then information on the ellipticity can be obtained by (2.31).

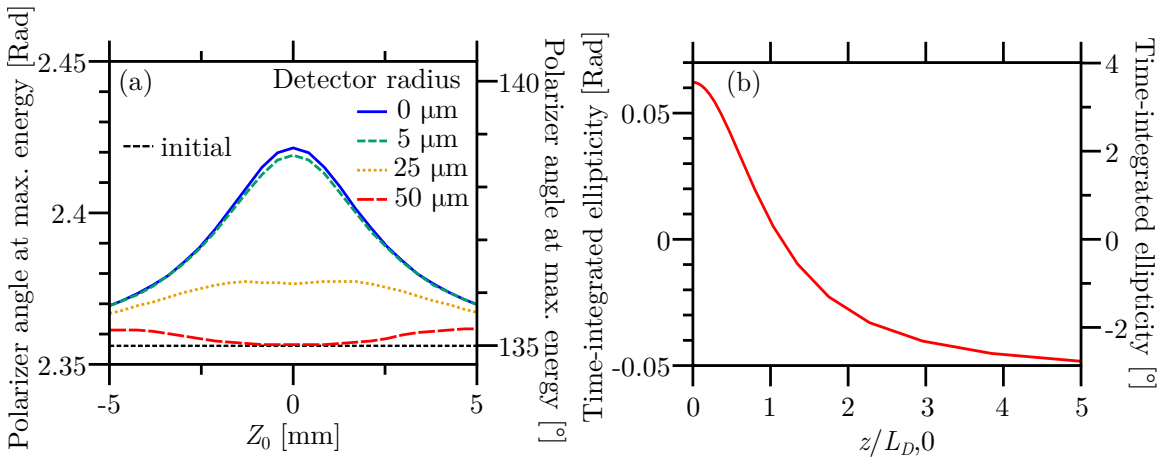

Figure 3.29. (a) The direction of polarizer at maximum energy with different detector radii (r_{det}) for a focused, chirped polarization-gating pulse. The pulse properties are the same as in Figure 3.24 except that $\Delta t = 12.68\,\mathrm{fs}$. An $s = 5\,\mathrm{mm}$ size beam is focused with an $f = 0.5\,\mathrm{m}$ focal length optics, both properties being wavelength independent. The black, dashed horizontal line shows the polarization direction at the source. (b) The on-axis ellipticity of the rotating pulse evaluated with the time-integrated Stokes parameters as a function of propagation distance. The properties of the pulse are the same as in Figure 3.26, while the beam properties are equivalent to that of Figure 3.28(b).

The result of a calculation is depicted in Figure 3.29(b). It can be seen that, even with the time-integrated measurement, the helicity reversal of the rotating pulse appears, and the ellipticity change increases with propagation distance, as expected. By comparing the instantaneous ellipticity of Figure 3.26(b) with the time-integrated one in Figure 3.29(b), it can be seen that the latter ones gives bigger values. So, unlike for the orientation of the polarization-gating pulse, the instantaneous ellipticity of the rotating pulse is not regained with classical measurement. This is because of the rotation of the pulse, which appears as a non-zero ellipticity during the time-integrated measurement. The effect of spatial integration is not studied here, since the pulse itself is already something that is experimentally hard to obtain. Still, a similar blurring effect is expected as for the polarization-gating pulse.

Summary IV. *I verified with numerical calculations the instantaneous polarization state changes of pulsed beams predicted by an analytical propagation theory. By choosing proper examples I also proved the simple polarization-change rule that the temporal variation of one polarization ellipse property (orientation or ellipticity) induces the change in the other property during propagation. With the help of the numerical study it was also highlighted that these propagation-induced changes are the consequences of beam diffraction, and as a result, they are general for all polarization-shaped pulsed beams. I also showed that the signatures of these local changes of instantaneous polarization*

state could be detected with simple experimental setups using spatially and temporally integrating detectors [T6, T7].

Chapter
Four

Summary

In this thesis a study has been presented on the phase and polarization properties of focused, pulsed Gaussian light beams. After a brief motivational introduction, a summary was given on the topics and methods related to, or necessary for, the theoretical and experimental investigations of the above mentioned characteristics of pulsed beams. In the chapter detailing the new scientific achievements of this work, specific attention was drawn to the carrier-envelope phase of few-cycle pulses, but closely related features were also examined. While the discussion of the polarization state takes only a small fraction of this text, the findings related to it might affect an explosively developing field of optical sciences. In short, the most important scientific results can be summarized in the following points:

I. I developed analytical formulas for the on-axis phase velocity and group velocity of focused Gaussian beams which take into account the wavelength-dependent properties of the focused beam. I specified the parameters which determine the changes of group velocity, and I established expressions for the calculation of these focused beam features using the characteristics of the source beam and the focusing system. Based on the previous attainments, I gave the specific conditions only under which the group velocity of a focused Gaussian beam is constant during propagation through the focal region. Using these results I highlighted that a chromatic aberration-like effect can occur not solely due to the focusing element, but also because of beam features.
I presented formulas for the calculation of the phase velocity and the group velocity of focused Gaussian beams when focusing is affected by chromatic and primary monochromatic aberrations. Specific attention is paid to the analytical evaluation of expressions

to increase the precision and to widen the applicability of the numerical simulations. I used these results to analyze the effect of beam truncation, monochromatic aberrations and chromatic aberration on the on-axis phase-velocity and group-velocity variations of pulsed Gaussian beams. I made a comparison between recent and previous results on primary aberrations and their affect on phase properties in the vicinity of focus [T1].

II. I developed an accurate model of focusing with lenses and lens systems based on ray tracing calculations and scalar diffraction theory. I used this model to verify numerically that it is possible to focus few-cycle pulses with refractive optics without relevant distortion of the pulse envelope by simply compensating for the material dispersion of a dielectric slab corresponding to the phase-modifying properties of the focusing system on axis. I also confirmed the validity of an analytical model describing the on-axis CEP variation of focused, pulsed Gaussian beams. Based on the above two findings, I showed that focused, few-cycle pulses can propagate in the focal region of lenses with unmodified temporal shape at the electric field level [T2–T4].

III. I designed and built an experimental setup which is capable of measuring the spatial phase changes of pulsed beams with high spatial resolution. This setup was used to deduce experimental information on the carrier-envelope phase variations of few-cycle pulses in the focal region of an achromatic lens. I carried out wavelength-resolved measurement of properties of the source beam that was focused, and the phase changes of which were examined. With the measured beam properties I performed numerical simulations on the focused phase variations that correspond to the analyzed experimental case. With the comparison of the simulation and experimental results, I verified the main aspect of the theory, that is, I showed the effect of the wavelength dependence of the focused beam on the carrier-envelope phase changes, and that it results in variations which are different from Gouy phase shift [T5].

IV. I verified with numerical calculations the instantaneous polarization state changes of pulsed beams predicted by an analytical propagation theory. By choosing proper examples I also proved the simple polarization-change rule that the temporal variation of one polarization ellipse property (orientation or ellipticity) induces the change in the other property during propagation. With the help of the numerical study it was also highlighted that these propagation-induced changes are the consequences of beam diffraction, and as a result, they are general for all polarization-shaped pulsed beams. I also showed that the signatures of these local changes of instantaneous polarization state could be detected with simple experimental setups using spatially and temporally integrating detectors [T6, T7].

Chapter
Five

Magyar nyelvű összefoglaló

5.1. Bevezetés

A Föld minden lakójának lételeme a nap*fény*, hiszen ez a növények és számos egysejtű — valamint rajtuk keresztül a többi életforma — elsődleges energiaforrása, meghatározza bolygónk klímáját, de emellett szintén a fény az, amely a legtöbb információval szolgál az ember számára környezetéről. Jól mutatja az emberi látás, mint információforrás jelentőségét például, hogy a tizenkét pár agyidegből négy szolgál a szemmel kapcsolatos funkciók ellátására, míg a többi érzéket egy, maximum kettő irányítja[I]. Feltehetően ennek egyik egyszerű oka, hogy számtalan fizikai, kémiai vagy biológiai folyamat, amely a környezetünkben történik, és mindennapjainkat meghatározza, fénykibocsátással vagy éppen fényelnyeléssel jár. Így az evolúció során is nagy hangsúly került az ilyen folyamatokon alapuló érzékelésre. Így lehet az is, hogy a tudományos kutatások egyik legfontosabb „eszköze" a fény, akár direkt, akár indirekt módon. Ahhoz azonban, hogy ezt a „kísérleti eszközt" megfelelően tudjuk használni, kutatási eredményeinket a tudomány által megkövetelt megalapozottsággal tudjuk interpretálni, kellő mértékben ismernünk kell azt.

Egy ilyen „megfelelően ismert" fényforrás került a kutatók kezébe a *lézer* 1960-as megjelenésével. Ez a felfedezés a fény jól kontrollálható módon való felhasználhatóságának lehetőségét nyújtja, és ami így azóta számos tudományág kutatásaiban kapott igen jelentős szerepet. A lézer által előállított fény egyedi tulajdonságai közé tartozik például, hogy megfelelő technológiával és beállításokkal rendkívül rövid elektromágneses hullám-

[I] Lásd például angolul a https://faculty.washington.edu/chudler/cranial.html, vagy akár magyar nyelven a http://tudasbazis.sulinet.hu/hu/termeszettudomanyok/biologia/emberi-test/az-idegrendszer/a-periferias-idegrendszer weboldalakon.

csomagok hozhatók létre. Ez két szempontból is fontos. Egyrészt, a másodperc törtrészéig tartó (napjaink lézereivel a 10^{-15} s nagyságrendbe eső) felvillanás lehetővé teszi nagyon gyors folyamatok vizsgálatát, olyanokét, amelyeket más módon (például elektronikával) nem tudnánk kellő időfelbontással elemezni. Másrészt, mivel az energia rövid időintervallumra korlátozódik, így a fellépő elektromos térerősség az egyéb módon előállítható terekhez képest nagyságrendekkel nagyobb lehet. Amennyiben a rövidimpulzusú lézernyalábot le is *fókuszál*juk, ez a térerősség már vetekszik az elektronok által az atomban érzékelt térerősségekkel, illetve sok esetben meg is haladhatja azt. Ez az, amit ugyan különböző fizikai folyamatokon keresztül, de sok rövidimpulzusú lézerrendszereket alkalmazó orvosi, anyagtudományi vagy éppen kémiai kísérletben kihasználnak.

A fókuszálás szükségessége és használata azonban egy újabb kérdést felvet. Mi történik az impulzusokkal a fókuszálás során? Megtartja-e a gondosan kialakított tulajdonságait a lézerrel vagy egyéb (legtöbbször a lézerhez szorosan kapcsolódó) módon előállított ultrarövid impulzus, ha a felhasználáshoz fókuszáljuk azt? Ezek azok a kérdések, amikre ez a dolgozat részben megpróbál választ adni.

A dolgozat rövid összefoglalójaként ismertetem az egyes fejezetek címét és rövid tartalmát. Egy rövid bevezető fejezet (Chapter One - Introduction) után a tudományos előzmények tárgyalása következik (Chapter Two - Scientific background). Ez utóbbinak nem csak az a célja, hogy bemutassa a később részletezett tudományos eredmények eléréséhez szükséges tudást és eszközöket, valamint az azokat megalapozó kutatásokat, hanem az is, hogy röviden szemléltesse a munka motivációját. Az ezután következő — a dolgozat nagy részét kitevő — fejezet a szerző új tudományos eredményeinek bemutatását szolgálja (Chapter Three - Results). Végül a dolgozat egy tézisszerű összefoglalással végződik (Chapter Four - Summary).

5.2. Tudományos előzmények

Az első kísérleti demonstrálás óta eltelt több mint 60 évben a lézertechnológia rengeteget fejlődött. A számos alkalmazási lehetőség arra sarkallta a kutatókat és mérnököket, hogy minél nagyobb teljesítményű, minél rövidebb elektromágneses impulzusokat előállító lézerrendszereket fejlesszenek ki. Ennek eredményeképp ma már néhány femtoszekundumos (10^{-15} s) impulzusok hozhatók létre lézeroszcillátorok vagy lézererősítők segítségével. Ez azt jeleneti, hogy legtöbbször a lézerből kilépő hullámcsomagok olyan rövidek, hogy az elektromos (és mágneses) térnek mindössze néhány oszcillációja következhet be ennyi idő alatt. Ezért nevezik ezeket néhány ciklusú impulzusoknak. Ezen impulzusok teszik lehetővé a napjainkban igen nagy érdeklődésre számot tartó nemlineáris optikai folyamatok, vagy az új tudományterület, az „attofizika” kérdésköreinek vizsgálatát. Emellett leg-

többször ilyen ultrarövid impulzusokat előállító lézerek segítségével hozhatók létre a más hullámhossztartományban müködő, sokszor szintén rövidimpulzusokat előállító, sugárzási források, elég csak a lézeres terahertz- vagy távoliultraibolya-fényforrásokra gondolni. Természetesen meg kell említeni, hogy számos anyagtudományi, orvosi, biológiai vagy éppen kémiai felhasználása is van a legújabb megoldásoknak, amelyeknek kiváló példája a Nobel-díjat jelentő „femtokémia".

Az, hogy az ultrarövid lézerimpulzusok ilyen sokrétűen használhatóak, többek között annak köszönhető, hogy jellemzőiket jól kontrollálható módon, az adott feladat igényeinek megfelelően lehet beállítani. Ezek közé tartozik például a polarizációs állapot vagy az úgynevezett „vivő-burkoló fázis" (angolul „carrier-envelope phase", CEP). Ez utóbbi a korábban említett néhány ciklusú impulzusoknál lényeges, hiszen az elektromos tér időbeli lefutását jelentősen befolyásolja azáltal, hogy értéke megadja a vivőhullám és a burkoló relatív fázisát (lásd. Figure 2.1.). Ennek jelentősége már több kísérlet során, nem sokkal a néhány ciklusú lézerimpulzusok megjelenése után megmutatkozott. Az elsőként említett jellemző, a polarizációs állapot esetén pedig elmondható, hogy bár az impulzusok polarizációja a legtöbbször lineáris, egyre gyakrabban alkalmaznak ettől eltérő, vagy akár időben változó polarizációs állapotú elektromágneses hullámcsomagokat. Mivel szinte minden alkalmazáskor fókuszálják a lézernyalábot, így a kérdés az, hogy ez a lépés befolyásolja-e, és ha igen, hogyan módosítja ezen jellemzőket. Ennek elméleti és kísérleti vizsgálatához először át kell tekinteni, hogy hogyan írhatók le az ultrarövid impulzusok és jellemzőik matematikai módszerekkel, miképpen tehető meg ugyanez a fókuszálás folyamatával, és milyen kísérleti eszközök állnak rendelkezésre ezek elemzésére.

5.2.1. Az ultrarövid lézerimpulzusok jellemzői és matematikai leírása

Az ultrarövid lézerimpulzusok matematikai leírásának egyik legfontosabb lépése a Fourier-transzformáció, amely Fourier tétele értelmében azt teszi lehetővé, hogy a rövid hullámcsomagot végtelen hosszú, monokromatikus, különböző frekvenciájú hullámok szuperpozíciójaként állítsuk elő. A Fourier-transzformáció így kapcsolatot teremt a hullámok időbeli alakja és spektrális reprezentációja között. Ez az eljárás azért széles körben alkalmazott, mert a szinuszhullámok könnyebben kezelhetők, sokkal nagyobb ismeret áll rendelkezésre leírásukhoz, valamint a hullámegyenlet megoldását is számos esetben ez a felbontás teszi lehetővé. Így a vizsgálni kívánt hullámterjedési probléma megoldható úgy, hogy a kezdeti impulzust komponenseire bontjuk, ezen komponensek változásait határozzuk meg, majd belőlük újra előállítjuk az időbeli alakot a vizsgálni kívánt helyen. A megoldandó tudományos probléma így a második lépés, az egyes komponensek változásainak meghatározása, amelyre számos megközelítés létezik attól függően, hogy milyen

aspektusból és milyen körülmények között vizsgáljuk a fény terjedését. Ezen megoldások néhány példáját egy későbbi fejezet taglalja. A következőkben három olyan, a néhány ciklusú elektromágneses hullámokat jellemző, paraméter bemutatására kerül sor, amelynek dolgozatomban kiemelt szerepe van.

A vivő-burkoló fázis A térerősség időbeli változását leíró valós vagy komplex kifejezés[II], azaz az impulzus időbeli alakja egy-egy szintén valós vagy komplex függvénnyel jellemzett, gyorsan változó vivőhullám és egy lassabban változó burkoló szorzataként írható fel. A CEP — bár a pontos definíció egy adott témakörben jellemző szokásoktól függ — minden esetben a vivőhullám és impulzusburkoló relatív időbeli helyzetét (amely fázisként is értelmezhető) adja meg. Ebben a munkában a CEP egy olyan definíciója használatos, amely az izolált impulzusok jellemzésére szolgál (nem impulzus-sorozatokéra). Eszerint *egy impulzus vivő-burkoló fázisa a hullámcsomag fázisa abban az időpillanatban, amikor az időbeli burkoló (abszolút értéke) maximális*[III]. Ez a definíció lehetővé teszi a CEP értelmezésének kiterjesztését változó-polarizációs állapotú impulzusokra, valamint a meghatározásból adódóan a CEP zérus volta biztosítja a legnagyobb térerősség elérését adott időbeli burkoló esetén. Olyan kísérleteknél, ahol a céltárggyal való kölcsönhatás nagyobb térfogatban történik, vagy nem pont a fókuszsíkban, fontos kérdés, hogy a fókuszpont környezetében hogyan változik meg a CEP, hiszen a fény-anyag kölcsönhatás eredményét a térerősség pontos időbeli lefutása határozza meg számos esetben.

Polarizáció Az elektromágneses hullámok egy másik nagyon fontos jellemzője polarizációjuk. Rövidimpulzusok esetén is a monokromatikus hullámoknál használt eszközök szolgálhatnak alapul ennek leírására. Különös figyelmet igényel azonban az, a vizsgált folyamat — a fókuszálás — miatt, hogy a valóságban csak a síkhullámok lennének tisztán transzverzális elektromágneses hullámok. Szerencsére azonban a legtöbb esetben, a paraxiális közelítés érvényességekor, az esetlegesen megjelenő longitudinális térkomponens elhanyagolható, és a (fókuszált) Gauss-nyalábok is kezelhetők transzverzális hullámként. Ez azért előnyös, mert így használhatók a monokromatikus síkhullámok polarizációját jellemző mennyiségek, hiszen a nyaláb is kezelhető úgy, mint két skaláris, oszcilláló térmennyiség összege. Az egyik, a polarizációs állapotot megadó leírásmód, a polarizációs ellipszissel való leírás (lásd. Figure 2.5.). Mivel két egymásra merőleges rezgés összege általános esetben egy ellipszispályát ír le, így ennek az ellipszisnek a jellemzőivel (a ψ orientációval, χ ellipticitással és A_M félnagytengely hosszal) írható le a polarizációs állapot. Egy másik, a kísérletekben nagyon elterjedt, megoldás a Stokes-paraméterekkel való

[II] A két leírás fizikailag ekvivalens. A komplex írásmód sok esetben az egyszerűbb matematikai kezelést szolgálja.

[III] Az abszolút értéknek a komplex írásmód esetén van jelentősége.

jellemzés. Ennek előnye, hogyaz egyes paraméterek már definíciójukban megadják a mérés módját. Természetesen a két leírásmód között közvetlen kapcsolat áll fent.

Az (ultra)rövid lézerimpulzusoknál a monokromatikus esethez képest változást jelent, hogy azok polarizációs állapota időben változhat. Egyre több olyan kutatás van, ahol ezt a lehetőséget ki is használják, például az úgynevezett koherens kontroll egyik eszközeként. Megmutatható, hogy mind a polarizációs ellipszissel, mind a Stokes-paraméterekkel való leírás kiterjeszthető időben változó polarizációs állapot leírására. Ez esetben azonban oda kell figyelni, hogy a polarizációs ellipszis már kevesebb jelentést hordoz, mint a monokromatikus hullámoknál. A térerősség időbeli változása már nem követi az ellipszissel leírt pályát, az időfüggő ellipszis csak azt adja meg, hogy a mindkét merőleges komponenst érő időfüggetlen fázistolás eredményeképp hogyan változna a tér. A Stokes-paraméterek esetében az első, S_0 paraméter elveszíti jelentőségét a pillanatnyi állapot jellemzéskor, hiszen a polarizálatlanság ilyenkor nem értelmezhető. Mindkét leírásmód azonban jól szemlélteti, ha valamilyen okból (például szabad terjedéskor vagy fókuszáláskor) változás történik a polarizációs állapotban, hiszen annak egyértelmű jellemzési módját adják.

Fázis- és csoportsebesség A fázissebesség a nemlineáris optikában fontos paraméter, hiszen meghatározza számos folyamat hatásfokát. Megadja, hogy a hullám azonos fázisú pontjai milyen sebességgel haladnak a térben. Síkhullámokra ez esetben is nagyon egyszerű összefüggések adódnak, nyalábok esetén azonban figyelembe kell venni, hogy a fázisfrontok görbültek. Ennek eredménye, hogy a hullámok fázissebessége nem csak terjedési irányban, de arra merőlegesen is változhat, a síkhullám-esettel ellentétben. Egy érdekesség a fókuszálás során bekövetkező fázissebesség-változással kapcsolatban, hogy a fázisfrontok a fókuszpont közelében akár a fénysebességnél is gyorsabban haladhatnak a Gouy-féle fázistolás következtében. Ez azonban nem sérti a kauzalitás elvét, mert a fázissal információ nem terjed. A problémát inkább az jelenti, hogy ez a változás a nemlineáris folyamatokhoz jó hatásfokú kihasználásához szükséges fázisillesztést gátolja.

A csoportsebesség egy hullámcsomag, mint egész terjedési sebességét írja le. Erre is igaz, akárcsak a fázissebességre, hogy a nyalábok esetén kiszámítása bonyolultabb, mint síkhullámokra, és a fókuszpont közelében ennek értéke is szuperluminális (fénysebességnél nagyobb) lehet. Ez sem sérti azonban a relativitáselmélet elveit, mivel a csoportsebesség sincs kapcsolatban az információterjedés sebességével, ugyanis az energia ettől eltérő sebességgel terjedhet. A csoportsebesség jelentősége ebben a munkában az, hogy a fázissebességgel együtt befolyásolják, hogy a CEP a terjedés során hogyan változik.

5.2.2. Nyalábterejedési és fókuszálási modellek

A lézerekkel előállított hullámcsomagok nem csak időben, de térben is korlátozott kiterjedésűek. Így, hogy az elektromágneses hullámok nyalábok, és nem végtelen síkhullámok formájában terjednek, leírásuk is komplikáltabb. Az optikai tartományban nagy előnyt jelent, hogy a kicsiny hullámhosszaknak köszönhetően egyszerűsítések tehetők, amelyek például a szabad terjedés egyszerűbb modellezését teszik lehetővé. A fókuszálás azonban egy olyan eset, aminek kellően pontos leírásához ezek az egyszerűsítő feltételezések nem használhatók ki. Az alábbiakban néhány olyan modell rövid leírása következik, amely a korábban említett három főbb lépésből álló impulzusterjedési szimulációk második, a két Fourier-transzformáció közti lépéseként használhatók.

Sugárkövetés A fényterjedés modellezésére használt egyik legegyszerűbb és legrobosztusabb megoldást a sugárkövetés jelenti, amely a geometriai optika egyik eszköze. Ez esetben a hullámokat a terjedési irányban haladó fénysugarak segítségével írhatjuk le. A hullámterjedési problémát a különböző törő- és visszaverő felületeken való irányváltozások kiszámításával oldhatjuk meg, a fénytörés és fényvisszaverődés egyszerű törvényei alapján. Az eljárás előnye, hogy a kevés paraméternek köszönhetően a fény terjedése igen bonyolult optikai rendszerek esetén is viszonylag kis számításigénnyel kezelhető. Hátránya azonban, hogy a fény hullámtermészete több tekintetben a közelítések miatt elveszik, ezáltal olyan esetekben, ahol a fény diffrakciója vagy interferenciája releváns mértékű, (például a fókuszálásnál) ott nem ad teljesen helytálló eredményeket. Ilyen, a hullámtermészetből adódó effektusok többségében olyan pontokban lépnek fel, ahol több fénysugár találkozik. Így ameddig a szimulációkban azok távol haladnak egymástól, a sugárkövetés jól használható. Ilyen esetben a sugárkövetés, részben a hullámtermészetet is megtartva, hullámfrontok meghatározására is alkalmas lehet.

Mátrixoptika Amennyiben a geometriai optika közelítései mellett még a hengerszimmetriát is feltételezhetjük, akkor a sugárkövetés egy analitikus modelljét, a mátrixoptikát is használhatjuk. A mátrixoptika jól alkalmazható például a paraxiális hullámegyenlet egy megoldásának, a Gauss-nyalábok terjedésének leírására. Bár a diffrakció és interferencia jelenségeinek leírására ez a modell sem alkalmas, a Gauss-nyalábok fókuszálásnak számos aspektusát helyesen jellemzi (megjelenik például a nyalábnyak fókuszáló elem felé történő eltolódása laza fókuszáláskor). Így a monokromatikus Gauss-nyalábok mátrixoptikával való jellemzése az ultrarövid impulzusok leírásánál nagy segítséget jelent, amennyiben a monokromatikus komponensek és a hullámcsomagok közti átmenet (a Fourier-transzformáció) is analitikusan kezelhető.

A fókuszálás skalárdiffrakciós modellje Ahogy ez korábban szerepelt, a geometriai optika eszközei nem alkalmasak a hullámtermészet minden velejárójának leírására. Például közismerten a kísérleti tapasztalatoktól eltérő eredményt adnak a geometriai fény és árnyék határán. Ez a tartomány fókuszálás esetén magában foglalja a fókuszálási tartomány legrelevánsabb részeit. Így a fókuszálás helyes leírásához hullámoptikai modellt kell alkalmaznunk. Ennek egyik megoldása lehet a Huygens–Fresnel-elven alapuló skalárdiffrakciós elmélet használata, aminek eszközei Maxwell-egyenletekből közvetlenül is levezethetők. A Kirchhoff-féle diffrakciós integrál, például, már a XIX. század végén kidolgozásra került, és azóta számos esetben bizonyította, hogy a kísérleti megfigyelésekkel nagyon jól egyező eredményt ad. Ez az integrál a Maxwell-egyenletek közvetlen numerikus megoldásánál kisebb számításigényű, de a hullámtermészet következményeit nagy pontossággal leíró formulát jelent. Így attól a ponttól, hogy a lézernyaláb a fókuszáló elemből kilépett (vagy azon visszaverődött), a fókuszált hullám fázis- és amplitúdójellemzői ezen leírás segítségével kiválóan modellezhetők.

5.2.3. A vivő-burkoló fázis változásainak mérési módszerei

A vivőhullám és a burkoló relatív fázisának mérése nagyon nehéz feladat az optikai tartományban. A legtöbb megoldás, amelyik a CEP-re vonatkozóan kíván információval szolgálni, nem is képes annak értékét, csak impulzusról impulzusra történő változásának mértékét megadni. A lézerimpulzusok CEP-jét, amit sokszor „abszolút” fázisnak is neveznek, jelenleg közvetlenül csak egyetlen módszerrel lehet megbízhatóan mérni. Ez a „stereo-ATI”, ami a küszöb feletti ionizáció erős térerősség függését használja ki, és két egymással szemben elhelyezett detektor jelének viszonyából következtet a CEP értékére. Ez azonban nagyon költséges kísérleti eszközparkot, valamint bonyolult mérési és kiértékelési eljárást jelent. Így napjainkban is aktív kutatási téma olyan fizikai folyamatokat keresni, és így egy olyan egyszerű kísérleti eszközt építeni, amivel a CEP értéke egyszerűen, bármely laboratóriumban megmérhető.

Azonban nincs ezen bonyolult eljárásra szükség, amennyiben csak a CEP változásait akarjuk mérni. Ez esetben lineáris optikai eszközök, például a spektrális interferometria, megfelelő eszközt jelentenek a CEP változásának detektálására. Bár az eljárás első ilyen céllal történő alkalmazása eredetileg egymást követő impulzusok „CEP-csúszásának” mérésére lett tervezve, az alapelv lehetővé teszi, hogy térbeli változások is mérhetők legyenek, megfelelő kísérleti összeállítással. A spektrális interferometria nevéhez hűen hullámok interferenciájának, pontosabban annak spektrális felbontásának segítségével (az interferogram felvételével) ad információt a vizsgálni kívánt széles spektrumú fényforrás (például egy oszcillátorból kilépő lézerimpulzus) spektrális fázisáról. Ennek a fázisnak a mért interferogramból való kinyerésére számos különböző eljárás létezik, különböző előnyökkel

és hátrányokkal. Az, hogy a spektrális fázisból a CEP értékének meghatározása hogyan történik, a körülményektől függően eltérő bonyolultságú lehet, ahogy azt jelen dolgozat eredményei is mutatják. Fontos azonban itt is kiemelni, hogy a mért fázis relatív fázist jelent a referenciaként szolgáló másik fényforráshoz képest, amivel a vizsgált impulzus interferál. Így a spektrális interferometria nem alkalmas az „abszolút" fázis mérésére.

5.3. Eredmények

A felvázolt tudományos előzmények ismeretében célul tűztem ki fókuszált, rövidimpulzusú Gauss-nyalábok szabad terjedése és fókuszálása során bekövetkező fázis- és polarizációsállapot-változásainak elméleti és kísérleti vizsgálatát. A kutatás egyik kiemelt témája a fókuszált nyalábok fázis- és csoportsebességének elemzése, amely a térbeli fázisviszonyok két fontos jellemzője. Ehhez kapcsolódóan munkám során kiemelt figyelmet fordítottam a fókuszálási tartományon áthaladó impulzus vivő-burkoló fázisának elméleti és kísérleti tanulmányozására, különös tekintettel arra, hogy annak értéke a térbeli terjedés során hogyan változik. A kitűzött célok között szerepelt az is, hogy a fókuszálás, mint elhajlási jelenség, hatásait önmagában, illetve több különböző fókuszálást befolyásoló tényező jelenlétében is megvizsgáljam. Ezen tényezők a Gauss-nyaláb csonkolása, a nyaláb jellemzőinek hullámhosszfüggése, illetve a fókuszáló elem kromatikus valamint monokromatikus leképezési hibái (gömbi hiba, asztigmatizmus, kóma, képmező görbület és torzítás). Végül megvizsgáltam, hogy időben változó polarizációs állapottal rendelkező impulzusok a szabad terjedés során megváltoztatják-e polarizációjukat, és ha igen, milyen módon. Fontos volt tisztázni azt is, hogy ezen módosulásokat milyen törvényszerűségek írják le. A munka főbb eredményei az alábbi pontokban foglalhatók össze.

I. Olyan analitikus kifejezéseket vezettem le, amelyek megadják fókuszált Gauss-nyalábok fázis- és csoportsebességét az optikai tengelyen, figyelembe véve a hullámhosszfüggő nyalábparaméterek hatását. A levezetéskor konkrétan meghatároztam, hogy melyek ezen csoportsebességet befolyásoló nyalábjellemzők. Analitikus kifejezéseket adtam arra, hogy ezek hogyan határozhatók meg a bejövő nyaláb valamint a fókuszáló optika paramétereiből. Az előző eredmények alapján pontosan megadtam azon kizárólagos feltételeket, amelyek teljesülése esetén a fókuszált Gauss-nyaláb csoportsebessége nem változik a fókuszálási tartományon való áthaladás során. A kidolgozott képletek azt is megmutatták, hogy egy, a kromatikus aberrációhoz hasonló effektus felléphet fókuszáláskor abban az esetben is, amikor a fókuszáló elem ilyen típusú képalkotási hibával nem rendelkezik. Ez esetben a jelenség okául a nyaláb hullámhosszfüggő paraméterei szolgálnak.

Olyan összefüggéseket dolgoztam ki, amelyekkel kiszámítható a fókuszált Gauss-nyaláb

fázis- és csoportsebessége az optikai tengelyen abban az esetben is, amikor a fókuszálás az optikai elem kromatikus- vagy elsődleges monokromatikus hibái által terhelt. Ezen kifejezések kidolgozása során külön figyelmet szenteltem annak, hogy, a lehetőségekhez mérten, a számítások minél nagyobb részét analitikusan végezzem el, ezáltal növelve azok alkalmazhatósági körét és pontosságát a numerikus számítások során. Emellett, az így kapott eredményeimet arra használtam, hogy megvizsgáljam, hogy a nyaláb csonkolása, a kromatikus hiba vagy az elsődleges monokromatikus leképezési hibák hogyan befolyásolják egy fókuszált, rövidimpulzusú Gauss-nyaláb fázis- és csoportsebességét az optikai tengelyen. Eredményeimet összevetettem más kutatók elsődleges aberrációk fázismódosító hatásaira vonatkozó konklúzióival, és azokkal nagyon jó egyezésben lévő eredményeket kaptam [T1].

II. Kifejlesztettem egy sugárkövetésen és a fókuszálás skalárdiffrakciós modelljén alapuló numerikus számítást, ami alkalmas az elektromos tér lencsék vagy lencserendszerek fókuszpontjának környezetében történő meghatározására. Ezt a modellt arra használtam, hogy numerikus szimulációk segítségével igazoljam azt, hogy transzmissziós optikai elemek segítségével is lehetséges néhány ciklusú optikai impulzusokat úgy lefókuszálni, hogy az ne járjon a fókuszált impulzus releváns torzulásával. Megmutattam, hogy ennek eléréséhez elegendő a fókuszáló elemet az optikai tengelyen jellemző diszperziós effektusok kompenzálása. A szimulációk segítségével igazoltam egy, a fókuszált, rövidimpulzusú Gauss-nyalábok vivő-burkoló fázis változását az optikai tengelyen leíró analitikus kifejezés helyességét is. Az előző két eredmény segítségével megmutattam azt, hogy lencsékkel történő fókuszálás esetén elérhető az, hogy néhány ciklusú optikai impulzusok a fókuszálási tartományban az optikai tengelyen mentén úgy haladjanak, hogy a hullámterjedés során az elektromos tér időbeli lefutása ne változzon [T2–T4].

III. Megterveztem és megépítettem egy kísérleti elrendezést, amely alkalmas rövidimpulzusú optikai nyalábok fázisának térbeli változásainak mérésére nagy térbeli feloldással. Ezt az elrendezést arra használtam, hogy kísérleti úton megvizsgáljam egy néhány ciklusú impulzus vivő-burkoló fázisának változásait egy akromatikus lencse fókuszpontjának környezetében. Elvégeztem a fókuszálás előtti lézernyaláb paramétereinek hullámhosszfelbontott mérését. A mérési eredményeket felhasználva, a kísérleti vizsgálatokkal megegyező körülményekre, szimulációkat végeztem a tanulmányozott vivő-burkoló fázis változásokra vonatkozóan. Az összehasonlítás eredménye igazolta az elemezni kívánt elmélet legfontosabb aspektusait, azaz, hogy a fókuszált nyaláb paramétereinek hullámhosszfüggése befolyásolja az impulzus vivő-burkoló fázisának térbeli változását a fókuszálási tartományban, és azt, hogy ez a térbeli változás a Gouy-fázistól eltérhet [T5].

IV. Numerikus szimulációk segítségével igazoltam egy olyan analitikus nyalábterjedési elméletet, amely leírja a rövidimpulzusok pillanatnyi polarizációs állapotának változását szabad terjedés vagy fókuszálás során. Megfelelő példák segítségével szintén alátámasztottam azt a törvényszerűséget, hogy a pillanatnyi polarizációt jellemző polarizációs ellipszis egyik paraméterének (orientáció vagy ellipticitás) időbeli változása a terjedés során a másik jellemző megváltozását eredményezi. A numerikus szimulációim rámutattak arra, hogy ezek a hullámterjedés okozta polarizációsállapot-változások a nyalábok szabad térben történő „diffrakciójának" következményei, így a módosulások minden rövidimpulzusú nyalábra jellemzőek. Szimulációim segítségével megmutattam, hogy a pillanatnyi polarizációs állapotban bekövetkező ezen változások jelei kísérleti módon, térben és időben integráló detektorok segítségével, is megfigyelhetők [T6, T7].

References

[1] T. H. Maiman. "Stimulated Optical Radiation in Ruby". *Nature* 187.4736 (1960), 493–494. DOI: 10.1038/187493a0.

[2] A. M. Prokhorov. "Molecular amplifier and generator for submillimeter waves". *Sov. Phys. JETP* 7 (1958). (English translation of *Sov. Phys. JETP*, 34, 1658–1659), 1140–1141. URL: http://www.physics-online.ru/php/paper.phtml?jrnid=ble&paperid=11792&option_lang=eng.

[3] A. L. Schawlow and C. H. Townes. "Infrared and Optical Masers". *Phys. Rev.* 112.6 (6 1958), 1940–1949. DOI: 10.1103/PhysRev.112.1940.

[4] A. Javan and J. W. R. Bennett. *Gas optical maser*. US Patent 3149290, Filing date: Dec 28, 1960. 1964. URL: http://www.google.com/patents/US3149290.

[5] F. J. McClung and R. W. Hellwarth. "Giant Optical Pulsations from Ruby". *J. Appl. Phys.* 33.3 (1962), 828–829. DOI: 10.1063/1.1777174.

[6] P. Kafalas, J. I. Masters, and E. M. E. Murray. "Photosensitive Liquid used as a Nondestructive Passive Q-Switch in a Ruby Laser". *J. Appl. Phys.* 35.8 (1964), 2349–2350. DOI: 10.1063/1.1702862.

[7] A. E. Siegman. *Lasers*. University Science Books, 1986. ISBN: 0-935702-11-5. URL: http://books.google.hu/books?id=1BZVwUZLTkAC.

[8] Z. Bor and A. Müller. "Picosecond distributed feedback dye lasers". *IEEE J. Quantum. Electron.* 22.8 (1986), 1524–1533. DOI: 10.1109/JQE.1986.1073136.

[9] S. Szatmári and F. P. Schäfer. "Subpicosecond, widely tunable distributed feedback dye laser". *Appl. Phys. B: Lasers Opt.* 46.4 (1988), 305–311. DOI: 10.1007/BF00686453.

[10] J. Hebling. "20 ps pulse generation by an excimer laser pumped double self-Q-switched distributed feedback dye laser". *Appl. Phys. B: Lasers Opt.* 47.3 (1988), 267–272. DOI: 10.1007/BF00697348.

[11] L. E. Hargrove, R. L. Fork, and M. A. Pollack. "Locking of He-Ne laser modes induced by synchronous intracavity modulation". *Appl. Phys. Lett.* 5.1 (1964), 4–5. DOI: 10.1063/1.1754025.

[12] F. Krausz, M. E. Fermann, T. Brabec, P. F. Curley, M. Hofer, M. H. Ober, C. Spielmann, E. Wintner, and A. J. Schmidt. "Femtosecond solid-state lasers". *IEEE J. Quantum. Electron.* 28.10 (1992), 2097–2122. DOI: 10.1109/3.159520.

[13] P. M. W. French. "The generation of ultrashort laser pulses". *Rep. Prog. Phys.* 58.2 (1995), 169–267. DOI: 10.1088/0034-4885/58/2/001.

[14] U. Keller. "Ultrafast all-solid-state laser technology". *Appl. Phys. B: Lasers Opt.* 58.5 (1994), 347–363. DOI: 10.1007/BF01081874.

[15] P. M. W. French. "Ultrafast solid-state lasers". *Contemp. Phys.* 37.4 (1996), 283–301. DOI: 10.1080/00107519608222155.

[16] R. Szipőcs, K. Ferencz, C. Spielmann, and F. Krausz. "Chirped multilayer coatings for broadband dispersion control in femtosecond lasers". *Opt. Lett.* 19.3 (1994), 201–203. DOI: 10.1364/OL.19.000201.

[17] T. Brabec and F. Krausz. "Intense few-cycle laser fields: Frontiers of nonlinear optics". *Rev. Mod. Phys.* 72.2 (2000), 545–591. DOI: 10.1103/RevModPhys.72.545.

[18] J.-C. Diels and W. Rudolph. *Ultrashort Laser Pulse Phenomena*. 2nd. Academic Press, 2006. ISBN: 978-0-12-215493-5. URL: http://www.sciencedirect.com/science/book/9780122154935.

[19] G. A. Mourou, T. Tajima, and S. V. Bulanov. "Optics in the relativistic regime". *Rev. Mod. Phys.* 78.2 (2006), 309–371. DOI: 10.1103/RevModPhys.78.309.

[20] S. Witte and K. S. E. Eikema. "Ultrafast Optical Parametric Chirped-Pulse Amplification". *IEEE J. Sel. Topics in Quantum Electron.* 18.1 (2012), 296–307. DOI: 10.1109/JSTQE.2011.2118370.

[21] M. E. Fermann and I. Hartl. "Ultrafast fibre lasers". *Nature Photon.* 7.11 (2013), 868–874. DOI: 10.1038/nphoton.2013.280.

[22] R. W. Boyd. *Nonlinear Optics*. 3rd. Academic Press, 2008. ISBN: 978-0-123-69470-6. URL: http://www.sciencedirect.com/science/book/9780123694706.

[23] R. H. Stolen and C. Lin. "Self-phase-modulation in silica optical fibers". *Phys. Rev. A: At., Mol., Opt. Phys.* 17.4 (1978), 1448–1453. DOI: 10.1103/PhysRevA.17.1448.

[24] A. Baltuška, Z. Wei, M. S. Pshenichnikov, and D. A. Wiersma. "Optical pulse compression to 5 fs at a 1-MHz repetition rate". *Opt. Lett.* 22.2 (1997), 102–104. DOI: 10.1364/OL.22.000102.

[25] M. Nisoli, S. D. Silvestri, O. Svelto, R. Szipöcs, K. Ferencz, C. Spielmann, S. Sartania, and F. Krausz. "Compression of high-energy laser pulses below 5 fs". *Opt. Lett.* 22.8 (1997), 522–524. DOI: 10.1364/OL.22.000522.

[26] C. Hauri, A. Guandalini, P. Eckle, W. Kornelis, J. Biegert, and U. Keller. "Generation of intense few-cycle laser pulses through filamentation – parameter dependence". *Opt. Express* 13.19 (2005), 7541–7547. DOI: 10.1364/OPEX.13.007541.

[27] O. D. Mücke, S. Ališauskas, A. J. Verhoef, A. Pugžlys, A. Baltuška, V. Smilgevičius, J. Pocius, L. Giniunas, R. Danielius, and N. Forget. "Self-compression of millijoule 1.5 µm pulses". *Opt. Lett.* 34.16 (2009), 2498–2500. DOI: 10.1364/OL.34.002498.

[28] A. Braun, G. Korn, X. Liu, D. Du, J. Squier, and G. Mourou. "Self-channeling of high-peak-power femtosecond laser pulses in air". *Opt. Lett.* 20.1 (1995), 73–75. DOI: 10.1364/OL.20.000073.

[29] R. A. Baumgartner and R. Byer. "Optical parametric amplification". *IEEE J. Quantum. Electron.* 15.6 (1979), 432–444. DOI: 10.1109/JQE.1979.1070043.

[30] D. Brida, C. Manzoni, G. Cirmi, M. Marangoni, S. Bonora, P. Villoresi, S. D. Silvestri, and G. Cerullo. "Few-optical-cycle pulses tunable from the visible to the mid-infrared by optical parametric amplifiers". *J. Opt.* 12.1 (2010), 013001. DOI: 10.1088/2040-8978/12/1/013001.

[31] S. T. Cundiff and A. M. Weiner. "Optical arbitrary waveform generation". *Nature Photon.* 4.11 (2010), 760–766. DOI: 10.1038/nphoton.2010.196.

[32] C. Manzoni, O. D. Mücke, G. Cirmi, S. Fang, J. Moses, S.-W. Huang, K.-H. Hong, G. Cerullo, and F. X. Kärtner. "Coherent pulse synthesis: towards sub-cycle optical waveforms". *Laser & Photon. Rev.* 9.2 (2015), 129–171. DOI: 10.1002/lpor.201400181.

[33] M. T. Hassan, A. Wirth, I. Grguraš, A. Moulet, T. T. Luu, J. Gagnon, V. Pervak, and E. Goulielmakis. "Invited Article: Attosecond photonics: Synthesis and control of light transients". *Rev. Sci. Instrum.* 83.11 (2012), 111301. DOI: 10.1063/1.4758310.

[34] H.-S. Chan, Z.-M. Hsieh, W.-H. Liang, A. H. Kung, C.-K. Lee, C.-J. Lai, R.-P. Pan, and L.-H. Peng. "Synthesis and Measurement of Ultrafast Waveforms from Five Discrete Optical Harmonics". *Science* 331.6021 (2011), 1165–1168. DOI: 10.1126/science.1198397.

[35] J. A. Cox, W. P. Putnam, A. Sell, A. Leitenstorfer, and F. X. Kärtner. "Pulse synthesis in the single-cycle regime from independent mode-locked lasers using attosecond-precision feedback". *Opt. Lett.* 37.17 (2012), 3579–3581. DOI: 10.1364/OL.37.003579.

[36] G. Krauss, S. Lohss, T. Hanke, A. Sell, S. Eggert, R. Huber, and A. Leitenstorfer. "Synthesis of a single cycle of light with compact erbium-doped fibre technology". *Nature Photon.* 4.1 (2010), 33–36. DOI: 10.1038/nphoton.2009.258.

[37] S.-W. Huang, G. Cirmi, J. Moses, K.-H. Hong, S. Bhardwaj, J. R. Birge, L.-J. Chen, E. Li, B. J. Eggleton, G. Cerullo, and F. X. Kärtner. "High-energy pulse synthesis with sub-cycle waveform control for strong-field physics". *Nature Photon.* 5.8 (2011), 475–479. DOI: 10.1038/nphoton.2011.140.

[38] M. C. Hoffmann and J. A. Fülöp. "Intense ultrashort terahertz pulses: generation and applications". *J. Phys. D: Appl. Phys.* 44.8 (2011), 083001. DOI: 10.1088/0022-3727/44/8/083001.

[39] G. Sansone, E. Benedetti, F. Calegari, C. Vozzi, L. Avaldi, R. Flammini, L. Poletto, P. Villoresi, C. Altucci, R. Velotta, S. Stagira, S. De Silvestri, and M. Nisoli. "Isolated Single-Cycle Attosecond Pulses". *Science* 314.5798 (2006), 443–446. DOI: 10.1126/science.1132838.

[40] M. Hentschel, R. Kienberger, C. Spielmann, G. A. Reider, N. Milosevic, T. Brabec, P. Corkum, U. Heinzmann, M. Drescher, and F. Krausz. "Attosecond metrology". *Nature* 414.6863 (2001), 509–513. DOI: 10.1038/35107000.

[41] M. Chini, K. Zhao, and Z. Chang. "The generation, characterization and applications of broadband isolated attosecond pulses". *Nature Photon.* 8.3 (2014), 178–186. DOI: 10.1038/nphoton.2013.362.

[42] C. Hernández-García, J. A. Pérez-Hernández, T. Popmintchev, M. M. Murnane, H. C. Kapteyn, A. Jaron-Becker, A. Becker, and L. Plaja. "Zeptosecond High Harmonic keV X-Ray Waveforms Driven by Midinfrared Laser Pulses". *Phys. Rev. Lett.* 111.3 (2013), 033002. DOI: 10.1103/PhysRevLett.111.033002.

[43] B. W. J. McNeil and N. R. Thompson. "X-ray free-electron lasers". *Nature Photon.* 4.12 (2010), 814–821. DOI: 10.1038/nphoton.2010.239.

[44] Z. Tibai, G. Tóth, M. I. Mechler, J. A. Fülöp, G. Almási, and J. Hebling. "Proposal for Carrier-Envelope-Phase Stable Single-Cycle Attosecond Pulse Generation in the Extreme-Ultraviolet Range". *Phys. Rev. Lett.* 113.10 (2014), 104801. DOI: 10.1103/PhysRevLett.113.104801.

[45] G. Steinmeyer, B. Borchers, and F. Lücking. "Carrier-Envelope Phase Stabilization". In: *Progress in Ultrafast Intense Laser Science*. Ed. by K. Yamanouchi and K. Midorikawa. Vol. 104. Springer Series in Chemical Physics. Springer Berlin Heidelberg, 2013, 89–110. ISBN: 978-3-642-35051-1. DOI: 10.1007/978-3-642-35052-8_6.

[46] G. Cerullo, A. Baltuška, O. Mücke, and C. Vozzi. "Few-optical-cycle light pulses with passive carrier-envelope phase stabilization". *Laser & Photon. Rev.* 5.3 (2011), 323–351. DOI: 10.1002/lpor.201000013.

[47] F. Krausz and M. Ivanov. "Attosecond physics". *Rev. Mod. Phys.* 81.1 (2009), 163–234. DOI: 10.1103/RevModPhys.81.163.

[48] A. H. Zewail. "Femtochemistry: Atomic-Scale Dynamics of the Chemical Bond". *J. Phys. Chem. A* 104.24 (2000), 5660–5694. DOI: 10.1021/jp001460h.

[49] V. Sundström. "Femtobiology". *Annu. Rev. Phys. Chem.* 59.1 (2008), 53–77. DOI: 10.1146/annurev.physchem.59.032607.093615.

[50] K. Sugioka and Y. Cheng. "Ultrafast lasers—reliable tools for advanced materials processing". *Light. Sci. Appl.* 3 (2014), e149. DOI: 10.1038/lsa.2014.30.

[51] J. Yoon, J. Park, M. Choi, W. Jong Choi, and C. Choi. "Application of femtosecond-pulsed lasers for direct optical manipulation of biological functions". *Ann. Phys. (Berlin)* 525.3 (2013), 205–214. DOI: 10.1002/andp.201200099.

[52] P. S. Tsai, P. Blinder, B. J. Migliori, J. Neev, Y. Jin, J. A. Squier, and D. Kleinfeld. "Plasma-mediated ablation: an optical tool for submicrometer surgery on neuronal and vascular systems". *Curr. Opin. Biotechnol.* 20.1 (2009), 90–99. DOI: 10.1016/j.copbio.2009.02.003.

[53] W. Min, C. W. Freudiger, S. Lu, and X. S. Xie. "Coherent Nonlinear Optical Imaging: Beyond Fluorescence Microscopy". *Annu. Rev. Phys. Chem.* 62.1 (2011), 507–530. DOI: 10.1146/annurev.physchem.012809.103512.

[54] W. Drexler. "Ultrahigh-resolution optical coherence tomography". *J. Biomed. Opt.* 9.1 (2004), 47–74. DOI: 10.1117/1.1629679.

[55] F. Krausz and M. I. Stockman. "Attosecond metrology: from electron capture to future signal processing". *Nature Photon.* 8.3 (2014), 205–213. DOI: 10.1038/nphoton.2014.28.

[56] C. A. Haworth, L. E. Chipperfield, J. S. Robinson, P. L. Knight, J. P. Marangos, and J. W. G. Tisch. "Half-cycle cutoffs in harmonic spectra and robust carrier-envelope phase retrieval". *Nature Phys.* 3.1 (2007), 52–57. DOI: 10.1038/nphys463.

[57] N. Ishii, K. Kaneshima, K. Kitano, T. Kanai, S. Watanabe, and J. Itatani. "Carrier-envelope phase-dependent high harmonic generation in the water window using few-cycle infrared pulses". *Nat. Commun.* 5 (2014), 3331. DOI: 10.1038/ncomms4331.

[58] P. Rudawski, A. Harth, C. Guo, E. Lorek, M. Miranda, C. M. Heyl, E. W. Larsen, J. Ahrens, O. Prochnow, T. Binhammer, U. Morgner, J. Mauritsson, A. L'Huillier, and C. L. Arnold. "Carrier-envelope phase dependent high-order harmonic generation with a high-repetition rate OPCPA-system". *Eur. Phys. J. D* 69.3, 70 (2015), 70. DOI: 10.1140/epjd/e2015-50568-y.

[59] A. Apolonski, P. Dombi, G. G. Paulus, M. Kakehata, R. Holzwarth, T. Udem, C. Lemell, K. Torizuka, J. Burgdörfer, T. W. Hänsch, and F. Krausz. "Observation of light-phase-sensitive photoemission from a metal". *Phys. Rev. Lett.* 92.7 (2004), 073902. DOI: 10.1103/PhysRevLett.92.073902.

[60] E. Goulielmakis, M. Schultze, M. Hofstetter, V. S. Yakovlev, J. Gagnon, M. Uiberacker, A. L. Aquila, E. M. Gullikson, D. T. Attwood, R. Kienberger, F. Krausz, and U. Kleineberg. "Single-Cycle Nonlinear Optics". *Science* 320.5883 (2008), 1614–1617. DOI: 10.1126/science.1157846.

[61] M. Krüger, M. Schenk, and P. Hommelhoff. "Attosecond control of electrons emitted from a nanoscale metal tip". *Nature* 475.7354 (2011), 78–81. DOI: 10.1038/nature10196.

[62] S. E. Irvine, P. Dombi, G. Farkas, and A. Y. Elezzabi. "Influence of the carrier-envelope phase of few-cycle pulses on ponderomotive surface-plasmon electron acceleration". *Phys. Rev. Lett.* 97.14 (2006), 146801. DOI: 10.1103/PhysRevLett.97.146801.

[63] T. M. Fortier, P. A. Roos, D. J. Jones, S. T. Cundiff, R. D. R. Bhat, and J. E. Sipe. "Carrier-envelope phase-controlled quantum interference of injected photocurrents in semiconductors". *Phys. Rev. Lett.* 92.14 (2004), 147403. DOI: 10.1103/PhysRevLett.92.147403.

[64] M. Sato, T. Higuchi, N. Kanda, K. Konishi, K. Yoshioka, T. Suzuki, K. Misawa, and M. Kuwata-Gonokami. "Terahertz polarization pulse shaping with arbitrary field control". *Nature Photon.* 7.9 (2013), 724–731. DOI: 10.1038/nphoton.2013.213.

[65] D. Oron, N. Dudovich, and Y. Silberberg. "Femtosecond Phase-and-Polarization Control for Background-Free Coherent Anti-Stokes Raman Spectroscopy". *Phys. Rev. Lett.* 90.21 (2003), 213902. DOI: 10.1103/PhysRevLett.90.213902.

[66] T. Suzuki, S. Minemoto, T. Kanai, and H. Sakai. "Optimal Control of Multiphoton Ionization Processes in Aligned I_2 Molecules with Time-Dependent Polarization Pulses". *Phys. Rev. Lett.* 92.13 (2004), 133005. DOI: 10.1103/PhysRevLett.92.133005.

[67] T. Brixner, G. Krampert, T. Pfeifer, R. Selle, G. Gerber, M. Wollenhaupt, O. Graefe, C. Horn, D. Liese, and T. Baumert. "Quantum Control by Ultrafast Polarization Shaping". *Phys. Rev. Lett.* 92.20 (2004), 208301. DOI: 10.1103/PhysRevLett.92.208301.

[68] F. Weise, S. Weber, M. Plewicki, and A. Lindinger. "Application of phase, amplitude, and polarization shaped pulses for optimal control on molecules". *Chem. Phys.* 332.2–3 (2007), 313–317. DOI: 10.1016/j.chemphys.2006.12.022.

[69] G. Karras, M. Ndong, E. Hertz, D. Sugny, F. Billard, B. Lavorel, and O. Faucher. "Polarization Shaping for Unidirectional Rotational Motion of Molecules". *Phys. Rev. Lett.* 114.10 (2015), 103001. DOI: 10.1103/PhysRevLett.114.103001.

[70] C. T. Middleton, D. B. Strasfeld, and M. T. Zanni. "Polarization shaping in the mid-IR and polarization-based balanced heterodyne detection with application to 2D IR spectroscopy". *Opt. Express* 17.17 (2009), 14526–14533. DOI: 10.1364/OE.17.014526.

[71] P. Tyagi, J. I. Saari, B. Walsh, A. Kabir, V. Crozatier, N. Forget, and P. Kambhampati. "Two-Color Two-Dimensional Electronic Spectroscopy Using Dual Acousto-Optic Pulse Shapers for Complete Amplitude, Phase, and Polarization Control of Femtosecond Laser Pulses". *J. Phys. Chem. A* 117.29 (2013), 6264–6269. DOI: 10.1021/jp400603r.

[72] M. Kakehata, Y. Kobayashi, H. Takada, and K. Torizuka. "Single-shot measurement of a carrier-envelope phase by use of a time-dependent polarization pulse". *Opt. Lett.* 27.14 (2002), 1247–1249. DOI: 10.1364/OL.27.001247.

[73] C. Bourassin-Bouchet, S. de Rossi, F. Delmotte, and P. Chavel. "Spatiotemporal distortions of attosecond pulses". *J. Opt. Soc. Am. A* 27.6 (2010), 1395–1403. DOI: 10.1364/JOSAA.27.001395.

[74] C. Bourassin-Bouchet, M. M. Mang, F. Delmotte, P. Chavel, and S. de Rossi. "How to focus an attosecond pulse". *Opt. Express* 21.2 (2013), 2506–2520. DOI: 10.1364/OE.21.002506.

[75] Z. Bor. "Distortion of Femtosecond Laser Pulses in Lenses and Lens Systems". English. *J. Mod. Opt.* 35.12 (1988), 1907–1918. DOI: 10.1080/713822325.

[76] M. Kempe and W. Rudolph. "Impact of chromatic and spherical aberration on the focusing of ultrashort light pulses by lenses". *Opt. Lett.* 18.2 (1993), 137–139. DOI: 10.1364/OL.18.000137.

[77] L. G. Gouy. "Sur une propriete nouvelle des ondes lumineuses". *C. R. Acad. Sci. Paris* 110 (1890). (in French), 1251. URL: https://books.google.hu/books?id=8UHNGwAACAAJ.

[78] Z. L. Horváth and Z. Bor. "Reshaping of femtosecond pulses by the Gouy phase shift". *Phys. Rev. E: Stat., Nonlinear, Soft Matter Phys.* 60.2 (1999), 2337–2346. DOI: 10.1103/PhysRevE.60.2337.

[79] E. Karimi, C. Altucci, V. Tosa, R. Velotta, and L. Marrucci. "Influence of generalized focusing of few-cycle Gaussian pulses in attosecond pulse generation". *Opt. Express* 21.21 (2013), 24991–24999. DOI: 10.1364/OE.21.024991.

[80] G. Lamouche, M. L. Dufour, B. Gauthier, and J.-P. Monchalin. "Gouy phase anomaly in optical coherence tomography". *Opt. Commun.* 239.4–6 (2004), 297–301. DOI: 10.1016/j.optcom.2004.06.002.

[81] B. Richards and E. Wolf. "Electromagnetic Diffraction in Optical Systems. II. Structure of the Image Field in an Aplanatic System". *P. Roy. Soc. Lond. A Mat.* 253.1274 (1959), 358–379. DOI: 10.1098/rspa.1959.0200.

[82] M. Lax, W. H. Louisell, and W. B. McKnight. "From Maxwell to paraxial wave optics". *Phys. Rev. A: At., Mol., Opt. Phys.* 11.4 (1975), 1365–1370. DOI: 10.1103/PhysRevA.11.1365.

[83] C. Spindler, W. Pfeiffer, and T. Brixner. "Field control in the tight focus of polarization-shaped laser pulses". *Appl. Phys. B: Lasers Opt.* 89.4 (2007), 553–558. DOI: 10.1007/s00340-007-2814-4.

[84] P. Balcou, P. Saliéres, A. L'Huillier, and M. Lewenstein. "Generalized phase-matching conditions for high harmonics: The role of field-gradient forces". *Phys. Rev. A: At., Mol., Opt. Phys.* 55.4 (1997), 3204–3210. DOI: 10.1103/PhysRevA.55.3204.

[85] T. Popmintchev, M.-C. Chen, P. Arpin, M. M. Murnane, and H. C. Kapteyn. "The attosecond nonlinear optics of bright coherent X-ray generation". *Nature Photon.* 4 (2010), 822–832. DOI: 10.1038/nphoton.2010.256.

[86] A. Buck, M. Nicolai, K. Schmid, C. M. S. Sears, A. Savert, J. M. Mikhailova, F. Krausz, M. C. Kaluza, and L. Veisz. "Real-time observation of laser-driven electron acceleration". *Nature Phys.* 7.7 (2011), 543–548. DOI: 10.1038/nphys1942.

[87] R. Xu, Y. Bai, L. Song, P. Liu, R. Li, and Z. Xu. "Initial carrier-envelope phase of few-cycle pulses determined by terahertz emission from air plasma". *Appl. Phys. Lett.* 103.6 (2013), 061111. DOI: 10.1063/1.4817975.

[88] J. B. J. Fourier. *Théorie analytique de la chaleur*. (in French). Didot, 1822. URL: https://archive.org/details/thorieanalytiqu00fourgoog.

[89] N. R. Hanson. "The Mathematical Power of Epicyclical Astronomy". *Isis* 51.2 (1960), 150–158. DOI: 10.1086/348869.

[90] M. Born and E. Wolf. *Principles of Optics*. 7th (expanded). Cambridge University Press, 1999. ISBN: 978-0-521-64222-4. URL: http://www.cambridge.org/us/academic/subjects/physics/optics-optoelectronics-and-photonics/principles-optics-electromagnetic-theory-propagation-interference-and-diffraction-light-7th-edition.

[91] I. N. Bronshtein, K. A. Semendyayev, G. Musiol, and H. Muehlig. *Handbook of Mathematics*. Springer Berlin Heidelberg, 2007, 1–46. ISBN: 978-3-54-072121-5. DOI: 10.1007/978-3-540-72122-2_1.

[92] L. D. Landau and E. M. Lifshitz. *The Classical Theory of Fields*. 4th. Course of theoretical physics. Pergamon Press, 1975. ISBN: 978-0-080-25072-4. URL: http://www.sciencedirect.com/science/book/9780080250724.

[93] S. Akturk, X. Gu, P. Bowlan, and R. Trebino. "Spatio-temporal couplings in ultrashort laser pulses". *J. Opt.* 12.9 (2010), 093001. DOI: 10.1088/2040-8978/12/9/093001.

[94] M. Kolesik and J. V. Moloney. "Modeling and simulation techniques in extreme nonlinear optics of gaseous and condensed media". *Rep. Prog. Phys.* 77.1 (2014), 016401. DOI: 10.1088/0034-4885/77/1/016401.

[95] T. Brabec and F. Krausz. "Nonlinear Optical Pulse Propagation in the Single-Cycle Regime". *Phys. Rev. Lett.* 78.17 (1997), 3282–3285. DOI: 10.1103/PhysRevLett.78.3282.

[96] D. Marcuse. "Pulse distortion in single-mode fibers". *Appl. Opt.* 19.10 (1980), 1653–1660. DOI: 10.1364/AO.19.001653.

[97] W. Heisenberg. "Über den anschaulichen Inhalt der quantentheoretischen Kinematik und Mechanik". *Z. Phys.* 43.3–4 (1927). (in German), 172–198. DOI: 10.1007/BF01397280.

[98] D. C. Champeney. *Fourier Transforms and Their Physical Applications*. International Geophysics. Academic Press, 1973. ISBN: 978-0-121-67450-2. URL: https://books.google.hu/books?id=5cE5AAAAMAAJ.

[99] J. P. Marfice and O. R. Baiocchi. "Dispersion approximation using higher-order Taylor series terms". *Appl. Opt.* 26.19 (1987), 4043–4045. DOI: 10.1364/AO.26.004043.

[100] M. Miyagi and S. Nishida. "Pulse spreading in a single-mode fiber due to third-order dispersion". *Appl. Opt.* 18.5 (1979), 678–682. DOI: 10.1364/AO.18.000678.

[101] Z. Diveki. "Generation and application of attosecond pulses". PhD thesis. Paris: Université Paris-Sud, 2011. URL: https://tel.archives-ouvertes.fr/tel-00722473/.

[102] W. P. Schleich. "Quantum Optics in Phase Space". In: *Quantum Optics in Phase Space*. Wiley-VCH Verlag GmbH & Co. KGaA, 2005. Chap. E: Airy Function, 621–627. ISBN: 978-3-527-60297-1. DOI: 10.1002/3527602976.app5.

[103] I. Walmsley, L. Waxer, and C. Dorrer. "The role of dispersion in ultrafast optics". *Rev. Sci. Instrum.* 72.1 (2001), 1–29. DOI: 10.1063/1.1330575.

[104] I. A. Walmsley and C. Dorrer. "Characterization of ultrashort electromagnetic pulses". *Adv. Opt. Photon.* 1.2 (2009), 308–437. DOI: 10.1364/AOP.1.000308.

[105] I. Thomann, L. Hollberg, S. A. Diddams, and R. Equall. "Chromium-doped forsterite: dispersion measurement with white-light interferometry". *Appl. Opt.* 42.9 (2003), 1661–1666. DOI: 10.1364/AO.42.001661.

[106] H. Xiao and K. E. Oughstun. "Failure of the group-velocity description for ultrawideband pulse propagation in a causally dispersive, absorptive dielectric". *J. Opt. Soc. Am. B* 16.10 (1999), 1773–1785. DOI: 10.1364/JOSAB.16.001773.

[107] R. Paschotta. *Encyclopedia of laser physics and technology*. (freely available online). Wiley-VCH Berlin, 2008. ISBN: 978-3-527-40828-3. URL: https://www.rp-photonics.com/encyclopedia.html.

[108] L. Xu, T. W. Hänsch, C. Spielmann, A. Poppe, T. Brabec, and F. Krausz. "Route to phase control of ultrashort light pulses". *Opt. Lett.* 21.24 (1996), 2008–2010. DOI: 10.1364/OL.21.002008.

[109] J. Ye and S. Cundiff. *Femtosecond optical frequency comb: principle, operation and applications*. Springer Science & Business Media, 2005. ISBN: 978-0-387-23791-6. URL: http://www.springer.com/us/book/9780387237909.

[110] S. T. Cundiff. "Phase stabilization of ultrashort optical pulses". *J. Phys. D: Appl. Phys.* 35.8 (2002), R43. DOI: 10.1088/0022-3727/35/8/201.

[111] F. W. Helbing, G. Steinmeyer, J. Stenger, H. R. Telle, and U. Keller. "Carrier–envelope-offset dynamics and stabilization of femtosecond pulses". *Appl. Phys. B: Lasers Opt.* 74.1 (2002), s35–s42. DOI: 10.1007/s00340-002-0898-4.

[112] H. R. Telle, G. Steinmeyer, A. E. Dunlop, J. Stenger, D. H. Sutter, and U. Keller. "Carrier-envelope offset phase control: A novel concept for absolute optical frequency measurement and ultrashort pulse generation". *Appl. Phys. B: Lasers Opt.* 69.4 (1999), 327–332. DOI: 10.1007/s003400050813.

[113] Á. Budó. *Kísérleti fizika I.* (in Hungarian). Nemzeti Tankönyvkiadó, 1997. ISBN: 963-19-5313-0. URL: http://www.tankonyvtar.hu/hu/tartalom/tamop425/2011_0001_519_04292_1_Fizika1/adatok.html.

[114] F. Lücking, V. Crozatier, N. Forget, A. Assion, and F. Krausz. "Approaching the limits of carrier-envelope phase stability in a millijoule-class amplifier". *Opt. Lett.* 39.13 (2014), 3884–3887. DOI: 10.1364/OL.39.003884.

[115] M. A. Porras. "Propagation-induced changes in the instantaneous polarization state, phase, and carrier–envelope phase of few-cycle pulsed beams". *J. Opt. Soc. Am. B* 30.6 (2013), 1652–1659. DOI: 10.1364/JOSAB.30.001652.

[116] D. Frantzeskakis, H. Leblond, and D. Mihalache. "Nonlinear optics of intense few-cycle pulses: An overview of recent theoretical and experimental developments". *Rom. J. Phys.* 59.7–8 (2014), 767–784. URL: http://www.nipne.ro/rjp/2014_59_7-8/0767_0784.pdf.

[117] L. Polachek, D. Oron, and Y. Silberberg. "Full control of the spectral polarization of ultrashort pulses". *Opt. Lett.* 31.5 (2006), 631–633. DOI: 10.1364/OL.31.000631.

[118] O. Masihzadeh, P. Schlup, and R. A. Bartels. "Complete polarization state control ofultrafast laser pulses with a single linearspatial light modulator". *Opt. Express* 15.26 (2007), 18025–18032. DOI: 10.1364/OE.15.018025.

[119] C. Schwarz, O. Hüter, and T. Brixner. "Full vector-field control of ultrashort laser pulses utilizing a single dual-layer spatial light modulator in a common-path setup". *J. Opt. Soc. Am. B* 32.5 (2015), 933–945. DOI: 10.1364/JOSAB.32.000933.

[120] F. Weise, M. Pawłowska, G. Achazi, and A. Lindinger. "Full control of polarization and temporal shape of ultrashort laser pulses transmitted through an optical fibre". *J. Opt.* 13.7 (2011), 075301. DOI: 10.1088/2040-8978/13/7/075301.

[121] H. Seiler, B. Walsh, S. Palato, A. Thai, V. Crozatier, N. Forget, and P. Kambhampati. "Kilohertz generation of high contrast polarization states for visible femtosecond pulses via phase-locked acousto-optic pulse shapers". *J. Appl. Phys.* 118.10 (2015), 103110. DOI: 10.1063/1.4929954.

[122] M. R. Shcherbakov, P. P. Vabishchevich, V. V. Komarova, T. V. Dolgova, V. I. Panov, V. V. Moshchalkov, and A. A. Fedyanin. "Ultrafast Polarization Shaping with Fano Plasmonic Crystals". *Phys. Rev. Lett.* 108.25 (2012), 253903. DOI: 10.1103/PhysRevLett.108.253903.

[123] K. Lee, M. Yi, J. D. Song, and J. Ahn. "Polarization shaping of few-cycle terahertz waves". *Opt. Express* 20.11 (2012), 12463–12472. DOI: 10.1364/OE.20.012463.

[124] P. Nuernberger, R. Selle, F. Langhojer, F. Dimler, S. Fechner, G. Gerber, and T. Brixner. "Polarization-shaped femtosecond laser pulses in the ultraviolet". *J. Opt. A-Pure Appl. Op.* 11.8 (2009), 085202. DOI: 10.1088/1464-4258/11/8/085202.

[125] T. Brixner, G. Krampert, P. Niklaus, and G. Gerber. "Generation and characterization of polarization-shaped femtosecond laser pulses". *Appl. Phys. B: Lasers Opt.* 74.1 Suppl. (2002), s133–s144. DOI: 10.1007/s00340-002-0911-y.

[126] T. Brixner. "Poincaré representation of polarization-shaped femtosecond laser pulses". *Appl. Phys. B: Lasers Opt.* 76.5 (2003), 531–540. DOI: 10.1007/s00340-003-1137-3.

[127] M. V. Klein and T. E. Furtak. *Optics*. 2nd. Wiley, 1986. ISBN: 978-0-471-87297-9. URL: http://eu.wiley.com/WileyCDA/WileyTitle/productCd-0471872970.html.

[128] A. G. Santos, J. Q. M. Sugon, and D. J. McNamara. "Polarization ellipse and Stokes parameters in geometric algebra". *J. Opt. Soc. Am. A* 29.1 (2012), 89–98. DOI: 10.1364/JOSAA.29.000089.

[129] D. Goldstein. *Polarized light*. 2nd. Marcel Dekker Inc., 2003. ISBN: 978-0-203-91158-7. URL: https://www.crcpress.com/Polarized-Light-Revised-and-Expanded/Goldstein-Goldstein/p/book/9780203911587.

[130] E. Hecht. *Optics*. 4th. Pearson Education, Inc., 2002. ISBN: 0-321188-78-0. URL: https://books.google.hu/books?id=wcMWpBMMzIkC.

[131] Y.-S. Lee. *Principles of Terahertz Science and Technology*. Springer Science & Business Media, 2009. ISBN: 978-0-387-09540-0. URL: http://www.springer.com/gp/book/9780387095394.

[132] R. Boge, S. Heuser, M. Sabbar, M. Lucchini, L. Gallmann, C. Cirelli, and U. Keller. "Revealing the time-dependent polarization of ultrashort pulses with sub-cycle resolution". *Opt. Express* 22.22 (2014), 26967–26975. DOI: 10.1364/OE.22.026967.

[133] L. Xu, P. Schlup, O. Masihzadeh, R. A. Bartels, and R. Trebino. "Analysis of the measurement of polarization-shaped ultrashort laser pulses by tomographic ultrafast retrieval of transverse light E fields". *J. Opt. Soc. Am. B* 26.12 (2009), 2363–2369. DOI: 10.1364/JOSAB.26.002363.

[134] G. H. Spencer and M. V. R. K. Murty. "General Ray-Tracing Procedure". *J. Opt. Soc. Am.* 52.6 (1962), 672–678. DOI: 10.1364/JOSA.52.000672.

[135] Z. Horváth. "Femtoszekundumos fényimpulzusok fókuszálása". (in Hungarian). PhD thesis. Szeged: JATE Optikai és Kvantumelektronikai Tanszék, 1997.

[136] J. W. Goodman. *Introduction to Fourier Optics*. 2nd. The McGraw-Hill Companies, Inc., 1996. ISBN: 0-070242-54-2. URL: https://books.google.hu/books?id=QllRAAAAMAAJ.

[137] H. Kogelnik and T. Li. "Laser Beams and Resonators". *Appl. Opt.* 5.10 (1966), 1550–1567. DOI: 10.1364/AO.5.001550.

[138] T. C. Petersen, D. M. Paganin, M. Weyland, T. P. Simula, S. A. Eastwood, and M. J. Morgan. "Unifying interpretations of the Gouy phase anomaly for electron waves". *Phys. Rev. A: At., Mol., Opt. Phys.* 89.6 (2014), 063801. DOI: 10.1103/PhysRevA.89.063801.

[139] M. A. Porras. "Characterization of the electric field of focused pulsed Gaussian beams for phase-sensitive interactions with matter". *Opt. Lett.* 34.10 (2009), 1546–1548. DOI: 10.1364/OL.34.001546.

[140] A. Taflove. *Advances in Computational Electrodynamics: The Finite-difference Time-domain Method*. Artech House, 1998. ISBN: 978-0-890-06834-2. URL: https://books.google.hu/books?id=Ht0eAQAAIAAJ.

[141] J.-M. Jin. *The Finite Element Method in Electromagnetics*. Wiley, 2002. ISBN: 978-0-471-43818-2. URL: https://books.google.hu/books?id=N6yVQgAACAAJ.

[142] M. A. Yurkin and A. G. Hoekstra. "The discrete dipole approximation: An overview and recent developments". *J. Quant. Spectrosc. Ra.* 106.1–3 (2007), 558–589. DOI: 10.1016/j.jqsrt.2007.01.034.

[143] Z. L. Horváth and Z. Bor. "Focusing of truncated Gaussian beams". *Opt. Commun.* 222.1–6 (2003), 51–68. DOI: 10.1016/S0030-4018(03)01562-1.

[144] A. Sommerfeld. *Optics*. Lectures on theoretical physics. Academic Press, 1964. URL: https://books.google.hu/books?id=nhEvAAAAIAAJ.

[145] E. Wolf and W. Marchand. "Comparison of the Kirchhoff and the Rayleigh—Sommerfeld Theories of Diffraction at an Aperture". *J. Opt. Soc. Am.* 54.5 (1964), 587–594. DOI: 10.1364/JOSA.54.000587.

[146] Y. Li and E. Wolf. "Focal shift in focused truncated gaussian beams". *Opt. Commun.* 42.3 (1982), 151–156. DOI: 10.1016/0030-4018(82)90128-6.

[147] Z. Bor and Z. L. Horváth. "Distortion of femtosecond pulses in lenses. Wave optical description". *Opt. Commun.* 94.4 (1992), 249–258. DOI: 10.1016/0030-4018(92)90022-J.

[148] H.-M. Heuck, P. Neumayer, T. Kuehl, and U. Wittrock. "Chromatic aberration in petawatt-class lasers". English. *Appl. Phys. B: Lasers Opt.* 84.3 (2006), 421–428. DOI: 10.1007/s00340-006-2230-1.

[149] M. Kempe and W. Rudolph. "Femtosecond pulses in the focal region of lenses". English. *Phys. Rev. A: At., Mol., Opt. Phys.* 48.6 (1993), 4721–4729. DOI: 10.1103/PhysRevA.48.4721.

[150] Y. Li and E. Wolf. "Focal shifts in diffracted converging spherical waves". *Opt. Commun.* 39.4 (1981), 211–215. DOI: 10.1016/0030-4018(81)90108-5.

[151] E. Wolf and Y. Li. "Conditions for the validity of the Debye integral representation of focused fields". *Opt. Commun.* 39.4 (1981), 205–210. DOI: 10.1016/0030-4018(81)90107-3.

[152] C. J. R. Sheppard. "Validity of the Debye approximation". *Opt. Lett.* 25.22 (2000), 1660–1662. DOI: 10.1364/OL.25.001660.

[153] C. J. R. Sheppard. "Limitations of the paraxial Debye approximation". *Opt. Lett.* 38.7 (2013), 1074–1076. DOI: 10.1364/OL.38.001074.

[154] E. Wolf. "Electromagnetic Diffraction in Optical Systems. I. An Integral Representation of the Image Field". *P. Roy. Soc. Lond. A Mat.* 253.1274 (1959), 349–357. DOI: 10.1098/rspa.1959.0199.

[155] R. Kant. "An Analytical Solution of Vector Diffraction for Focusing Optical Systems with Seidel Aberrations". *J. Mod. Opt.* 40.11 (1993), 2293–2310. DOI: 10.1080/09500349314552301.

[156] R. Kant. "An Analytical Method of Vector Diffraction for Focusing Optical Systems with Seidel Aberrations II: Astigmatism and Coma". *J. Mod. Opt.* 42.2 (1995), 299–320. DOI: 10.1080/09500349514550291.

[157] P. Varga and P. Török. "The Gaussian wave solution of Maxwell's equations and the validity of scalar wave approximation". *Opt. Commun.* 152.1–3 (1998), 108–118. DOI: 10.1016/S0030-4018(98)00092-3.

[158] C. G. Chen, P. T. Konkola, J. Ferrera, R. K. Heilmann, and M. L. Schattenburg. "Analyses of vector Gaussian beam propagation and the validity of paraxial and spherical approximations". *J. Opt. Soc. Am. A* 19.2 (2002), 404–412. DOI: 10.1364/JOSAA.19.000404.

[159] M. Kempe, U. Stamm, B. Wilhelmi, and W. Rudolph. "Spatial and temporal transformation of femtosecond laser pulses by lenses and lens systems". *J. Opt. Soc. Am. B* 9.7 (1992), 1158–1165. DOI: 10.1364/JOSAB.9.001158.

[160] G. O. Mattei and M. A. Gil. "Spherical aberration in spatial and temporal transforming lenses of femtosecond laser pulses". *Appl. Opt.* 38.6 (1999), 1058–1064. DOI: 10.1364/AO.38.001058.

[161] F. C. Estrada-Silva, J. Garduño-Mejía, M. Rosete-Aguilar, C. J. Román-Moreno, and R. Ortega-Martínez. "Aberration effects on femtosecond pulses generated by nonideal achromatic doublets". *Appl. Opt.* 48.24 (2009), 4723–4734. DOI: 10.1364/AO.48.004723.

[162] P. Bowlan, P. Gabolde, and R. Trebino. "Directly measuring the spatio-temporal electric field of focusing ultrashort pulses". *Opt. Express* 15.16 (2007), 10219–10230. DOI: 10.1364/OE.15.010219.

[163] P. Saari, P. Bowlan, H. Valtna-Lukner, M. Lõhmus, P. Piksarv, and R. Trebino. "Basic diffraction phenomena in time domain". *Opt. Express* 18.11 (2010), 11083–11088. DOI: 10.1364/OE.18.011083.

[164] M. A. Porras. "Diffraction effects in few-cycle optical pulses". *Phys. Rev. E: Stat., Nonlinear, Soft Matter Phys.* 65.2, Part 2 (2002), 026606. DOI: 10.1103/PhysRevE.65.026606.

[165] I. Coddington, W. C. Swann, L. Nenadovic, and N. R. Newbury. "Rapid and precise absolute distance measurements at long range". *Nature Photon.* 3 (2009), 351–356. DOI: 10.1038/nphoton.2009.94.

[166] A. Einstein. "Zur Elektrodynamik bewegter Körper". *Ann. Phys. (Berlin)* 322.10 (1905). (in German), 891–921. DOI: 10.1002/andp.19053221004.

[167] L. J. Wang, A. Kuzmich, and A. Dogariu. "Gain-assisted superluminal light propagation". *Nature* 406.6793 (2000), 277–279. DOI: 10.1038/35018520.

[168] Z. L. Horváth, J. Vinkó, Z. Bor, and D. von der Linde. "Acceleration of femtosecond pulses to superluminal velocities by Gouy phase shift". *Appl. Phys. B: Lasers Opt.* 63.5 (1996), 481–484. DOI: 10.1007/s003400050112.

[169] M. A. Porras, I. Gonzalo, and A. Mondello. "Pulsed light beams in vacuum with superluminal and negative group velocities". *Phys. Rev. E: Stat., Nonlinear, Soft Matter Phys.* 67.6 (2003), 066604. DOI: 10.1103/PhysRevE.67.066604.

[170] G. Diener. "Superluminal group velocities and information transfer". *Phys. Lett. A* 223.5 (1996), 327–331. DOI: 10.1016/S0375-9601(96)00767-0.

[171] G. Diener. "Energy transport in dispersive media and superluminal group velocities". *Phys. Lett. A* 235.2 (1997), 118–124. DOI: 10.1016/S0375-9601(97)00600-2.

[172] A. Baltuška, T. Fuji, and T. Kobayashi. "Controlling the Carrier-Envelope Phase of Ultrashort Light Pulses with Optical Parametric Amplifiers". *Phys. Rev. Lett.* 88 (2002), 133901. DOI: 10.1103/PhysRevLett.88.133901.

[173] D. J. Jones, S. A. Diddams, J. K. Ranka, A. Stentz, R. S. Windeler, J. L. Hall, and S. T. Cundiff. "Carrier-Envelope Phase Control of Femtosecond Mode-Locked Lasers and Direct Optical Frequency Synthesis". *Science* 288.5466 (2000), 635–639. DOI: 10.1126/science.288.5466.635.

[174] T. Fuji, A. Apolonski, and F. Krausz. "Self-stabilization of carrier-envelope offset phase by use of difference-frequency generation". *Opt. Lett.* 29.6 (2004), 632–634. DOI: 10.1364/OL.29.000632.

[175] T. Wittmann, B. Horvath, W. Helml, M. G. Schaetzel, X. Gu, A. L. Cavalieri, G. G. Paulus, and R. Kienberger. "Single-shot carrier-envelope phase measurement of few-cycle laser pulses". *Nature Phys.* 5.5 (2009), 357–362. DOI: 10.1038/NPHYS1250.

[176] A. M. Sayler, T. Rathje, W. Müller, K. Rühle, R. Kienberger, and G. G. Paulus. "Precise, real-time, every-single-shot, carrier-envelope phase measurement of ultrashort laser pulses". *Opt. Lett.* 36.1 (2011), 1–3. DOI: 10.1364/OL.36.000001.

[177] S. Micheau, Z. Chen, T. Morishita, A.-T. Le, and C. D. Lin. "Robust carrier-envelope phase retrieval of few-cycle laser pulses from high-energy photoelectron spectra in the above-threshold ionization of atoms". *J. Phys. B: At., Mol. Opt. Phys.* 42.6 (2009), 065402. DOI: 10.1088/0953-4075/42/6/065402.

[178] A. M. Sayler, M. Arbeiter, S. Fasold, D. Adolph, M. Möller, D. Hoff, T. Rathje, B. Fetić, D. B. Milošević, T. Fennel, and G. G. Paulus. "Accurate determination of absolute carrier-envelope phase dependence using photo-ionization". *Opt. Lett.* 40.13 (2015), 3137–3140. DOI: 10.1364/OL.40.003137.

[179] G. G. Paulus, F. Lindner, H. Walther, A. Baltuska, E. Goulielmakis, M. Lezius, and F. Krausz. "Measurement of the Phase of Few-Cycle Laser Pulses". *Phys. Rev. Lett.* 91.25 (2003), 253004. DOI: 10.1103/PhysRevLett.91.253004.

[180] F. Lindner, G. G. Paulus, H. Walther, A. Baltuska, E. Goulielmakis, M. Lezius, and F. Krausz. "Gouy phase shift for few-cycle laser pulses". *Phys. Rev. Lett.* 92.11 (2004), 113001. DOI: 10.1103/PhysRevLett.92.113001.

[181] S. Chelkowski, A. D. Bandrauk, and A. Apolonski. "Measurement of the carrier-envelope phase of few-cycle laser pulses by use of asymmetric photoionization". *Opt. Lett.* 29.13 (2004), 1557–1559. DOI: 10.1364/OL.29.001557.

[182] T. Paasch-Colberg, A. Schiffrin, N. Karpowicz, S. Kruchinin, S. Ozge, S. Keiber, O. Razskazovskaya, S. Muhlbrandt, A. Alnaser, M. Kubel, V. Apalkov, D. Gerster, J. Reichert, T. Wittmann, J. V. Barth, M. I. Stockman, R. Ernstorfer, V. S. Yakovlev, R. Kienberger, and F. Krausz. "Solid-state light-phase detector". *Nature Photon.* 8.3 (2014), 214–218. DOI: 10.1038/nphoton.2013.348.

[183] M. Kakehata, H. Takada, Y. Kobayashi, K. Torizuka, Y. Fujihira, T. Homma, and H. Takahashi. "Single-shot measurement of carrier-envelope phase changes by spectral interferometry". *Opt. Lett.* 26.18 (2001), 1436–1438. DOI: 10.1364/OL.26.001436.

[184] K. Osvay, M. Görbe, C. Grebing, and G. Steinmeyer. "Bandwidth-independent linear method for detection of the carrier-envelope offset phase". *Opt. Lett.* 32.21 (2007), 3095–3097. DOI: 10.1364/OL.32.003095.

[185] M. Görbe, C. Grebing, G. Steinmeyer, and K. Osvay. "A linear optical method for measuring the carrier-envelope phase drift". *Appl. Phys. B: Lasers Opt.* 95.2 (2009), 273–280. DOI: 10.1007/s00340-009-3424-0.

[186] P. Jójárt, Á. Börzsönyi, B. Borchers, G. Steinmeyer, and K. Osvay. "Agile linear interferometric method for carrier-envelope phase drift measurement". *Opt. Lett.* 37.5 (2012), 836–838. DOI: 10.1364/OL.37.000836.

[187] P. Jójárt, Á. Börzsönyi, V. Soskov, F. Zomer, R. Chiche, E. Cormier, and K. Osvay. "Carrier-envelope phase drift measurement of picosecond pulses by an all-linear-optical means". *Opt. Lett.* 39.20 (2014), 5913–5916. DOI: 10.1364/OL.39.005913.

[188] O. Gobert, N. Fedorov, O. Tcherbakoff, J. F. Hergott, M. Perdrix, F. Lepetit, D. Guillaumet, and M. Comte. "Measurement of Carrier-Envelope-Phase shifts using spectral interferometry with a broad frequency laser source". *Opt. Commun.* 285.3 (2012), 322–327. DOI: 10.1016/j.optcom.2011.09.047.

[189] Z. Yu and Y. Weng. "Spatial distribution of carrier-envelope phase for femtosecond pulsed laser beam profile determined by asymmetric spectral interferometry". *Opt. Lett.* 35.13 (2010), 2275–2277. DOI: 10.1364/OL.35.002275.

[190] T. Grósz, A. P. Kovács, M. Kiss, and R. Szipőcs. "Measurement of higher order chromatic dispersion in a photonic bandgap fiber: comparative study of spectral interferometric methods". *Appl. Opt.* 53.9 (2014), 1929–1937. DOI: 10.1364/AO.53.001929.

[191] L. Lepetit, G. Chériaux, and M. Joffre. "Linear techniques of phase measurement by femtosecond spectral interferometry for applications in spectroscopy". *J. Opt. Soc. Am. B* 12.12 (1995), 2467–2474. DOI: 10.1364/JOSAB.12.002467.

[192] M.-S. Kim, A. Naqavi, T. Scharf, K. J. Weible, R. Völkel, C. Rockstuhl, and H. P. Herzig. "Experimental and theoretical study of the Gouy phase anomaly of light in the focus of microlenses". *J. Opt.* 15.10 (2013), 105708. DOI: 10.1088/2040-8978/15/10/105708.

[193] X. Pang, D. G. Fischer, and T. D. Visser. "Generalized Gouy phase for focused partially coherent light and its implications for interferometry". *J. Opt. Soc. Am. A* 29.6 (2012), 989–993. DOI: 10.1364/JOSAA.29.000989.

[194] T. Visser and E. Wolf. "The origin of the Gouy phase anomaly and its generalization to astigmatic wavefields". *Opt. Commun.* 283.18 (2010), 3371–3375. ISSN: 0030-4018. DOI: 10.1016/j.optcom.2010.04.099.

[195] X. Pang, D. G. Fischer, and T. D. Visser. "Wavefront spacing and Gouy phase in presence of primary spherical aberration". *Opt. Lett.* 39.1 (2014), 88–91. DOI: 10.1364/OL.39.000088.

[196] B. S. Davis and L. Kaplan. "Transverse phase variation of a Gaussian beam". *J. Opt.* 15.7 (2013), 075706. DOI: 10.1088/2040-8978/15/7/075706.

[197] S. Feng, H. G. Winful, and R. W. Hellwarth. "Spatiotemporal evolution of focused single-cycle electromagnetic pulses". *Phys. Rev. E: Stat., Nonlinear, Soft Matter Phys.* 59.4 (4 1999), 4630–4649. DOI: 10.1103/PhysRevE.59.4630.

[198] L. M. Gillman. "Chromatic variation of spherical aberration in cemented doublets". *Trans. Opt. Soc.* 21.2 (1919), 53–64. DOI: 10.1088/1475-4878/21/2/301.

[199] W. Weinstein. "Chromatic Variation of Spherical Aberration". *Br. J. Appl. Phys.* 1.3 (1950), 67–73. DOI: 10.1088/0508-3443/1/3/304.

[200] **B. Major**. "Fókuszált ultrarövid fényimpulzusok alakjának és vivő-burkoló fázisának meghatározása". (in Hungarian). MSc Thesis. Szeged: Szegedi Tudományegyetem, 2012.

[201] Z. Mei. "Focal shift of focused truncated random electromagnetic beams". *Opt. Commun.* 284.22 (2011), 5248–5252. DOI: 10.1016/j.optcom.2011.07.041.

[202] C. Mafusire and A. Forbes. "Generalized beam quality factor of aberrated truncated Gaussian laser beams". *J. Opt. Soc. Am. A* 28.7 (2011), 1372–1378. DOI: 10.1364/JOSAA.28.001372.

[203] Y. Qiu, M. Gong, L. Huang, Q. Liu, P. Yan, H. Zhang, and T. Li. "The beam quality of a truncated Gaussian beam with aberrations". *Laser Phys. Lett.* 10.5 (2013), 055001. DOI: 10.1088/1612-2011/10/5/055001.

[204] R. Zoli, G. Oliva, R. Zocca, G. Tartarini, and P. Bassi. "Propagation of truncated focused astigmatic laser beams". *J. Opt. A-Pure Appl. Op.* 5.5 (2003), S315. DOI: 10.1088/1464-4258/5/5/385.

[205] J. P. Rolland, K. P. Thompson, K.-S. Lee, J. Tamkin, T. Schmid, and E. Wolf. "Observation of the Gouy phase anomaly in astigmatic beams". *Appl. Opt.* 51.15 (2012), 2902–2908. DOI: 10.1364/AO.51.002902.

[206] A. Weiner. "Femtosecond optical pulse shaping and processing". *Prog. Quant. Electron.* 19.3 (1995), 161–237. DOI: 10.1016/0079-6727(94)00013-O.

[207] A. M. Weiner. "Ultrafast optical pulse shaping: A tutorial review". *Opt. Commun.* 284.15 (2011), 3669–3692. DOI: 10.1016/j.optcom.2011.03.084.

[208] Á. Budó. *Kísérleti fizika III.* (in Hungarian). Tankönyvkiadó, 1977. ISBN: 963-19-0309-5. URL: http://www.tankonyvtar.hu/hu/tartalom/tamop425/2011_0001_519_04292_3_Fizika3/adatok.html.

[209] F. W. J. Olver, D. W. Lozier, R. F. Boisvert, and C. W. Clark, eds. *NIST Handbook of Mathematical Functions*. 1st. Cambridge University Press, 2010. ISBN: 0-521192-25-0. URL: http://dlmf.nist.gov/.

[210] M. A. Porras and P. Dombi. "Freezing the carrier-envelope phase of few-cycle light pulses about a focus". *Opt. Express* 17.22 (2009), 19424–19434. DOI: 10.1364/OE.17.019424.

[211] S. Feng and H. G. Winful. "Physical origin of the Gouy phase shift". *Opt. Lett.* 26.8 (2001), 485–487. DOI: 10.1364/OL.26.000485.

[212] R. Simon and N. Mukunda. "Bargmann invariant and the geometry of the Güoy effect". *Phys. Rev. Lett.* 70.7 (1993), 880–883. DOI: 10.1103/PhysRevLett.70.880.

[213] Z. Dačić and E. Wolf. "Changes in the spectrum of a partially coherent light beam propagating in free space". *J. Opt. Soc. Am. A* 5.7 (1988), 1118–1126. DOI: 10.1364/JOSAA.5.001118.

[214] A. Börzsönyi, R. S. Nagymihály, and K. Osvay. "Drift and noise of the carrier–envelope phase in a Ti:sapphire amplifier". *Laser Phys. Lett.* 13.1 (2016), 015301. DOI: 10.1088/1612-2011/13/1/015301.

[215] T. Tritschler, K. D. Hof, M. W. Klein, and M. Wegener. "Variation of the carrier-envelope phase of few-cycle laser pulses owing to the Gouy phase: a solid-state-based measurement". *Opt. Lett.* 30.7 (2005), 753–755. DOI: 10.1364/OL.30.000753.

[216] D. R. Austin, T. Witting, C. A. Arrell, F. Frank, A. S. Wyatt, J. P. Marangos, J. W. Tisch, and I. A. Walmsley. "Lateral shearing interferometry of high-harmonic wavefronts". *Opt. Lett.* 36.10 (2011), 1746–1748. DOI: 10.1364/OL.36.001746.

[217] E. Frumker, G. G. Paulus, H. Niikura, D. M. Villeneuve, and P. B. Corkum. "Frequency-resolved high-harmonic wavefront characterization". *Opt. Lett.* 34.19 (2009), 3026–3028. DOI: 10.1364/OL.34.003026.

[218] Z. Guang, M. Rhodes, M. Davis, and R. Trebino. "Complete characterization of a spatiotemporally complex pulse by an improved single-frame pulse-measurement technique". *J. Opt. Soc. Am. B* 31.11 (2014), 2736–2743. DOI: 10.1364/JOSAB.31.002736.

[219] K. Petermann. "Constraints for fundamental-mode spot size for broadband dispersion-compensated single-mode fibres". *Electron. Lett.* 19.18 (1983), 712–714. DOI: 10.1049/el:19830485.

[220] L. E. Helseth. "Strongly focused polarized light pulse". *Phys. Rev. E: Stat., Nonlinear, Soft Matter Phys.* 72.4 (2005), 047602. DOI: 10.1103/PhysRevE.72.047602.

[221] O. Korotkova and E. Wolf. "Changes in the state of polarization of a random electromagnetic beam on propagation". *Opt. Commun.* 246.1–3 (2005), 35–43. DOI: 10.1016/j.optcom.2004.10.078.

[222] D. F. V. James. "Change of polarization of light beams on propagation in free space". *J. Opt. Soc. Am. A* 11.5 (1994), 1641–1643. DOI: 10.1364/JOSAA.11.001641.

[223] G. C. Sherman. "Short pulses in the focal region". *J. Opt. Soc. Am. A* 6.9 (1989), 1382–1387. DOI: 10.1364/JOSAA.6.001382.

[224] E. Wolf. "Non-cosmological redshifts of spectral lines". *Nature* 326.6111 (1987), 363–365. DOI: 10.1038/326363a0.

Own publications

Publications related to the thesis

[T1] **B. Major**, Z. L. Horváth, and M. A. Porras. "Phase and group velocity of focused, pulsed Gaussian beams in the presence and absence of primary aberrations". *J. Opt.* 17.6 (2015), 065612. DOI: 10.1088/2040-8978/17/6/065612.

[T2] M. A. Porras, **B. Major**, and Z. L. Horvath. "Focusing to transform-limited, phase-controlled, few-cycle pulses with lenses". *AIP Conf. Proc.* 1462 (2012). Ed. by K. Osvay, P. Dombi, J. A. Fulop, and K. Varju, 49–52. DOI: 10.1063/1.4736758.

[T3] M. A. Porras, Z. L. Horvath, and **B. Major**. "On the use of lenses to focus few-cycle pulses with controlled carrier–envelope phase". *Appl. Phys. B: Lasers Opt.* 108.3 (2012), 521–531. DOI: 10.1007/s00340-012-5073-y.

[T4] M. A. Porras, **B. Major**, and Z. L. Horvath. "Carrier-envelope phase shift of few-cycle pulses along the focus of lenses and mirrors beyond the nonreshaping pulse approximation: the effect of pulse chirp". *J. Opt. Soc. Am. B* 29.12 (2012), 3271–3276. DOI: 10.1364/JOSAB.29.003271.

[T5] **B. Major**, D. Nemes, M. A. Porras, Z. L. Horváth, and A. P. Kovács. "Carrier-envelope phase changes in the focal region: propagation effects measured by spectral interferometry". *Appl. Opt.* 54.36 (2015), 10717–10724. DOI: 10.1364/AO.54.010717.

[T6] **B. Major**, M. A. Porras, and Z. L. Horváth. "Rotation of the polarization direction and reversal of helicity of ultrashort pulsed beams propagating in free space". *J. Opt. Soc. Am. A* 31.6 (2014), 1200–1205. DOI: 10.1364/JOSAA.31.001200.

[T7] **B. Major**, M. A. Porras, A. P. Kovács, and Z. L. Horváth. "The Influence of Generalized Focusing on Polarization-Shaped Few-Cycle Pulsed Beams". In: *Ultrafast Phenomena XIX*. Ed. by K. Yamanouchi, S. Cundiff, R. de Vivie-Riedle, M. Kuwata-Gonokami, and L. DiMauro. Vol. 162. Springer Proceedings in Physics. 2015, 813–816. DOI: 10.1007/978-3-319-13242-6_199.

Other scientific publications

[O1] V. Tosa, K. Kovács, **B. Major**, E. Balogh, and K. Varjú. "Propagation effects in highly ionised gas media". *Quantum Electron.* 46.4 (2016), 321–326. DOI: 10.1070/QEL16039.

[O2] B. Schütte, P. Weber, K. Kovács, E. Balogh, **B. Major**, V. Tosa, S. Han, M. J. J. Vrakking, K. Varjú, and A. Rouzée. "Bright attosecond soft X-ray pulse trains by transient phase-matching in two-color high-order harmonic generation". *Opt. Express* 23.26 (2015), 33947–33955. DOI: 10.1364/OE.23.033947.

[O3] K. Kovacs, V. Tosa, **B. Major**, E. Balogh, and K. Varju. "High-Efficiency Single Attosecond Pulse Generation With a Long-Wavelength Pulse Assisted by a Weak Near-Infrared Pulse". *IEEE J. Sel. Topics in Quantum Electron.* 21.5 (2015), 1–7. DOI: 10.1109/JSTQE.2015.2411580.

[O4] T. Ajtai, N. Utry, M. Pintér, **B. Major**, Z. Bozóki, and G. Szabó. "A method for segregating the optical absorption properties and the mass concentration of winter time urban aerosol". *Atmos. Environ.* 122 (2015), 313–320. DOI: 10.1016/j.atmosenv.2015.09.072.

[O5] Z. L. Horváth, **B. Major**, A. P. Kovács, and Z. Bor. "Pulse front distortions caused by primary aberrations". *J. Opt. Soc. Am. B* 30.7 (2013), 1853–1863. DOI: 10.1364/JOSAB.30.001853.

Conference presentations

(O) - oral presentation, ***(P)*** - poster presentation, * - Presenting author.
(Conference presentations are listed with their title presented, which might differ from the one accessible at the given urls.)

[O6] **B. Major***, K. Kovács, B. Manschwetus, E. Balogh, S. Maclot, L. Rading, P. Rudawski, C. Heyl, H. Coudert-Alteirac, B. Farkas, P. Johnsson, V. Tosa, A. L'Huillier, and K. Varjú. "Macroscopic Optimization of High Harmonic Generation for High Power Laser Pulses". In: *High-Brightness Sources and Light-Driven Interactions, 20–22nd March 2016, Long Beach, California, USA*. ***(O)***. 2016, HM6B.4. DOI: 10.1364/HILAS.2016.HM6B.4.

[O7] K. Kovács, **B. Major***, B. Manschwetus, E. Balogh, S. Maclot, L. Rading, P. Rudawski, C. Heyl, H. Coudert-Alteirac, B. Farkas, V. Tosa, P. Johnsson, A. L'Huillier, and K. Varjú. "Macroscopic optimization of high harmonic generation for high power laser pulses". In: *5th International Conference on Attosecond Physics, 6–10th July 2015, Saint-Sauveur, Canada*. ***(P)***. 2015, P2–39. URL: http://www.atto2015.inrs.ca/?page_id=1165.

[O8] E. Balogh*, K. Kovács, **B. Major**, A. Rouzée, S. Han, B. Schütte, P. Weber, M. J. Vrakking, V. Tosa, and K. Varjú. "Spectral shifts and asymmetries in two-color high-order harmonic generation". In: *5th International Conference on Attosecond Physics, 6–10th July 2015, Saint-Sauveur, Canada*. ***(P)***. 2015, P3–33. URL: http://www.atto2015.inrs.ca/?page_id=1200.

[O9] E. Balogh, P. Weber, K. Kovács, B. Schütte, **B. Major**, V. T. S, Han, M. J. Vrakking, A. Rouzée, and K. Varjú*. "Bright attosecond pulse generation under transient phase-matching in two-colour high-order harmonic generation". In: *5th International Conference on Attosecond Physics, 6–10th July 2015, Saint-Sauveur, Canada*. ***(P)***. 2015, P3–3. URL: http://www.atto2015.inrs.ca/?page_id=1200.

[O10] B. Schütte, P. Weber, K. Kovács, E. Balogh, **B. Major**, V. Tosa, S. Han, M. J. Vrakking, K. Varjú*, and A. Rouzée. "Bright attosecond pulse generation under transient phase-matching in two-colour high-order harmonic generation". In: *2015 European Conference on Lasers and Electro-Optics - European Quantum Electronics Conference, 21–25th June 2015, Munich, Germany.* ***(O)***. 2015, CG.1.4. URL: http://www.osapublishing.org/abstract.cfm?URI=CLEO_Europe-2015-CG_1_4.

[O11] K. Kovács*, E. Balogh, **B. Major**, P. Weber, B. Schütte, A. Rouzee, V. Tosa, K. Varjú, and M. Vrakking. "Single Attosecond Pulse Generation from Combined 50 fs NIR and MIR Laser Pulses — Case Study". In: *14th International Balkan Workshop on Applied Physics, 2–4th July 2014, Constanta, Romania.* ***(P)***. 2014, S2 P10. URL: http://www.ibwap.ro/2013/uploads/abstracts/Final_list_of_accepted_abstracts_June_16.pdf.

[O12] K. Kovács*, **B. Major**, E. Balogh, P. Weber, B. Schütte, A. Rouzee, V. Tosa, K. Varjú, and M. J. J. Vrakking. "Obtaining Single Attosecond Pulse from Two 50-fs Laser Pulses". In: *33rd European Conference on Laser Interaction with Matter, 31st August–5th September 2014, Paris, France.* ***(P)***. 2014, TuP2–15. URL: http://web.luli.polytechnique.fr/ECLIM2014/ECLIM_BoA_revised_bis.pdf.

[O13] **B. Major***, M. A. Porras, D. Nemes, A. P. Kovacs, and Z. L. Horvath. "Carrier-envelope Phase Changes of Few-cycle Pulses Focused by Lenses: Simulations and Measurements". In: *6th Europhoton Conference, 24–29th August 2014, Neuchatel, Switzerland.* ***(P)***. 2014, WePT1–P23. URL: http://2014.europhoton.org/files/europhoton%202014%20web-2.pdf.

[O14] **B. Major***, M. A. Porras, A. P. Kovacs, and Z. L. Horvath. "Polarization State Changes of Femtosecond, Polarization-shaped Pulsed Beams on Free Space Propagation". In: *19th International Conference on Ultrafast Phenomena, 7–11th July 2014, Okinawa, Japan.* ***(P)***. 2014, 07.Mon.P1.37. DOI: 10.1364/UP.2014.07.Mon.P1.37.

[O15] **B. Major***, M. A. Porras, and Z. L. Horváth. "Carrier-envelope phase shift manipulation of focused ultrashort pulses with the use of separable achromatic doublets". In: *4th International Conference on Attosecond Physics, 7–12th July 2013. Paris, France.* ***(P)***. 2013, P3.8. URL: http://atto2013.celia.u-bordeaux1.fr/images/program_online/Book_of_Abstracts.pdf.

[O16] M. A. Porras, Z. L. Horvath, and **B. Major***. "On the use of lenses to freeze the carrier-envelope phase of femtosecond light pulses about a focus". In: *Light at Extreme Intensities 2011, 14-18th November 2011, Szeged, Hungary.* ***(P)***. 2011, P19. URL: http://lei2011.eli-hungary.hu/Timetable_111114.pdf.

[O17] A. Sütő*, I. Hanyecz, **B. Major**, A. Cheesman, J. Budai, L. Lugosi, Á. Mayer, G. Nádudvari, Z. Tóth, and T. Pavelka. "Ellipsometric Investigations of Thin SiN Films Deposited Onto Plain Si and Textured Si Surfaces by Pulsed Laser Deposition". In: *5th International Conference on Spectroscopic Ellipsometry, 23–28th May 2010, Albany, New York, USA.* ***(P)***. 2010.

Popular science publications (in Hungarian)

[O18] **B. Major**, Z. Horváth, A. P. Kovács, and Z. Bor. "A fényelhajlás Young-féle elmélete és annak alkalmazása az ultrarövid fényimpulzusok diffrakciójakor — a szélihullám-impulzus". *Fizikai Szemle* LXIV.9 (2014), 294–298. URL: http://fizikaiszemle.hu/archivum/fsz1409/MajorB_HorvathZ_KovacsAP_BorZs.pdf.

[O19] Z. Farkas, T. Gajdos, **B. Major**, and A. Nagy. "Korok és tudósok – a színpadon Arkhimédész, Galilei és Newton". *Fizikai Szemle* LXI.7–8 (2011), 267–272. URL: http://fizikaiszemle.hu/archivum/fsz110708/Farkas-Zsuzsanna.pdf.

Appendices

Appendix

A

Description of pulse properties

A.1 Analytical pulse shapes in the presence of higher order phase derivatives

The temporal variation of the electric field of linearly polarized pulses with Gaussian spectral amplitude $p(\omega)$ can be calculated analytically if the spectral phase $\varphi(\omega)$ can be described by a third order polynomial. This is the reason why in most cases of theoretical studies the temporal envelope is assumed to be Gaussian, since analytical solutions have several advantages. Following the notation of Section 2.2.1, the amplitude spectrum is written as

$$p(\omega) = F_0 \frac{\sqrt{2\pi}}{\sigma} \exp\left[-\frac{(\omega-\omega_0)^2}{2\sigma^2}\right] . \tag{A.1}$$

The factor before the exponential in the previous expression, with the arbitrary amplitude F_0, has been chosen as such to yield simpler formulas later. The reason behind the variation of $\varphi(\omega)$ is usually the dispersion during propagation, so it can be written as $\varphi(\omega) = k(\omega)z$ in most cases when the propagation direction is along axis z, $k(\omega)$ being the wave number of the radiation. The temporal shape of a pulse with given complex spectrum $\tilde{U}(\omega) = p(\omega)\exp[\imath\varphi(\omega)]$ can be calculated using the inverse Fourier transform (see (2.2)). In the following, the calculation of the analytical pulse shapes will be detailed, assuming a spectral phase given by zeroth, first, second and third order polynomials, detailing the discussion of [101] in a consistent manner.

Constant spectral phase The constant spectral phase means that only the zeroth order term in (2.6) is assumed to be present, that is $\varphi(\omega) = \varphi(\omega_0)$. Applying integration

by substitution using the variable $\mu = \omega - \omega_0$ ($\omega = \mu + \omega_0$, $\mathrm{d}\mu = \mathrm{d}\omega$) during calculating the integral of the inverse Fourier transform $\mathscr{F}^{-1}\{p(\omega)\exp[\iota\varphi(\omega)]\}$ in this case yields

$$\tilde{E}(t) = \frac{\sqrt{2\pi}}{\sigma} F_0 \exp[\iota\varphi(\omega_0)] \exp[-\iota\omega_0 t] \underbrace{\frac{1}{2\pi}\int_{-\infty}^{\infty} \exp\left[-\frac{\mu^2}{2\sigma^2}\right] \exp[-\iota\mu t]\ \mathrm{d}\mu}_{\mathscr{F}^{-1}\left\{\exp\left[-\frac{\mu^2}{2\sigma^2}\right]\right\}} . \tag{A.2}$$

Knowing that

$$\mathscr{F}^{-1}\left\{\exp\left[-\frac{\mu^2}{2\sigma^2}\right]\right\} = \frac{\sigma}{\sqrt{2\pi}}\exp\left[-\frac{t^2\sigma^2}{2}\right], \tag{A.3}$$

the electric field is

$$\tilde{E}(t) = F_0 \exp\left[-\frac{t^2\sigma^2}{2}\right] \exp[\iota\varphi(\omega_0) - \iota\omega_0 t] . \tag{A.4}$$

The above result shows that a non-zero constant spectral phase only means a phase shift in the temporal domain compared to the $\varphi(\omega) \equiv 0$ case. In this example, this appears as a Gaussian pulse with $\sqrt{4\ln(2)}/\sigma$ transform-limited FWHM duration and with a CEP equal to $\varphi(\omega_0)$, like the two pulses in Figure 2.1 or the one in Figure 2.2(a) ($\varphi(\omega_0) = 0$ case). Since the phase $\varphi(\omega_0)$ is only a constant factor not influencing the integral in (A.2), it is easy to see that the constant spectral phase only means a CEP change for any pulse shape with arbitrary $p(\omega)$.

Linear spectral phase As a next step, the assumption is that the spectral phase is given by a first order polynomial according to $\varphi(\omega) = \varphi(\omega_0) + \mathrm{GD}\,(\omega - \omega_0)$, following the nomenclature of Section 2.2.1. Substituting the amplitude (A.1) with this linear phase into the formula (2.2) of the inverse Fourier transform yields

$$\tilde{E}(t) = \frac{\sqrt{2\pi}}{\sigma} F_0 \exp[\iota\varphi(\omega_0)] \exp[-\iota\omega_0 t] \frac{1}{2\pi}\int_{-\infty}^{\infty} \exp\left[-\frac{\mu^2}{2\sigma^2}\right] \exp[-\iota\mu(t - \mathrm{GD})]\ \mathrm{d}\mu\,, \tag{A.5}$$

which is obtained by using the same $\mu = \omega - \omega_0$ variable substitution as in (A.2). It can be easily seen that the integral in (A.5) has the same form as the integral in (A.2), but with the variable $\tau = t - \mathrm{GD}$ instead of t. This means that the temporal variation of the field can be expressed as

$$\tilde{E}(t) = F_0 \exp\left[-\frac{\tau^2\sigma^2}{2}\right] \exp[\iota\varphi(\omega_0) - \iota\omega_0 t] . \tag{A.6}$$

So the linear term of the spectral phase results in a temporal shift in time by GD, as discussed in Section 2.2.1. Note, however, that only the envelope function is moved in time, while the phase of the exponential function describing the carrier wave in (A.6) is

unaltered. So, the value of GD also changes the CEP of the pulse, as it can be seen in the example of Figure 2.2(c). Since only the shift theorem of Fourier transform has been utilized [98], these findings are valid for any $p(\omega)$ shape, just like it was in the case of constant spectral phase.

Quadratic spectral phase Let us assume that $\varphi(\omega)$ is given by a second-order polynomial, that is, the spectral phase is given by

$$\varphi(\omega) = \varphi(\omega_0) + \mathrm{GD}\,(\omega - \omega_0) + \frac{\mathrm{GDD}}{2}(\omega - \omega_0)^2\,. \tag{A.7}$$

Expressing the inverse Fourier transform of $p(\omega)\exp[\iota\varphi(\omega)]$ with the substitutions $\mu = \omega - \omega_0$ and $\tau = t - \mathrm{GD}$ used in the previous two cases yields

$$\tilde{E}(t) = \frac{\sqrt{2\pi}}{\sigma} F_0 \exp[\iota\varphi(\omega_0)] \exp[-\iota\omega_0 t]\, \frac{1}{2\pi} \int_{-\infty}^{\infty} \exp\left[-\left(\frac{1}{2\sigma^2} - \iota\frac{\mathrm{GDD}}{2}\right)\mu^2\right] \exp[-\iota\mu\tau]\ \mathrm{d}\mu\,. \tag{A.8}$$

If the expression

$$\left(\frac{1}{2\sigma^2} - \iota\frac{\mathrm{GDD}}{2}\right) = \frac{1}{2\Omega^2} \quad \Rightarrow \quad \Omega^2 = \left(\frac{1}{\sigma^2} - \iota\mathrm{GDD}\right)^{-1} \tag{A.9}$$

is introduced, the integral in (A.8) is again formally exactly the same as in the previous two cases. So the electric field is given by

$$\tilde{E}(t) = F_0 \frac{\Omega}{\sigma} \exp\left[-\frac{\tau^2\Omega^2}{2}\right] \exp[\iota\varphi(\omega_0) - \iota\omega_0 t]\ . \tag{A.10}$$

While the above expression is short, it is worth to expand it to a more expressive form. To achieve this the

$$\Pi^2 \equiv 1 + \mathrm{GDD}^2\sigma^4 \tag{A.11}$$

parameter is introduced and the following replacements can be made:

$$\Omega^2 = \frac{\sigma^2}{\Pi^2} + \iota\frac{\mathrm{GDD}\sigma^4}{\Pi^2}\,, \tag{A.12}$$

$$\frac{\Omega}{\sigma} = \frac{\sqrt{1 + \iota\mathrm{GDD}\sigma^2}}{\Pi} = \frac{1}{\sqrt{\Pi}} \exp\left[\frac{\iota}{2}\mathrm{atan}\left[\mathrm{GDD}\sigma^2\right]\right]\ . \tag{A.13}$$

So the expression for the temporal variation can be rewritten as

$$\tilde{E}(t) = \frac{F_0}{\sqrt{\Pi}} \exp\left[-\frac{\tau^2\sigma^2}{2\Pi^2}\right] \exp\left[\iota\left(\frac{1}{2}\mathrm{atan}\left[\mathrm{GDD}\sigma^2\right] - \frac{\tau^2\mathrm{GDD}\sigma^4}{2\Pi^2} + \varphi(\omega_0) - \omega_0 t\right)\right]\ . \tag{A.14}$$

The above expression (A.14) shows that the pulse still has a Gaussian envelope, but it is Π times longer then the possible minimum (the transform-limited) duration, and its amplitude is decreased by the multiplication factor $1/\sqrt{\Pi}$. The temporal phase is also altered. On one hand, a constant phase given by the first factor in the exponential of (A.14) is added, shifting the CEP. It is also visible that $\omega_0 t$ is not the only time-dependent part of the phase, but a quadratic expression is also present. Usually the first derivative of the temporal phase with respect to time is considered as the frequency of the carrier wave. For (A.14) this means that $\omega(\tau) = \omega_0 + (\mathrm{GDD}\sigma^4/\Pi^2)\tau$, so the angular frequency of the wave changes linearly in time, and it equals to ω_0 only at the envelope peak. So quadratic spectral phase causes the linear chirp of the wave packet, mentioned in Section 2.2.1. An example pulse shape given by (A.14) can be seen in Figure 2.2(d) with normalized amplitude.

Cubic spectral phase Finally, consider the spectral phase described by the third order polynomial

$$\varphi(\omega) = \varphi(\omega_0) + \mathrm{GD}\,(\omega - \omega_0) + \frac{\mathrm{GDD}}{2}(\omega - \omega_0)^2 + \frac{\mathrm{TOD}}{6}(\omega - \omega_0)^3\,. \tag{A.15}$$

To calculate the temporal shape, the first step is again the variable substitution $\mu = \omega - \omega_0$ and $\tau = t - \mathrm{GD}$ during the evaluation of the inverse Fourier transform, and the results is

$$\begin{aligned}\tilde{E}(t) =& \frac{\sqrt{2\pi}}{\sigma} F_0 \exp[\iota\,(\varphi(\omega_0) - \omega_0 t)] \\ &\times \frac{1}{2\pi}\int_{-\infty}^{\infty} \exp\left[-\left(\frac{1}{2\sigma^2} - \iota\frac{\mathrm{GDD}}{2}\right)\mu^2\right] \exp\left[\iota\frac{\mathrm{TOD}}{6}\mu^3\right] \exp[-\iota\mu\tau]\;\mathrm{d}\mu\,.\end{aligned} \tag{A.16}$$

With the new variable

$$\eta^3 = \frac{\mathrm{TOD}}{2}\mu^3 \quad \Rightarrow \quad \mu^m = \left(\frac{2}{\mathrm{TOD}}\right)^{m/3}\eta^m, \quad \frac{\mathrm{d}\mu}{\mathrm{d}\eta} = \left(\frac{2}{\mathrm{TOD}}\right)^{1/3}\,. \tag{A.17}$$

and the simplified naming

$$a = -\left(\frac{1}{\iota 2\sigma^2} - \frac{\mathrm{GDD}}{2}\right)\left(\frac{2}{\mathrm{TOD}}\right)^{2/3}\,, \tag{A.18}$$

$$b = -\left(\frac{2}{\mathrm{TOD}}\right)^{1/3}\tau\,, \tag{A.19}$$

(A.16) becomes

$$\tilde{E}(t) = \frac{\sqrt{2\pi}}{\sigma} F_0 \exp[\iota\left(\varphi(\omega_0) - \omega_0 t\right)] \left(\frac{2}{\mathrm{TOD}}\right)^{1/3} \frac{1}{2\pi} \int_{-\infty}^{\infty} \exp\left[\iota a \eta^2\right] \exp\left[\iota \frac{\eta^3}{3}\right] \exp[\iota b \eta] \, \mathrm{d}\eta \,. \tag{A.20}$$

The expression in the integral can be rewritten as

$$\exp\left[\iota a \eta^2\right] \exp\left[\iota \frac{\eta^3}{3}\right] \exp[\iota b \eta] = \exp\left[\frac{\iota}{3}(a+\eta)^3\right] \exp\left[-\iota \frac{a^3}{3}\right] \exp\left[\iota(b-a^2)\eta\right] \,, \tag{A.21}$$

and with the variable $q = a + \eta$ ($\eta = q - a$) and a little algebra the wave form becomes

$$\begin{aligned} \tilde{E}(t) = & \frac{\sqrt{2\pi}}{\sigma} F_0 \exp[\iota\left(\varphi(\omega_0) - \omega_0 t\right)] \left(\frac{2}{\mathrm{TOD}}\right)^{1/3} \exp\left[-\iota \frac{a^3}{3}\right] \exp[-\iota a b] \exp\left[\iota a^3\right] \\ & \times \underbrace{\frac{1}{2\pi} \int_{-\infty}^{\infty} \exp\left[\iota \frac{q^3}{3}\right] \exp\left[\iota(b-a^2)q\right] \, \mathrm{d}q}_{\mathrm{Ai}(b-a^2)} \,. \end{aligned} \tag{A.22}$$

The introduced special function $\mathrm{Ai}(z)$ above is the Airy function [102], the integral representation of which is

$$\mathrm{Ai}(z) = \frac{1}{2\pi} \int_{-\infty}^{\infty} \exp\left[\iota\left(\frac{x^3}{3} + zx\right)\right] \mathrm{d}x \,. \tag{A.23}$$

So, in a short form, the pulse shape in the presence of third-order spectral phase is given by

$$\tilde{E}(t) = F_0 \frac{\sqrt{2\pi}}{\sigma} \left(\frac{2}{\mathrm{TOD}}\right)^{1/3} \exp[\iota\left(\varphi(\omega_0) - \omega_0 t\right)] \exp\left[\iota a \left(\frac{2}{3}a^2 - b\right)\right] \mathrm{Ai}(b - a^2) \,. \tag{A.24}$$

As it can be seen from (A.24), the analytical expression is very complex, not much direct implications can be made on how the third-order term modifies the pulse shape. However, a typical wave form can be seen in Figure 2.2(d), which shows that TOD causes an asymmetric distortion in time and additional side-wings appear. Note that (A.24) can not be interpreted when TOD ≤ 0, and does not reproduce directly (A.14) in an analytical form, like (A.14) reproduces (A.6) when GDD $\equiv 0$. In the case TOD $\equiv 0$ (A.24) gives (A.14) as an asymptotic limit. For this reason, when the cubic phase term is small, using (A.24) is not necessarily the most reliable source for temporal shape determination, as the "zero times infinity" type limit is a general source of numerical error.

A.2 Instantaneous polarization state and -ellipse

A.2.1 Derivation of the instantaneous polarization properties in Cartesian coordinates

The description of time-dependent polarization state of polarization-shaped ultrashort pulses is based on discussion of the same property of transverse monochromatic waves [90]. The only difference is that while for infinite harmonic waves the amplitudes and relative phases of the perpendicular components are constant, for non-monochromatic waves they are time dependent [115, 125, 126], they have the same form as (2.3), that is,

$$\tilde{E}_x(t) = A_x(t)\exp[\iota\,(\hat{\varphi}_x(t) - \omega_0 t)]\ , \tag{A.25}$$

$$\tilde{E}_y(t) = A_y(t)\exp[\iota\,(\hat{\varphi}_y(t) - \omega_0 t)]\ . \tag{A.26}$$

Note that References [90, 125, 126] and [115], on which the following considerations are based, use an opposite sign convention, $+\omega_0 t$ and $-\omega_0 t$, respectively. Here, consistent with other parts of this work, the latter is used, and as a result sign differences may appear from the expressions in the references.

As discussed in textbooks, the sum of the real part of the (A.25) and (A.26) perpendicular waves — the electric field vectors — draws an ellipse in the $x-y$ plane if $A_{x,y}(t)$ and $\hat{\varphi}_{x,y}(t)$ are time-independent [90, 127, 130]. This allow us to similarly define a polarization ellipse for every instant of time for (A.25) and (A.26), which can be thought as the trajectory along which the electric field would traverse if we would freeze the amplitudes $A_{x,y}(t)$ and phases $\hat{\varphi}_{x,y}(t)$ at that moment. This ellipse describes how the instantaneous electric field would change due to phase transformations, meaning what would happen by adding a time independent phase to both components (A.25) and (A.26) [115]. By rotating the frame of reference by $\Psi(t)$, the oscillations happening along the major- and minor axes of the instantaneous ellipse can be given, so in the complex formalism they are written as

$$\tilde{E}_M(t) = \tilde{E}_x(t)\cos[\Psi(t)] + \tilde{E}_y(t)\sin[\Psi(t)]\ , \tag{A.27}$$

$$\tilde{E}_m(t) = -\tilde{E}_x(t)\sin[\Psi(t)] + \tilde{E}_y(t)\cos[\Psi(t)]\ , \tag{A.28}$$

or they can be expressed in a different form resembling the equation of ellipse (given again in complex form)

$$\tilde{E}_M(t) = A_M(t)\exp[\iota\,(\hat{\varphi}_M(t) - \omega_0 t)]\ , \tag{A.29}$$

$$\tilde{E}_m(t) = \pm A_m(t)\exp[\iota\,(\hat{\varphi}_M(t) - \omega_0 t - \pi/2)]\ . \tag{A.30}$$

In the last expression the $\pm$ sign distinguishes the rotation direction of the field vector (can be described by another parameter introduced later, see Figure 2.5), and $A_M(t) \geq A_m(t) \geq 0 \quad (\forall t)$. By introducing the two angles

$$\tan[\alpha(t)] = \frac{A_y(t)}{A_x(t)}, \quad \alpha(t) \in [0, \pi/2]\,, \tag{A.31}$$

$$\tan[\chi(t)] = \pm\frac{A_M(t)}{A_m(t)}, \quad \chi(t) \in [-\pi/4, \pi/4]\,, \tag{A.32}$$

and the phase difference $\Delta\hat{\varphi}$ between the two components given by (2.10) one can get the following equations for the ellipse properties with some algebra from (A.27), (A.28), (A.29) and (A.30) [90, 127]:

$$\sin[2\chi(t)] = \sin[2\alpha(t)]\sin[\Delta\hat{\varphi}(t)]\ , \tag{A.33}$$

$$\tan[2\Psi(t)] = \tan[2\alpha(t)]\cos[\Delta\hat{\varphi}(t)]\ , \tag{A.34}$$

$$[A_x(t)]^2 + [A_y(t)]^2 = [A_M(t)]^2 + [A_m(t)]^2\,. \tag{A.35}$$

The instantaneous ellipticity $-\pi/4 \leq \chi(t) \leq \pi/4$ can be obtained by rearranging (A.33), giving

$$\chi(t) = \frac{1}{2}\mathrm{asin}[\sin[2\alpha(t)]\sin[\Delta\hat{\varphi}(t)]]\ . \tag{A.36}$$

As it was noted already, the sign of $\chi(t)$ puts distinction between left- (negative) and right (positive) helicity, that is the electric field rotates counterclockwise or clockwise as time passes, respectively, if someone looks towards the source of the wave. This means that the $\pm$ sign can be replaced in this case by $\mathrm{sgn}\,[\chi(t)]$, just like it was written in (2.15). The equation for $\Psi(t)$, (A.34), can be similarly rearranged, and it yields

$$\hat{\Psi}(t) = \frac{1}{2}\mathrm{atan}[\tan[2\alpha(t)]\cos[\Delta\hat{\varphi}(t)]]\ . \tag{A.37}$$

Note, however, that $\hat{\Psi}(t)$ can only have a value between $-\pi/4$ and $\pi/4$, while the possible range for the orientation of an ellipse is the $[-\pi/2, \pi/2)$ interval. Exploiting the π periodicity of the tangent function it is easy to see that if $\hat{\Psi}$ is a solution of (A.34), then $\hat{\Psi} \pm \pi/2$ is solution as well. This way it can be shown that orientation $-\pi/2 \leq \Psi(t) < \pi/2$ is given by (2.11). Using simple algebraic manipulations applied on (A.35) using the definitions of $\alpha(t)$ and $\chi(t)$ ((A.31) and (A.32)) it can be seen that

$$A_M^2(t)\left[1 + \tan^2[\chi(t)]\right] = A_x^2(t)\left[1 + \tan^2[\alpha(t)]\right] \tag{A.38}$$

from which the size of the semi-major axis can be found to be (2.13). The (2.14) size of

the minor axis is simply obtained by rearranging (A.32).

To describe the wave using the ellipse equations (A.29) and (A.30) (or (2.15) and (2.16)), one quantity is still missing, the phase $\hat{\varphi}_M(t)$ associated with the major axis of the ellipse. One method to find the expression is a graphical solution [125], or it can be done in a pure mathematical way [90]. Here a different algebraic approach is presented. Consider a moment t_M when the electric field is parallel to the major axis, so $\hat{\varphi}_M(t_M) - \omega_0 t_M = 0 \Rightarrow -\omega_0 t_M = -\hat{\varphi}_M(t_M)$. The substitution of this expression into (A.25) and (A.29) yields

$$E_x(t_M) = A_x(t_M)\cos[\hat{\varphi}_x(t_M) - \hat{\varphi}_M(t_M)]\ , \tag{A.39}$$

$$E_M(t_M) = A_M(t_M)\,. \tag{A.40}$$

It is easy to see geometrically (look at Figure 2.5) that also

$$E_y(t_M) = A_M(t_M)\cos[\Psi(t_M)]\ . \tag{A.41}$$

By substituting (A.39), (A.40) and (A.41) into the real part of (A.27), utilizing some trigonometric identities and the easily obtainable $A_M(t)/A_x(t) = \cos[\chi(t)]\,/\cos[\alpha(t)]$ expression, one can get

$$\cos[\hat{\varphi}_x(t_M) - \hat{\varphi}_M(t_M)] = \frac{\cos[\chi(t_M)]\cos[\Psi(t_M)]}{\cos[\alpha(t_M)]}\,. \tag{A.42}$$

Of course, the equation above is valid for arbitrary t, introducing t_M was only necessary to simply obtain the formula. Due to the even nature of the cosine function, this means

$$\hat{\varphi}_x(t) - \hat{\varphi}_M(t) = \pm\mathrm{acos}\left[\frac{\cos[\chi(t)]\cos[\Psi(t)]}{\cos[\alpha(t)]}\right]\,. \tag{A.43}$$

With a similar logic to that of the graphical solution of [125] one can replace $\pm$ with a direct expression, and have (2.17).

A.2.2 Instantaneous polarization properties in circular basis

To express the characteristics of the polarization ellipse using the amplitudes and phases of the left- and right circularly polarized components, first let us write down how the total electric field can be expressed using them. By looking at (2.18) and (2.19) it is easy to see that the total field is given by

$$\tilde{\mathbf{E}}(t) = \left\{\frac{A_l(t)}{\sqrt{2}}\exp[\iota\hat{\varphi}_l(t)]\,(\mathbf{u}_x + \iota\mathbf{u}_y) + \frac{A_r(t)}{\sqrt{2}}\exp[\iota\hat{\varphi}_r(t)]\,(\mathbf{u}_x - \iota\mathbf{u}_y)\right\}\exp[-\iota\omega_0 t]\ . \tag{A.44}$$

In the following expressions, for the sake of brevity, all temporal dependence will be neglected as only algebraic manipulations will be made. Let us introduce new variables, which are named as (not by accident, as it will be seen later),

$$\Psi = \frac{\hat{\varphi}_r - \hat{\varphi}_l}{2}\,, \tag{A.45}$$

$$\hat{\varphi}_M = \frac{\hat{\varphi}_r + \hat{\varphi}_l}{2}\,. \tag{A.46}$$

By applying the substitutions of (A.45) and (A.46) ($\hat{\varphi}_r = \hat{\varphi}_M + \Psi$, $\hat{\varphi}_l = \hat{\varphi}_M - \Psi$) in (A.44) it can be shown that the ampltiude and phase of the x and y components read as

$$A_x \exp[\iota\hat{\varphi}_x] = \frac{1}{\sqrt{2}}\left(A_l \exp[-\iota\Psi] + A_r \exp[\iota\Psi]\right)\exp[\iota\hat{\varphi}_M]\,, \tag{A.47}$$

$$A_y \exp[\iota\hat{\varphi}_y] = \frac{\iota}{\sqrt{2}}\left(A_l \exp[-\iota\Psi] - A_r \exp[\iota\Psi]\right)\exp[\iota\hat{\varphi}_M]\,. \tag{A.48}$$

The inverse relations can also be simply obtained from (A.47) and (A.48), that is,

$$A_r \exp[\iota\hat{\varphi}_M] = \frac{1}{\sqrt{2}}\left(A_x \exp[\iota\hat{\varphi}_x] + \iota A_y \exp[\iota\hat{\varphi}_y]\right)\exp[-\iota\Psi]\,, \tag{A.49}$$

$$A_l \exp[\iota\hat{\varphi}_M] = \frac{1}{\sqrt{2}}\left(A_x \exp[\iota\hat{\varphi}_x] - \iota A_y \exp[\iota\hat{\varphi}_y]\right)\exp[\iota\Psi]\,. \tag{A.50}$$

Using (A.49), (A.50) and the well known relations $\cos(\Psi) = (\exp[\iota\Psi] + \exp[-\iota\Psi])/2$, $\sin(\Psi) = (\exp[\iota\Psi] - \exp[-\iota\Psi])/2\iota$, one can get that

$$\frac{1}{\sqrt{2}}\left(A_r + A_l\right)\exp[\iota\hat{\varphi}_M] = A_x \exp[\iota\hat{\varphi}_x]\cos(\Psi) + A_y \exp[\iota\hat{\varphi}_y]\sin(\Psi)\,. \tag{A.51}$$

Notice that if the $\exp[-\iota\omega_0 t]$ term is not considered then the right-hand side of (A.51) is equivalent to the right-hand side of (A.27), which means that the equivalence of (A.51) and (A.29) yields

$$A_M = \frac{A_r + A_l}{\sqrt{2}}\,. \tag{A.52}$$

Express similarly

$$\frac{1}{\sqrt{2}}\left(A_r - A_l\right)\exp[\iota(\hat{\varphi}_M - \pi/2)] = -A_x \exp[\iota\hat{\varphi}_x]\sin(\Psi) + A_y \exp[\iota\hat{\varphi}_y]\cos(\Psi)\,. \tag{A.53}$$

Comparing (A.53), (A.28) and (A.30) gives, like for the amplitude of the semi-major axis,

$$A_m = \frac{|A_r - A_l|}{\sqrt{2}}\,. \tag{A.54}$$

Taking the modulus is necessary in the previous expression, because $A_m \geq 0$. This does not contradict the derivation before, because using (A.32) with (A.52) and (A.54) yields

$$\tan(\chi) = \frac{A_r - A_l}{A_r + A_l}\,, \tag{A.55}$$

having a consistent sign convention with the previous definition of χ.

Appendix

B

Pulsed beam propagation

B.1 Gaussian beam focusing using ABCD formalism

In the following, simple formulas describing the focused complex field of a Gaussian beam is given using the ABCD formalism to treat the propagation through the focusing system and free space. An important limiting assumption of the expressions below is that the focusing element is placed directly at the beam waist. Analytical formula for a case when the position of the focal element does not coincide with the plane of the beam waist is also obtainable, but will not be given here.

The quantity of interest here is the field in the vicinity of the focal region, so in the ABCD analysis the matrix describing the focal element of focal length f and the matrix giving the free-space propagation of distance z behind it has to be used, which is

$$\begin{pmatrix} 1 & z \\ 0 & 1 \end{pmatrix} \begin{pmatrix} 1 & 0 \\ -1/f & 1 \end{pmatrix} = \begin{pmatrix} 1 - z/f & z \\ -1/f & 1 \end{pmatrix} . \tag{B.1}$$

The presumption of focusing at waist means that the field in the plane just before the focusing element is given by

$$\tilde{G}(\mathbf{r}) = \exp\left[\iota k \frac{r^2}{2\tilde{q}}\right] , \tag{B.2}$$

similarly to (2.43), with the $k = \omega/c$ wave number, the $r = (x^2 + y^2)^{1/2}$ transverse radial coordinate, and the complex beam parameter at the beam waist (that is, $z = 0$ in (2.39)) is $\tilde{q} = -\iota L$. The Rayleigh length L is given by its definition (2.38). Using the transformation law of the complex beam parameter (2.42) [137], it can be easily obtained

that the beam parameter of the focused field is [139]

$$\tilde{q}_f(Z) = Z + \frac{f}{1 + \iota L/f}\,, \tag{B.3}$$

with $Z = z - f$ being the distance measured from the geometrical focal point. From this, the Rayleigh length of the focused beam can be expressed as

$$L_f = \frac{L}{1 + L^2/f^2}\,. \tag{B.4}$$

To get the full field, the "amplitude" transformation of (2.44) also has to be used, which with (B.1) results in

$$\frac{1}{A + B/\tilde{q}} = \frac{1}{\tilde{q}_f(Z)} \frac{-\iota L}{1 + \iota L/f} = \frac{\tilde{q}_f(-f)}{\tilde{q}_f(Z)}\,. \tag{B.5}$$

From the formula above, it can be easily seen (of course not forgetting about the $\exp[\iota kz] = \exp[\iota k(Z + f)]$ factor) that the focused Gaussian beam is given by (2.45).

For later convenience, it is advantageous to expand the $\tilde{G}_f(\mathbf{r})$ function describing the focused Gaussian beam using the Euler's formula as (similarly to how it is done for several functions in this work)

$$\tilde{G}_f(\mathbf{r}) = \mathcal{G}_f(\mathbf{r}) \exp[\iota \varphi_f(\mathbf{r})]\,. \tag{B.6}$$

By using simple algebra it can bee shown that

$$\mathcal{G}_f(\mathbf{r}) = \frac{L}{\sqrt{(Z + f)^2 + (LZ/f)^2}} \exp\left[-\frac{r^2}{w_f(Z)^2}\right] = \frac{s}{w_f(Z)} \exp\left[-\frac{r^2}{w_f(Z)^2}\right]\,, \tag{B.7}$$

where $s = \sqrt{2cL/\omega}$ is the beam waist radius of the input beam and

$$w_f(Z) = \sqrt{\frac{2c}{\omega L}\left[(Z + f)^2 + \left(\frac{L}{f} Z\right)^2\right]} \tag{B.8}$$

is the beam radius of the focused beam, which can be obtained by using definition (2.40) on (B.3). Using the phase calculation method when the real and imaginary parts of the complex number are known [91], the phase can be found to be

$$\varphi_f(\mathbf{r}) = -\frac{\pi}{2} - \operatorname{atan}\left[\frac{LZ}{(Z + f)f}\right] + \frac{\omega r^2}{2cR_f(Z)} + \frac{\omega}{c}(Z + f)\,, \tag{B.9}$$

with the phase-front radius of the the focus field's spherical wave front

$$R_f(Z) = \frac{(Z+f)^2 + (LZ/f)^2}{Z + f + (L/f)^2 Z}\,. \tag{B.10}$$

This expression for the phase-front radius can be obtained by applying (2.40) on (B.3).

Debye approximation The above expressions for Gaussian beams can often be simplified. For example, the above formulas contain the well-known focal shift of Gaussian beams when a focusing element with long focal length is used [146]. However, for stronger focusing when $L \gg f$ (that is, $L/f \gg 1$), the shift of the diffraction focus disappears, it coincides with the geometrical focus, and the above expressions are simplified. It is easy to see from (B.3) that if $L/f \gg 1$ (called Debye approximation) then the complex beam parameter is [139]

$$\tilde{q}_D(Z) = Z - \iota \frac{f^2}{L}\,, \tag{B.11}$$

resulting in the focused Rayleigh range

$$L_D = \frac{f^2}{L}\,. \tag{B.12}$$

The amplitude transformation of (B.5) gives

$$\frac{\tilde{q}_D(-f)}{\tilde{q}_D(Z)} = \frac{-f}{\tilde{q}_D(Z)}\,. \tag{B.13}$$

So the electric field of the focused Gaussian beam in the Debye approximation is given by

$$\begin{aligned}\tilde{G}_D(\mathbf{r}) =& \frac{f}{L_D}\frac{1}{\sqrt{1+(Z/L_D)^2}}\exp\left[-\frac{r^2}{w_D(Z)^2}\right] \\ &\times \exp\left[\iota\left(-\frac{\pi}{2} - \operatorname{atan}\left[\frac{Z}{L_D}\right] + \frac{\omega r^2}{2cR_D(Z)} + \frac{\omega}{c}(Z+f)\right)\right]\,.\end{aligned} \tag{B.14}$$

The beam radius and the phase-front radius in the Debye approximation are

$$w_D(Z) = \sqrt{\frac{2cf^2}{\omega L}}\sqrt{1 + \frac{Z^2}{f^4/L^2}} = s_D\sqrt{1+\frac{Z^2}{L_D^2}} \tag{B.15}$$

and

$$R_D(Z) = Z + \frac{f^4}{L^2 Z} = Z + \frac{L_D^2}{Z}, \tag{B.16}$$

consistent with the definitions (2.36) and (2.37), respectively.

B.2 First-order theory of pulsed beam diffraction

The aim is to provide an analytical approximate formula for the electric field $\tilde{E}^{(p)}(\mathbf{r},t)$ of a propagated pulsed beam [164]. First, the temporal variation will be expressed in the form of (2.3) leading to

$$\tilde{E}^{(p)}(\mathbf{r},t)=\tilde{\mathcal{E}}^{(p)}(\mathbf{r},t)\exp[-\iota\omega_0 t]\ . \tag{B.17}$$

Since $\tilde{E}^{(p)}(\mathbf{r},t)$ is the inverse Fourier transform of $\tilde{\mathcal{P}}(\mathbf{r},\omega)$ (see (2.59)), it is easy to see from (B.17) that the complex temporal envelope of the propagated field is

$$\tilde{\mathcal{E}}^{(p)}(\mathbf{r},t)=\frac{1}{2\pi}\int_{-\infty}^{\infty}\tilde{\mathcal{P}}(\mathbf{r},\omega)\exp[-\iota(\omega-\omega_0)t]\ \mathrm{d}\omega\,. \tag{B.18}$$

Utilizing the decomposition (2.58) of $\tilde{\mathcal{P}}(\mathbf{r},\omega)$ into $\tilde{U}(\omega)$ and $\tilde{G}(\mathbf{r},\omega)$; and applying the Taylor expansions (2.61) and (2.62) of the amplitude and phase of $\tilde{G}(\mathbf{r},\omega)$ up to the first order, the complex envelope is rewritten as

$$\begin{aligned}\tilde{\mathcal{E}}^{(p)}(\mathbf{r},t)\simeq&\frac{1}{2\pi}\int_{-\infty}^{\infty}\tilde{U}(\omega)\left[\mathcal{G}_0(\mathbf{r})+\mathcal{G}_0'(\mathbf{r})(\omega-\omega_0)\right]\\&\times\exp\Big[\iota\left\{\varphi_{G,0}(\mathbf{r})+\varphi_{G,0}'(\mathbf{r})(\omega-\omega_0)\right\}\Big]\exp[-\iota(\omega-\omega_0)t]\ \mathrm{d}\omega\,.\end{aligned} \tag{B.19}$$

By the substitution of $\tau=t-\varphi_{G,0}'(\mathbf{r})$, utilizing that the expansion coefficients are independent of ω and that from (2.66) (assuming that the order of integration and differentiation is commutable)

$$\frac{\mathrm{d}\tilde{\mathcal{E}}^{(i)}(\tau)}{\mathrm{d}\tau}=-\iota\frac{1}{2\pi}\int_{-\infty}^{\infty}(\omega-\omega_0)\tilde{U}(\omega)\exp[-\iota(\omega-\omega_0)\tau]\ \mathrm{d}\omega\,, \tag{B.20}$$

one can arrive to

$$\tilde{\mathcal{E}}^{(p)}(\mathbf{r},t)\simeq\left[\mathcal{G}_0(\mathbf{r})\tilde{\mathcal{E}}^{(i)}(\tau)+\iota\mathcal{G}_0'(\mathbf{r})\frac{\mathrm{d}\tilde{\mathcal{E}}^{(i)}(\tau)}{\mathrm{d}\tau}\right]\exp[\iota\varphi_{G,0}(\mathbf{r})]\ . \tag{B.21}$$

By the substitution $t=\tau+\varphi_{G,0}'(\mathbf{r})$ in (B.17) it is easy to see that

$$\tilde{\mathcal{E}}^{(p)}(\mathbf{r},\tau)\simeq\left[\mathcal{G}_0(\mathbf{r})\tilde{\mathcal{E}}^{(i)}(\tau)+\iota\mathcal{G}_0'(\mathbf{r})\frac{\mathrm{d}\tilde{\mathcal{E}}^{(i)}(\tau)}{\mathrm{d}\tau}\right]\exp\Big[\iota\left(\varphi_{G,0}(\mathbf{r})-\omega_0\varphi_{G,0}'(\mathbf{r})\right)\Big]\ , \tag{B.22}$$

being the same as (2.65), yielding the field at τ by $\tilde{E}^{(p)}(\mathbf{r},\tau)=\tilde{\mathcal{E}}^{(p)}(\mathbf{r},\tau)\exp[-\iota\omega_0\tau]$.

Relationship between initial an propagated real envelopes and phases To obtain the expression (2.67) and (2.68) one further assumption is needed [115]. If

$$\left|\frac{\mathcal{G}_0'(\mathbf{r})}{\mathcal{G}_0(\mathbf{r})}\frac{\mathrm{d}\tilde{\mathcal{E}}^{(i)}(\tau)/\mathrm{d}\tau}{\tilde{\mathcal{E}}^{(i)}(\tau)}\right| \ll 1\,, \tag{B.23}$$

then (B.22) can be expressed in an other form using the Taylor series of the exponential function ($\exp(x) = 1 + x + \dots$), giving

$$\tilde{\mathcal{E}}^{(p)}(\mathbf{r},\tau) \simeq \mathcal{G}_0(\mathbf{r})\tilde{\mathcal{E}}^{(i)}(\tau)\exp\left[\iota\frac{\mathcal{G}_0'(\mathbf{r})}{\mathcal{G}_0(\mathbf{r})}\frac{\mathrm{d}\tilde{\mathcal{E}}^{(i)}(\tau)/\mathrm{d}\tau}{\tilde{\mathcal{E}}^{(i)}(\tau)}\right]\exp\Big[\iota\left(\varphi_{G,0}(\mathbf{r}) - \omega_0\varphi_{G,0}'(\mathbf{r})\right)\Big]\,. \tag{B.24}$$

The derivative in the first exponential is evaluated using $\tilde{\mathcal{E}}^{(i)}(\tau) = A^{(i)}(\tau)\exp\Big[\iota\hat{\varphi}^{(i)}(\tau)\Big]$ as

$$\frac{\mathrm{d}\tilde{\mathcal{E}}^{(i)}(\tau)/\mathrm{d}\tau}{\tilde{\mathcal{E}}^{(i)}(\tau)} = \frac{\mathrm{d}\ln\Big(A^{(i)}(\tau)\Big)}{\mathrm{d}\tau} + \iota\frac{\mathrm{d}\hat{\varphi}^{(i)}(\tau)}{\mathrm{d}\tau}\,. \tag{B.25}$$

Substituting the above into (B.24) yields

$$\begin{aligned}\tilde{\mathcal{E}}^{(p)}(\mathbf{r},\tau) \simeq \mathcal{G}_0(\mathbf{r})A^{(i)}(\tau)\exp&\left[-\frac{\mathcal{G}_0'(\mathbf{r})}{\mathcal{G}_0(\mathbf{r})}\frac{\mathrm{d}\hat{\varphi}^{(i)}(\tau)}{\mathrm{d}\tau}\right]\\ &\times\exp\left[\iota\left(\hat{\varphi}^{(i)}(\tau) + \frac{\mathcal{G}_0'(\mathbf{r})}{\mathcal{G}_0(\mathbf{r})}\frac{\mathrm{d}\ln\Big(A^{(i)}(\tau)\Big)}{\mathrm{d}\tau} + \varphi_{G,0}(\mathbf{r}) - \omega_0\varphi_{G,0}'(\mathbf{r})\right)\right]\,,\end{aligned} \tag{B.26}$$

the amplitude and phase of which is exactly (2.67) and (2.68), respectively.

Appendix

C

Phase and group velocity of focused Gaussian beams — undistorted case

C.1 On-axis phase velocity of an untruncated, undistorted beam

It was detailed in Section 2.3.5 how the phase velocity of waves can be calculated generally. According to expression (2.69) for the phase velocity, it requires the calculation of the gradient of the spatio-spectral phase. The explicit expression of the phase (3.1) for an untruncated Gaussian beam is given by Equation (21) of [143], which rewritten with the notation of this work is

$$\begin{aligned}\varphi_G(r, Z_0, \omega) = &-\frac{\pi}{2} + \frac{\omega}{c}(Z_0 + R_0 - R) - \operatorname{atan}[\omega\mathcal{T}(Z_0, \omega)] \\ &+ \frac{\omega}{c}\frac{r^2}{2(Z_0 + R_0)} + \frac{\omega^2(\partial_z\mathcal{T})}{2c}\frac{r^2}{1 + (\omega\mathcal{T})^2}\omega\mathcal{T}\,,\end{aligned} \tag{C.1}$$

where $\mathcal{T}$ and $\partial_z\mathcal{T}$ are given by (3.3) and (3.5), respectively. Expression (C.1) is independent of ψ, also the derivative with respect to r still depends on r. So if one calculates the gradient of (C.1) and takes the value on axis, its magnitude is equivalent to calculating the derivative of the on-axis expression (3.2) with respect to Z_0. The physical reason behind this is the cylindrical symmetry of the phase, due to which the gradient points

towards the propagation axis. So the gradient of (3.1) taken on axis is simply

$$\begin{aligned}\nabla\varphi_G(r,Z_0,\omega)|_{r=0} &= \mathbf{u}_z\frac{\partial}{\partial Z_0}\left(-\frac{\pi}{2}+\frac{\omega}{c}(Z_0+R_0-R)-\operatorname{atan}[\omega\mathcal{T}(Z_0,\omega)]\right)\\ &= \left(\frac{\omega}{c}-\frac{1}{1+\omega^2\mathcal{T}^2}\omega\partial_z\mathcal{T}\right)\mathbf{u}_z\,.\end{aligned} \tag{C.2}$$

Substituting this into (2.69) yields

$$v_p(Z_0,\omega)=\frac{\omega}{\omega/c-\omega\partial_z\mathcal{T}/(1+\omega^2\mathcal{T}^2)}=\frac{c\,(1+\omega^2\mathcal{T}^2)}{1+\omega^2\mathcal{T}^2-c\partial_z\mathcal{T}}\,, \tag{C.3}$$

which when divided by c is equivalent to (3.4).

It is worth examining in which Z_0 coordinate the on-axis phase velocity reaches its maximum. Following the elementary mathematical considerations, the first step to obtain the position of maximum is to calculate the derivative of the phase velocity with respect to the axial coordinate, giving

$$\frac{\partial}{\partial Z_0}\left(\frac{v_p(Z_0,\omega)}{c}\right)=\frac{(1+\omega^2\mathcal{T}^2)c\partial_z^2\mathcal{T}-\omega^2 2c\mathcal{T}(\partial_z\mathcal{T})^2}{(1+\omega^2\mathcal{T}^2-c\partial_z\mathcal{T})^2}\,, \tag{C.4}$$

where $\partial_z^2\mathcal{T}=\partial^2\mathcal{T}(Z_0,\omega)/\partial Z_0^2$. Finding the zero of (C.4) means obtaining the Z_0 value for which the numerator of (C.4) is zero, so the question is the solution $Z_{0,\max(v_p)}$ of the equation

$$(1+\omega^2\mathcal{T}^2)\partial_z^2\mathcal{T}=\omega^2 2\mathcal{T}(\partial_z\mathcal{T})^2\,. \tag{C.5}$$

To have the explicit dependence on Z_0 and to solve (C.5) it is worth introducing

$$\omega\mathcal{T}=\pi N_w\frac{Z_0+R_0-R}{Z_0+R_0}\,, \tag{C.6}$$

$$\frac{\omega\partial_z\mathcal{T}}{R}=\frac{\pi N_w}{(Z_0+R_0)^2}\,, \tag{C.7}$$

$$\frac{\omega\partial_z^2\mathcal{T}}{R}=-\frac{2\pi N_w}{(Z_0+R_0)^3}\,. \tag{C.8}$$

Substituting the above expressions into (C.5) multiplied by ω/R^2 yields the equation

$$\begin{aligned}&-\left(1+\pi^2N_w^2\frac{(Z_{0,\max(v_p)}+R_0-R)^2}{(Z_{0,\max(v_p)}+R_0)^2}\right)\frac{2\pi N_w}{R(Z_{0,\max(v_p)}+R_0)^3}\\ &=2\pi N_w\frac{Z_{0,\max(v_p)}+R_0-R}{Z_{0,\max(v_p)}+R_0}\frac{\pi^2N_w^2}{(Z_{0,\max(v_p)}+R_0)^4}\,.\end{aligned} \tag{C.9}$$

With simple algebraic steps, the solution is

$$Z_{0,\max(v_p)} = -R_0 + R\left(1 - \frac{1}{1+\pi^2 N_w^2}\right), \tag{C.10}$$

which is equivalent to (3.6).

Debye approximation It is easy to see from [78, 135] that in the Debye approximation the spatial phase $\varphi_G(r=0, Z_0, \omega)$ and its gradient are formally exactly the same as (C.2), only the variable $\mathcal{T}$ has to be replaced with its form $\mathcal{T}_D$ valid in the Deybe approximation. So the expressions

$$\mathcal{T}_D(Z_0, \omega) = \frac{u_D}{2\kappa\omega}, \tag{C.11}$$

$$\partial_z \mathcal{T}_D = \frac{\mathrm{NA}_w^2}{2c} \tag{C.12}$$

have to be used instead of $\mathcal{T}$ and $\partial_z \mathcal{T}$, where u_D and κ are given by (2.56) and (2.50), respectively, and

$$\mathrm{NA}_w = \frac{w}{R} \tag{C.13}$$

is the numerical aperture associated with the Gaussian beam of frequency ω emerging from the exit pupil. This way the phase velocity expression in Debye approximation can be expressed with dimensionless parameters according to

$$\frac{v_p^{(D)}(u_D, \omega)}{c} = \frac{1 + u_D^2/(4\kappa^2)}{1 + u_D^2/(4\kappa^2) - \mathrm{NA}_w^2/2}. \tag{C.14}$$

Note here that with a coordinate scaling $u_{D,w} = u_D/\kappa$ the number of dimensionless parameters can be reduced to two from three.

C.2 On-axis group velocity of an untruncated, undistorted beam

To calculate the group velocity from (3.1) using (2.70), the derivative with respect to angular frequency has to be calculated first. For the same reason as in the case of the phase velocity, the on-axis phase (3.2) can be used, giving

$$\varphi_G'(r=0, Z_0, \omega) = \frac{\partial}{\partial\omega}\varphi_G(r=0, Z_0, \omega) = \frac{Z_0 + R_0 - R}{c} - \frac{\omega}{c}R'(\omega) - \frac{\mathcal{T} + \omega\mathcal{T}'}{1+\omega^2\mathcal{T}^2}. \tag{C.15}$$

Component $\mathbf{u}_z$ of the gradient along the axis at ω_0 is

$$\begin{aligned}&\frac{\partial}{\partial Z_0}\left[\varphi'_G(r=0,Z_0,\omega)|_{\omega=\omega_0}\right]\\&=\frac{1}{c}-\frac{\left[\partial_z\mathcal{T}_0+\omega_0\partial_z(\mathcal{T}'_0)\right](1+\omega_0^2\mathcal{T}_0^2)-(\mathcal{T}_0+\omega_0\mathcal{T}'_0)\omega_0^2 2\mathcal{T}_0(\partial_z\mathcal{T}_0)}{(1+\omega_0^2\mathcal{T}_0^2)^2}\,,\end{aligned}\tag{C.16}$$

all other components are zero along the axis, because of the symmetry (this is also why the order of operations can be and are interchanged). The derivatives of $\mathcal{T}$ that appear in the previous expression are $\partial_z\mathcal{T}$, given in (3.5),

$$\mathcal{T}'=2\frac{w'}{w}\mathcal{T}-\frac{R'}{R}\frac{w^2}{2cR}\tag{C.17}$$

and

$$\partial_z(\mathcal{T}')=2\frac{w'}{w}\partial_z\mathcal{T}\,.\tag{C.18}$$

Substituting the above derivatives into (C.16) and performing some algebraic manipulations give

$$\begin{aligned}&\frac{\partial}{\partial Z_0}\left[\varphi'_G(r=0,Z_0,\omega)|_{\omega=\omega_0}\right]\\&=\frac{1}{c}-\frac{\left[1+2(w'_0/w_0)\omega_0\right](\partial_z\mathcal{T}_0)(1-\omega_0^2\mathcal{T}_0^2)-\left[-(R'_0/R_0)\omega_0\right]\omega_0^2\mathcal{T}_0(\partial_z\mathcal{T}_0)w_0^2/(cR_0)}{(1+\omega_0^2\mathcal{T}_0^2)^2}\,.\end{aligned}\tag{C.19}$$

The variables appearing in square brackets in the previous expression are $g_v=1+2(w'_0/w_0)\omega_0$ and $\gamma_v=-(R'_0/R_0)\omega_0$ (see also (3.8) and (3.9)). By introducing them the gradient is given by

$$\begin{aligned}&\frac{\partial}{\partial Z_0}\left[\varphi'_G(r=0,Z_0,\omega)|_{\omega=\omega_0}\right]\\&=\frac{(1+\omega_0^2\mathcal{T}_0^2)^2-g_v c(\partial_z\mathcal{T}_0)(1-\omega_0^2\mathcal{T}_0^2)+\gamma_v\omega_0^2\mathcal{T}_0(\partial_z\mathcal{T}_0)w_0^2/R_0}{c(1+\omega_0^2\mathcal{T}_0^2)^2}\,,\end{aligned}\tag{C.20}$$

the reciprocal of which divided by c is (3.7), giving the ratio of the group velocity at ω_0 and the speed of light c.

C.3 Dependence of group-velocity parameters on the properties of the source Gaussian beam

Parameter g_v According to the description of Section 3.1.1 on Page 50 the g_v parameter of the focused, pulsed beam describes the wavelength dependence of the Gaussian beam radius in the exit pupil of the focusing element. With the assumption that the beam size just before the focusing element is identical to the size right behind it, g_v can be described by the parameters of the source Gaussian beam. In order to obtain parameter g_v one has to calculate the derivative of the beam size w with respect to the angular frequency ω (see (3.8)). Using expression (2.36) to calculate the beam radius at distance d from the beam waist, the required derivative is

$$w' = \frac{\partial}{\partial\omega}\left(s\sqrt{1+\left(\frac{d}{L}\right)^2}\right) = s'\sqrt{1+\left(\frac{d}{L}\right)^2} + s\frac{d/L}{\sqrt{1+(d/L)^2}}\frac{d'L - L'd}{L^2}\,, \tag{C.21}$$

and as a result

$$\frac{w_0'}{w_0}\omega_0 = \frac{s_0'}{s_0}\omega_0 + \frac{d_0'}{d_0}\omega_0\frac{\xi_s^2}{1+\xi_s^2} - \frac{L_0'}{L_0}\omega_0\frac{\xi_s^2}{1+\xi_s^2} \tag{C.22}$$

with $\xi_s = d_0/L_0$, beam waist radius s and Rayleigh length L. By introducing $g_s = (L_0'/L_0)\omega_0$ (see (3.11)) it is easy to see that

$$\frac{s_0'}{s_0}\omega_0 = \frac{1}{2}(g_s - 1)\,, \tag{C.23}$$

and derivatives in (C.22) can be substituted with dimensionless parameters g_s and ε_s of the source (see expressions (3.11) and (3.12)). So

$$g_v = 1 + 2\frac{w_0'}{w_0}\omega_0 = g_s + \varepsilon_s\frac{2\xi_s^2}{1+\xi_s^2} - g_s\frac{2\xi_s^2}{1+\xi_s^2}\,, \tag{C.24}$$

which is equivalent to (3.10).

Parameter γ_v The other parameter appearing in expression (3.7) of the group velocity is γ_v expressing how the wave-front curvature changes with wavelength according to (3.9). This case is more complex compared to calculating g_v, as the wave-front curvature is changed not just during propagation, but also modified by the focusing element. Using the well-known expression from paraxial optics that a spherical wave with radius of curvature R_s is transformed into a spherical wave with radius of curvature R by an optical element

of focal length f according to [130]

$$\frac{1}{R} = \frac{1}{f} - \frac{1}{R_s}\,, \tag{C.25}$$

γ_v can be expressed with characteristics of the source beam and the focusing element. Following definition (3.9) of γ_v the derivative of R with respect to angular frequency is necessary, which from (C.25) is

$$R' = \frac{\partial}{\partial\omega}\left(\frac{fR_s}{R_s - f}\right) = \frac{f'R_s^2 - f^2R_s'}{(R_s - f)^2}\,. \tag{C.26}$$

This gives

$$\gamma_v = -\frac{R_0'}{R_0}\omega_0 = -\frac{(f_0'/f_0)R_{s,0} - (R_{s,0}'/R_{s,0})f_0}{R_{s,0} - f_0}\omega_0\,. \tag{C.27}$$

As the first factor in the numerator of the previous expression is γ_f given by (3.15), only the second term needs evaluation, which describes the wave front curvature of the source beam at the entrance pupil of the focusing element. Using expression (2.37) for the wave-front curvature at distance $d = d(\omega)$ from the source beam's waist, the derivative can be obtained to be

$$R_s' = \frac{\partial}{\partial\omega}\left(d\left[1 + \left(\frac{L}{d}\right)^2\right]\right) = d'\left[1 - \left(\frac{L}{d}\right)^2\right] + 2\frac{L'L}{d}\,. \tag{C.28}$$

With the expression above

$$\frac{R_{s,0}'}{R_{s,0}}\omega_0 = \frac{d_0'\left[1 - (L_0/d_0)^2\right]}{d_0\left[1 + (L_0/d_0)^2\right]}\omega_0 + \frac{2L_0'L_0/d_0}{d_0\left[1 + (L_0/d_0)^2\right]}\omega_0\,, \tag{C.29}$$

which with some algebra and with the introduction of g_s and ε_s (see their definitions in (3.11) and (3.12), respectively) gives

$$\frac{R_{s,0}'}{R_{s,0}}\omega_0 = \frac{\left[(d_0/L_0)^2 - 1\right]\varepsilon_s + 2g_s}{1 + (d_0/L_0)^2}\,. \tag{C.30}$$

Substituting (C.30) into (C.27) results in

$$\gamma_v = \frac{\gamma_f R_{s,0} - f_0\left(\left[(d_0/L_0)^2 - 1\right]\varepsilon_s + 2g_s\right)/\left(1 + (d_0/L_0)^2\right)}{R_{s,0} - f_0}\,. \tag{C.31}$$

It is worth multiplying the previous expression with L_0/L_0 because this way all parameters become dimensionless. The new parameters are $\zeta_f = f_0/L_0$ (see also (3.16)) and

$$\frac{R_{s,0}}{L_0} = \frac{d_0}{L_0}\left[1 + \left(\frac{L_0}{d_0}\right)^2\right] = \xi_s + \frac{1}{\xi_s}\,, \tag{C.32}$$

with $\xi_s = d_0/L_0$ (see also (3.13)). With these modifications (C.31) becomes

$$\gamma_v = \frac{\gamma_f(\xi_s + 1/\xi_s) - \zeta_f\left(\left[\xi_s^2 - 1\right]\varepsilon_s + 2g_s\right)/\left(1 + \xi_s^2\right)}{\xi_s + 1/\xi_s - \zeta_f}\,, \tag{C.33}$$

which with different grouping of terms can be written as (3.14).

Appendix

D

Phase and group velocity of focused Gaussian beams — distorted case

D.1 Evaluation of derivatives of complex phases

Calculating the numerical derivative of the phase of a complex-valued function, especially if the function is an integral, can lead to numerical errors. So it is worth simplifying by analytical evaluations. Assume a complex-valued function written as the sum of its real and imaginary parts

$$\tilde{C}(x,y) = X(x,y) + \imath Y(x,y)\,. \tag{D.1}$$

The complex phase of this function can be calculated as

$$\varphi_C(x,y) = \arg\left[\tilde{C}(x,y)\right] = \operatorname{atan}\left[\frac{Y(x,y)}{X(x,y)}\right] + \varphi_{\text{const.}}\,, \tag{D.2}$$

where $\varphi_{\text{const.}} = 0, \pm\pi$, depending on the sign of $Y(x,y)$ and $X(x,y)$ [91]. By calculating the first derivative of $\varphi_C(x,y)$ with respect to x using its form (D.2) one can get

$$\frac{\partial\varphi_C(x,y)}{\partial x} = \frac{X\partial_x Y - Y\partial_x X}{X^2+Y^2}\,, \tag{D.3}$$

containing partial derivatives of $X(x,y)$ and $Y(x,y)$ with respect to x. This expression can be further shortened to only contain $\tilde{C}$ instead of its real and imaginary parts. First thing needed for that is

$$|\tilde{C}|^2 = X^2 + Y^2\,. \tag{D.4}$$

Second, knowing that

$$\frac{\partial \tilde{C}}{\partial x} = \frac{\partial X}{\partial x} + \iota \frac{\partial Y}{\partial x} \Rightarrow \iota \left(\frac{\partial \tilde{C}}{\partial x} \right)^* = \iota \frac{\partial X}{\partial x} + \frac{\partial Y}{\partial x} , \tag{D.5}$$

superscript * meaning complex conjugation, it is easy to see that

$$\iota \tilde{C} \left(\frac{\partial \tilde{C}}{\partial x} \right)^* = \left(X \frac{\partial Y}{\partial x} - Y \frac{\partial X}{\partial x} \right) + \iota \left(Y \frac{\partial Y}{\partial x} + X \frac{\partial X}{\partial x} \right) , \tag{D.6}$$

or

$$\tilde{C} \left(\frac{\partial \tilde{C}}{\partial x} \right)^* = \left(X \frac{\partial X}{\partial x} + Y \frac{\partial Y}{\partial x} \right) + \iota \left(Y \frac{\partial X}{\partial x} - X \frac{\partial Y}{\partial x} \right) . \tag{D.7}$$

Picking the appropriate terms from the right-hand side of (D.6) or (D.7) for the numerator of (D.3), and using (D.4) as its denominator, the result is

$$\frac{\partial \varphi_C(x,y)}{\partial x} = \frac{\mathrm{Re}\left[\iota \tilde{C} (\partial_x \tilde{C})^*\right]}{|\tilde{C}|^2} = \frac{-\mathrm{Im}\left[\tilde{C} (\partial_x \tilde{C})^*\right]}{|\tilde{C}|^2} . \tag{D.8}$$

For the second derivative a mixed derivative is calculated first for general result, then it is specialized to a double derivative with respect to the same variable. Using simple algebra

$$\begin{aligned} \frac{\partial^2 \varphi_C(x,y)}{\partial y \partial x} =& \frac{\left[X \partial^2_{yx} Y + (\partial_x Y)(\partial_y X) - (\partial_y Y)(\partial_x X) - Y \partial^2_{yx} X\right] (X^2 + Y^2)}{(X^2 + Y^2)^2} \\ & - \frac{(X \partial_x Y - Y \partial_x X)\, 2\, (X \partial_y X + Y \partial_y Y)}{(X^2 + Y^2)^2} , \end{aligned} \tag{D.9}$$

with $\partial^2_{yx} f(x,y) = \partial^2 f(x,y) / \partial y \partial x$. With a similar logic to the substitution into the first derivative the above expression can be rewritten to contain $\tilde{C}$, giving

$$\frac{\partial^2 \varphi_C(x,y)}{\partial y \partial x} = \frac{\mathrm{Re}\left[\iota \tilde{C} (\partial^2_{yx} \tilde{C})^* + \iota (\partial_y \tilde{C})(\partial_x \tilde{C})^*\right] |\tilde{C}|^2 - 2\mathrm{Re}\left[\iota \tilde{C} (\partial_x \tilde{C})^*\right] \mathrm{Im}\left[\iota \tilde{C} (\partial_y \tilde{C})^*\right]}{|\tilde{C}|^4} . \tag{D.10}$$

If the second derivative is with respect to the same variable as the first, the expression can be simplified using that for every complex number $\tilde{C}$ it is true that $\mathrm{Re}\left[\iota \tilde{C} \tilde{C}^*\right] = 0$, so

$$\frac{\partial^2 \varphi_C(x,y)}{\partial x^2} = \frac{\mathrm{Re}\left[\iota \tilde{C} (\partial^2_{xx} \tilde{C})^*\right] |\tilde{C}|^2 - 2\mathrm{Re}\left[\iota \tilde{C} (\partial_x \tilde{C})^*\right] \mathrm{Im}\left[\iota \tilde{C} (\partial_x \tilde{C})^*\right]}{|\tilde{C}|^4} . \tag{D.11}$$

The main advantage of these transformation is that if $\tilde{C}(x,y)$ is given by an integral, and it is assumed that the order of differentiation and integration can be varied, then the

numerical effort needed is reduced. Only integrals have to be calculated, and the complex conjugate, real or imaginary parts of them have to be added or multiplied, leading to less chance for numerical errors. See examples in the next section of the Appendix and in Section 3.1.2.

D.2 Calculation of phase and group velocity in the presence of aberrations

This section aims to provide a short summary on how to evaluate the phase and group velocity of focused Gaussian beams in the vicinity of focus when aberrations are present. The formulation is shaped to reduce computation time and decrease the chance of numerical errors.

The task is to calculate the phase velocity using (2.69) in cylindrical coordinate system, giving

$$v_p(\mathbf{r},\omega) = \omega \left[\left(\frac{\partial \varphi_G(\mathbf{r},\omega)}{\partial r} \right)^2 + \left(\frac{1}{r} \frac{\partial \varphi_G(\mathbf{r},\omega)}{\partial \phi} \right)^2 + \left(\frac{\partial \varphi_G(\mathbf{r},\omega)}{\partial Z_0} \right)^2 \right]^{-1/2} , \tag{D.12}$$

and the group velocity applying (2.70), yielding

$$\begin{aligned} v_g(\mathbf{r},\omega_0) = c \Bigg\{ & \left[\frac{\partial}{\partial r} \left(\frac{\partial \varphi_G(\mathbf{r},\omega)}{\partial \omega} \bigg|_{\omega=\omega_0} \right) \right]^2 + \left[\frac{1}{r} \frac{\partial}{\partial \phi} \left(\frac{\partial \varphi_G(\mathbf{r},\omega)}{\partial \omega} \bigg|_{\omega=\omega_0} \right) \right]^2 \\ & + \left[\frac{\partial}{\partial Z_0} \left(\frac{\partial \varphi_G(\mathbf{r},\omega)}{\partial \omega} \bigg|_{\omega=\omega_0} \right) \right]^2 \Bigg\}^{-1/2} . \end{aligned} \tag{D.13}$$

The spatial phase to be used here following (3.1) is

$$\varphi_G(\mathbf{r},\omega) = -\frac{\pi}{2} + \frac{\omega}{c}(Z_0 + R_0 - R) + \frac{\omega}{c} \frac{r^2}{2(Z_0 + R_0)} + \arg\left[\tilde{\mathcal{I}}(u,v,\psi) \right] , \tag{D.14}$$

with $\mathbf{r} = (r, \psi, Z_0)$ and $\tilde{\mathcal{I}}(u,v,\psi)$ defined by (2.52). For the sake of brevity the function

$$\tilde{\Upsilon}(\rho,\theta) = \exp\left(-\kappa\rho^2 + \imath k \Phi(\rho,\theta) - \imath v \rho \cos(\theta - \psi) - \imath \frac{u}{2} \rho^2 \right) \tag{D.15}$$

is introduced, so $\tilde{\mathcal{I}}$ can be be written shortly as

$$\tilde{\mathcal{I}}(u,v,\psi) = \int_0^1 \int_0^{2\pi} \tilde{\Upsilon}(\rho,\theta) \rho \, \mathrm{d}\theta \, \mathrm{d}\rho \, . \tag{D.16}$$

The derivatives of $\varphi_{\mathcal{I}}(u,v,\psi) = \arg\left[\tilde{\mathcal{I}}(u,v,\psi)\right]$ are calculated using the expressions in the previous section (see Appendix D.1), so only the derivatives of $\tilde{\mathcal{I}}(u,v,\psi)$ itself are given, then the results can be substituted into (D.8) and (D.10). It is also noted that the azimuthal angle ψ of $\mathbf{r}$ is different from the usual ϕ of the cylindrical coordinate system, so also from the one present in the formulas of gradient in (D.12) and (D.14). But as $\psi = \pi/2 - \phi$ (see Figure 2.9), the derivative with respect to ϕ is simply $\partial_\phi = -\partial_\psi$.

D.2.1 Phase velocity in the presence of aberrations

To obtain the gradient present in (D.12) the following derivatives are needed for vector components $\mathbf{u}_r$, $\mathbf{u}_\phi$ and $\mathbf{u}_z$:

$$\frac{\partial\varphi_G}{\partial r} = \frac{\partial\varphi_{\mathcal{I}}(u,v,\psi)}{\partial r} + \frac{\omega}{c}\frac{r}{Z_0+R_0}\,, \tag{D.17}$$

$$\frac{1}{r}\frac{\partial\varphi_G}{\partial\phi} = -\frac{1}{r}\frac{\partial\varphi_{\mathcal{I}}(u,v,\psi)}{\partial\psi}\,, \tag{D.18}$$

$$\frac{\partial\varphi_G}{\partial Z_0} = \frac{\omega}{c} + \frac{\partial\varphi_{\mathcal{I}}(u,v,\psi)}{\partial Z_0} - \frac{\omega}{c}\frac{r^2}{2(Z_0+R_0)^2}\,. \tag{D.19}$$

In the case of on-axis evaluation ($r = 0$) the last term disappears in (D.17) and (D.19). Expression (D.18) does not have a singularity with $r = 0$, which can be seen if the derivative with respect to ψ is evaluated (see later).

Component $\mathbf{u}_r$ of the phase velocity Looking at (D.17) and taking into account (D.8) the necessary derivative is $\partial_r\tilde{\mathcal{I}}$. The integral $\tilde{\mathcal{I}}$ depends on r through coordinate v, so by looking at definition (2.54) of the dimensionless coordinate v the necessary derivative is

$$\frac{\partial\tilde{\mathcal{I}}}{\partial r} = \frac{\partial\tilde{\mathcal{I}}}{\partial v}\frac{\partial v}{\partial r} = \frac{\omega}{c}\frac{a}{Z_0+R_0}\frac{\partial\tilde{\mathcal{I}}}{\partial v}\,. \tag{D.20}$$

So taking the derivative of $\tilde{\mathcal{I}}$ with respect to v, assuming the interchangeability of derivation and integration, results finally in

$$\frac{\partial\tilde{\mathcal{I}}}{\partial r} = -\iota\frac{\omega}{c}\frac{a}{Z_0+R_0}\int_0^1\int_0^{2\pi}\cos(\theta-\psi)\tilde{\Upsilon}(\rho,\theta)\rho^2\,\mathrm{d}\theta\,\mathrm{d}\rho\,, \tag{D.21}$$

or its on-axis value for a chosen (for example, the carrier frequency) ω_0 is

$$\left.\frac{\partial\tilde{\mathcal{I}}}{\partial r}\right|_{\substack{r=0\\ \omega=\omega_0}} = -\iota\frac{\omega_0}{c}\frac{a}{Z_0+R_0}\int_0^1\int_0^{2\pi}\cos(\theta-\psi)\tilde{\Upsilon}_{a,0}(\rho,\theta)\rho^2\,\mathrm{d}\theta\,\mathrm{d}\rho\,, \tag{D.22}$$

where $\tilde{\Upsilon}_{a,0}(\rho,\theta)$ is the on-axis ($r=0$) version of $\tilde{\Upsilon}(\rho,\theta)$ taken at $\omega=\omega_0$ (see explicitly in (3.27)). So component $\mathbf{u}_r$ can be obtained by evaluating (D.21), substituting it into (D.8) to obtain $\partial_r\varphi_{\mathcal{I}}$, which then can be used to calculate the whole component using (D.17).

Component $\mathbf{u}_\phi$ of the phase velocity For (D.18) one has to consider the $1/r$ factor expressible as (see (2.54))

$$\frac{1}{r}=\frac{\omega}{c}\frac{a}{Z_0+R_0}\frac{1}{v}\,. \tag{D.23}$$

It is easy to see from (D.8) that to calculate $(1/r)\partial_\phi\varphi_{\mathcal{I}}$ the $(1/r)\partial_\phi\tilde{\mathcal{I}}$ derivative is necessary, and the $1/r$ factor makes no difference in the applicability of (D.8). As a result

$$\frac{1}{r}\frac{\partial\tilde{\mathcal{I}}}{\partial\phi}=\iota\frac{\omega}{c}\frac{a}{Z_0+R_0}\int_0^1\int_0^{2\pi}\sin(\theta-\psi)\tilde{\Upsilon}(\rho,\theta)\rho^2\,\mathrm{d}\theta\,\mathrm{d}\rho\,. \tag{D.24}$$

On axis, for frequency ω_0, the expression simplifies a bit to

$$\left.\frac{1}{r}\frac{\partial\tilde{\mathcal{I}}}{\partial\phi}\right|_{\substack{r=0\\ \omega=\omega_0}}=\iota\frac{\omega_0}{c}\frac{a}{Z_0+R_0}\int_0^1\int_0^{2\pi}\sin(\theta-\psi)\tilde{\Upsilon}_{a,0}(\rho,\theta)\rho^2\,\mathrm{d}\theta\,\mathrm{d}\rho\,, \tag{D.25}$$

This means component $\mathbf{u}_\phi$ is simply evaluated using (D.24) substituted into (D.8), which is the expression appearing in (D.18).

Component $\mathbf{u}_z$ of the phase velocity The longitudinal component of the phase velocity is harder to calculate compared to the other two, because coordinate Z_0 appears in two arguments of $\tilde{\mathcal{I}}$, both in u and v (see (2.53) and (2.54)). As there is no uv cross term in the integral of $\tilde{\mathcal{I}}$, its derivative with respect to Z_0 can be given as

$$\frac{\partial\tilde{\mathcal{I}}}{\partial Z_0}=\frac{\partial\tilde{\mathcal{I}}}{\partial u}\frac{\partial u}{\partial Z_0}+\frac{\partial\tilde{\mathcal{I}}}{\partial v}\frac{\partial v}{\partial Z_0}=\frac{\omega}{c}\frac{a^2}{(Z_0+R_0)^2}\frac{\partial\tilde{\mathcal{I}}}{\partial u}-\frac{\omega}{c}\frac{ar}{(Z_0+R_0)^2}\frac{\partial\tilde{\mathcal{I}}}{\partial v}\,. \tag{D.26}$$

Calculating the derivative of $\tilde{\mathcal{I}}$ with respect to u and v and taking into account the previous expression the necessary derivative is

$$\begin{aligned}\frac{\partial\tilde{\mathcal{I}}}{\partial Z_0}=&-\frac{\iota}{2}\frac{\omega}{c}\frac{a^2}{(Z_0+R_0)^2}\int_0^1\int_0^{2\pi}\tilde{\Upsilon}(\rho,\theta)\rho^3\,\mathrm{d}\theta\,\mathrm{d}\rho\\&+\iota\frac{\omega}{c}\frac{ar}{(Z_0+R_0)^2}\int_0^1\int_0^{2\pi}\cos(\theta-\psi)\tilde{\Upsilon}(\rho,\theta)\rho^2\,\mathrm{d}\theta\,\mathrm{d}\rho\,.\end{aligned} \tag{D.27}$$

In the on-axis case it simplifies to

$$\left.\frac{\partial\tilde{\mathcal{I}}}{\partial Z_0}\right|_{\substack{r=0\\ \omega=\omega_0}}=-\frac{\iota}{2}\frac{\omega_0}{c}\frac{a^2}{(Z_0+R_0)^2}\int_0^1\int_0^{2\pi}\tilde{\Upsilon}_{a,0}(\rho,\theta)\rho^3\,\mathrm{d}\theta\,\mathrm{d}\rho\,. \tag{D.28}$$

Finally component $\mathbf{u}_z$ is calculated using (D.27), which is applied to get the phase derivative (D.8) for this component, then this latter is substituted into (D.19).

Symmetries of the phase velocity on axis By comparing the on-axis result for components $\mathbf{u}_r$ and $\mathbf{u}_\phi$ (expression (D.22) and (D.25)) one can notice that the only differences between the integrands are a sign and the $\cos(\theta-\psi) \leftrightarrow \sin(\theta-\psi)$ exchange. Knowing that $\tilde{\Upsilon}_{a,0}(\rho,\theta)$ depends on θ only through the aberration function $\Phi(\rho,\theta)$ (see (3.27)), which for primary aberrations is an even function of θ because it only contains $\cos^m(\theta)$ (see (2.47) and Table 2.1), it can be seen that for every ψ

$$\sqrt{\left(\left.\frac{\partial\tilde{\mathcal{I}}}{\partial r}\right|_{r=0}\right)^2+\left(\left.\frac{1}{r}\frac{\partial\tilde{\mathcal{I}}}{\partial\phi}\right|_{r=0}\right)^2}=\left|\left.\frac{\partial\tilde{\mathcal{I}}}{\partial r}\right|_{\substack{r=0\\\psi=0}}\right|. \tag{D.29}$$

This simplifies evaluation for on-axis points if the aberration functions is an even function of θ (like primary aberrations), because it is enough to calculate the components $\mathbf{u}_z$ and $\mathbf{u}_\psi$ at $\psi=0$. Also note for on-axis points that if $\Phi(\rho,\theta)$ is a π-periodic function of θ (like primary aberrations with even value of m) on the $[0,2\pi]$ domain, then both the $\mathbf{u}_\psi$ and $\mathbf{u}_r$ components are zero, as the integrals of both $\cos(\theta)$ and $\sin(\theta)$ on $[0,2\pi]$ are zero.

D.2.2 Group delay in the presence of aberrations

While group delay is not a direct aim of the present section, as it means the derivative of the spectral phase with respect to angular frequency [107], the calculation of it is an intermediary step for group velocity (see that in (2.70) and (D.14) first the derivative of φ_G with respect to frequency has to be evaluated). Group delay is also closely related to the CEP, as it gives the time for the wave packet to traverse a given distance, which compared to the time necessary for the carrier wave can give the value of CEP [47, 107].

So the group delay of a focused, pulsed Gaussian beam can be calculated as

$$\left.\frac{\partial\varphi_G(\mathbf{r},\omega)}{\partial\omega}\right|_{\omega=\omega_0}=\frac{Z_0}{c}+\gamma_v\frac{R_0}{c}+\frac{1}{c}\frac{r^2}{2(Z_0+R_0)}+\left.\frac{\partial\varphi_{\mathcal{I}}}{\partial\omega}\right|_{\omega=\omega_0}. \tag{D.30}$$

The first term in the previous expression simply gives the time that is needed for a plane wave to travel distance Z_0. The second term is a factor related to group velocity changes caused by the chromatic aberration-like effect of having different components focused to different points. The third term is the off-axis contribution known for Gaussian beams and their spherical wave fronts. The last term is again what needs numerical evaluation, and following the same logic as previously the partial derivative of $\tilde{\mathcal{I}}$ with respect to ω is what necessary to obtain this term using (D.8). Looking at the integrand of $\tilde{\mathcal{I}}$ (see

(D.16)), which mainly is $\tilde{\Upsilon}$, it can be seen that there are several quantities in the integral that depend on ω (see (D.16)): truncation coefficient κ through the beam size (see (2.50)), the wave number k, the aberration function $\Phi(\rho,\omega)$ (see (2.47)), the dimensionless radial coordinate v (see (2.54)) and the dimensionless longitudinal coordinate u (see (2.53)). By calculating their derivatives with respect to the angular frequency, and taking them at $\omega=\omega_0$, one arrives at

$$\left.\frac{\partial\kappa}{\partial\omega}\right|_{\omega=\omega_0} = \frac{\kappa_0}{\omega_0}(1-g_v)\,, \tag{D.31}$$

$$\left.\frac{\partial v}{\partial\omega}\right|_{\omega=\omega_0} = \frac{v_0}{\omega_0}\,, \tag{D.32}$$

$$\left.\frac{\partial u}{\partial\omega}\right|_{\omega=\omega_0} = \frac{u_0}{\omega_0}+\gamma_v\frac{a^2}{cR_0}\,. \tag{D.33}$$

An other auxiliary function can be defined as

$$\tilde{\Lambda}(\rho,\theta) = -\rho^2\kappa_0(1-g_v)+\imath k_0\Phi_0+\imath k_0\omega_0\left.\frac{\partial\Phi}{\partial\omega}\right|_{\omega=\omega_0}-\imath v_0\rho\cos(\theta-\psi)-\frac{\imath}{2}\rho^2\left(u_0+\gamma_v\frac{\omega_0 a^2}{cR_0}\right)\,. \tag{D.34}$$

All variables in the previous expression with subscript 0 are evaluated at ω_0, and the definitions of g_v and γ_v are given by (3.8) and (3.9), respectively. So, according to (D.8), the derivative that is necessary to obtain group delay is given by

$$\left.\frac{\partial\tilde{\mathcal{I}}}{\partial\omega}\right|_{\omega=\omega_0} = \frac{1}{\omega_0}\int_0^1\int_0^{2\pi}\tilde{\Lambda}(\rho,\theta)\tilde{\Upsilon}_0(\rho,\theta)\rho\,\mathrm{d}\theta\,\mathrm{d}\rho\,. \tag{D.35}$$

Whit this everything is available to evaluate the group delay by substituting (D.35) into (D.8), then putting this result into (D.30).

D.2.3 Group velocity in the presence of aberrations

Using the results of the previous subsection (see (D.30)) and following definition (D.14) of the group velocity the three terms that are necessary for the calculation of v_g are

$$\frac{\partial}{\partial r}\left(\left.\frac{\partial\varphi_G}{\partial\omega}\right|_{\omega=\omega_0}\right) = \frac{\partial}{\partial r}\left(\left.\frac{\partial\varphi_{\mathcal{I}}(u,v,\psi)}{\partial\omega}\right|_{\omega=\omega_0}\right)+\frac{1}{c}\frac{r}{Z_0+R_0}\,, \tag{D.36}$$

$$\frac{1}{r}\frac{\partial}{\partial\phi}\left(\left.\frac{\partial\varphi_G}{\partial\omega}\right|_{\omega=\omega_0}\right) = -\frac{1}{r}\frac{\partial}{\partial\psi}\left(\left.\frac{\partial\varphi_{\mathcal{I}}(u,v,\psi)}{\partial\omega}\right|_{\omega=\omega_0}\right)\,, \tag{D.37}$$

$$\frac{\partial}{\partial Z_0}\left(\left.\frac{\partial\varphi_G}{\partial\omega}\right|_{\omega=\omega_0}\right) = \frac{1}{c}+\frac{\partial}{\partial Z_0}\left(\left.\frac{\partial\varphi_{\mathcal{I}}(u,v,\psi)}{\partial\omega}\right|_{\omega=\omega_0}\right)-\frac{1}{c}\frac{r^2}{2(Z_0+R_0)^2}\,. \tag{D.38}$$

which are the three vector components of the gradient present in (2.70). The last term in (D.36) and (D.38) are zero on axis.

Component $\mathbf{u}_r$ of the group velocity For the double derivative of $\varphi_{\mathcal{I}}$ present in (D.36) the only unknown is the double derivative of $\tilde{\mathcal{I}}$, as all the single derivatives of $\tilde{\mathcal{I}}$ have already been calculated for either the phase velocity or the group delay which are necessary to calculate the double derivative of a complex phase according to (D.10). The complex integral $\tilde{I}(u, v, \psi)$ depends on r through the dimensionless coordinate v, so

$$\frac{\partial}{\partial r}\left(\left.\frac{\partial\tilde{\mathcal{I}}}{\partial\omega}\right|_{\omega=\omega_0}\right) = \frac{\partial}{\partial v_0}\left(\left.\frac{\partial\tilde{\mathcal{I}}}{\partial\omega}\right|_{\omega=\omega_0}\right)\frac{\partial v_0}{\partial r} = \frac{\omega_0}{c}\frac{a}{Z_0+R_0}\frac{\partial}{\partial v_0}\left(\left.\frac{\partial\tilde{\mathcal{I}}}{\partial\omega}\right|_{\omega=\omega_0}\right). \tag{D.39}$$

Knowing that

$$\frac{\partial\tilde{\Lambda}}{\partial v_0} = -\iota\rho\cos(\theta-\psi) \tag{D.40}$$

and

$$\frac{\partial\tilde{\Upsilon}_0}{\partial v_0} = -\iota\rho\cos(\theta-\psi)\tilde{\Upsilon}_0\,, \tag{D.41}$$

with some algebra it can be shown that

$$\frac{\partial}{\partial r}\left(\left.\frac{\partial\tilde{\mathcal{I}}}{\partial\omega}\right|_{\omega=\omega_0}\right) = -\frac{\iota}{c}\frac{a}{Z_0+R_0}\int_0^1\int_0^{2\pi}\cos(\theta-\psi)\left[1+\tilde{\Lambda}(\rho,\theta)\right]\tilde{\Upsilon}_0(\rho,\theta)\rho^2\,\mathrm{d}\theta\,\mathrm{d}\rho\,. \tag{D.42}$$

For on-axis expressions one should use the on-axis versions $\tilde{\Lambda}_a$ and $\tilde{\Upsilon}_{a,0}$ of $\tilde{\Lambda}$ and $\tilde{\Upsilon}_0$, respectively, which can be obtained by substituting $v_0 = 0$ into the original formulas of $\tilde{\Lambda}$ and $\tilde{\Upsilon}_0$. So one can get component $\mathbf{u}_r$ by using (D.42), (D.21) and (D.35) to get the double derivative of complex phase $\varphi_{\mathcal{I}}$ through (D.10), and applying this in (D.36).

Component $\mathbf{u}_\phi$ of the group velocity The derivative necessary for component $\mathbf{u}_\phi$ according to (D.37) is

$$\frac{1}{r}\frac{\partial}{\partial\phi}\left(\left.\frac{\partial\tilde{\mathcal{I}}}{\partial\omega}\right|_{\omega=\omega_0}\right) = -\frac{1}{r}\frac{\partial}{\partial\psi}\left(\left.\frac{\partial\tilde{\mathcal{I}}}{\partial\omega}\right|_{\omega=\omega_0}\right) = -\frac{\omega_0}{c}\frac{a}{Z_0+R_0}\frac{1}{v_0}\frac{\partial}{\partial\psi}\left(\left.\frac{\partial\tilde{\mathcal{I}}}{\partial\omega}\right|_{\omega=\omega_0}\right). \tag{D.43}$$

With

$$\frac{\partial\tilde{\Lambda}}{\partial\psi} = -\iota v_0\rho\sin(\theta-\psi) \tag{D.44}$$

and

$$\frac{\partial\tilde{\Upsilon}_0}{\partial\psi} = -\iota v_0\rho\sin(\theta-\psi)\tilde{\Upsilon}_0 \tag{D.45}$$

one can get

$$\frac{1}{r}\frac{\partial}{\partial\phi}\left(\left.\frac{\partial\tilde{\mathcal{I}}}{\partial\omega}\right|_{\omega=\omega_0}\right)=\frac{\iota}{c}\frac{a}{Z_0+R_0}\int_0^1\int_0^{2\pi}\sin(\theta-\psi)\left[1+\tilde{\Lambda}(\rho,\theta)\right]\tilde{\Upsilon}_0(\rho,\theta)\rho^2\,\mathrm{d}\theta\,\mathrm{d}\rho\,. \tag{D.46}$$

For on-axis values again $\tilde{\Lambda}_a$ and $\tilde{\Upsilon}_{a,0}$ should be used. As a summary, component $\mathbf{u}_\phi$ is a result of substituting (D.46), (D.24) and (D.35) into (D.10), which gives the sought result with (D.37).

Component $\mathbf{u}_z$ of the group velocity Just like in the case of the phase velocity, the most computation-demanding component is the longitudinal one, as $\tilde{\mathcal{I}}$ depends on Z_0 through both dimensionless coordinates u and v, giving

$$\frac{\partial}{\partial Z_0}\left(\left.\frac{\partial\tilde{\mathcal{I}}}{\partial\omega}\right|_{\omega=\omega_0}\right)=\frac{\partial u_0}{\partial Z_0}\frac{\partial}{\partial u_0}\left(\left.\frac{\partial\tilde{\mathcal{I}}}{\partial\omega}\right|_{\omega=\omega_0}\right)+\frac{\partial v_0}{\partial Z_0}\frac{\partial}{\partial v_0}\left(\left.\frac{\partial\tilde{\mathcal{I}}}{\partial\omega}\right|_{\omega=\omega_0}\right)\,. \tag{D.47}$$

Using

$$\frac{\partial u_0}{\partial Z_0}=\frac{\omega_0}{c}\frac{a^2}{(Z_0+R_0)^2}\,, \tag{D.48}$$

$$\frac{\partial v_0}{\partial Z_0}=-\frac{\omega_0}{c}\frac{ar}{(Z_0+R_0)^2}\,, \tag{D.49}$$

$$\frac{\partial\tilde{\Lambda}}{\partial u_0}=-\frac{\iota}{2}\rho^2\,, \tag{D.50}$$

$$\frac{\partial\tilde{\Upsilon}_0}{\partial u_0}=-\frac{\iota}{2}\rho^2\tilde{\Upsilon}_0 \tag{D.51}$$

results in

$$\begin{aligned}\frac{\partial}{\partial Z_0}\left(\left.\frac{\partial\tilde{\mathcal{I}}}{\partial\omega}\right|_{\omega=\omega_0}\right)=&-\frac{\iota}{2c}\frac{a^2}{(Z_0+R_0)^2}\int_0^1\int_0^{2\pi}\left[1+\tilde{\Lambda}(\rho,\theta)\right]\tilde{\Upsilon}_0(\rho,\theta)\rho^3\,\mathrm{d}\theta\,\mathrm{d}\rho\\&+\frac{\iota}{c}\frac{ar}{(Z_0+R_0)^2}\int_0^1\int_0^{2\pi}\cos(\theta-\psi)\left[1+\tilde{\Lambda}(\rho,\theta)\right]\tilde{\Upsilon}_0(\rho,\theta)\rho^2\,\mathrm{d}\theta\,\mathrm{d}\rho\,.\end{aligned} \tag{D.52}$$

For on-axis points ($r=0$) the expression simplifies to

$$\left.\frac{\partial}{\partial Z_0}\left(\left.\frac{\partial\tilde{\mathcal{I}}}{\partial\omega}\right|_{\omega=\omega_0}\right)\right|_{r=0}=-\frac{\iota}{2c}\frac{a^2}{(Z_0+R_0)^2}\int_0^1\int_0^{2\pi}\left[1+\tilde{\Lambda}_a(\rho,\theta)\right]\tilde{\Upsilon}_{a,0}(\rho,\theta)\rho^3\,\mathrm{d}\theta\,\mathrm{d}\rho\,. \tag{D.53}$$

Finally, the way to obtain component $\mathbf{u}_z$ is to use (D.52), (D.27) and (D.35) to get $\partial^2_{z\omega}\varphi_{\mathcal{I}}$ through (D.10), and to substitute this into (D.38).

Symmetries of the group velocity on axis and additional notes Similarly to the phase velocity, the points on axis ($r = 0$) have favorable properties. It is easy to see from the on-axis version of (D.42) and (D.46) that

$$\sqrt{\left(\left[\frac{\partial}{\partial r}\left(\frac{\partial\tilde{\mathcal{I}}}{\partial\omega}\bigg|_{\omega=\omega_0}\right)\right]\bigg|_{r=0}\right)^2+\left(\left[\frac{1}{r}\frac{\partial}{\partial\phi}\left(\frac{\partial\tilde{\mathcal{I}}}{\partial\omega}\bigg|_{\omega=\omega_0}\right)\right]\bigg|_{r=0}\right)^2}=\left|\left[\frac{\partial}{\partial r}\left(\frac{\partial\tilde{\mathcal{I}}}{\partial\omega}\bigg|_{\omega=\omega_0}\right)\right]\bigg|_{\substack{r=0\\ \psi=0}}\right|, \tag{D.54}$$

so the same conclusions can be drawn regarding the on-axis points as for the phase velocity.

Also note that in Section 3.1.2 a different grouping of terms is presented, where the derivatives of $\tilde{\mathcal{I}}$ with respect to its explicit arguments u, v and ψ are given, and they are multiplied by given factors in summarizing expressions. This way of calculating is only possible for on-axis points, due to the sum term in component $\mathbf{u}_z$.

D.3 Aberration-distorted phase and group velocity in Debye approximation

Debye approximation means a simplified calculation of the focused field in the vicinity of focus. For undistorted cases the usual assumption for the validity of Debye approximation is the high value of Fresnel number $N_w \gg 1$ [143, 151]. This because the regions of interest, where the light intensity is highest, is close to the focal point. However, in general, the Debye approximation has more strict limits, and it is limited how far from focus one can study the field distribution ($Z_0 \ll R_0$) [152]. This is important when aberrations are present, because the region of interest might lie outside this limited spatial volume. However, Debye approximation might still serve as good and simplified tool for calculation of the focused field. So a short summary is given for its applicability for phase and group velocity calculations in the vicinity of focus.

In the Debye approximation the focused field is given by (see Section 2.3.3)

$$\tilde{G}_D(P) = -\frac{\iota\omega}{2c}\frac{a^2}{R^2}\exp[\iota k(Z_0 + R_0 - R)]\,\frac{1}{\pi}\tilde{\mathcal{I}}_D(u_D, v_D, \psi)\,, \tag{D.55}$$

where $\tilde{\mathcal{I}}_D(u_D, v_D, \psi)$ is given by (2.52), and the D subscript has only been added because for brevity sometimes the arguments of $\tilde{\mathcal{I}}_D(u_D, v_D, \psi)$ will omitted, but it should not be forgotten, that the dimensionless coordinated u_D and v_D are of the Debye type, given by (2.56) and (2.57), respectively. The complex phase of this expression is

$$\varphi_D(\mathbf{r}, \omega) = -\frac{\pi}{2} + \frac{\omega}{c}(Z_0 + R_0 - R(\omega)) + \arg\left[\tilde{\mathcal{I}}_D(u_D, v_D, \psi)\right]. \tag{D.56}$$

The phase and group velocity is evaluated the same way from this expressions as in the case when the Debye approximation is not applied.

D.3.1 Phase velocity in Debye approximation

Following the same logic as in the previous section dealing with the more general case, to obtain phase velocity using (D.12) with the replacement of φ_G with φ_D given by (D.56), the following three derivatives are needed

$$\frac{\partial\varphi_D(\mathbf{r},\omega)}{\partial r} = \frac{\partial}{\partial r}\arg\left[\tilde{\mathcal{I}}_D(u_D,v_D,\psi)\right], \tag{D.57}$$

$$\frac{1}{r}\frac{\partial\varphi_D(\mathbf{r},\omega)}{\partial\phi} = -\frac{1}{r}\frac{\partial}{\partial\psi}\arg\left[\tilde{\mathcal{I}}_D(u_D,v_D,\psi)\right], \tag{D.58}$$

$$\frac{\partial\varphi_D(\mathbf{r},\omega)}{\partial Z_0} = \frac{\omega}{c} + \frac{\partial}{\partial Z_0}\arg\left[\tilde{\mathcal{I}}_D(u_D,v_D,\psi)\right]. \tag{D.59}$$

As $\tilde{\mathcal{I}}_D$ is formally the same as $\tilde{\mathcal{I}}$, the definition of u_D and v_D compared to u and v being the only difference, the same expressions are needed to be evaluated as is Appendix D.2.1. With

$$\frac{\partial v_D}{\partial r} = \frac{\omega}{c}\frac{a}{R}, \tag{D.60}$$

$$\frac{\partial v_D}{\partial Z_0} = 0, \tag{D.61}$$

$$\frac{\partial u_D}{\partial Z_0} = \frac{\omega}{c}\frac{a^2}{R^2}, \tag{D.62}$$

the three derivatives of the complex phase $\arg\left[\tilde{\mathcal{I}}_D(u_D,v_D,\psi)\right]$ can be calculated using the derivatives

$$\frac{\partial\tilde{\mathcal{I}}_D}{\partial r} = -\iota\frac{\omega}{c}\frac{a}{R}\int_0^1\int_0^{2\pi}\cos(\theta-\psi)\tilde{\Upsilon}_D(\rho,\theta)\rho^2\,\mathrm{d}\theta\,\mathrm{d}\rho, \tag{D.63}$$

$$\frac{1}{r}\frac{\partial\tilde{\mathcal{I}}_D}{\partial\phi} = \iota\frac{\omega}{c}\frac{a}{R}\int_0^1\int_0^{2\pi}\sin(\theta-\psi)\tilde{\Upsilon}_D(\rho,\theta)\rho^2\,\mathrm{d}\theta\,\mathrm{d}\rho, \tag{D.64}$$

$$\frac{\partial\tilde{\mathcal{I}}_D}{\partial Z_0} = -\frac{\iota}{2}\frac{\omega}{c}\frac{a^2}{R^2}\int_0^1\int_0^{2\pi}\tilde{\Upsilon}_D(\rho,\theta)\rho^3\,\mathrm{d}\theta\,\mathrm{d}\rho, \tag{D.65}$$

with (D.8). The function $\tilde{\Upsilon}_D(\rho,\theta)$ only differs from definition (D.15) that the Debye dimensionless coordinates are used in it, so

$$\tilde{\Upsilon}_D(\rho,\theta) = \exp\left(-\kappa\rho^2 + \iota k\Phi(\rho,\theta) - \iota v_D\rho\cos(\theta-\psi) - \iota\frac{u_D}{2}\rho^2\right). \tag{D.66}$$

By comparing the above expressions with the corresponding ones of Appendix D.2.1 it can be seen that if the phase velocity of the carrier wave is the question, then the Debye approximation simply means the replacement of factor $a/(Z_0 + R_0)$ with a/R_0 in all occurrences, and the second term of (D.19) can be omitted even for on-axis points. So special care must be taken for off-axis points in the applicability of the Debye approximation. When the phase velocity of an other frequency $\omega \neq \omega_0$ is the question, the factor $a/(Z_0 + R_0)$ should be replaced with $a/R(\omega)$ (second term of (D.19) can again be disregarded), which means that in this case the two approaches are strictly the same only if $\gamma_v = 0$. These give new restrictions for the validity of Debye approximation.

D.3.2 Group delay in Debye approximation

The group delay in Debye approximation is given by

$$\left.\frac{\partial\varphi_D(\mathbf{r},\omega)}{\partial\omega}\right|_{\omega=\omega_0} = \frac{Z_0}{c} + \gamma_v\frac{R_0}{c} + \left.\frac{\partial}{\partial\omega}\arg\left[\tilde{\mathcal{I}}_D(u_D, v_D, \psi)\right]\right|_{\omega=\omega_0} . \tag{D.67}$$

Also because the formal identity of $\tilde{\mathcal{I}}_D$ and $\tilde{\mathcal{I}}$, only the changes related to u_D and v_D are needed to be taken into account. Since

$$\left.\frac{\partial v_D}{\partial\omega}\right|_{\omega=\omega_0} = \frac{v_{D,0}}{\omega_0}(1+\gamma_v)\,, \tag{D.68}$$

$$\left.\frac{\partial u_D}{\partial\omega}\right|_{\omega=\omega_0} = \frac{1}{\omega_0}\left[u_{D,0} + \gamma_v\frac{\omega_0 a^2}{cR_0}\left(\frac{2(Z_0+R_0)}{R_0} - 1\right)\right]\,, \tag{D.69}$$

the necessary derivative to apply (D.8) on the last term of (D.67) is

$$\begin{aligned}\tilde{\Lambda}_D(\rho,\theta) = -\rho^2\kappa_0(1-g_v) + \iota k_0\Phi_0 + \iota k_0\omega_0\left.\frac{\partial\Phi}{\partial\omega}\right|_{\omega=\omega_0} - \iota v_{D,0}(1+\gamma_v)\rho\cos(\theta-\psi) \\ - \frac{\iota}{2}\rho^2\left[u_{D,0} + \gamma_v\frac{\omega_0 a^2}{cR_0}\left(\frac{2(Z_0+R_0)}{R_0} - 1\right)\right]\,.\end{aligned} \tag{D.70}$$

Equivalence with formulas in D.2.2 for cases with $\gamma_v = 0$ and when $Z_0 \ll R_0$ (meaning $u_D \approx u$ and $v_D \approx v$) is easy to see.

D.3.3 Group velocity in Debye approximation

Following the same logic as in D.2.3 and calculating the derivative of $\tilde{\Upsilon}_{D,0}$ and $\tilde{\Lambda}_D$ with respect to $u_{D,0}$, $v_{D,0}$ and ψ gives

$$\frac{\partial}{\partial r}\left(\left.\frac{\partial\tilde{\mathcal{I}}_D}{\partial\omega}\right|_{\omega=\omega_0}\right) = -\frac{\iota}{c}\frac{a}{R_0}\int_0^1\int_0^{2\pi}\cos(\theta-\psi)\left[1+\gamma_v+\tilde{\Lambda}_D(\rho,\theta)\right]\tilde{\Upsilon}_{D,0}(\rho,\theta)\rho^2\,\mathrm{d}\theta\,\mathrm{d}\rho\,, \tag{D.71}$$

$$\frac{1}{r}\frac{\partial}{\partial\phi}\left(\left.\frac{\partial\tilde{\mathcal{I}}_D}{\partial\omega}\right|_{\omega=\omega_0}\right) = \frac{\iota}{c}\frac{a}{R_0}\int_0^1\int_0^{2\pi}\sin(\theta-\psi)\left[1+\gamma_v+\tilde{\Lambda}_D(\rho,\theta)\right]\tilde{\Upsilon}_{D,0}(\rho,\theta)\rho^2\,\mathrm{d}\theta\,\mathrm{d}\rho\,, \tag{D.72}$$

$$\frac{\partial}{\partial Z_0}\left(\left.\frac{\partial\tilde{\mathcal{I}}_D}{\partial\omega}\right|_{\omega=\omega_0}\right) = -\frac{\iota}{2c}\frac{a^2}{R_0^2}\int_0^1\int_0^{2\pi}\left[1+2\gamma_v+\tilde{\Lambda}_D(\rho,\theta)\right]\tilde{\Upsilon}_{D,0}(\rho,\theta)\rho^3\,\mathrm{d}\theta\,\mathrm{d}\rho\,. \tag{D.73}$$

The comparison of the above results with the ones in Appendix D.2.3 shows — like in the case of phase velocity — that Debye approximation is strictly valid only for on-axis points and when $\gamma_v = 0$. If these conditions are met, Debye approximation means the replacement of factor $a/(Z_0+R_0)$ with a/R_0 in every occurrence.

Appendix

E

Calculation of the pulse shape in the focus

E.1 Focused electric field in the presence of primary spherical aberration in Debye approximation

Following what is described in Section 3.2.1, the expression that needs evaluation for the focused field in the presence of primary aberration using Debye approximation is (see (3.37))

$$\begin{aligned}\tilde{\mathcal{P}}(\omega) = &-\frac{\iota\omega\tilde{U}(\omega)a^2}{2cR}\exp[\iota k(R+l_a)]\exp\left[\iota\left(\frac{R}{a}\right)^2 u_D\right]\frac{1}{\pi}\\ &\times\int_0^1\int_0^{2\pi}\exp\left[-\kappa\rho^2\right]\exp\left[\iota\left(\alpha_S\rho^4 - v_D\rho\cos(\theta-\psi) - \frac{u_D}{2}\rho^2\right)\right]\rho\,\mathrm{d}\theta\,\mathrm{d}\rho\,.\end{aligned} \tag{E.1}$$

Since the aberration function $\Phi(\rho,\omega) = \alpha_S\rho^4$ does not depend on θ, the integration with respect to the azimuthal angle can be analytically calculated. The same way as described in [90] it gives $2\pi J_0(v_D\rho)$, J_0 being the zeroth-order Bessel function of the first kind, resulting in

$$\begin{aligned}\tilde{\mathcal{P}}(\omega) = &-\frac{\iota\omega\tilde{U}(\omega)a^2}{cR}\exp[\iota k(R+l_a)]\exp\left[\iota\left(\frac{R}{a}\right)^2 u_D\right]\\ &\times\int_0^1 J_0(v_D\rho)\exp\left[\iota\left(\alpha_S\rho^4 - \frac{\tilde{u}_D}{2}\rho^2\right)\right]\rho\,\mathrm{d}\rho\,.\end{aligned} \tag{E.2}$$

If only on-axis points are relevant, with $v_D = 0$ the integral simplifies to

$$\tilde{\mathcal{P}}(\omega) = -\frac{\iota\omega\tilde{U}(\omega)a^2}{2cR}\exp[\iota k(R+l_a)]\exp\left[\iota\left(\frac{R}{a}\right)^2 u_D\right]\underbrace{2\int_0^1 \exp\left[\iota\left(\alpha_S\rho^4 - \frac{\tilde{u}_D}{2}\rho^2\right)\right]\rho\,\mathrm{d}\rho}_{\tilde{\mathcal{I}}_S}\,. \tag{E.3}$$

The main steps of the calculation from this point can be found in [200], but a more detailed summary is presented here. If $\alpha_S \neq 0$, the exponent in integral $\tilde{\mathcal{I}}_S$ can be rewritten using the completing the square method, giving

$$\tilde{\mathcal{I}}_S = 2\exp\left[-\iota\frac{\tilde{u}_D^2}{16\alpha_S}\right]\int_0^1 \exp\left[\iota\alpha_S\left(\rho^2 - \frac{\tilde{u}_D}{4\alpha_S}\right)^2\right]\rho\,\mathrm{d}\rho\,. \tag{E.4}$$

It is easy to see that these modifications are only applicable if $\alpha_S \neq 0$, as if $\alpha_s = 0$ then the exponents in (E.4) diverge. With the $\tau = \rho^2 - \tilde{u}_D/(4\alpha_S)$ substitution ($\mathrm{d}\tau = 2\rho\mathrm{d}\rho$) $\tilde{\mathcal{I}}_S$ can be rewritten as the sum of two integrals

$$\begin{aligned}\tilde{\mathcal{I}}_S &= \exp\left[-\iota\frac{\tilde{u}_D^2}{16\alpha_S}\right]\int_{-\tilde{u}_D/(4\alpha_S)}^{1-\tilde{u}_D/(4\alpha_S)} \exp\left[\iota\alpha_S\tau^2\right]\,\mathrm{d}\tau \\ &= \exp\left[-\iota\frac{\tilde{u}_D^2}{16\alpha_S}\right]\left(\int_{-\tilde{u}_D/(4\alpha_S)}^{1-\tilde{u}_D/(4\alpha_S)} \cos\left(\alpha_S\tau^2\right)\mathrm{d}\tau + \iota\int_{-\tilde{u}_D/(4\alpha_S)}^{1-\tilde{u}_D/(4\alpha_S)} \sin\left(\alpha_S\tau^2\right)\mathrm{d}\tau\right)\,.\end{aligned} \tag{E.5}$$

By changing the argument of cos and sin functions according to

$$\begin{aligned}&\text{If } \alpha_S \geq 0: \quad \alpha_S = |\alpha_S| \quad \Rightarrow \quad \cos(\alpha_S\tau^2) = \cos(|\alpha_S|\tau^2) \\ &\qquad\qquad\qquad\qquad\qquad\quad \sin(\alpha_S\tau^2) = \sin(|\alpha_S|\tau^2) \\ &\text{If } \alpha_S < 0: \quad \alpha_S = -|\alpha_S| \quad \Rightarrow \quad \cos(\alpha_S\tau^2) = \cos(-|\alpha_S|\tau^2) = \cos(|\alpha_S|\tau^2) \\ &\qquad\qquad\qquad\qquad\qquad\quad \sin(\alpha_S\tau^2) = \sin(-|\alpha_S|\tau^2) = -\sin(|\alpha_S|\tau^2)\,,\end{aligned}$$

one can get

$$\tilde{\mathcal{I}}_S = \exp\left[-\iota\frac{\tilde{u}_D^2}{16\alpha_S}\right]\left(\int_{-\tilde{u}_D/(4\alpha_S)}^{1-\tilde{u}_D/(4\alpha_S)} \cos\left(|\alpha_S|\tau^2\right)\mathrm{d}\tau + \iota\frac{\alpha_S}{|\alpha_S|}\int_{-\tilde{u}_D/(4\alpha_S)}^{1-\tilde{u}_D/(4\alpha_S)} \sin\left(|\alpha_S|\tau^2\right)\mathrm{d}\tau\right)\,. \tag{E.6}$$

With an other exchange of variables

$$x = \sqrt{\frac{2|\alpha_S|}{\pi}}\tau \quad \Rightarrow \quad |\alpha_S|\tau^2 = \frac{\pi x^2}{2}, \quad \mathrm{d}x = \sqrt{\frac{2|\alpha_S|}{\pi}}\,\mathrm{d}\tau\,, \tag{E.7}$$

the first factor of $\tilde{\mathcal{I}}_S$ is written as

$$\begin{aligned}\int_{\tau_1}^{\tau_2} \cos(|\alpha_S|\tau^2)\,\mathrm{d}\tau &= \sqrt{\frac{\pi}{2|\alpha_S|}} \int_{\tau_1\sqrt{2|\alpha_S|/\pi}}^{\tau_2\sqrt{2|\alpha_S|/\pi}} \cos\left(\frac{\pi}{2}x^2\right)\,\mathrm{d}x \\ &= \sqrt{\frac{\pi}{2|\alpha_S|}} \left[C\left(\sqrt{\frac{2|\alpha_S|}{\pi}}\tau_2\right) - C\left(\sqrt{\frac{2|\alpha_S|}{\pi}}\tau_1\right)\right] \end{aligned} \tag{E.8}$$

$$\text{where} \quad \tau_1 = -\frac{\tilde{u}_D}{4\alpha_S}, \quad \tau_2 = 1 - \frac{\tilde{u}_D}{4\alpha_S},$$
$$C(z) = \int_0^z \cos\left(\frac{\pi}{2}t^2\right)\,\mathrm{d}t \qquad \text{is the Fresnel Cosine integral [209].}$$

Similarly, the second factor of $\tilde{\mathcal{I}}_S$ can be rewritten using the Fresnel Sine integral, and together $\tilde{\mathcal{I}}_S$ can be interpreted as the sum of four Fresnel integrals

$$\begin{aligned}\tilde{\mathcal{I}}_S = \exp\left[-\iota\frac{\tilde{u}_D^2}{16\alpha_S}\right] \sqrt{\frac{\pi}{2|\alpha_S|}} \Bigg[C\left(\sqrt{\frac{2|\alpha_S|}{\pi}}\tau_2\right) - C\left(\sqrt{\frac{2|\alpha_S|}{\pi}}\tau_1\right) + \\ +\iota\frac{\alpha_S}{|\alpha_S|}\left\{S\left(\sqrt{\frac{2|\alpha_S|}{\pi}}\tau_2\right) - S\left(\sqrt{\frac{2|\alpha_S|}{\pi}}\tau_1\right)\right\}\Bigg]\,,\end{aligned} \tag{E.9}$$

$$\text{where} \quad S(z) = \int_0^z \sin\left(\frac{\pi}{2}t^2\right)\,\mathrm{d}t \qquad \text{is the Fresnel Sine integral [209].}$$

As a last step further simplification of special functions is possible if one uses the complex error function (see (3.42)) and expresses the Fresnel integrals using them according to [209]

$$\begin{aligned}C(z) &= \frac{1-\iota}{4}\left[\mathrm{erf}\left(\frac{1+\iota}{2}\sqrt{\pi}z\right) + \iota\cdot\mathrm{erf}\left(\frac{1-\iota}{2}\sqrt{\pi}z\right)\right]\,, \\ S(z) &= \frac{1+\iota}{4}\left[\mathrm{erf}\left(\frac{1+\iota}{2}\sqrt{\pi}z\right) - \iota\cdot\mathrm{erf}\left(\frac{1-\iota}{2}\sqrt{\pi}z\right)\right]\,.\end{aligned} \tag{E.10}$$

Substituting (E.10) into (E.9) gives

$$\begin{aligned}
&\tilde{\mathcal{I}}_S \Bigg/ \left(\exp\left[-\iota \frac{\tilde{u}_D^2}{16\alpha_S} \right] \sqrt{\frac{\pi}{2|\alpha_S|}} \right) = \\
&\left[\frac{1-\iota}{4} + \iota \frac{\alpha_S}{|\alpha_S|} \frac{1+\iota}{4} \right] \operatorname{erf}\left[(1+\iota) \sqrt{\frac{|\alpha_S|}{2}} \left(1 - \frac{\tilde{u}_D}{4\alpha_S} \right) \right] \\
&+ \left[\frac{1-\iota}{4}\iota + \iota \frac{\alpha_S}{|\alpha_S|} \frac{1+\iota}{4}(-\iota) \right] \operatorname{erf}\left[(1-\iota) \sqrt{\frac{|\alpha_S|}{2}} \left(1 - \frac{\tilde{u}_D}{4\alpha_S} \right) \right] \\
&- \left[\frac{1-\iota}{4} + \iota \frac{\alpha_S}{|\alpha_S|} \frac{1+\iota}{4} \right] \operatorname{erf}\left[-(1+\iota) \sqrt{\frac{|\alpha_S|}{2}} \frac{\tilde{u}_D}{4\alpha_S} \right] \\
&- \left[\frac{1-\iota}{4}\iota + \iota \frac{\alpha_S}{|\alpha_S|} \frac{1+\iota}{4}(-\iota) \right] \operatorname{erf}\left[-(1-\iota) \sqrt{\frac{|\alpha_S|}{2}} \frac{\tilde{u}_D}{4\alpha_S} \right] .
\end{aligned} \tag{E.11}$$

The multiplication factors of the error functions give a way to further simply as

$$\pm \left[\frac{1-\iota}{4} + \iota \frac{\alpha_S}{|\alpha_S|} \frac{1+\iota}{4} \right] = \begin{cases} 0 & \text{if } \alpha_S > 0 \\ \pm(1-\iota)/2 & \text{if } \alpha_S < 0 \end{cases} , \tag{E.12}$$

and

$$\pm \left[\frac{1-\iota}{4}\iota + \iota \frac{\alpha_S}{|\alpha_S|} \frac{1+\iota}{4}(-\iota) \right] = \begin{cases} \pm(1+\iota)/2 & \text{if } \alpha_S > 0 \\ 0 & \text{if } \alpha_S < 0 \end{cases} . \tag{E.13}$$

It can be seen with simple algebra and by utilizing the odd nature of the error function ($\operatorname{erf}(-z) = -\operatorname{erf}(z)$) that the simplified form is

$$\begin{aligned}
&\tilde{\mathcal{I}}_S \Bigg/ \left(\exp\left[-\iota \frac{\tilde{u}_D^2}{16\alpha_S} \right] \sqrt{\frac{\pi}{2|\alpha_S|}} \right) = \frac{1 + \iota \operatorname{sgn}(\alpha_S)}{2} \\
&\times \left[\operatorname{erf}\left(\frac{1 - \iota \operatorname{sgn}(\alpha_S)}{2} \sqrt{2|\alpha_S|} \left(1 - \frac{\tilde{u}_D}{4\alpha_S} \right) \right) + \operatorname{erf}\left(\frac{1 - \iota \operatorname{sgn}(\alpha_S)}{2} \sqrt{2|\alpha_S|} \frac{\tilde{u}_D}{4\alpha_S} \right) \right] ,
\end{aligned} \tag{E.14}$$

where $\alpha_S/|\alpha_S|$ has been replaced by $\operatorname{sgn}(\alpha_S)$ (see definition (3.42)). Substituting this result into (E.3) gives (3.41) which also results in the same values as the formula of [195].

E.2 On-axis CEP variation of focused, pulsed beams

In the following main steps of the derivation of the on-axis CEP-variation formula (see (3.49)) developed by M. A Porras is summarized [T3, T4]. The expressions are originally based on the expression obtained for focused Gaussian beams using ABCD formalism, but can derived from scalar diffraction theory, as it is mentioned in Section 3.2.2. The equiv-

alence can be shown easy as follows. The electric field spectrum of a focused, truncated pulsed Gaussian beam in the absence of aberration can be given by

$$\tilde{\mathcal{P}}^{(f)}(Z_0,\omega) = -\frac{\iota\omega\tilde{U}(\omega)a^2}{2cf}\exp[\iota k l_a]\exp[\iota k(Z_0+f_0)]\,\frac{\exp[-\kappa-\iota u_D/2]-1}{-\kappa-\iota u_D/2}\,. \tag{E.15}$$

The above equation has been modified compared to (3.43) by the $R = f$ replacement (also in u_D), because it is assumed that the beam is focused at its waist. If negligible truncation is assumed ($\kappa \to \infty$)

$$\frac{\exp[-\kappa-\iota u_D/2]-1}{-\kappa-\iota u_D/2} \approx \frac{1}{\kappa+\iota u_D/2} = \frac{s^2}{a^2}\frac{L_D}{L_D+\iota Z}\,, \tag{E.16}$$

where $Z = Z_0 + f_0 - f$ and the modified definition of $u_D = kZa^2/f^2$ (see (2.56)) and $L_D = 2cf^2/(\omega s^2)$ (see (B.12)) is used. Substituting (E.16) into (E.15) gives

$$\tilde{\mathcal{P}}^{(f)}(Z_0,\omega) = \tilde{U}(\omega)\exp[\iota k l_a]\exp[\iota k(Z_0+f_0)]\,\frac{-f}{Z-\iota L_D} = \tilde{U}(\omega)\exp[\iota k l_a]\,\tilde{G}_D(Z_0,\omega)\,, \tag{E.17}$$

where the introduced $\tilde{G}_D(Z_0,\omega)$ is equivalent to $\tilde{G}_D(\mathbf{r})$ of (B.14) with $r = 0$. The amplitude and phase of $\tilde{G}_D(Z_0,\omega) = \mathcal{G}_D(Z_0,\omega)\exp[\iota\varphi_D(Z_0,\omega)]$ are

$$\mathcal{G}_D(Z_0,\omega) = \frac{f}{L_D}\frac{1}{\sqrt{1+(Z/L_D)^2}} \tag{E.18}$$

and

$$\varphi_D(Z_0,\omega) = -\frac{\pi}{2} - \operatorname{atan}\left[\frac{Z}{L_D}\right] + \frac{\omega}{c}(Z_0+f_0)\,, \tag{E.19}$$

where it has been used that $Z + f = Z_0 + f_0$. With the above expression, the analytical theory of pulsed beam propagation — described in Section 2.3.4 can be used to obtain information on the CEP changes induced by focusing. In the following it is assumed that the $\exp[\iota k l_0]$ term caused by the dispersion on axis is either fully or partially compensated in (E.17) ($l_a = 0$ can be taken), so the temporal variation of the electric field is given by

$$\tilde{E}^{(f)}(Z_0,t) = \mathscr{F}^{-1}\left\{\tilde{\mathcal{P}}^{(f)}(Z_0,\omega)\right\} = \mathscr{F}^{-1}\left\{\tilde{U}(\omega)\tilde{G}_D(Z_0,\omega)\right\}\,, \tag{E.20}$$

with

$$\tilde{U}(\omega) = p(\omega)\exp\left[\iota\frac{C}{2}(\omega-\omega_0)^2\right]\,. \tag{E.21}$$

The $C \equiv 0$ case corresponds to the fully compensated case, and when $C \neq 0$ there is some residual second order dispersion remaining from the not full compensation of lens center material.

E.2.1 On-axis CEP changes of pulses with non-reshaping envelope

Following the description of Section 2.3.4 we expand the temporal variation of the focused, on-axis electric field $\tilde{E}^{(f)}(Z_0,t)$ to a complex envelope and a carrier wave, so

$$\tilde{E}^{(f)}(Z_0,t)=\tilde{\mathcal{E}}^{(f)}(Z_0,t)\exp[-\imath\omega_0 t]\ . \tag{E.22}$$

Let us assume that the analytical theory of pulsed beam propagation of Section 2.3.4 properly describes the focusing using only the zeroth order term in the amplitude expansion of (2.65) (see explicit expression in time t instead of local time τ in (B.21), which should be taken with $\mathcal{G}'_{D,0}(Z)=0$ here), so

$$\tilde{\mathcal{E}}^{(f)}(Z_0,t)\simeq\mathcal{G}_{D,0}(Z_0)\tilde{\mathcal{E}}^{(i)}(\tau)\exp[\imath\varphi_{D,0}(Z_0)]\ , \tag{E.23}$$

where $\tilde{\mathcal{E}}^{(i)}(\tau)=\mathscr{F}^{-1}\left\{\tilde{U}(\omega-\omega_0)\right\}$ is the complex temporal envelope of the pulse right behind the focusing element, $\mathcal{G}_{D,0}(Z)$ and $\varphi_{D,0}(Z)$ are given by (E.18) and (E.19), respectively, taken at $\omega=\omega_0$. Let us assume that the complex envelope reaches its maximum in coordinate Z_0 in time $t_p=\tau_p+\varphi'_{D,0}(Z_0)$ (still, prime is differentiation with respect to ω). The phase $\varphi_{\mathrm{CEP}}(Z_0)=\arg\left[\tilde{E}^{(f)}(Z_0,t_p)\right]$ of the electric field (or the carrier wave in other sense) in this moment is

$$\varphi_{\mathrm{CEP}}(Z_0)=-\omega_0(\tau_p+\varphi'_{D,0}(Z_0))+\varphi_{D,0}(Z_0)+\varphi_{\mathcal{E}}\ . \tag{E.24}$$

where $\varphi_{\mathcal{E}}=\arg\left[\mathcal{G}_{D,0}(Z_0)\tilde{\mathcal{E}}^{(i)}(\tau)\right]$ is the phase of the not separated part of the complex envelope. As the complex temporal envelope does not change in this zeroth order[I], the value of t_p and $\varphi_{\mathcal{E}}$ is the same for every Z_0 coordinate. This means the CEP change with respect to the phase value in the focal point is

$$\begin{aligned}\Delta\varphi_{\mathrm{CEP}}(Z_0)&=\varphi_{\mathrm{CEP}}(Z_0)-\varphi_{\mathrm{CEP}}(0)\\&=-\omega_0\varphi'_{D,0}(Z_0)+\varphi_{D,0}(Z_0)-\left[-\omega_0\varphi'_{D,0}(0)+\varphi_{D,0}(0)\right]\ .\end{aligned} \tag{E.25}$$

Calculating the derivative $\varphi'_{D,0}(Z_0)$ using (E.19) gives

$$\varphi'_{D,0}(Z_0)=\left.\frac{\partial\varphi_D(Z_0)}{\partial\omega}\right|_{\omega=\omega_0}=-\frac{1}{1+(Z_0/L_{D,0})^2}\left(\frac{Z'_0}{L_{D,0}}-\frac{Z_0}{L^2_{D,0}}L'_{D,0}\right)+\frac{Z_0+f_0}{c}\ , \tag{E.26}$$

[I] Please note that if the complex envelope is unchanging for any other reason the followings are still valid. Using the zeroth-order approximation just an example of this case. If it is enough to describe the studied case, the findings are valid for any pulse shape. Envelope reshaping connected to pulse chirp, for exmaple, is described in the next subsection.

where $Z_0' = \partial Z/\partial\omega|_{\omega=\omega_0} = -f_0'$. By introducing $g_p = -L_{D,0}'\omega_0/L_{D,0}$ and $\gamma_p = f_0'\omega_0/L_{D,0}$ (see (3.53) and (3.54)) one can get

$$-\omega_0\varphi_{D,0}'(Z_0) = \frac{1}{1+(Z_0/L_{D,0})^2}\left(-\gamma_p + g_p\frac{Z_0}{L_{D,0}}\right) - \frac{\omega_0}{c}(Z_0+f_0)\,. \tag{E.27}$$

Substitution of the above expression and (E.19) into (E.25) with the appropriate argument gives

$$\Delta\varphi_{\mathrm{CEP}}(Z_0) = -\mathrm{atan}\,(\xi) + g_p\frac{\xi}{1+\xi^2} + \gamma_p\frac{\xi^2}{1+\xi^2}\,, \tag{E.28}$$

which is equivalent to (3.49) with $C = 0$, so $g_C = g_p$ and $\gamma_C = \gamma_p$ (see (3.51) and (3.52)). The dimensionless coordinate is gain $\xi = Z_0/L_{D,0}$. The above results show that the validity of this CEP-change expression only requires that the phase of the beam is determined by the Gouy phase shift and that the envelope does not change it shape upon propagation.

When the focusing element is a singlet thin lens, $f(\omega) = (n(\omega_0)-1)f(\omega_0)/(n(\omega)-1)$ approximation can be used [135], and g_p and γ_p are

$$g_p = \frac{L_0'}{L_0}\omega_0 + 2\frac{n_0'}{n_0-1}\omega_0\,, \tag{E.29}$$

and

$$\gamma_p = -\frac{n_0'}{n_0-1}\frac{L_0}{f_0}\omega_0\,, \tag{E.30}$$

where L_0 is the Rayleigh length of the input beam at carrier wavelength [T3].

E.2.2 On-axis CEP changes of a focused, chirped Gaussian pulse with first-order approximation of envelope reshaping

For Gaussian pulses it is possible to obtain analytical expressions for the focal CEP change [T4]. The key is to use the analytical theory of pulsed beam propagation described in Section 2.3.4 up to the first order in envelope, so the envelope of the focused pulse on axis is given by (see (2.65), or more explicitly (B.21))

$$\tilde{\mathcal{E}}^{(f)}(Z_0,t) \simeq \left[\mathcal{G}_{D,0}(Z_0)\tilde{\mathcal{E}}^{(i)}(\tau) + \iota\mathcal{G}_{D,0}'(Z_0)\frac{\mathrm{d}\tilde{\mathcal{E}}^{(i)}(\tau)}{\mathrm{d}\tau}\right]\exp[\iota\varphi_{D,0}(Z_0)]\,. \tag{E.31}$$

The necessary quantity $\mathcal{G}_D'(Z_0)$, for focused Gaussian beams the derivative of (E.18) with respect to frequency, can be obtained to be

$$\mathcal{G}_D'(Z_0) = \mathcal{H}(Z_0)\mathcal{G}_D(Z_0) \tag{E.32}$$

with

$$\mathcal{H}(Z_0) = \frac{f'}{f}\left[1 + \frac{f}{L_D}\frac{Z/L_D}{1+(Z/L_D)^2}\right] - \frac{L_D'}{L_D}\left[1 - \frac{(Z/L_D)^2}{1+(Z/L_D)^2}\right] . \tag{E.33}$$

The simple expression of (E.32) mean that (E.31) can be expressed as

$$\begin{aligned}\tilde{\mathcal{E}}^{(f)}(Z_0,t) &\simeq \left[\tilde{\mathcal{E}}^{(i)}(\tau) + \iota\mathcal{H}(Z_0)\frac{\mathrm{d}\tilde{\mathcal{E}}^{(i)}(\tau)}{\mathrm{d}\tau}\right]\mathcal{G}_{D,0}(Z_0)\exp[\iota\varphi_{D,0}(Z_0)] \\ &\simeq \tilde{\mathcal{E}}^{(i)}(\tau+\iota\mathcal{H}(Z_0))\mathcal{G}_{D,0}(Z_0)\exp[\iota\varphi_{D,0}(Z_0)] ,\end{aligned} \tag{E.34}$$

where in the second step the $f(x+\iota h) \approx f(x) + (\mathrm{d}f(x)/\mathrm{d}x)\iota h + \ldots$ expansion for the expression in square brackets is used. The meaning of the above is that for focused Gaussian beams in the first-order approximation of envelope reshaping means that the complex envelope has to be taken at a time shifted by $\iota\mathcal{H}(Z_0)$. The complex time shift means that the pulse is chirped. Let us assume that the complex envelope $\tilde{\mathcal{E}}^{(i)}(\tau)$ of the input pulse is a chirped Gaussian pulse written as

$$\tilde{\mathcal{E}}^{(i)}(\tau) = \frac{T_{\mathrm{G,min}}}{\tilde{b}}\exp\left[-\frac{\tau^2}{\tilde{b}^2}\right] , \tag{E.35}$$

where

$$\tilde{b}^2 = T_{\mathrm{G,min}}^2 - 2\iota C , \tag{E.36}$$

$T_{\mathrm{G,min}}$ being the transform-limited Gaussian duration and C is a second order phase derivative giving a temporal chirp of the pulse, originating from, for example, not full compensation of lens material (see (E.21)). The envelope has been given in the form of (E.35) for later convenience, but it can be easily seen that it equals to the complex envelope of a chirped Gaussian pulse written in Appendix A.1 (without the carrier term $\exp[\iota\varphi(\omega_0) - \iota\omega_0 t]$ of (A.10) it equals to (E.35) with $T_{\mathrm{G,min}}^2 = 2/\sigma^2$ and $C = \mathrm{GDD}$). Using that

$$\frac{1}{\tilde{b}^2} = \frac{1}{T_{\mathrm{G}}^2} + \iota\frac{2C/T_{\mathrm{G,min}}^2}{T_{\mathrm{G}}^2} , \tag{E.37}$$

where

$$T_{\mathrm{G}}^2 = T_{\mathrm{G,min}}^2\left[1 + \left(\frac{2C}{T_{\mathrm{G,min}}^2}\right)^2\right] \tag{E.38}$$

is the square of the Gaussian duration of the chirped Gaussian pulse, it can be shown that the substitution of (E.35) into (E.34) gives

$$\left|\tilde{\mathcal{E}}^{(f)}(Z_0,t)\right| \simeq \frac{T_{\mathrm{G,min}}}{|b|}\exp\left[\frac{\mathcal{H}^2(Z_0)}{T_{\mathrm{G,min}}^2}\right]\exp\left[-\frac{1}{T_{\mathrm{G}}^2}\left(\tau - \frac{2C}{T_{\mathrm{G,min}}^2}\mathcal{H}(Z_0)\right)^2\right]\mathcal{G}_{D,0}(Z_0) . \tag{E.39}$$

The above means that the distortion of the real envelope of a chirped, pulsed Gaussian beam on axis due to focusing — which is relevant regarding the CEP — is a Z_0-dependent temporal shift of the envelope given by

$$\Delta\tau(Z_0) = \frac{2C}{T_{\mathrm{G,min}}^2}\mathcal{H}(Z_0)\,. \tag{E.40}$$

The phase of the complex envelope (E.34) similarly can be shown to be

$$\arg\left[\tilde{\mathcal{E}}^{(f)}(Z_0,t)\right] \simeq \varphi_{D,0}(Z_0) - \frac{2C}{T_{\mathrm{G,min}}^2}\frac{\mathcal{H}^2(Z_0)}{T_{\mathrm{G,min}}^2} \approx \varphi_{D,0}(Z_0)\,. \tag{E.41}$$

The second term of the previous expression is second order in $\mathcal{H}(Z_0)$, so can be disregarded in this first-order theory, meaning that the phase change of the complex envelope due to the time shift (E.40) is negligible.

The above findings on the complex envelope means that the results of the zeroth-order approximation of the previous section only have to be extended by taking into account the temporal shift of the envelope peak, giving a CEP shift of $\Delta\varphi = -\omega_0\Delta\tau$ (compare (E.23) with (E.39) and (E.41)). So the on-axis CEP change during propagation of a focused, pulsed Gaussian beam with chirped Gaussian envelope is given by

$$\Delta\varphi_{\mathrm{CEP,tot}}(Z_0) = \Delta\varphi_{\mathrm{CEP}}(Z_0) + \Delta\varphi_C(Z_0)\,, \tag{E.42}$$

where $\Delta\varphi_{\mathrm{CEP}}$ is given by (E.28),

$$\Delta\varphi_C = -\omega_0\left(\Delta\tau(Z_0) - \Delta\tau(0)\right)\,, \tag{E.43}$$

and the change of the CEP is again the change from its value in the geometrical focus. Substituting (E.40) into (E.43) gives

$$\Delta\varphi_C(Z_0) = \frac{2C}{T_{\mathrm{G,min}}}\left(-\gamma_p\frac{Z_0/L_{D,0}}{1+(Z_0/L_{D,0})^2} + g_p\frac{(Z_0/L_{D,0})^2}{1+(Z_0/L_{D,0})^2}\right)\,, \tag{E.44}$$

with g_p and γ_p given by (3.53)and (3.54), respectively. Substitution of (E.44) and (E.28) into (E.42) gives (3.49).

It is to be noted that while the shape of a pulse with Gaussian spectrum and third order phase derivative can be derived analytically (see Appendix A.1), the above theory can not be extended to that case. The reason is simply the following. For the Airy function with complex argument in (A.24) the maximum of the envelope is not possible to be obtained analytically, like it can be done for a chirped Gaussian pulse given by (E.39). Analytical expressions for other types of beams than Gaussian might be possible

to obtain, depending on the shape of $\mathcal{G}_{D,0}(Z_0)$, whether it gives the possibility of a similar simplification like (E.34) for focused Gaussian beams or not.

Appendix

F

Changes of the instantaneous polarization state during propagation

F.1 Polarization-state changes with first-order theory of beam propagation

In the following the calculations of M. A. Porras are summarized which show what simple rules govern the instantaneous polarization-state changes in the first order theory of beam propagation/focusing [T6]. The aim is to obtain simple formulas on how the orientation $\Psi^{(p)}(\tau)$ and ellipticity $\chi^{(p)}(\tau)$ of the instantaneous polarization ellipse of the propagated pulse relate to the same properties of the source pulse ($\Psi^{(i)}(\tau)$ and $\chi^{(i)}(\tau)$). When the left- and right circularly polarized components are the expansion basis for the polarization state, according to (A.45) the instantaneous orientation of the propagated field can be expressed as

$$\Psi^{(p)}(\mathbf{r},\tau) = \frac{\hat{\varphi}_r^{(p)}(\mathbf{r},\tau) - \hat{\varphi}_l^{(p)}(\mathbf{r},\tau)}{2}\,, \tag{F.1}$$

where $\hat{\varphi}_{r,l}^{(p)}(\mathbf{r},\tau)$ are the temporal phases of the right- and left components. If one expresses the temporal phases of each component with the first-order theory of Section 2.3.4 (see (2.68)) and substitutes into (F.1), the result is

$$\Psi^{(p)}(\mathbf{r},\tau) \simeq \frac{\hat{\varphi}_r^{(i)}(\tau) - \hat{\varphi}_l^{(i)}(\tau)}{2} + \frac{\mathcal{G}_0'(\mathbf{r})}{\mathcal{G}_0(\mathbf{r})}\left[\frac{\mathrm{d}\ln\left(A_r^{(i)}(\tau)\right)}{\mathrm{d}\tau} - \frac{\mathrm{d}\ln\left(A_l^{(i)}(\tau)\right)}{\mathrm{d}\tau}\right], \tag{F.2}$$

where, following Section 2.3.4, $A_{l,r}(\tau)$ are real temporal envelopes and $\mathcal{G}(\mathbf{r})$ describes the beam amplitude. Using that the first term in (F.2) equals to $\Psi^{(i)}(\tau)$ and applying the linearity of derivation and the identities of logarithm on the second term one can arrive to

$$\Psi^{(p)}(\mathbf{r},\tau) \simeq \Psi^{(i)}(\tau) + \frac{1}{2}\frac{\mathcal{G}_0'(\mathbf{r})}{\mathcal{G}_0(\mathbf{r})}\frac{1}{A_l^{(i)}(\tau)A_r^{(i)}(\tau)}\left[\frac{\mathrm{d}\,A_r^{(i)}(\tau)}{\mathrm{d}\tau}A_l^{(i)}(\tau) - A_r^{(i)}(\tau)\frac{\mathrm{d}\,A_l^{(i)}(\tau)}{\mathrm{d}\tau}\right], \tag{F.3}$$

Based on the definition (A.55)

$$\frac{\mathrm{d}\,\tan\left[\chi^{(i)}(\tau)\right]}{\mathrm{d}\tau} = \frac{2}{\left[A_l^{(i)}(\tau) + A_r^{(i)}(\tau)\right]^2}\left[\frac{\mathrm{d}\,A_r^{(i)}(\tau)}{\mathrm{d}\tau}A_l^{(i)}(\tau) - A_r^{(i)}(\tau)\frac{\mathrm{d}\,A_l^{(i)}(\tau)}{\mathrm{d}\tau}\right]. \tag{F.4}$$

Substituting (F.4) into (F.3) and using that $\left[A_M^{(i)}(\tau)\right]^2 = 0.5\left[A_l^{(i)}(\tau) + A_r^{(i)}(\tau)\right]^2$ (see (A.52)) the instantaneous orientation of the propagated pulse's polarization ellipse is

$$\Psi^{(p)}(\mathbf{r},\tau) \simeq \Psi^{(i)}(\tau) + \frac{1}{2}\frac{\mathcal{G}_0'(\mathbf{r})}{\mathcal{G}_0(\mathbf{r})}\frac{\left[A_M^{(i)}(\tau)\right]^2}{A_l^{(i)}(\tau)A_r^{(i)}(\tau)}\frac{\mathrm{d}\,\tan\left[\chi^{(i)}(\tau)\right]}{\mathrm{d}\tau}. \tag{F.5}$$

It can be shown that $\left(A_M^{(i)}(\tau)\right)^2 / \left(2A_l^{(i)}(\tau)A_r^{(i)}(\tau)\right) = 1/\left(1-\tan^2\left[\chi^{(i)}(\tau)\right]\right)$, so (F.5) is equal to (3.66).

To similarly evaluate the ellipticity of the propagated pulse one needs the following identities which can be obtained with simple algebra from expressions of Appendix A.2.2:

$$\hat{\varphi}_r(\tau) = \hat{\varphi}_M(\tau) + \Psi(\tau), \quad \hat{\varphi}_l(\tau) = \hat{\varphi}_M(\tau) - \Psi(\tau), \tag{F.6}$$

$$A_r(\tau) = \frac{A_M(\tau) + \mathrm{sgn}(\chi)A_m(\tau)}{\sqrt{2}}, \quad A_l(\tau) = \frac{A_M(\tau) - \mathrm{sgn}(\chi)A_m(\tau)}{\sqrt{2}}. \tag{F.7}$$

Following the definition of $\chi(\tau)$ one can get from (A.55), (A.52) and (A.54) that

$$\tan\left[\chi^{(p)}(\mathbf{r},\tau)\right] = \mathrm{sgn}\left[\chi^{(p)}(\mathbf{r},\tau)\right]\frac{A_m^{(p)}(\mathbf{r},\tau)}{A_M^{(p)}(\mathbf{r},\tau)}, \tag{F.8}$$

so the size of the semi-major and semi-minor axes has to be determined to get the ellipticity of the propagated pulse. According to (A.52) the semi-major axis is

$$A_M^{(p)}(\mathbf{r},\tau) = \frac{A_r^{(p)}(\mathbf{r},\tau) + A_l^{(p)}(\mathbf{r},\tau)}{\sqrt{2}}. \tag{F.9}$$

Expressing the real envelopes $A_{r,l}^{(p)}(\mathbf{r},\tau)$ with the first-order theory (see (2.67)) in the

previous expression and utilizing (F.6) and (F.7) results in

$$\begin{aligned} A_M^{(p)}(\mathbf{r},\tau) \simeq & \frac{\mathcal{G}_0(\mathbf{r})}{2}\exp\left[-\frac{\mathcal{G}_0'(\mathbf{r})}{\mathcal{G}_0(\mathbf{r})}\frac{\mathrm{d}\hat{\varphi}_M^{(i)}(\tau)}{\mathrm{d}\tau}\right] \\ & \times\left\{\exp\left[-\frac{\mathcal{G}_0'(\mathbf{r})}{\mathcal{G}_0(\mathbf{r})}\frac{\mathrm{d}\Psi^{(i)}(\tau)}{\mathrm{d}\tau}\right]\left(A_M^{(i)}(\tau)+\mathrm{sgn}\left[\chi^{(i)}(\tau)\right]A_m^{(i)}(\tau)\right)\right. \\ & \left.+\exp\left[+\frac{\mathcal{G}_0'(\mathbf{r})}{\mathcal{G}_0(\mathbf{r})}\frac{\mathrm{d}\Psi^{(i)}(\tau)}{\mathrm{d}\tau}\right]\left(A_M^{(i)}(\tau)-\mathrm{sgn}\left[\chi^{(i)}(\tau)\right]A_m^{(i)}(\tau)\right)\right\} \end{aligned} \tag{F.10}$$

The above expression can be simplified with the Taylor-series expansion $\exp[x]=1+x+\ldots$ of the exponential terms in the curly brackets, giving

$$A_M^{(p)}(\mathbf{r},\tau)\approx\mathcal{G}_0(\mathbf{r})\exp\left[-\frac{\mathcal{G}_0'(\mathbf{r})}{\mathcal{G}_0(\mathbf{r})}\frac{\mathrm{d}\hat{\varphi}_M^{(i)}(\tau)}{\mathrm{d}\tau}\right]\left\{A_M^{(i)}(\tau)-\frac{\mathcal{G}_0'(\mathbf{r})}{\mathcal{G}_0(\mathbf{r})}\frac{\mathrm{d}\Psi^{(i)}(\tau)}{\mathrm{d}\tau}\mathrm{sgn}\left[\chi^{(i)}(\tau)\right]A_m^{(i)}(\tau)\right\}. \tag{F.11}$$

The same way the semi-minor axis can also be evaluated, resulting in

$$\begin{aligned} \mathrm{sgn}\left[\chi^{(p)}(\mathbf{r},\tau)\right]A_m^{(p)}(\mathbf{r},\tau)\approx & \mathcal{G}_0(\mathbf{r})\exp\left[-\frac{\mathcal{G}_0'(\mathbf{r})}{\mathcal{G}_0(\mathbf{r})}\frac{\mathrm{d}\hat{\varphi}_M^{(i)}(\tau)}{\mathrm{d}\tau}\right] \\ & \times\left\{\mathrm{sgn}\left[\chi^{(i)}(\tau)\right]A_m^{(i)}(\tau)-\frac{\mathcal{G}_0'(\mathbf{r})}{\mathcal{G}_0(\mathbf{r})}\frac{\mathrm{d}\Psi^{(i)}(\tau)}{\mathrm{d}\tau}A_M^{(i)}(\tau)\right\}. \end{aligned} \tag{F.12}$$

Substituting (F.12) and (F.11) into (F.8) gives

$$\begin{aligned} \tan\left[\chi^{(p)}(\mathbf{r},\tau)\right]\approx & \left\{\mathrm{sgn}\left[\chi^{(i)}(\tau)\right]A_m^{(i)}(\tau)-\frac{\mathcal{G}_0'(\mathbf{r})}{\mathcal{G}_0(\mathbf{r})}\frac{\mathrm{d}\Psi^{(i)}(\tau)}{\mathrm{d}\tau}A_M^{(i)}(\tau)\right\} \\ & \Big/\left\{A_M^{(i)}(\tau)-\frac{\mathcal{G}_0'(\mathbf{r})}{\mathcal{G}_0(\mathbf{r})}\frac{\mathrm{d}\Psi^{(i)}(\tau)}{\mathrm{d}\tau}\mathrm{sgn}\left[\chi^{(i)}(\tau)\right]A_m^{(i)}(\tau)\right\}. \end{aligned} \tag{F.13}$$

Extracting $A_M^{(i)}(\tau)$ from the denominator, applying $1/(1-x)=1+x+\ldots$ on the remaining terms of the denominator gives the result

$$\tan\left[\chi^{(p)}(\mathbf{r},\tau)\right]\approx\left(\tan\left[\chi^{(i)}(\tau)\right]-\frac{\mathcal{G}_0'(\mathbf{r})}{\mathcal{G}_0(\mathbf{r})}\frac{\mathrm{d}\Psi^{(i)}(\tau)}{\mathrm{d}\tau}\right)\left(1+\frac{\mathcal{G}_0'(\mathbf{r})}{\mathcal{G}_0(\mathbf{r})}\frac{\mathrm{d}\Psi^{(i)}(\tau)}{\mathrm{d}\tau}\tan\left[\chi^{(i)}(\tau)\right]\right). \tag{F.14}$$

This, by neglecting the quadratic term in $\mathcal{G}_0'(\mathbf{r})/\mathcal{G}_0(\mathbf{r})$, gives

$$\tan\left[\chi^{(p)}(\mathbf{r},\tau)\right]\simeq\tan\left[\chi^{(i)}(\tau)\right]-\frac{\mathcal{G}_0'(\mathbf{r})}{\mathcal{G}_0(\mathbf{r})}\frac{\mathrm{d}\Psi^{(i)}(\tau)}{\mathrm{d}\tau}\left(1-\tan^2\left[\chi^{(i)}(\tau)\right]\right), \tag{F.15}$$

which is equivalent to (3.67). Note that to obtain the approximate formula (F.15) for the ellipticity of the propagated pulse much more approximations were used than for the

orientation (F.5). So it is expected that the ellipticity expression is less accurate than the one for the orientation of the instantaneous polarization ellipse.

F.2 Instantaneous polarization attributes of the polarization-gating and the rotating pulse

There are two pulses ideal for visualizing the polarization-state change rules of the first-order propagation theory (see (3.66) and (3.67)). These state that a polarization-shaped pulse with time-varying instantaneous orientation is subject to a change in the instantaneous ellipticity upon propagation, and vice versa, a pulse with time-varying instantaneous ellipticity will suffer a modification of the instantaneous orienation while propagating. So a pulse that has a time-varying orientation but time-independent ellipticity, and one of which the ellipticity changes with time and the orientation is constant can picture expression (3.66) and (3.67) nicely. The polarization-gating pulse and the rotating pulse, which are good examples for this, can be both examined analytically.

The polarization-gating pulse As discussed in Section 3.4.1, the polarization-gating pulse consists of two circularly polarized components with opposite helicity that are delayed in time with respect to each other. So it can be given as

$$\tilde{E}(t) = \frac{1}{2}\tilde{E}_{\text{pulse}}\left(t + \frac{\Delta t}{2}\right)(\mathbf{u}_x + \iota\mathbf{u}_y) + \frac{1}{2}\tilde{E}_{\text{pulse}}\left(t - \frac{\Delta t}{2}\right)(\mathbf{u}_x - \iota\mathbf{u}_y)\,, \tag{F.16}$$

where $\tilde{E}_{\text{pulse}}(t) = \tilde{\mathcal{E}}(t)\exp[-\iota\omega_0 t]$ is a pulse shape, Δt is the mentioned delay. In the simple empirical picture of how the polarization-gating pulse is generated experimentally, the above formula can be verified to give a pulse shape that is equivalent to the one used for isolated attosecond pulse generation [39]. In the experiments, a linearly polarized short pulse with normal incidence passes through a higher-order quarter-wave plate. The polarization of the pulse makes an angle of 45° with the optical axis of the birefringent plate. This produces two pulses with perpendicular polarization and which are delayed with respect to each other. The delay is caused by the different dispersion properties of the principal refractive indexes which result in different group delays. Simultaneously, the quarter-wave plate introduces a phase shift of $\pi/4$ between the two carrier waves. In the temporally overlapping region the polarization is circular behind this first quarter-wave plate. Then a second, zeroth-order quarter-wave plate is used. The angle of the optical axes of the two waveplates is 45°. Passing through this second plate the two delayed, linearly polarized pulses are converted to circularly polarized, as they are both in 45° with the optical axis of the second waveplate. Since they make an angle with

the optical axis in an opposite direction, they are circularly polarized with the opposite helicity. It is easy to see, and is verified by the expressions below, that the first plate does not have to be a quarter-wave plate, its role is to produce two delayed, perpendicular, linearly polarized components. In reality, of course, the two components are not perfectly circularly polarized, but elliptically, and they do not have the same $\tilde{E}_{\text{pulse}}(t)$ pulse shape.

By comparing (A.44) with (F.16) it can be seen that the complex envelopes of the left- and right circular components are

$$\tilde{\mathcal{E}}_l(t) = \frac{1}{\sqrt{2}} A\left(t + \frac{\Delta t}{2}\right) \exp\left[\iota\hat{\varphi}\left(t + \frac{\Delta t}{2}\right)\right] \exp\left[-\iota\omega_0 \frac{\Delta t}{2}\right] , \tag{F.17}$$

$$\tilde{\mathcal{E}}_r(t) = \frac{1}{\sqrt{2}} A\left(t - \frac{\Delta t}{2}\right) \exp\left[\iota\hat{\varphi}\left(t - \frac{\Delta t}{2}\right)\right] \exp\left[+\iota\omega_0 \frac{\Delta t}{2}\right] , \tag{F.18}$$

where the complex envelopes have been decomposed to real envelopes and phases, like in (2.3). Let us choose the pulse shape $\tilde{E}_{\text{pulse}}(t)$ as a linearly chirped Gaussian pulse, so the real envelope is

$$A(t) = \exp\left[-\frac{t^2}{T_{\text{G}}^2}\right] , \tag{F.19}$$

while the real temporal phase is

$$\hat{\varphi}(t) = -\frac{\hat{C}_t}{T_{\text{G}}^2} t^2 , \tag{F.20}$$

obtained from (3.73). With the above $\hat{\varphi}(t)$ substituted into (F.17) and (F.18) one can get the orientation of the chirped, Gaussian, polarization-gating pulse using (A.45), giving

$$\Psi^{(i)}(t) = \frac{\Delta t}{2}\omega_0 + \frac{\hat{C}_t \Delta t}{T_{\text{G}}^2} t . \tag{F.21}$$

The above is a time-independent quantity if $\hat{C}_t \equiv 0$, as it is mentioned in Section 3.4.1. Similarly, using (A.55) on the amplitudes of the complex envelopes (F.17) and (F.18) one can get the ellipticity as

$$\tan\left[\chi^{(i)}(t)\right] = \frac{A(t - \Delta t/2) - A(t + \Delta t/2)}{A(t - \Delta t/2) + A(t + \Delta t/2)} . \tag{F.22}$$

Since

$$A\left(t \pm \frac{\Delta t}{2}\right) = \exp\left[-\frac{t^2}{T_{\text{G}}^2} - \frac{\Delta t^2}{4T_{\text{G}}^2} \mp \frac{t\Delta t}{T_{\text{G}}^2}\right] , \tag{F.23}$$

the ellipticity of the polarization-gating pulse is

$$\tan\left[\chi^{(i)}(t)\right] = \tanh\left[\frac{t\Delta t}{T_{\text{G}}^2}\right] . \tag{F.24}$$

The derivative of $\tan\left[\chi^{(i)}(\tau)\right]$ with respect to local time τ (for the initial pulse $t = \tau$, since the group delay is zero, see definition (2.63) of the local time), which is necessary for the orientation of the propagated pulse according to (3.66), is (using hyperbolic identities)

$$\frac{\mathrm{d}\tan\left[\chi^{(i)}(\tau)\right]}{\mathrm{d}\tau} = \left(1 - \tanh^2\left[\frac{\tau\Delta t}{T_{\mathrm{G}}^2}\right]\right)\frac{\Delta t}{T_{\mathrm{G}}^2}\,. \tag{F.25}$$

Substitution of (F.25) and (F.24) into (3.66) gives

$$\Psi^{(p)}(\tau) \simeq \Psi^{(i)}(\tau) + \frac{\mathcal{G}_0'(\mathbf{r})}{\mathcal{G}_0(\mathbf{r})}\frac{\Delta t}{T_{\mathrm{G}}^2}\,, \tag{F.26}$$

which is a constant shift, and in the far field with $\mathcal{G}_0'(\mathbf{r})/\mathcal{G}_0(\mathbf{r}) = 1/\omega_0$ results in (3.72).

With the time derivative of (F.21) the propagated ellipticity using (3.67) is

$$\tan\left[\chi^{(p)}(\tau)\right] \simeq \underbrace{\tanh\left[\frac{\tau\Delta t}{T_{\mathrm{G}}^2}\right]}_{\tan\left[\chi^{(i)}(\tau)\right]} - \frac{\mathcal{G}_0'(\mathbf{r})}{\mathcal{G}_0(\mathbf{r})}\left(1 - \tanh^2\left[\frac{\tau\Delta t}{T_{\mathrm{G}}^2}\right]\right)\frac{\hat{C}_t\Delta t}{T_{\mathrm{G}}^2}\,. \tag{F.27}$$

In practical cases the second term is much smaller than the first in (F.27) which means that there is almost no change in the instantaneous ellipticity of a chirped, Gaussian, polarization-gating pulse upon propagation (see Figure 3.24). This is without doubt true for the transform-limited pulse ($\hat{C}_t \equiv 0$). While it is only done for Gaussian here, other real envelope shapes $A(t)$ can be treated analytically as well.

The rotating pulse Similarly to the case of the polarization-gating pulse it can be shown that in the left- and right circularly polarized representation the rotating pulse of Section 3.4.1 is

$$\tilde{E}_l(t) = a_l\tilde{E}_{\mathrm{pulse}}(t)\exp[-\iota\omega_d t]\,, \tag{F.28}$$

$$\tilde{E}_r(t) = a_r\tilde{E}_{\mathrm{pulse}}(t)\,, \tag{F.29}$$

which verifies the description given previously that this pulse consists of circularly polarized components of opposite helicity with different amplitudes (a_l and a_r) and carrier frequencies ($\omega_0 + \omega_d$ and ω_0, where $\omega_d \ll \omega_0$). Substituting the real envelopes and phases of (F.28) and (F.29) into (A.45) and (A.55) gives

$$\Psi^{(i)}(t) = \frac{\omega_d t}{2} \tag{F.30}$$

and

$$\tan\left[\chi^{(i)}\right] = \frac{a_r - a_l}{a_r + a_l} \tag{F.31}$$

irrespective of the exact shape of $\tilde{E}_{\text{pulse}}(t) = \tilde{\mathcal{E}}(t)\exp[-\iota\omega_0 t]$. Using (3.67) the ellipticity of the propagated pulse is given by

$$\tan\left[\chi^{(p)}\right] \simeq \tan\left[\chi^{(i)}\right] - \frac{\mathcal{G}_0'(\mathbf{r})}{\mathcal{G}_0(\mathbf{r})}\frac{\omega_d}{2}\left(1 - \tan^2\left[\chi^{(i)}\right]\right) . \tag{F.32}$$

In the far field with an other approach an approximate analytical expression can be given. Using that $\mathcal{G}_0|_{\text{far field}} \sim 1/\omega_0$ the propagated amplitudes of the components are $a_r^{(p)} \sim \omega_0 a_r$ and $a_l^{(p)} \sim (\omega_0 + \omega_d)a_l$. Substituting this into (A.55) definition of the ellipticity gives

$$\tan\left[\chi^{(p)}\right] \simeq \frac{\omega_0 a_r - (\omega_0 + \omega_d)a_l}{\omega_0 a_r + (\omega_0 + \omega_d)a_l} \approx \frac{a_r - a_l\exp[\omega_d/\omega_0]}{a_r + a_l\exp[\omega_d/\omega_0]} , \tag{F.33}$$

where in the second step the $\exp[x] = 1 + x + \ldots$ approximation was used from right to left, as $\omega_d \ll \omega_0$. This analytical formula nicely reproduces the ellipticity obtained with numerical calculations. The instantaneous orientation of the rotating pulse does not change during propagation according to (3.66), as (F.31) does not depend on time.

Acknowledgments

Writing an acknowledgment is always a thankless task because the fear is always inside you that you forget to mention someone's name. To avoid this little inconvenience, I would like to express my gratitude in an explicit way only to those, by mentioning their names, who directly contributed to the results presented in this thesis.

First of all, I would like to thank my supervisor, Zoltán Horváth, who supported me during my whole PhD studies, and who was just the perfect guide in this period of my scientific carrier.

I am also greatly thankful to Miguel Angel Porras. Without his guidance not even half of the achievements would have been reached.

I thank the help of Attila Kovács in the experimental campaigns. His suggestions helped me to step further after each pitfall of the measurements.

I was also happy to work with Dániel Nemes, who proved to be a great assistance in the laboratory.

Of course, I am also grateful to my colleagues, friends and family, who — everyone in his/her own way — supported and assisted me during this time.

Naturally, the work presented in these pages could not have reached a conclusion without financial support. I thank the partial assistance of the TÁMOP-4.2.2/B-10/1-2010-0012, TÁMOP-4.2.2.A-11/1/KONV-2012-0060, and TÁMOP-4.2.2.D-15/1/KONV-2015-0024 projects. Some of my conference presentation would not have been possible without the help of TÁMOP-4.2.4B/2-11/1-2012-0001 "Campus Hungary Program". I am specifically grateful for the support of TÁMOP 4.2.4.A/2-11-1-2012-0001 "National Excellence Program".